Multimodal analysis of intracranial aneurysm walls

DISSERTATION

zur Erlangung des akademischen Grades

Doktoringenieurin (Dr.-Ing.)

angenommen durch die Fakultät für Informatik
der Otto-von-Guericke-Universität Magdeburg

von M.Sc. Annika Niemann

geb. am 03.04.1995   in Peine

Gutachterinnen/Gutachter

PD Dr. Sylvia Saalfeld
Prof. Dr. Vasileios Belagiannis
Prof. Dr. Anja Hennemuth

Magdeburg, den 27.09.2022

Contents

Abstract

Intracranial aneurysms are pathological dilatations of brain vessel walls. As aneurysm rupture can have fatal consequences, treatment of intracranial aneurysms aims to prevent aneurysm rupture. Treatment decisions depend on the assessment of aneurysm rupture risk. While the factors leading to aneurysm rupture are not completely understood yet, it is suspected that changes in the aneurysm wall play a major role in aneurysm rupture.

In this thesis, several tools for analysis of the intracranial aneurysm wall were developed. First, the wall of an aneurysm and its parent vessel are reconstructed as a 3D model based on 2D histologic data. These data were collected post mortem. Second, histologic and microCT images of a tissue sample were combined with preoperative data. Both projects include histologic data, which are useful in research but cannot be used in clinical routine, as the necessary tissue collection requires opening the skull. Two further projects on how the aneurysm wall could be included into clinical routine are part of this thesis. In the near future, rupture risk assessment could be aided by vessel wall imaging, wall enhancement segmentation and geometric deep learning rupture prediction. In the distant future, hemodynamic parameters like the wall shear stress could also be included in clinical routine. Here, first steps towards this are presented.

From 2D histologic images a 3D model of the aneurysm wall is constructed. This includes the definition of tissue classes occurring in the aneurysm wall, segmentation of the images into these classes and extraction of the contours of each tissue section. Then, the contours are registered, 3D point clouds are derived and meshes are generated. For the mesh generation a new algorithm based on the behaviour of a shrinking tube was developed. The final 3D model of the wall includes over 100 smaller meshes showing the various tissue sections of the aneurysm wall.

The second project combines histologic images with additional pre- and post imaging. A preoperative 3D model of the aneurysm and a microCT scan of the tissue provide additional information about the shape. The model of the wall tissue from the microCT image is registered and deformed to fit the preoperative aneurysm shape. The histologic images are mapped to the corresponding microCT images. Together with the wall shear stress these information are combined in a user interface for visual exploration.

Current research indicates a correlation between wall enhancement and rupture of intracranial aneurysms. However, a problem is the objective and automatic segmentation of wall enhancement for research and clinical routines in the future. To integrate vessel wall imaging and wall enhancement in clinical routine, a

semi-automatic wall enhancement segmentation is developed. Additionalyl, the aneurysm shape is used for rupture prediction with geometric deep learning. A visualization of the deep learning to increase acceptance of the prediction is also presented.

Hemodynamic parameters like the wall shear stress are a major part of aneurysm research. For clinical routine, hemodynamic simulations are too time-consuming and require expert knowledge. As a first step towards inclusion of these parameters in clinical routine, geometric deep learning approaches to reduce the effort for hemodynamic simulations are presented. The wall shear stress of artificial as well as patient-specific aneurysms is predicted with geometric deep learning.

Zusammenfassung

Intrakranialle Aneurysmen sind krankhafte Veränderungen der Gefäßwände im Gehirn. Die Ruptur eines intrakraniallen Aneurysmas kann fatale Folgen haben, weswegen das Ziel der Therapie eine Verhinderung der Ruptur ist. Da das individuelle Rupturrisko stark variiert und viele Aneurysmen nicht rupturieren, ist die Analyse des Rupturrisikos ein wichtiger Teil der Therapieentscheidung. Die Faktoren, welche zur Ruptur eines Aneurysmas führen, werden noch erforscht. Aktuelle Forschung deutet darauf hin, dass Veränderungen in der Aneurysmenwand eine wichtige Rolle bei der Aneurysmenruptur spielen.

In dieser Arbeit wurden Algorithmen zur Analyse und Erstellung von 3D-Modellen patientenspezifischer Aneurysmenwände aus histologischen Bilddaten entwickelt. Im ersten Projekt wird die Rekonstruktion eines 3D-Modells eines Aneurysmas einschließlich des Elterngefäßes basierend auf 2D histologischen Daten beschrieben. Diese Daten wurden post mortem gewonnen. In einem weiteren Projekt wurden histologische und microCT-Bilder eines während einer Operation entfernten Gewebestückes mit präoperativen Daten kombiniert. Beide Projekte verwenden histologische Daten, welche zwar wichtig für die Erforschung der Aneurysmenwand, jedoch nicht für den klinischen Alltag geeignet sind, da sie die Entnahme des Aneurysmagewebes im Rahmen eines operativen Eingriffs erfordern. Zwei weitere Projekte in dieser Arbeit betrachten Möglichkeiten, die Aneurysmenwand im klinischen Alltag zu verwenden. In Zukunft könnte die Abschätzung des Rupturrisikos durch *vessel wall imaging*, Segmentierung des *wall enhancement* und *geometric deep learning* unterstützt werden. Des Weiteren könnten hämodynamische Parameter wie die Wandschubspannung in Zukunft Teil der klinischen Beurteilung von intrakraniallen Aneurysmen werden.

2D histologische Bilder wurden verwendet, um ein 3D-Modell der Gefäßwand eines intrakraniallen Aneusymas zu konstruieren. Diese Rekonstruktion beinhaltet die Definition verschiedener in der Wand auftretender Gewebetypen, die Segmentierung der Bilder und die Extraktion der Konturen der einzelnen Gewebestücke. Anschließend erfolgt eine Registrierung der Gewebe und Erstellung von 3D-Punktwolken sowie Meshes. Für die Meshgeneration wurde ein neuer Algorithmus basierend auf dem Verhalten eines Schrumpfschlauches entwickelt. Das resultierende 3D-Mo-dell der Wand besteht aus über 100 kleinen Meshes, welche die verschiedenen Gewebestücke der Aneurysmenwand zeigen.

Das zweite Projekt kombiniert histologische Bilder mit weiteren prä- und postoperativ gewonnenen Bildern. Ein 3D-Modell des Aneurysmas basierend auf präoperativen Bildern zeigt die Form des Aneurysmas und ein microCT-Scan die Form des Gewebes vor der Erstellung der histologischen Schnitte. Das aus dem microCT gewonnene Gewebemodell wurde auf das präoperative Aneurysma-Modell registriert und an die Aneurysmenform angepasst. In einem *visual exploration*

tool sind die Informationen aus histologischen Bildern, microCT, präoperativen Bildern und hämodynamischen Simulationen kombiniert.

Vorherige Studien legen einen Zusammenhang zwischen *wall enhancement* und Aneurysmenruptur nahe. Derzeit fehlt eine automatische und objektive Segmentierung für weitere Forschung und zukünftige Anwendung im klinischen Alltag. In dieser Arbeit wird eine semi-automatische Segmentierung vorgestellt. Des Weiteren wird mittels *geometric deep learning* die Form des Aneurysmas zur Vorhersage der Aneurysmenruptur verwendet. Eine Visualisierung der *deep learning* Resultate soll zur Akzeptanz dieser beitragen.

Hämodynamische Parameter wie die Wandschubspannung sind ein aktives Forschungsfeld der Aneurysmenforschung. Da die Simulation des Blutfluss Expertenkenntnisse voraussetzt und zeitaufwendig ist, ist sie nicht für den Klinikalltag geeignet. In dieser Arbeit wird *geometric deep learning* verwendet, um den Aufwand zu reduzieren. Für künstliche Aneurysmenmodelle sowie für patientenspezifische Aneurysmen wird die Wandschubspannung mittels *deep learning* vorhergesagt.

1 Introduction

Intracranial aneurysms are deformations of brain arteries (see Fig. 1.1). The berry-shaped bulges of the vessel can rupture, leading to blood inside the brain. As aneurysm rupture can have fatal consequences, treatment of intracranial aneurysms aims to prevent aneurysm rupture. Possible interventions are endovascular treatment or surgical clipping. Due to their location, both treatments also possess a risk for the patient. Not all aneurysms rupture. To avoid unnecessary risks for the patients, only aneurysms that would rupture without treatment should be treated. To decide whether treatment is recommended for a patient, the correct estimation of the aneurysm rupture risk is necessary. At the moment, this is hindered as the processes leading to aneurysm rupture are not fully understood yet. Previous research suggests that the aneurysm wall plays a major role in aneurysm rupture. In this thesis, several tools to advance aneurysm wall research are presented.

Current research of the aneurysm wall composition uses histologic images. Histologic images allow a detailed analysis because they provide information about the cells and tissues present in the wall, but they require the collection of aneurysm tissue and therefore an operative opening of the cranium. They are either collected post mortem or during surgery. While providing useful information about aneurysm forming and remodeling, these images are only used for research and not in clinical routine. The images are restricted to 2D, therefore loosing valuable information about the aneurysm shape.

In contrast to histologic images, black blood magnetic resonance imaging (BB-MRI) is non-invasive and might be used to evaluate the rupture risk of aneurysms in patients in the future. While not as detailed as histologic images, BB-MRI can show wall enhancement. Recent studies suggest that wall enhancement is a useful factor in predicting aneurysm rupture. A major limitation is the currently subjective evaluation of the wall enhancement.

Another ongoing research aspect is the behavior of the wall and hemodynamic wall features like the wall shear stress. Despite the large presence of hemodynamic simulations in research, they are not used in clinical routine. Hemodynamic simulations are time-consuming, labor-intensive and require expert knowledge.

This thesis provides tools for a better understanding of the wall of intracranial aneurysms. To improve research with histologic images, a 3D model based solely on post mortem collected histologic images is described. This includes semantic segmentation of the images, and registration and mesh generation with the newly developed shrinking tube mesh algorithm.
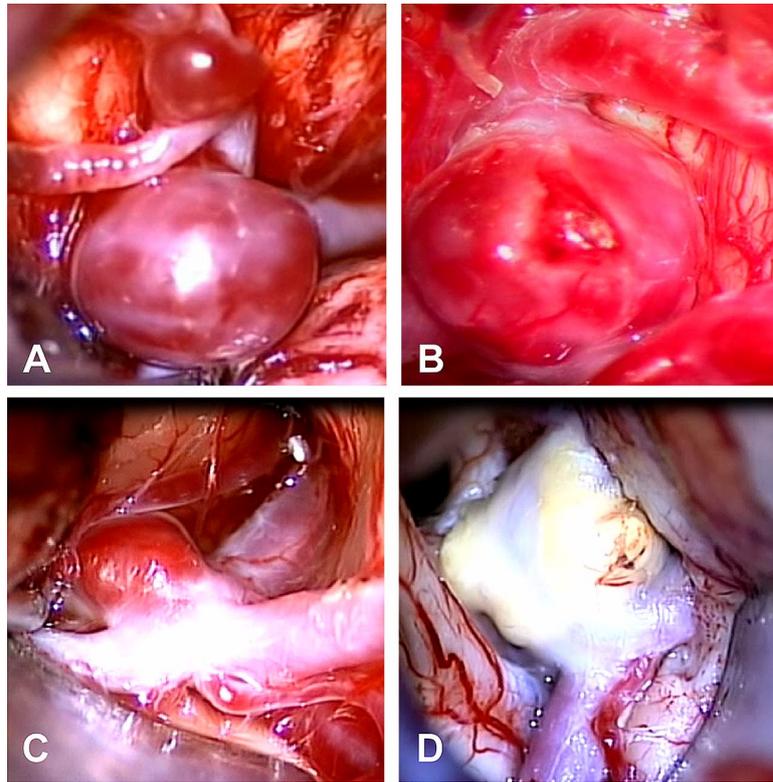
Figure 1.1: Intraoprative images of intracranial aneurysms with various wall structures [1]

The resulting model allows a 3D view of the wall composition of an intracranial aneurysm and can also be used for simulation. Moreover, a unique combination of pre- and postoperative imaging is presented. With preoperative data the aneurysm shape is preserved. MicroCT and histologic images of aneurysm wall tissue collected during surgery provide detailed information about the aneurysm wall. Hemodynamic simulation adds further information. All these aspects are combined in a user interface for a new visual exploration of the aneurysm wall.

In the future, BBMRI could be used in clinical routine. As a step towards reliable and easy segmentation of wall enhancement, a semi-automatic wall enhancement segmentation tool is developed. Furthermore, the impact of various BBMRI modalities on the segmentation is discussed.

To pave the way towards the inclusion of hemodynamic parameters into clinical routine, geometric deep learning applications are explored. The experiments presented in this thesis suggest that wall shear stress of artificial as well as patient-specific aneurysms can be predicted with geometric deep learning.

The thesis is structured into medical and technical background, related work, aneurysm research for wall understanding with histologic images and research towards the inclusion of the aneurysm wall in clinical routine.

First, the medical background of aneurysms is described and different medical imaging systems are explained in Chapter 2. Recent work in the area of image processing for histology and BBMRI is described in Chapter 3. Then, the current research on mesh processing and hemodynamic analysis is discussed in Chapter 4.

Chapter 5 summarizes the research questions arising from the current situation described in Chapter 2, 3 and 4. These questions are answered in detail in Chapters 6 to 9 and Chapter 10 provides a summary with short answers to the research questions.

Chapter 6 describes the construction of a 3D aneurysm wall model including the parent vessel based on post mortem histologic image data. It includes segmentation, virtual inflation, mesh generation and model generation. In the next Chapter, the combination of histologic images with further data is described. The wall tissue information from histology are combined with microCT shape and calcification data and hemodynamic parameters from a preoperative aneurysm model.

Chapter 8 presents a semi-automatic wall enhancement segmentation, deep learning rupture prediction and visualization of this deep learning approach. Chapter 9 focuses on tools to simplify hemodynamic simulations. The first part of that chapter discusses improvements of mesh processing for simulation and the second part presents geometric deep learning for wall shear stress prediction.

2 Background

Intracranial aneurysms are a complex disease. Several challenges occur during aneurysm detection, treatment decision and treatment. Imaging of intracranial aneurysms can be achieved with various imaging modalities. These have several limitations and not all techniques are suitable for clinical use. Here, the current options for aneurysm treatment and diagnosis are described. Especially risk factors for aneurysm development and rupture are discussed, as the assessment of the individual rupture risk of an aneurysm is a crucial part in clinical routine. At the moment, there is a gap between research on rupture risk and clinical rupture risk assessment. Chapter 8 and 9 will present how this gap could be closed with deep learning on surface meshes to predict rupture and include hemodynamic features.

2.1 Medical background - Intracranial aneurysms

Healthy vessels consist of three layers: the tunica externa, tunica media and tunica intima (see Fig. 2.1). Intracranial aneurysms are deformations of vessels in the brain. As Figure 2.2 shows, the aneurysm is separated from the parent vessel by the neck and ostium. Additional to the shown elements an aneurysm might also include a bleb, a further bulge on the aneurysm body.
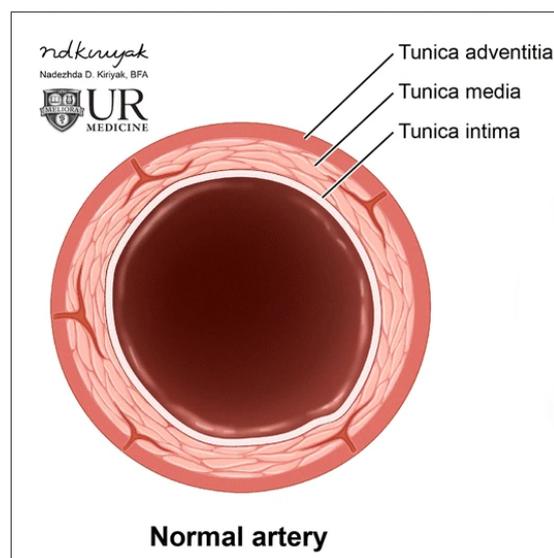
Figure 2.1: Structure of a healthy vessel wall [2]
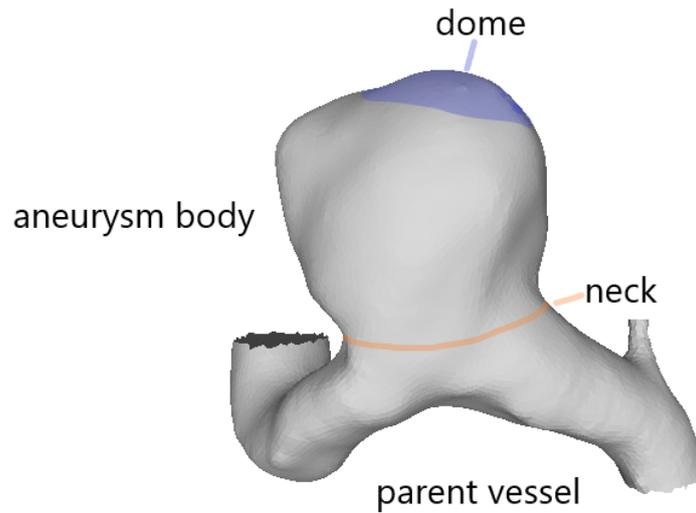
Figure 2.2: Structure of an aneurysm (based on [3])

Commonly, intracranial aneurysms are divided into saccular, fusiform, and dissecting aneurysms (Fig. 2.3). As saccular and fusiform aneurysms affect all three wall layers of the vessel, they are also called true aneurysms, while dissecting aneurysms are called false aneurysms. Besides this common morphology-based classification, aneurysms can be classified based on size, location and etiology [4].
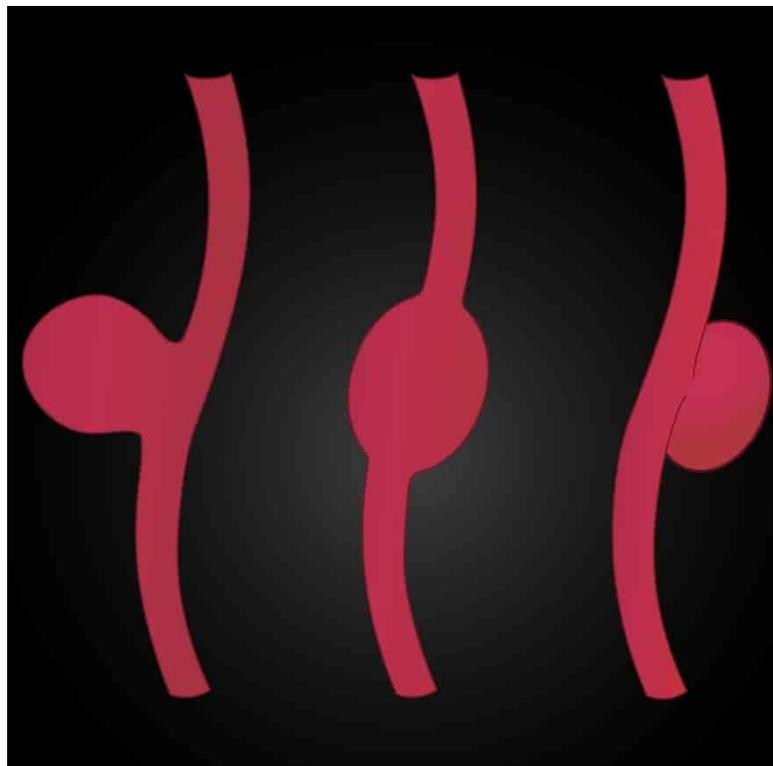
Figure 2.3: Different types of aneurysms [5]

Intracranial aneurysms are often asymptotic as long as they are not ruptured. Findings of unruptured intracranial aneurysms are normally coincidentally. Especially with the increased usage of imaging techniques, intracranial aneurysms are coincidentally found during diagnosis of other issues. Unruptured aneurysms may lead to symptoms due to their size. Common symptoms are headache, unilateral third cranial nerve palsy (posterior communicating artery aneurysm), bilateral temporal hemianopsia (anterior communication artery aneurysm), ischemic cerebrovascular disease and seizures [6]. The rupture of an aneurysm leads to subarachnoid hemorrhage (SAH) and has a mortality rate up to 50%. While the rupture of an aneurysm can have fatal results, only some aneurysms rupture. Intracranial aneurysms have a prevalence of 1-5 % and 50-80% of the aneurysms do not rupture during the patient's lifetime [7]. Common treatments of intracranial aneurysms are clipping and coiling. These are described in more detail in Section 2.1.3. Due to their location, the treatment of intracranial aneurysms has some risks. Therefore, the necessity of treatment and the best therapy for the patient have to be chosen carefully. At the moment, the mechanisms leading to aneurysm formation and aneurysm rupture are not fully understood [4]. Further research on the processes leading to aneurysm rupture is needed. Chapter 6 and Chapter 7 describe tools for 3D exploration of the intracranial aneurysm wall to gain insight in these processes.

Aneurysms are rare in children and are normally developed during life. As a result of a connective tissue disease, an aneurysm can occur in neonates or young babies. Persons of older age and women are more likely to develop an aneurysm. Other risk factors for aneurysm formation and SAH are smoking, heavy alcohol consumption, Finish or Japanese descent, hypertension, and atherosclerosis [4].

The most common type of intracranial aneurysms are saccular aneurysms [8]. They are berry-shaped vessel outpouchings [4]. The shape of saccular aneurysms varies. Some are rather small and round outpouchings while others are larger and elongated, and some may include blebs. Some examples are shown in Figure 2.4. This work is restricted to saccular aneurysms.

The exact reasons for aneurysm development are an ongoing research topic. Dörfler and Wanke [4] suspect that the most common reasons are vascular injuries, atherosclerosis, high flow states, or underlying vasculopathy, and uncommon reasons are trauma, infection, drug abuse, and neoplasms. Several studies suspect the involvement of inflammation in aneurysm formation [10, 11]. After intracranial aneurysm rupture, the inflammation-related protein levels in the peripheral blood are alternated. In peripheral blood cells the expression of miRNAs, which are related to inflammation and immune response, are influenced by aneurysm rupture [12]. Chalouhi et al. [7] proposed that hemodynamic stress induces endothelial dysfunction and is followed by an inflammatory reaction in the vessel wall. These theories may lead to new therapeutic approaches using pharmaceuticals and thus avoiding the risks of invasive therapies like clipping and coiling.
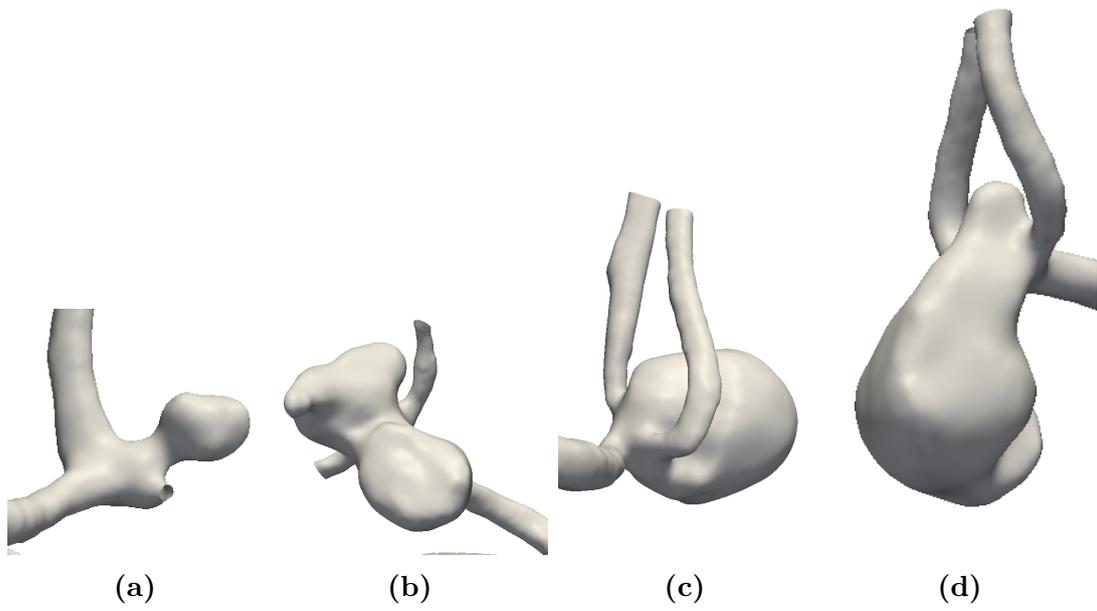
Figure 2.4: Examples of intracranial aneurysms (data from the Aneurisk dataset [9])

Figure 2.5 shows arteries in the brain. Aneurysms can occur at every artery. Most intracranial aneurysms arise at bifurcations of arteries. With 30-35% the anterior cerebral artery is the most common location for intracranial aneurysms, followed by the middle cerebral artery (30%). Around 7.5% of the intracranial aneurysms occur at the basilar tip and approximately as many develop from other posterior fossa vessels [4]. 7-34% of patients with intracranial aneurysms have more than one aneurysm. Patients with multiple aneurysms may have between 2 and 13 aneurysms [13]. Among other things, multiple aneurysms are associated with female sex, hypertension and blood group AB [14].
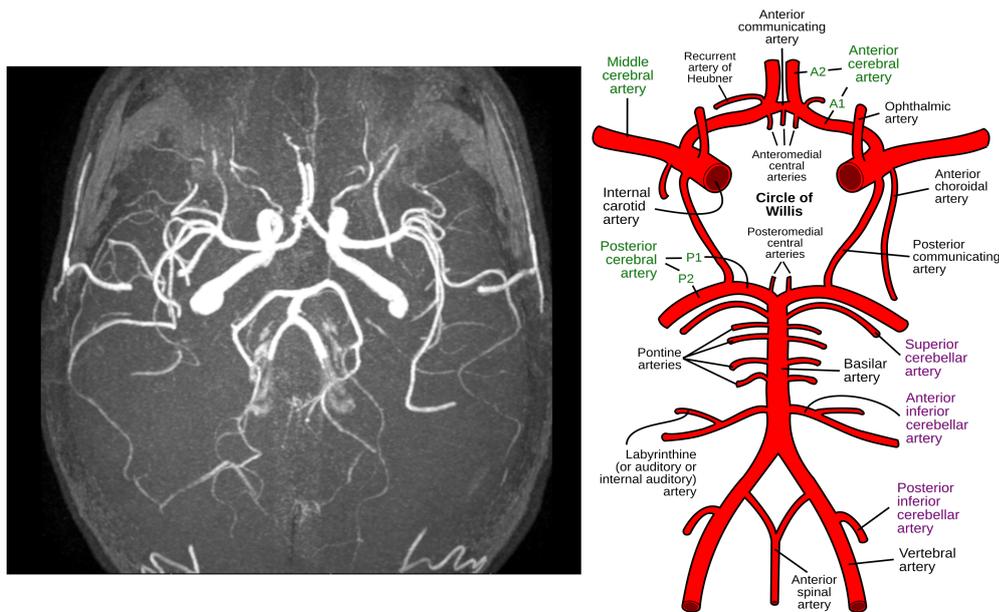
Figure 2.5: Arteries in the brain [15]

Blebs are additional outpouchings on the aneurysm, as shown in Figure 2.6. Blebs occur in 36% of the aneurysms. 77% of the aneurysms with blebs have a single bleb. Blebs most likely occur at the dome (48%) or the aneurysm body (46%) and only rarely at the neck. Aneurysms with blebs tend to be larger, more elongated, and with a wider neck. A positive correlation between dental infection and blebs and a negative correlation between treatment with hormone replacement therapy and bleb occurrence was found [16].
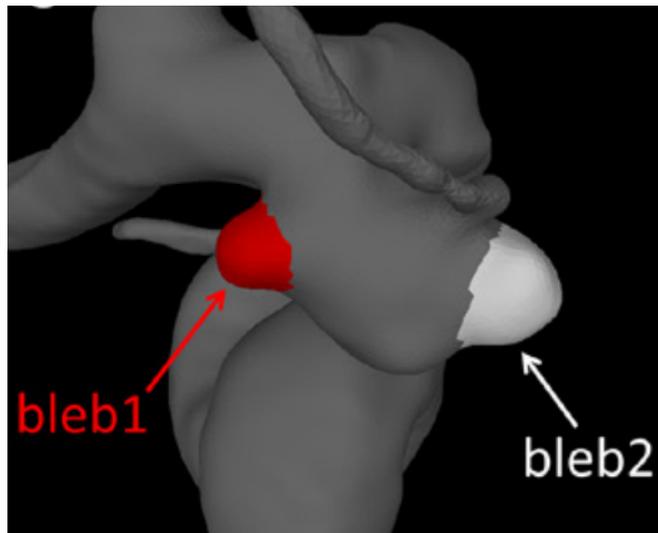
Figure 2.6: Example of aneurysm with two blebs [17]

Two grades commonly used in patient evaluation after aneurysm rupture are the Fisher scale and the Rankin scale. These are used in clinical routine and in Section 2.1.3 to compare different treatment methods. The Fisher scale [18] describes the amount of subarachnoid hemorrhage in CT scans. It consists of:

- grade 1: no SAH or intraventricular hemorrhage (IVH) visible

- grade 2: diffuse thin (>1mm) SAH, no clots

- grade 3: larger SAH or clots

- grade 4: diffuse or no SAH, IVH present

The Rankin scale measures the degree of disability after a stroke or other causes of neurological disability [19]. It includes 7 classes:

- 0: no symptoms

- 1: no significant disability, can carry out usual activities despite some symptoms

- 2: slight disability

- 3: moderate disability, walk without assistance

- 4: moderately severe disability, unable to walk, assistance needed

- 5: severe disability, constant care needed

- 6: dead

2.1.1 Detection & diagnosis of aneurysms

Here, the techniques used for diagnosis of intracranial aneurysms are described. The technical aspects of the various imaging techniques are discussed in Section 2.2. Chapter 8 and 9 use models derived from images used in clinical routine. Based on these models the rupture risk of patient-specific intracranial aneurysms is assessed. Evaluation of the individual rupture risk is necessary to select the optimal treatment. The currently available treatments are described in Section 2.1.3.

There are several imaging techniques used in the diagnosis and treatment of intracranial aneurysms. The most common ones are computer tomography angiography (CTA) and magnetic resonance angiography (MRA). A disadvantage of CTA is the usage of radiation. Besides these two non-invasive imaging techniques, intracranial aneurysms can be diagnosed with catheter angiography, which is expansive and invasive [7]. For aneurysm analysis outside of diagnostic tasks, additional imaging modalities are available. For example, optical coherence tomography (OCT) and histologic images of aneurysms from cadavers are used in the research of the aneurysm wall [20].

Digital Subtraction Angiography (DSA) with selective cerebral arterial injections and multiple projections is the most reliable technique for identification of intracranial aneurysms. It has a risk of 1% for transient and 0.5% for permanent neurological complications. This invasive imaging is not regularly used due to the risk of complications [21].

The sensitivity of CTA is between 77% and 97% and MRA exhibits a sensitivity between 70% and 99%. For aneurysms smaller than $3\,\mathrm{mm}$ the sensitivity drops significantly to 40% for MRA and 40% to 91% for CTA. The specificity of MRA is up to 100% and for CTA 87% to 100% [7].

Kwak et al. [22] analyzed 652 unruptured intracranial aneurysms from 530 patients to evaluate the sensitivity and accuracy of MRA for small unruptured aneurysms ($< 7\mathrm{mm}$). Two independent reviewers analyzed the shape of the aneurysms using MRA images. The aneurysms were divided into two groups: aneurysms with regular shape and aneurysms with a irregular shape, therefore more likely to rupture. DSA was used as a reference. The sensitivity for detecting shape irregularity was 60.4% for one reviewer and 60.9% for the other reviewer. Anterior cerebral artery aneurysms and aneurysms smaller than $3\,\mathrm{mm}$ had even lower sensitivities (under 47% and under 27%). The 1.5T MRA had a lower sensitivity than the 3T MRA.

To better discriminate between rupture-prone aneurysms needing treatment and aneurysms which do not require treatment, new diagnosis techniques are developed.

Recent research highlighted the role of macrophage-mediated chronic inflammation in aneurysm development. Based on this, Shimzu et al. [23] developed an imaging technique to visualizes macrophages infiltrating in lesions. They used

ferumoxytol, an ultrasmall superparamagnetic iron oxide particle, as contrast agent to detect macrophages using MRI. Based on the presence or absence of macrophages they divided aneurysms into active lesions and stable lesions [23].

Chapter 3 further discuss how different image types are used in research to analyze the aneurysm wall. In Chapter 8, research to include vessel wall imaging in clinical routine is presented.

2.1.2 Prognosis of development and rupture: risk factors

In this Section, research on factors leading to aneurysm rupture are discussed. In Chapter 9, tools for automatic mesh processing and morphological parameter extraction are presented. An alternative to the usage of these parameters could be deep learning, as described in Chapter 8. Risk factors related to the aneurysm wall and wall enhancement are discussed in Chapter 3.

The international study of unruptured aneurysms (ISUIA) determined that aneurysms larger than 10 mm or aneurysms at the posterior circulation or posterior communication artery have a higher rupture risk than other aneurysms. Another major risk factor was the occurrence of SAH of another aneurysm in patients with multiple aneurysms. The study included 2621 patients from 53 centers in the United States, Canada, and Europe [24].

The usage of the PHASES score (Population, Hypertension, Age, Size of aneurysm, Earlier subarachnoid hemorrhage, Site of aneurysm) is controversial. Feghali et al. [25] analyzed ruptured aneurysms and used scores to access which treatment would have been recommended if the aneurysms were detected before rupture. They calculated the PHASES score for 992 patients and the unruptured intracranial aneurysm treatment score (UIATS) for 266 patients. Based on the PHASES score, 54% of the ruptured aneurysms had a low rupture risk (5-year risk $\leq$ 1.3). Based on the UIATS, observation would be recommended for 23-34% of the patients.

A recent study analyzing 9940 patients, including 6555 women, confirmed that women had a higher risk of aneurysm rupture than men. This difference could not be explained by patient- or aneurysm-related risk factors. Women more often had aneurysms at the internal carotid artery and more aneurysms larger than 7 mm [26].

Suzuki et al. [27] analyzed the rupture risk of small intracranial aneurysms (aneurysms <10mm). They analyzed 338 aneurysms, 35 ruptured and 303 unruptured. The study population only consists of Japanese adults. Previous studies determined Japanese origin as a risk factor for aneurysm rupture. Based on CT images they carried out hemodynamic simulations. They found several risk factors for the rupture of small aneurysms: young age, multiple aneurysms, bifurcation aneurysms, aneurysms with bleb, and large aneurysm length.

Feng et al. [28] analyzed 1671 intracranial aneurysms from 700 patients with multiple aneurysms. Similar to the PHASES score, they developed a rupture risk prediction specifically for patients with multiple aneurysms. Their categories are all designed to be answered with yes or no. The highest weighted category is "history of SAH", followed by "located at posterior circulation", "aspect ratio > 1.55" and "female". Further categories are "drinking", "bifurcation" and "irregular shape".

Wang et al. [29] analyzed 20,280 patients with aortic aneurysms and 20,280 patients without aortic aneurysms. They found that intracranial aneurysms were associated with aortic aneurysms. This also depends on the treatment of the aortic aneurysms: open surgical repair was associated with fewer intracranial aneurysms than nonsurgical treatment.

Although aneurysms in children are rare, they are possible. They have a high risk for seizures. The risk of preoperative seizures in pediatric patients with intracranial aneurysms is increased by younger age (< 5years), head trauma history, lobe hematomas, modified Fisher grade 3-4, giant aneurysms, and distal arterial aneurysms. The risk of postoperative seizures is lower for surgical interventions than for endovascular treatment [30].

Molenberg et al. [31] evaluated the use of the UIATS for the prediction of aneurysm growth. 214 patients were followed for a mean period of 1.3 years. Their study showed that the UIATS was not able to predict aneurysm growth or rupture. However, the results are limited by the biased patient selection.

Especially for multiple aneurysms, the PHASES score is problematic [32]. The PHASES score is aimed at single aneurysms. Feng et al. [33] applied the PHASES score to 701 patients with altogether 1673 aneurysms. They tried to predict the occurrence of rupture in a patient based on the PHASES score of the largest aneurysm, highest PHASES score, sum of PHASES score and mean PHASES score. None of these were suitable and more accurate models are needed.

According to a study by Rousseau et al. [34] the location is the most significant factor in aneurysm rupture. This is followed by age. Their study included 2505 patients. In contrast to the PHASES and UIATS score, the size was not a factor relevant for aneurysm rupture.

More and more morphological and hemodynamic parameters were introduced in the last years to predict aneurysm rupture. Neyazi et al. [32] criticized this as unpractical and not applicable in clinical practice. Based on 87 aneurysms from 38 patients with multiple aneurysms they propose aneurysm rupture prediction based on two parameters: the aspect ratio (height of the aneurysm measured vertically to the aneurysm neck / maximum diameter of the aneurysm neck) and from the hemodynamic parameters the maximum relative residence time. These parameters showed differences between ruptured and unruptured aneurysms and low correlation to other risk factors.

Asgharzadeh et al. [35] propose a classification based on a single parameter, the aneurysm number. The number is calculated based on the parent artery diameter, the neck size, and the pulsatility index, which is derived from the average, minimum and maximum velocity in the parent artery. With this, a specificity of 33% was reached.

Varble et al. [36] compared small (<5mm) and large aneurysms. For both, morphological parameters, especially the undulation index, were important. To discriminate between small ruptured and unruptured aneurysms, the oscillatory shear index, previous SAH and number of aneurysms are useful, while for large aneurysms wall shear stress and aneurysm location are relevant factors.

Shi et al. [37] trained a support vector machine (SVM) to classify aneurysms as ruptured and unruptured. They used data from CTA and included clinical characteristics, morphological and hemodynamic parameters. For training, 410 aneurysms were used, and 94 aneurysms for testing. Further evaluation included data sets with 30 and 22 aneurysms from different hospitals. They reached a sensitivity between 54.5% and 81.8% and a specificity between 73.7% and 91.1%.

Yang et al. [38] classified aneurysms from 36 patients to predict whether they were stable or unstable over 36 months. They used a backpropagation neural net and 45 features. The best results were achieved by using clinical, morphological, and hemodynamic features. If only one of these three groups was used, morphological features achieved the best results. Amigo et al. [39] compared different machine learning algorithms and suggest the usage of a random forest classifier to classify ruptured and unruptured aneurysms. However, they only used a total of 71 patients which severely limits the result.

Ahn et al. [40] used a multi-view CNN architecture to predict the rupture risk of small unruptured aneurysms. They used 364 3D-DSA images for training and 93 for testing. An accuracy of 81.72% was reached.

The aneurysm size alone is not a reliable parameter for the prediction of aneurysm rupture. Especially for small aneurysms other factors like neck size and parent vessel diameter should be included. Ruptured aneurysms have a lower wall shear stress than unruptured aneurysms. Currently, no single factor can be identified as responsible for aneurysm rupture. A combination of shape and
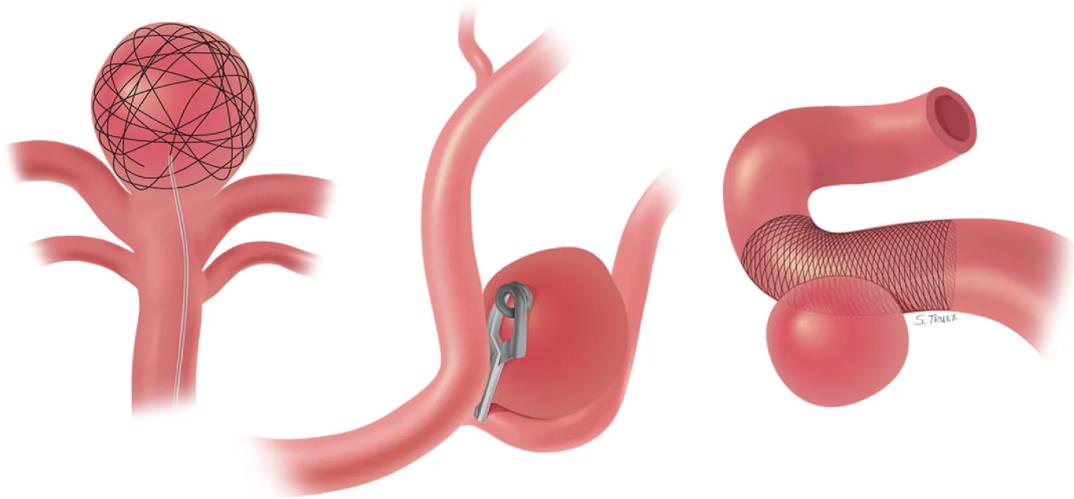
Figure 2.7: Left: minimally invasive placement of coils in the aneurysm, middle: clipping of an aneurysm, right: stent under aneurysm [42]

hemodynamics could lead to a better understanding of aneurysms and rupture risk [41]. The hemodynamic aspects of aneurysm research are further described in Section 4.2.

Predicting aneurysm rupture is an important step towards selecting the right treatment. While clinical routines only use a very limited number of factors, research studies explored a large number of factors related to aneurysm rupture. Some of these factors are further explored in this thesis: morphological parameters and hemodynamic parameters. The focus is on practical applications which could help including these parameters into clinical routine.

2.1.3 Treatment of intracranial aneurysms

There are several options for the treatment of intracranial aneurysms. Figure 2.7 shows the most common treatment methods. Aneurysms are treated by alternating the blood flow to prevent aneurysm rupture. Alternatively, the blood flow in the aneurysm can be completely stopped with clipping. To find the best treatment, the risk of treatment and the risk of aneurysm rupture are evaluated. Here, different treatments and their risks are described.

The main options for aneurysm treatment are micro-surgical clipping and endovascular treatment. Clipping involves opening the cranium and placing a clip around the aneurysm neck to prevent blood flow into the aneurysm. Combined

treatment with clipping and coiling is also possible [43]. For clipping, the mortality rates are between 1 and 3%. In some cases, technical failures like incomplete occlusion (5.2%), recurrence (1.5%) or hemorrhage (0.26%) can occur [44].

Coiling is a minimally invasive treatment option and as such less physiologically stressfull than clipping. By placing detachable coils inside the aneurysms the blood flow in the aneurysm is reduced or completely stopped. The mortality rate for coiling is between 1.1 and 1.5%. The risks of coiling are arterial dissection (0.7%), parent-artery occlusion (2.0%), thromboembolic phenomena (2.4%), and minor risks similar to the risks of diagnostic catheter angiography (for example reactions to material, groin hematomas and infections). In 1.4 to 2.7% of the cases the aneurysm ruptures during the catheter advancement or the coil placement and of these cases the mortality rate is between 30% and 40%. In 85 to 90.4% of the aneurysms treated with coiling an occlusion over 90% was reached. Coiling is less successful for larger aneurysms or aneurysms with a wide neck. The treatment of aneurysms with coiling is an active research field and with the development of new coils the treatment is improved [44].

The blood flow can also be alternated by placing a stent in the vessel. A stent can be used alone or to support treatment with coils. An example of a flow diverting stent is a pipeline embolization device. It consists of a tightly braided mesh. The mesh causes stagnation of blood in the aneurysm sac and leads to occlusion of the aneurysm while allowing blood flow in the vessel branches [7].

Meyers et al. [45] researched the usage of flow diverters for large or giant wide-neck intracranial aneurysms. Treatment of 180 patients in 26 medical centers showed that in 62.8% of the cases the treatment was effective (complete aneurysm occlusion, no significant parent artery stenosis, and no retreatment in 12 months).

In a multicenter cohort of 1088 patients, the treatment of intracranial aneurysms with coiling and balloon-assisted coiling was analyzed. Two risks of these interventions are thrombotic events and intraoperative rupture. Thrombotic events occurred in 113 of the 1088 patients, and of these 113 patients 29 were impaired in their daily life after the intervention (Rankin scale score of 3-6). Intraoperative rupture was less common, with 34 cases, but as dangerous (11 of 34 cases had a Rankin scale score of 3-6). Risk factors for thromboembolic events were female gender and middle cerebral artery location. Anterior communicating artery location and small aneurysm size were risk factors for intraoperative rupture [46].

Aneurysms can be occluded with flow diverters. These lead to an alternation of the blood flow resulting in intra-aneurysmal thrombosis (see Fig.2.8). In contrast to surgical treatment, this does not take immediate effect [47].

Another treatment option for unruptured intracranial aneurysms is medication. The anti-inflammatory effect of aspirin may decrease aneurysm growth and rupture risk. Roa et al. [48] analyzed 96 unruptured intracranial aneurysms. The wall enhancement in BBMRI was calculated based on the aneurysm-to-pituitary
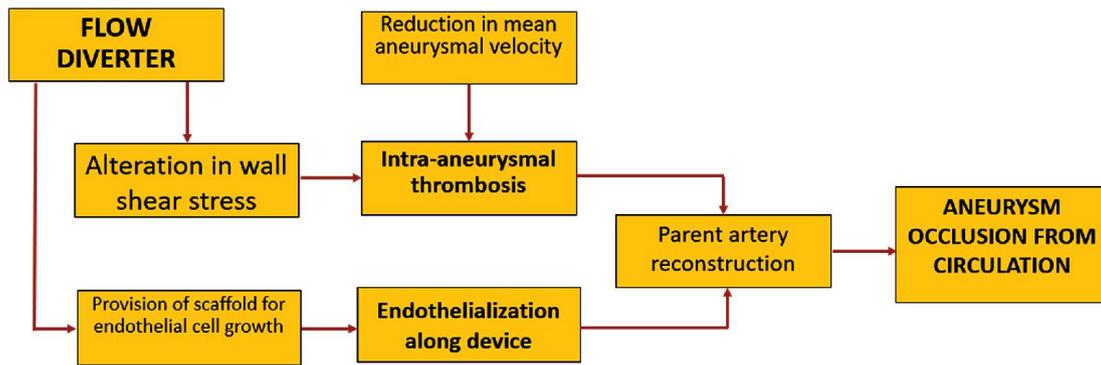
Figure 2.8: Process of aneurysm treatment with flow diverter [47]
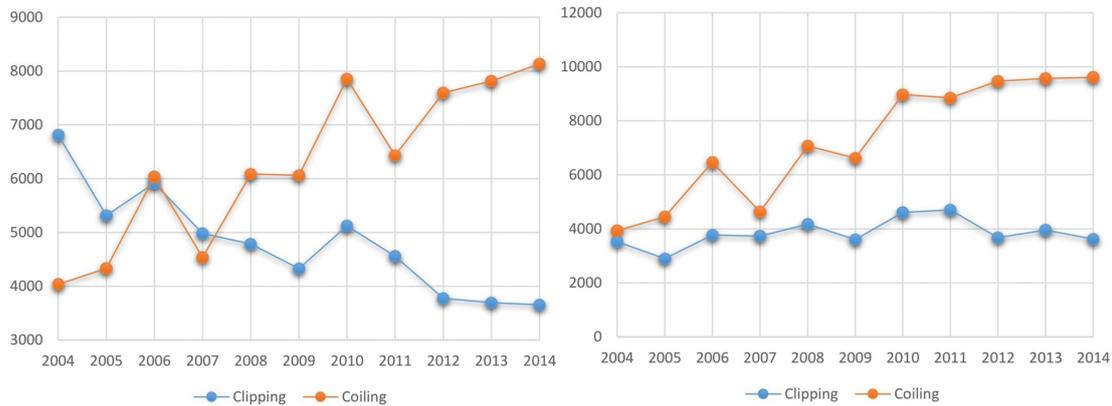
(a) Treatment of ruptured aneurysms in the United States between 2004 and 2014 [49]

(b) Treatment of unruptured aneurysms in the United States between 2004 and 2014 [49]

Figure 2.9: Development of preferred treatment method of ruptured and unruptured aneurysms

stalk contrast ratio. Wall enhancement was increased by age, aneurysm size over 7mm, and location in the anterior communicating, posterior communicating, and basilar artery. Daily usage of aspirin over at least six months significantly decreased wall enhancement. The usage of BBMRI in aneurysm research is further discussed in Section 3.3.

Another treatment option is the use of liquid embolic agents, for example Onyx HD-500, to close the aneurysm. It might be used to treat large, saccular aneurysms which have a large neck and cannot be treated by clipping or coiling. Due to the higher risk of unfavorable outcome (morbidity of up to 8%), its usage declined [7].

Over the years the preferred treatment methods changed. In 2004, 37% of ruptured aneurysms and 52% of unruptured aneurysms were treated with coiling. This largely increased over the years and in 2014 68% and 73% respectively, were treated with coiling. Similarly, the treatment with clipping decreased (Fig. 2.9a and Fig. 2.9b) [49].

Treatment of small unruptured aneurysms with surgical clipping or endovascular

treatment are similar in terms of procedure-related complications and neurological outcomes [50].

In a retrospective study, patients with ruptured aneurysms admitted to the University Hospital of Cologne and treated with microsurgical clipping between 2010 and 2019 were analyzed. The time of admission of the patient (during standard working hours or during on-call duty) did not significantly influence the outcome. Before multi-variable adjustment, an association between surgery during night time and worse patient outcome was found [51].

The Barrow Ruptured Aneurysm Trial (BRAT), a series of papers published between 2012 and 2015, evaluates the treatment of acutely ruptured cerebral aneurysms with clipping or coils. 358 patients who had undergone treatment were evaluated after one year. 33.7% of the patients treated with clipping and 23.2% of the patients treated with coiling had a modified Rankin Scale (mRS) score over 2 [52]. After three years, the difference was smaller (35.8% for clipping and 30% for coiling). In terms of aneurysm obliteration and recurrence, clipping was better [53]. This trend continued in the six-year follow-up. After six years, clipping resulted in complete aneurysm obliteration in 96% of the patients, coiling only in 48%. While the retreatment rates were higher for coiling, no recurrent hemorrhages occurred [54].

2.2 Technical background - Image acquisition

In this section, several image acquisition techniques are described. The focus is on the operating principle of image acquisitions. The commonly used techniques of CT and MRI for aneurysm diagnostics and their advantages and limitations regarding intracranial aneurysms are discussed in Section 2.1.1. Section 3.2 further discusses algorithms for processing histologic images and model generation from histologic images. The practical implications of BBMRI and studies regarding aneurysm wall enhancement in BBMRI are discussed in Section 3.3. Chapter 8 and 9 use 3D models derived from various imaging modalities used in clinical routine. Chapter 8 also discusses how wall enhancement in BBMRI can be segmented and which impact different imaging sequences have. Chapter 6 and 7 use histologic images for detailed insight into the intracranial aneurysm wall. Section 2.2.4 describes other image modalities which can be used to analyse the aneurysm wall.

2.2.1 CT

An early imaging technique used in medicine was X-ray imaging. This uses the X-rays discovered in 1895 by Wilhelm Röntgen [55]. X-ray imaging exploits that the energy of an X-ray passing material is attenuated by a material-specific amount. X-rays cannot penetrate lead and are not reflected, refracted, diffracted, or deflected by electrical fields. X-ray imaging produces projection images. As the skull would hide most of the other structures, X-ray imaging is not suitable for imaging

intracranial structures. For this, CT, an imaging technique developed based on X-ray imaging, can be used [56, 57, 58]. While X-ray images were produced by a film blackened by X-rays, CT images are computed from several projections. These are generated with a detector ring. With the ring, the X-ray source and the detector are rotated around the patient. By placing the patient on a movable table, a stack of images can be generated [59].

CT images require X-rays and therefore posses a risk for the patient. Radiation dose and slice thickness are important factors for image resolution and quality. Especially with smaller slice thickness imaging artifacts due to moving can occur. Another artifact is the partial volume effect due to attenuation within a voxel not being consistent. In patients with implants metal artifacts can arise.

In CT images, Hounsfield units with material-specific values are used. Air has -1000 Houndsfield units, water 0, blood 30-45, white matter 20-20, and grey matter 37-45 Houndsfield units. Thus, the difference for soft tissues is small and the distinction between tissues is less clear. The usage of the standardized Houndsfield units simplifies the comparison of several CT images [59].

As discussed in Section 2.1.1, CT images are used for aneurysm diagnosis.

2.2.2 MRI

Magnetic resonance imaging (MRI) is based on the spin of the nuclei. These are aligned in an external magnetic field. MRI uses the response of hydrogen nuclei to produce images. The hydrogen density varies in different human tissues, therefore MRI allows for a better soft tissue contrast than CT. Further advantages are the lack of radiation, arbitrary slice orientation (for example used to generate coronal or sagittal views), and several different subtypes of MRI for functional attributes [59]. This work only uses BBMRI.

There are several different imaging techniques to create an MR angiogram [60]:

- Black Blood MRI: In BBMRI, also called dark blood MRI or vessel wall MRI (VWMRI), the vessels appear black. This can be done by using the T1 and T2 properties of blood or by accentuating flow-related dephasing.

    - Fast Spin Echo (FSE)

        - optimized for half Fourier parallel imaging

        - long echo trains (100-250 echoes)

        - low flip angles (30-120 degree)

        - low specific absorption rates

        - imaging times between 5 and 10 min

    - Inversion recovery (IR)

    - Susceptibility-weighted imaging (SWI)

- Bright Blood MRI: In the currently more often used bright blood MRI the vessels appear bright in the image.

    - Non-contrast: These techniques rely on the MR properties of flowing blood.

        - Fast spin echo (FSE)

        - Time-of-flight (TOF)

        - Phase contrast (PC)

        - steady-state free precession (SSFP)

        - arterial spin labeling (ASL)

    - Contrast-enhanced: After the injection of a gadolinium-based contrast agent, the vessels are rendered bright on T1-weighted images.

In clinical practice, BBMRI is recommended to differentiate different causes of intracranial arterial narrowing (for example intracranial atherosclerotic plaque, vasculitis, arterial dissection) and to identify symptomatic, nonstenotic diseases of intracranial arteries. Furthermore, it can be used to access atherosclerotic plaque activity, access vasculitis activity, and determine which aneurysm has ruptured in patients with several aneurysms. Current research focuses on the use of BBMRI to predict the behavior of intracranial unruptured aneurysms [61, 62].

Delay alternating with nutation for tailored excitation (DANTE) pulse trains were developed by Mosher and Smith [63]. It can be used for frequency-selective excitation of a narrow frequency region in high-resolution nuclear magnetic resonance spectroscopy [64]. Li et al. [64] applied DANTE pulse trains with short interpulse repeat times (< 5ms) together with a field gradient along the direction of the flow. With this, an attenuation of flowing spins is achieved and, for example, blood and cerebrospinal fluid appear black.

Van der Kolk et al. [65] used inversion recovery turbo spin-echo (TSE) sequence to show the walls of intracranial vessels. They tested the sequence on 7 healthy volunteers and 35 patients with ischemic stroke or transient ischemic attack. They found that a good contrast between wall, blood and cerebrospinal fluid could be achieved independent of the vessel orientation relative to the plane of acquisition.

Imaging of intracranial vessels is challenging due to the slow blood flow. In the carotid artery residual blood signals are often detected, which could be falsely interpreted as plaque [66]. Xie et al. [66] compared the combination of delay alternating with nutation for tailored excitation (DANTE) and sampling perfection with application-optimized contrasts using different flip angle evolution (SPACE) to SPACE alone. As Fig. 2.10 shows, DANTE reduces artifacts and the vessel lumen is clear.
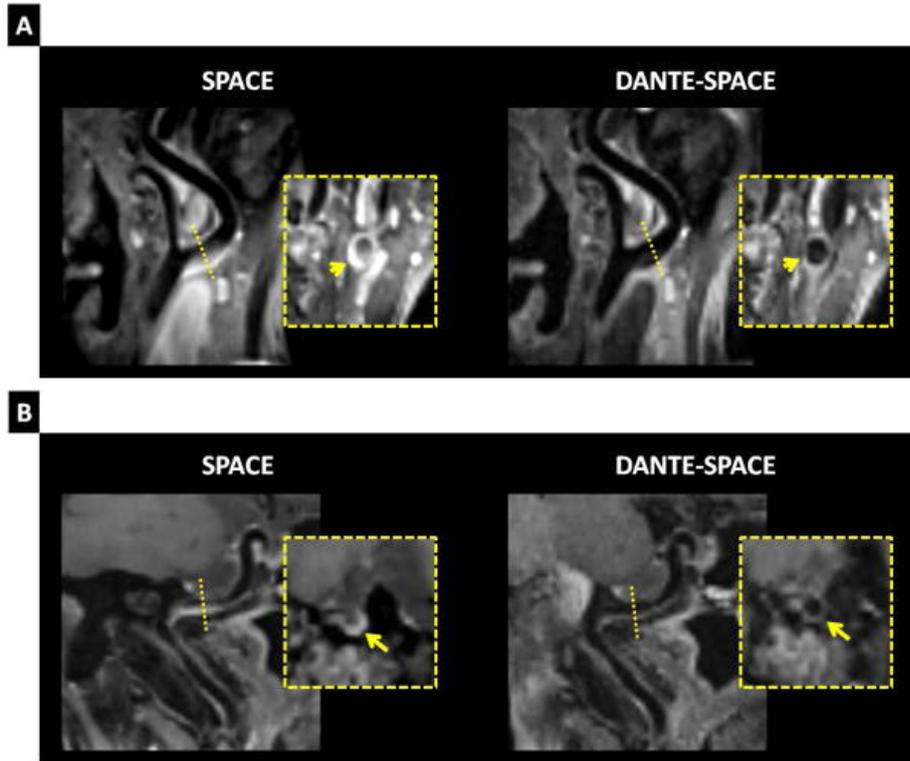
Figure 2.10: Comparison of SPACE and DANTE SPACE for a) carotid bifurcation of a healthy subject and b) internal carotid artery from a patient suspected of stroke [66]

The heart rate has an impact on the blood flow and the wall enhancement, as shown in Fig. 2.11. The figure shows a phantom that was modeled using a 7-T MRI from a patient with a stable MCA aneurysm. On the phantom different heart rates (48 and 77 beats per minute) were simulated. The images taken with the lower heart rate suggest more wall enhancement than the images of the faster heart rate. The wall intensities were dependent on the preparation. With DANTE the near-wall signal intensities decreased by approximately 50% [67].
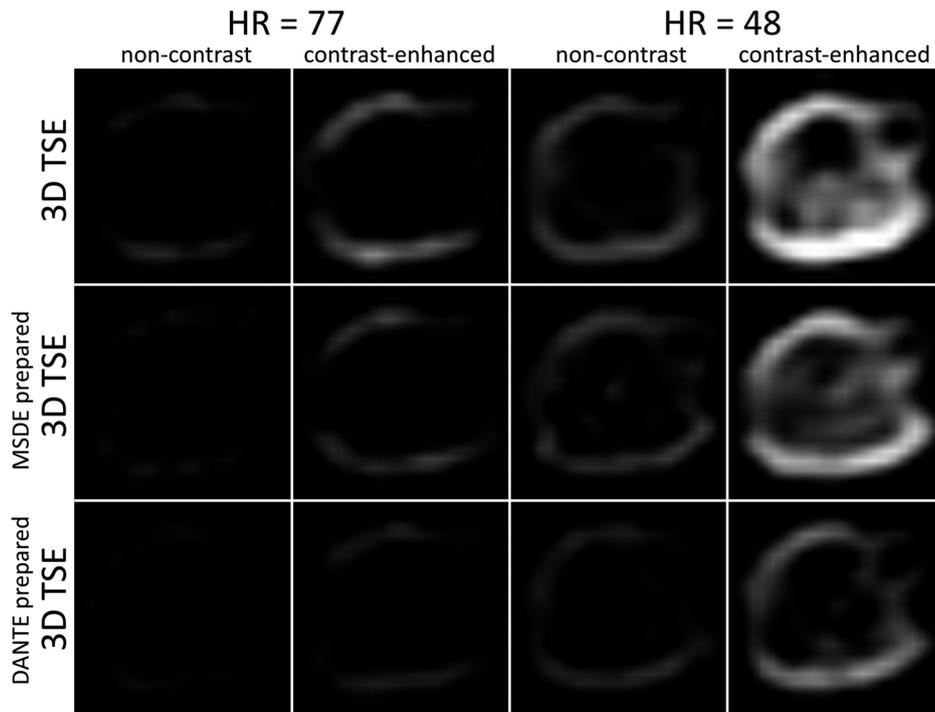
Figure 2.11: Effect of different heart rates (HR) on the wall visibility in different vessel wall imaging techniques with and without contrast agent [67]

Successful blood suppression with motion-sensitized driven equilibrium (MSDE) sequence depends on several factors. Instrumental factors affecting the image quality are eddy currents and B1 inhomogeneities. These are partially compensated by the iMSDE sequence which has an extra 180° refocusing pulse. Wang et al. [68] showed that the iMSDE sequence had a higher signal-to-noise ratio (SNR) compared to the MSDE sequence in a phantom and in vivo study.

Cho et al. [69] also compared SPACE images with and without DANTE and additionally compared them to BrainView with and without improved motion-sensitized driven equilibrium (iMSDE). The images were collected from 14 healthy volunteers. Two radiologists with more than five years of experience judged the image quality, vessel wall delineation, black blood and cerebrospinal fluid (CSF) signal, and the image acceptability. For the four imaging sequences no significant difference in black blood effect, image quality and acceptability were found. For cerebrospinal fluid, SPACE without DANTE was superior to SPACE with DANTE and BrainVIEW without iMSDE was superior to BrainVIEW with iMSDE. The signal-to-noise ratio in the vessel and the contrast-to-noise ratio were higher in the SPACE images (with and without DANTE) compared to the BrainVIEW images (with and without iMDSE).
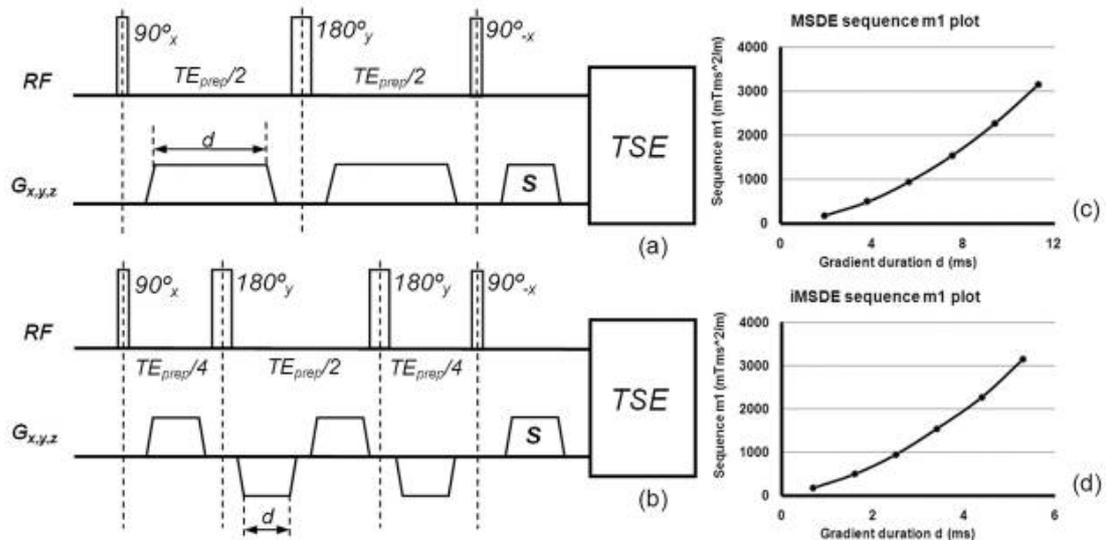
Figure 2.12: Traditional MSDE (top) and iMSDE (bottom) preparation pulse sequence. Trapezoids: motion sensitizing gradients, S: spoiling gradients, right: diagrams of m1 changes, assumed gradient strengths of 20 mT/m [68]
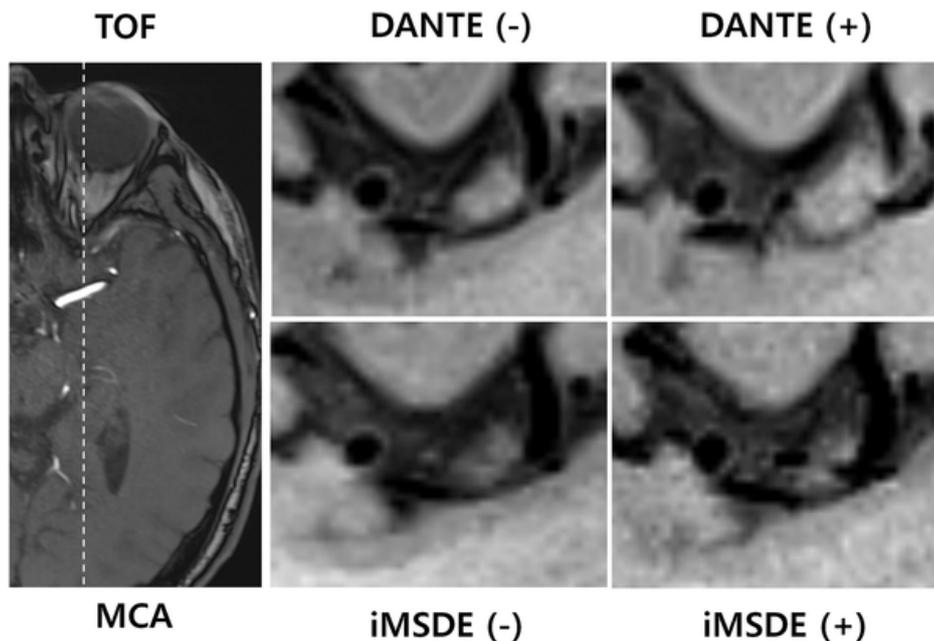
Figure 2.13: SPACE with and without DANTE and BrainVIEW with and without iMSDE sagittal images of a segment of the middle cranial artery from a 37 year old healthy volunteer [69]

Cornelissen et al. [70] analyzed factors contributing to wall enhancement in intracranial aneurysms. They included 14 aneurysms from 6 patients in their study. 10 aneurysms showed wall enhancement, 4 of these were unruptured. They could not confirm the hypothesis that wall enhancement is related to inflammatory

cell infiltration. In 60% of the cases, the intraluminal diameter was smaller in BBMRI compared to TOF MRA. They concluded that in these cases the wall enhancement was at least partially caused by slow intra-aneurysmal flow.

Currently, the research is mainly on saccular intracranial aneurysms. The results might not be applicable to dissecting or thrombosed aneurysms. Besides pseudo-enhancement due to slow blood flow, the interpretation of wall enhancement can be complicated by proximity to dura or adjacent veins [62].

Raz et al. [71] analyzed 28 variable flip-angle T1 black-blood MRI with DANTE images of aneurysms treated with flow diverters. They recommend these advanced BBMRI for treatment evaluation as the evaluation of parent vessel and aneurysm wall is superior to conventional MRI.

2.2.3 Histology

Histologic images are very detailed images of a tissue and show individual cells and nuclei. Often the H&E staining is used (see Fig. 2.14).
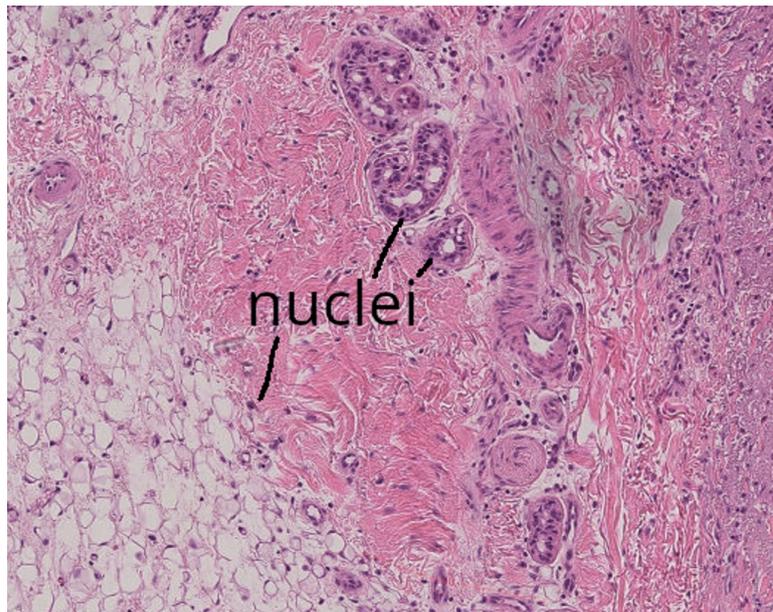
Figure 2.14: Nuclei of cells in H&E staining [72]

To create histologic images, tissue is fixated, thinly sliced, stained, and viewed under a microscope. Aneurysm tissue can only be collected after opening the skull and therefore is not used for rupture prediction and treatment decisions. Especially for research, aneurysm dome tissue is collected during clipping. Alternatively, aneurysms can be collected post mortem.

The five stages of histologic imaging are fixation, processing, embedding, sectioning and staining [73].

Table 2.1: Examples of different stainings, bold: stainings used in this thesis [74, 75, 76, 77]

staining	presented structures	example
Alcian blue	acid mucopolysaccarides	medical necrosis dissected aortic aneurysm
Elastin staining (according to Weigert)	elastic fibers (violet-black)	elastic fibers in aortic media
Elastica van Gieson (EvG)	collagen fibers (red) elastic fibers (black-brown) cytoplasma, musculature (yellow)	fibrosis in organs liver cirrhosis
Hematoxylin-eosin (H&E)	**cytoplasma (red) erythocytes (red) nuclei (blue)**	**routine staining**
alpha-smooth muscle actin (aSMA)	**smooth muscle cells myofibroblasts**	**stromal cells of mammary carcinomas**
Oil red O (Oro)	**neutral fat fatty acids triglycerides**	**lipid storage diseases fat embolism**
Massons's Trichrome (MT)	**acidophilic tissue (cytoplasma, muscle)**	**routine stain for liver and kidney biopsies**

1. Fixation: should preserve the structure of the cells, delay degradation and harden the tissue for sectioning. Different fixatives are used, for example:

   - Neutral buffered formalin: often used in combination with light microscopes, good tissue and cell structure preservation, but denatures DNA, miRNA and mRNA

   - Paraffin-formalin: requires fresh preparation to enhance effectiveness, suitable for immunostainings

   - Bouin's fixative: preservation of nuclei and glycogen, used for embryo and brain tissues, distorts mitochondria and kidney tissue

2. Processing: The tissue is dehydrated with ethanol and a hydrophobic clearing substance like xylene. This helps to solidify the tissue and preparation for sectioning.

3. Embedding: Often the tissue is embedded in paraffin wax. Alternatives are plastic resin, wax or combinations of fixatives.

4. Sectioning: For microscopic slide examination the tissue is sectioned in a series of thin slices.

5. Staining: To highlight important features and enhance contrast the tissue is stained.

The tissue is stained to highlight different aspects of the tissue. Several different histologic stainings exist and are used for different situations, as shown in Table 2.1.

Histologic images require the collection of tissue. Therefore, histologic analysis of aneurysms can only be done on samples collected during surgery or post-mortem. During surgery only a small part of the aneurysm can be collected. Samples collected post mortem are rare and can include the whole aneurysm and part of the parent vessel. Chapter 6 describes the reconstruction of a 3D model from post mortem data, while Chapter 7 uses tissue collected during surgery and preoperative images.

During the tissue collection and processing the shape of the tissue changes. Especially for whole aneurysms the missing blood flow alternates the shape. Current research on image processing for histology, among other things virtual inflation, is discussed in Section 3.2.

H&E Staining
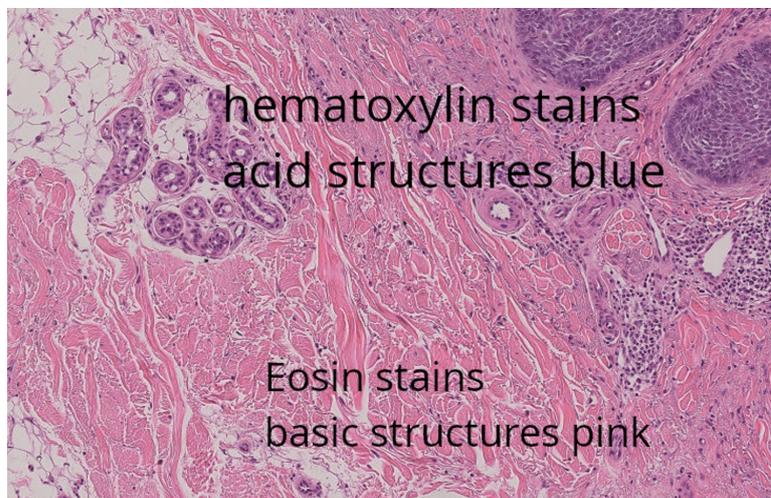
Figure 2.15: Example of the often used H&E staining [72]

Hematoxylin and Eosin (H&E) staining is used for routine diagnoses to view cellular and tissue structure details. The nuclei are dyed blue with hematoxylin (see Fig. 2.15). The depth of the color depends on the amount of DNA in the nuclei and on the time the sample spends in hematoxylin. Hematoxylin is extracted from the tree Hematoxylin campechianum. The ability to attach to anionic components of the tissue can be improved by adding a mordant. An often used mordant is aluminum ammonium sulfate. Eosin is used to dye connective tissue fibers in different shades of pink. Most commonly used is Eosin Y. To enhance the red, phloxine can be added [75].

H&E stains can be divided into progressive, modified progressive, and regressive. For progressive staining, hematoxylin is added to the tissue but not followed by a differentiator to remove excess dye. This can be useful in tumor diagnosis where a non-cellular material like mucin becomes stained with hematoxylin. In regressive and modified progressive staining a differentiator is used. Modified progressive staining uses a mild differentiator. This only removes background staining but not the excess from the nuclei [78].

aSMA Staining
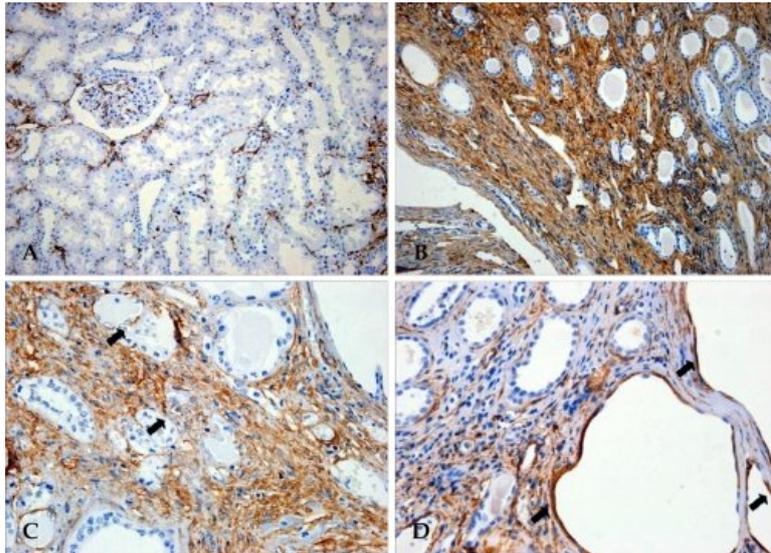
Figure 2.16: Examples of aSMA staining [79]

Alpha-smooth muscle actin (aSMA) (see Fig. 2.16) is a staining that helps to identify smooth muscle cells and myofibroblasts in normal, reactive, or neoplastic tissue. Besides in smooth muscle cells, alpha-smooth muscle actin is found in stromal cells of mammary carcinomas and used in tumor diagnostics. The antibodies which detect alpha-smooth actin were discovered in 1986 and they do not detect other actin isoforms [80] [81].

Oro Staining
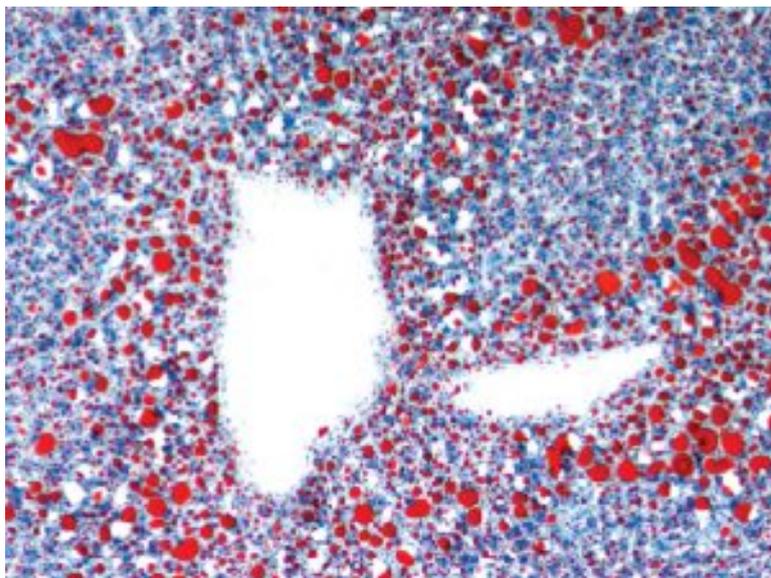
Figure 2.17: Example of Oro staining (Image provided by the Histology Research Core Facility in the Department of Cell Biology and Physiology at the University of North Carolina, Chapel Hill NC [76])

Oil red O (Oro) is used to dye neutral fat, fatty acids and triglycerides. The fat-soluble, hydrophobic diazo dye appears red (Fig. 2.17). As paraffin embedding or alcohol-based fixation removes neutral lipids, it has to be applied in fresh or frozen tissue. Common applications include muscle biopsies to assess the number of sarcoplasmic lipid droplets and the diagnosis of lipid storage diseases, fat embolism and steatosis in liver transplant biopsy. For complex phospholipids and glycolipids that have polar groups (like found in peripheral nerves or biological membranes), sudan black is better suited than Oro [76]. Blitz et al. [82] developed a method for quantification of fatty infiltration in skeletal muscle using Oro staining and computer support. They stained tissue collected from mice and acquired an image stack with 10μm step size. This stack was processed semi-automatically using a thresholding algorithm and a watershed algorithm to segment the images.

MT Staining
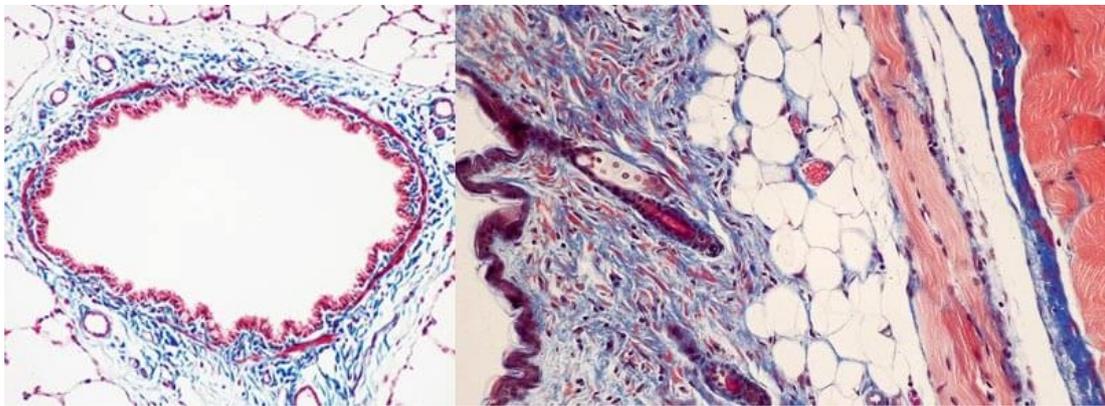
Figure 2.18: Example of MT staining [83]

Masson's Trichrome stain (MT) consists of three dyes: Weigert's hematoxylin to dye the nuclei, Biebrich scarlet-acid fuchsin solutions to stain acidophilic tissue elements (for example cytoplasm and muscle), and aniline blue to dye the collagen (Fig. 2.18). After the tissue is stained the nuclei are black, cytoplasm, muscle, and erythrocytes are red and the collagen is stained blue. This staining is a routine stain for liver and kidney biopsies and can be used to differentiate between collagen and smooth muscle cells [77].

2.2.4 Other imaging modalities

Especially for research additional imaging modalities can be used to get further insight into vessel and aneurysm structures.

Optical coherence tomography

Analog to the usage of sound in ultrasound imaging, light is used in optical coherence tomography (OCT). By measuring backscattered or back-reflected light,
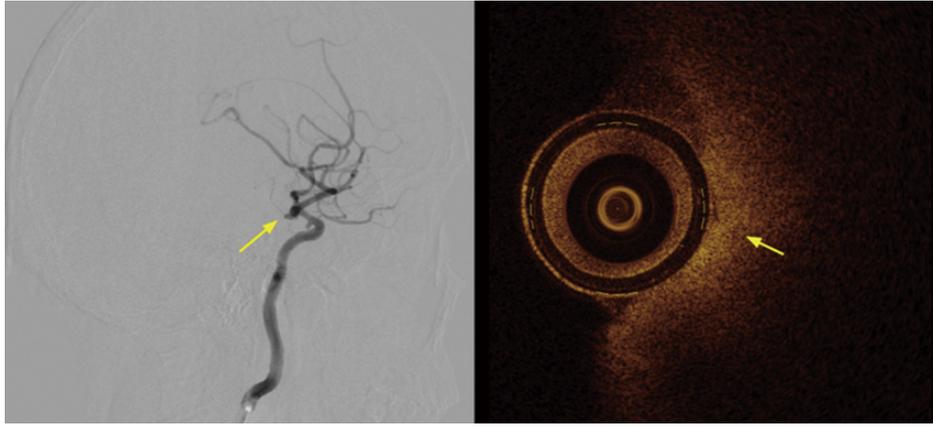
Figure 2.19: Left: angiography image of ruptured aneurysm (arrow). Right: OCT image (during open surgery), arrow: layer structure of the wall [85]

high-resolution cross-sectional tomographic imaging is performed (Fig. 2.19). OCT was first demonstrated in 1991. Initially, it was used for the eye. The images have a resolution between 1 to 15 μm. The imaging depth is limited by the optical attenuation of the tissue. In most tissues imaging up to 2 to 3 mm is possible. OCT is not yet common in clinical routines. Several studies explore possible applications, for example as guidance or alternative for challenging or hazardous biopsy. For imaging of gastrointestinal, pulmonary and urinary tracts and arterial imaging. catheter and endoscope OCT can be used [84].

Glaßer et al. [86] demonstrated the usage of OCT for intracranial aneurysms on three post mortem explanted Circle of Willis. Intravascular OCT image acquisition with an OCT catheter generated a 2D image stack. This stack was aligned with corresponding histologic images of the tissue. To account for the tissue deflation due to missing blood pressure they introduced virtual inflation for the histologic and OCT images. Later work included the segmentation of the nuclei in histologic images, analysis of the nuclei shape, and generation of nuclei cluster. The framework allows brushing and linking between OCT and histologic images and between original and virtual inflated images [87].

Another experiment combined 2D OCT with 3D structured light scanner data. 3D landmarks were collected using a touchprobe. In the OCT images, manual segmentation of intima and adventitia was carried out. The OCT images were aligned based on the centerline, and surface extraction for intima and adventitia was performed. This generated a 3D vessel thickness model [88].

Serial block facing

A newer technique to visualize cells and nanostructure in biological tissue in 3D is the serial block-face scanning electron microscopy presented by Denk and Horstmann in 2004 [89]. For this technique, a tissue sample is embedded in plastic. An image of the surface of the plastic-embedded tissue is taken with a
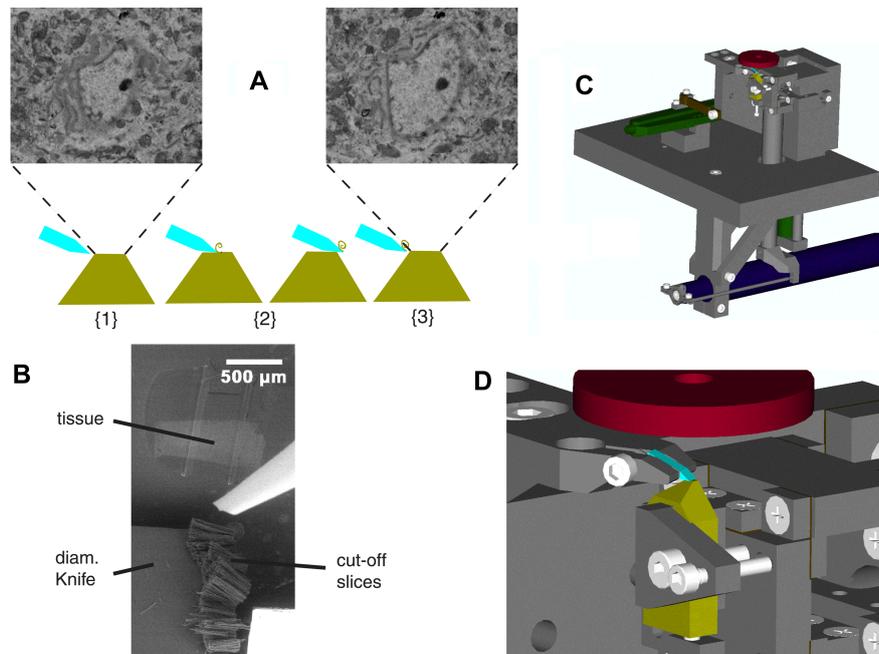
Figure 2.20: Serial block-face imaging: A) overview of the process, B) pilled up slices, C) and D) mechanical design [89]

scanning electron microscope. After that, an ultrathin slice of the block is removed with a diamond knife and the next image is taken. Occasionally, a pipette is used to remove the cut-off slices which can pile up on the knife (see Fig. 2.20). Serial block face imaging can achieve resolutions of up to 15-20nm. This technique is only suitable for very small samples (<5mm)[90].

O'Connel et al. [91] analyzed the nanostructures of a rat aorta using serial block-face scanning. An example of a $22\mu m \times 16\mu m \times 25\mu m$ large tissue block sampled from the aorta is shown in Figure 2.21. Mikula et al. [92] used serial block-face imaging to visualize a whole mouse brain and segment single axons in the brain.
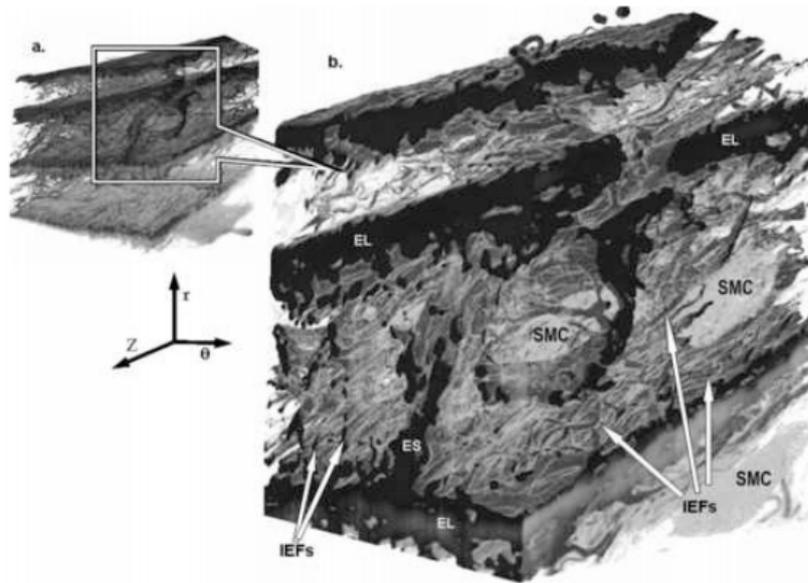
Figure 2.21: Serial block-face imaging of a rat aorta; SMC: SMC nuclei, EL: elastic lamellae, ES: elastin structure, IEFSs: interlamellar elastin fibers [91]

Multiphoton imaging

Over time optical imaging techniques have improved. With the introduction of multiphoton imaging in 1990 by Denk et al. [93] images of over 100μm were possible. This was further improved by Combs et al. [94] to image samples up to 2mm (see Fig. 2.22). This can be improved by reducing scattering and absorption of the tissue with optical clearing techniques. Alternatively, multimodal techniques which combine light with acoustic detection can be used [95].
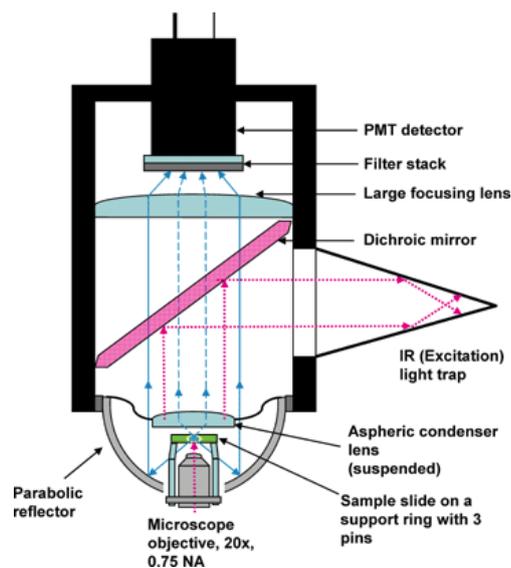
Figure 2.22: Construction of a mulitphoton imaging system; PMT: photomultiplier tube; IR: infrared [94]

Schriefl et al. [96] analyzed five post mortem collected human abdominal aortas. Their optical clearing included rinsing the tissue samples with phosphate-buffered saline to remove excess paraformaldehyde from the fixation step, dehydration with ethanol, and a solution of benzyl alcohol to benzyl benzoate. The result is shown in Fig. 2.23. With second-harmonic generation imaging and Fourier-based image analysis, they assessed the fiber orientation in the tissue. The three arterial layers differ in their fiber morphology (see Fig. 2.24, Section 2.1). Thick fiber bundles were found in the adventitia. They were mostly oriented diagonal to the major axes while the fiber in the media was organized in the circumferential direction of the vessel. Isotropic fiber morphologies were found in the intima.

Figure 2.23: Tissue before and after optical clearing [96]
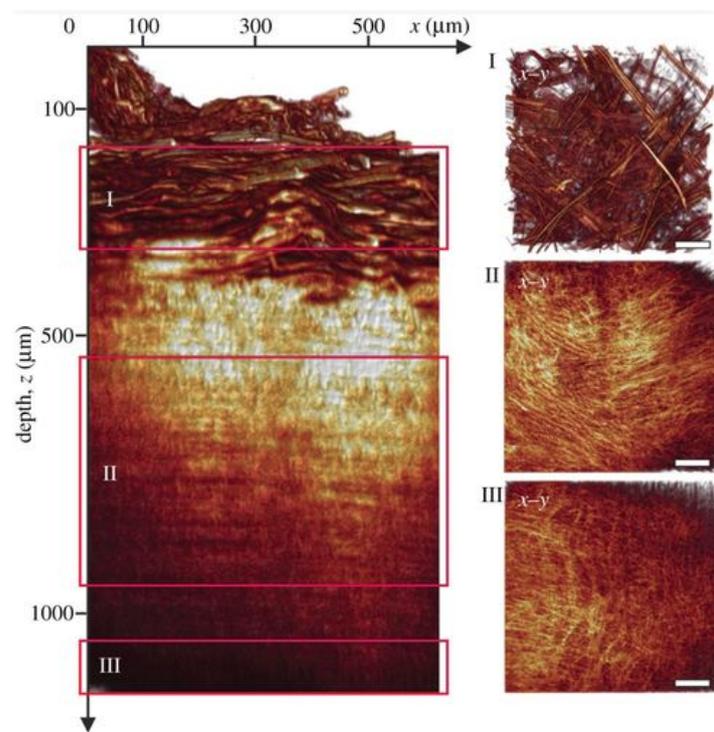
Figure 2.24: Aortic wall; image acquired using second-harmonic generation imaging. I: adventitia, II: media, III: intima [96]

Intravascular ultrasound

Intravascular ultrasound (IVUS) can be used to show vascular structures. Like other forms of ultrasound it is based on the varying acoustic impedance at the interface of different tissue structures. A catheter with an ultrasound transducer is placed in the vessel (see Fig. 2.25). IVUS imaging is not suitable to distinguish between fibrotic and calcified tissues in plaques [97]. Due to this limitation, Chapter 6 and 7 are using histologic images instead. IVUS is not used in clinical routine for intracranial aneurysms, but might be used to assist endovascular repair of aortic aneurysms [98].
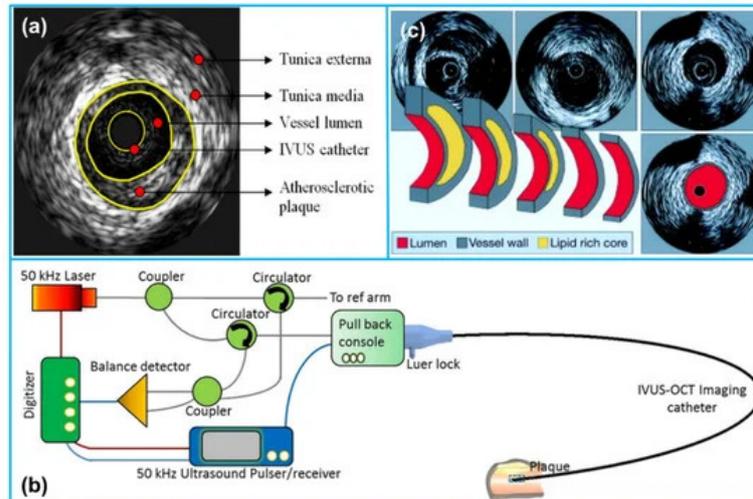
Figure 2.25: a) Example of intravascular ultrasound image of an arterial cross-section. b) Composition of an intravascular ultrasound imaging system. c) Series of images acquired during pullback of the ultrasound transducer [97]

Imaging aneurysm pulsation

Another aspect of aneurysm imaging is measuring aneurysm pulsation. Pulsating intracranial aneurysms are more likely to grow and rupture [99]. At the moment, no gold standard for this is available and imaging is challenging as pulsations are in the order of current imaging modalities. Most studies use ECG-gated 4D computed tomography angiography to get quantitative pulsatility measurements (see Fig. 2.26). Other options are MR imaging or DSA, which is rarely used for this. During a cardiac cycle, the aneurysm volume changes between 5% and 36%. This is correlated to the aneurysm diameter. Currently, there are major variations in pulsatile measurements and it is unclear whether this is because of true aneurysm pulsation or image noise and measurement errors [100].
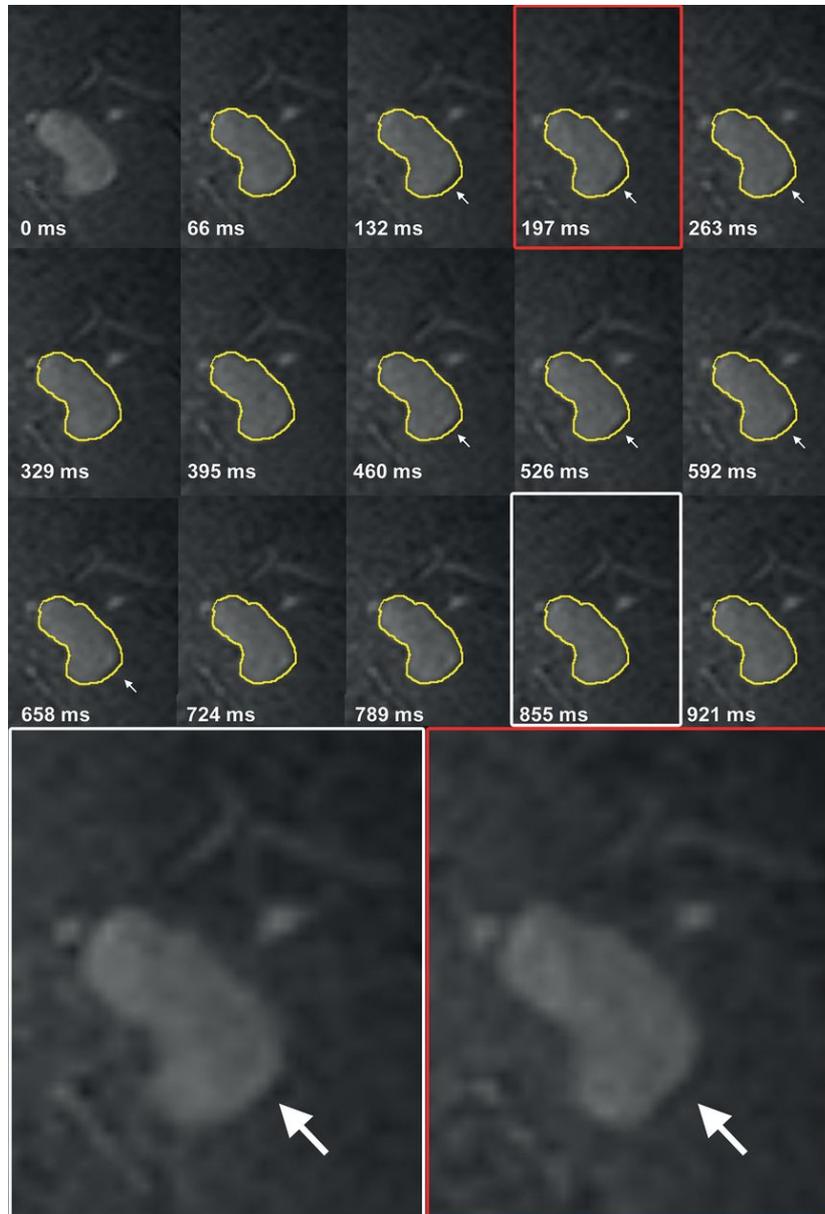
Figure 2.26: Pulsation of left middle cerebral artery, yellow: contour of aneurysm at time 0 ms, arrows: area of pulsation [101]

2.3 Summary

Intracranial aneurysms are a disease of the brain vessels that is complex to diagnose and treat. With increased usage of medical imaging, more aneurysms are incidentally found. These have to be evaluated regarding the patient-specific rupture and treatment risk. Several different imaging modalities are used in aneurysm research and in clinical routine.
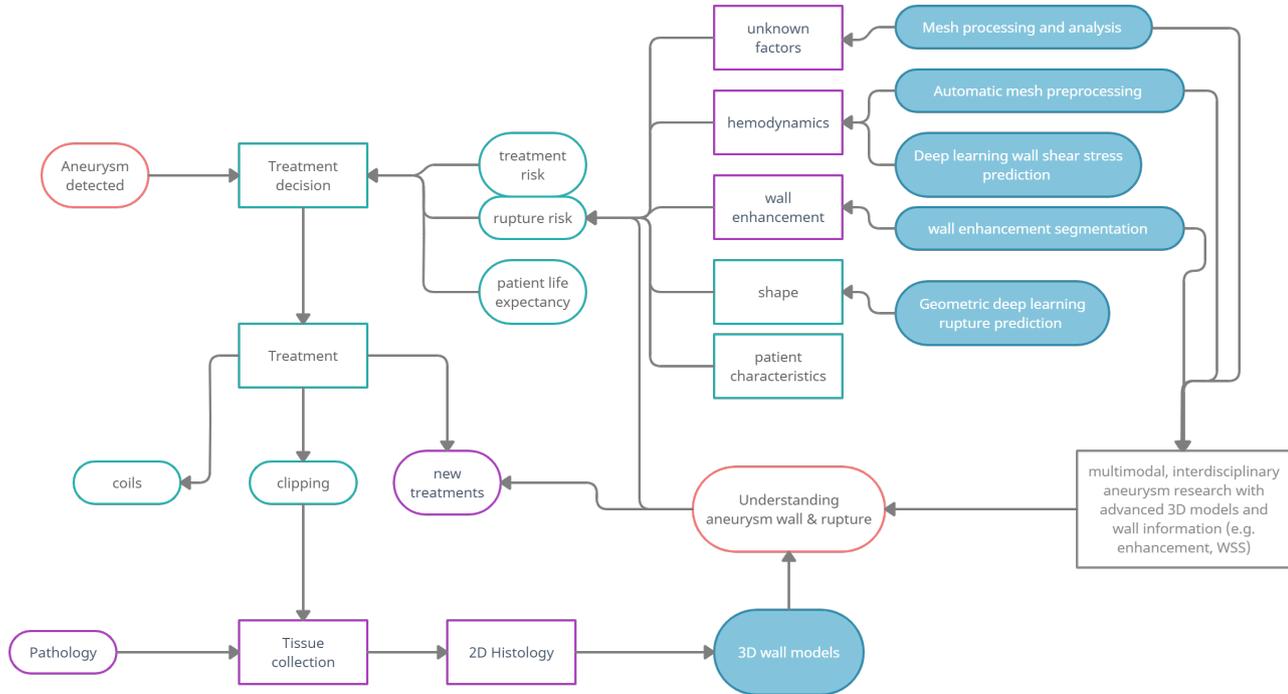
Figure 2.27: Treatment of intracranial aneurysms and related research; green: clinical routine, purple: ongoing research, blue: wall-related aneurysm research presented in this thesis

Figure 2.27 shows various aspects in aneurysm research and treatment. Tissue samples of the aneurysm wall can either be collected during treatment with clips or in the pathology. Analysis of aneurysm wall tissue could provide helpful insights into the wall composition and the processes leading to aneurysm development and rupture, with the potential to develop new treatments to prevent aneurysm rupture. Due to the risk of the currently available treatment methods, the rupture risk and the treatment risk play a major role in the treatment decision. In this thesis, only the rupture risk is considered. Several aspects influence the rupture risk of intracranial aneurysms. Therefore, several projects covering various aspects of aneurysm rupture are included in this thesis: wall composition, wall enhancement and wall shear stress. This includes a pipeline for semi-automatic mesh processing to analyze the aneurysm and surrounding vessels, mesh preprocessing for hemodynamic simulations, objective wall enhancement segmentation and geometric deep learning for rupture and wall shear stress prediction. In the future, this could enhance the rupture risk assessment in clinical routine.

The processes leading to aneurysm formation and rupture are an active research topic. An important aspect are the wall and the changes in the aneurysm wall. Imaging of the wall is challenging, as discussed in Section 2.2.4. To enhance the understanding of the aneurysm wall, Chapter 6 and 7 present how a 3D model based on histologic images can be generated and histologic information can be combined with various other aspects. The histologic images allow the most detailed view of the aneurysm wall and show individual cells of the tissue. While research has identified a large number of risk factors, clinical practices uses simple, but unreliable and outdated scores. In this thesis, tools which enable the usage of hemodynamic and morphological parameters are presented in Chapter 8 and 9. As they use deep learning on 3D models, they are fast and independent of the used image modality.

3 Related Work - Image processing

This chapter discusses related work regarding the analysis of the aneurysm wall and image processing for aneurysm diagnosis and research. In Chapter 6 and Chapter 7 the aneurysm wall structure will be assessed with histologic images. The clinically oriented Chapter 8 uses BBMRI. Histologic images were selected as they allow a detailed insight into the cells and tissues building the aneurysm wall. BBMRI has the potential to be used in clinical routines in the future. Other techniques used in research are briefly described in Section 3.1. These are neither as detailed as histologic images nor can they be used in clinical routines.

3.1 Aneurysm wall analysis

The aneurysm wall is an important aspect of aneurysm formation and rupture. Understanding the processes inside the wall could lead to new treatment options aiming at influencing the wall. The aneurysm wall is not visible in CT or MR images. Therefore, various other techniques are used. These are often in 2D and only highlight isolated aspects of the wall. In Chapter 6, a new 3D wall model based on histologic images is described. Chapter 7 describes the combination of histologic wall information, preoperative 3D information and hemodynamic simulation results.

Several studies analyzing the wall and testing various wall attributes were published in the last years. Research with a focus on the aneurysm wall mainly explores tissue samples collected during surgical clipping. Common diagnostic methods are polymerase chain reaction, immunostaining, western blotting, and microscopy. The often small number of samples limits the explanatory power of these studies [102]. Increased apoptosis, loss of smooth muscle cell layer, endothelial layer damage, infiltration of M2 macrophages, activity of matrix metalloproteinase-9, increase of intraluminal thrombus, lower number of collagen fibers, and atherosclerotic lesions are indications of aneurysm rupture. According to Jabbarli et al. [102], who compared the results of several studies, these had a moderate to high evidence quality. The level of evidence was based on several factors, for example, the number of patients and the existence of conflicting results from other studies. A detailed model of changes in the arterial wall, which are suspected to lead to aneurysm development and rupture is presented in Fig. 3.1 [102].

Cebral et al. [103] analyzed the mechanical properties of 8 unruptured cerebral aneurysms. After clipping, the aneurysms were tested with an uniaxial loading
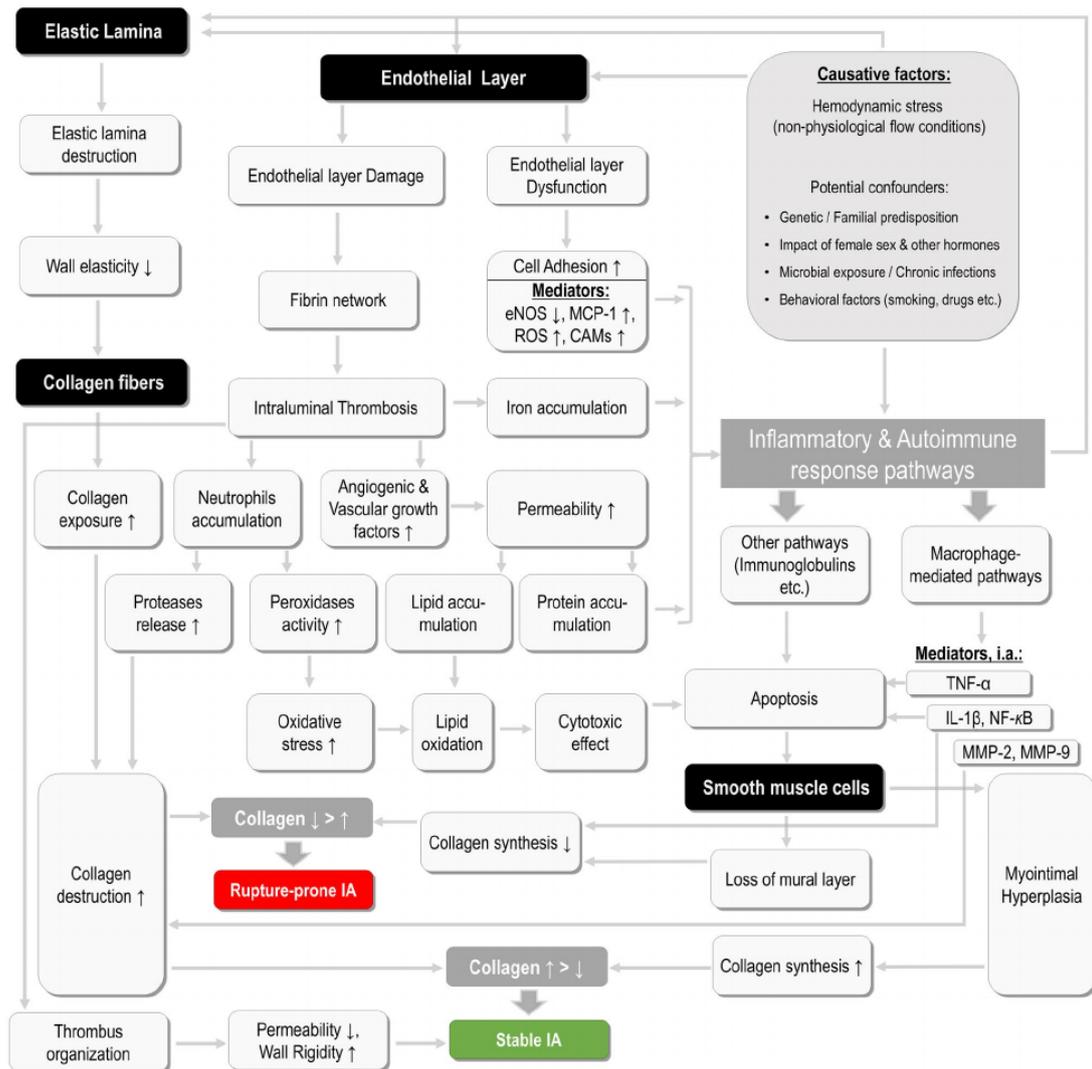
Figure 3.1: Model of pathopyhsiological processes and factors for intracranial aneurysm development; black: anatomical targets in the arterial wall, gray: processes. Abbreviations: eNOS = endothelial nitric oxide synthase, MCP-1=monocyte chemotactic protein 1, ROS=reactive oxygen species, CAMs=cell adhesion molecules, TNF-$alpha$=tumor necrosis factor alpha, IL-1$beta$ = interleukin 1 beta, NF-kB = nuclear factor kappa b, MMP-2/-9=matrix metalloproteinase-2/-9 [102]

system with a multiphoton microscope, allowing imaging, especially of collagen fibers, while mechanically testing the tissue. From preoperative 3D rotational angiography images, fluid simulations were derived. They found several correlations between the fluid simulations and the mechanical properties of the aneurysm tissue: The ultimate strain decreases with increasing inflow rate, mean velocity, and mean wall shear stress (WSS). High-stress wall stiffness increased with velocity, flow instability, WSS, and oscillatory shear index. Other relations were found but were statistically irrelevant.

Jiang et al. [104] analyzed 28 middle cerebral artery aneurysms. They performed hemodynamic simulation using models based on preoperative CTA. The simulation results were combined with information about thin-wall regions identified by intraoperative microscopy. Thin-wall regions correlated with higher pressure and lower wall shear stress.

Hackenberg et al. [105] analyzed collagen turnover in tissue samples from intracranial aneurysms. The collagen turnover rate was lower (32%) for patients without risk factors (like smoking or hypertension) compared to patients with risk factors (for example with arterial hypertension: annual collagen turnover rate of 2600% . Additionally, they found that spatial-temporal averaged wall shear stress can predict rapid collagen turnover.

Cebral et al. [106] analyzed 65 aneurysms. From preoperative imaging, 3D models were generated. Based on surgical videos, five different wall types (atherosclerotic wall, hyperplastic wall, thin wall, rupture site, normal) were identified and manually marked on the 3D model. Not all parts of the aneurysm were visible in the video, on average 28.9%±25.6% were not visible. The visible areas were compared with the results of a hemodynamic simulation. Slow flow was associated with an atherosclerotic and hyperplastic wall, while high flow was associated with wall thinning.

3.2 Histologic image processing

In this section, algorithms to process histologic images are described. The most used images in clinical and research settings are H&E stained images [107].

A problem for automated analysis is the color variation. Some slides are less or more saturated than others. This is addressed by stain normalization. Stain normalization can be done by histogram equalization per color channel or normalization after separating the image in H-only and E-only images. As in H&E stained images, two stains are successively applied to the tissue, one stain can be too intense and the other too weak. That problem can be addressed by separating the images into the two stains [108] (see Fig. 3.2 and Fig. 3.3).

During the processing, the tissue can be deformed. Two problematic artifacts may occur: tears in the tissue and folds. While folds might be detected based on color saturation [110], none of the deformation artifacts can be corrected [107].
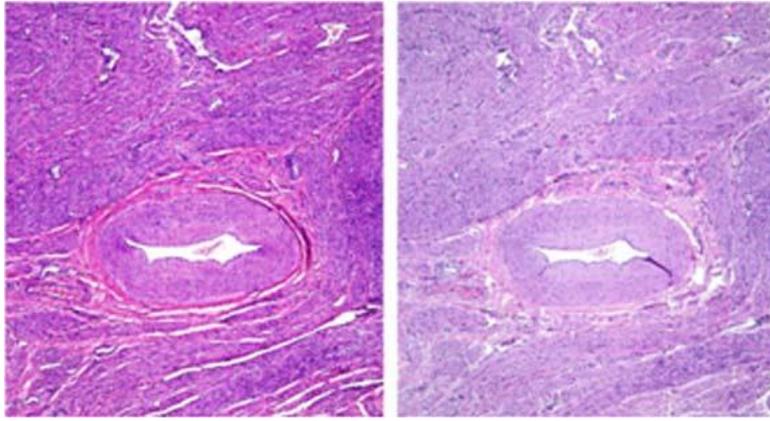
Figure 3.2: Different saturation of H&E staining [109]
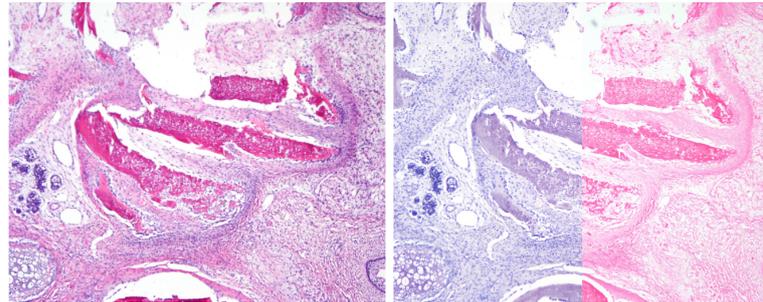
Figure 3.3: Left: H&E staining. Right: stain seperation [108]

Another challenge is the processing of large tissues, which have to be imaged as several pieces and the images have to be manually stitched together [107].

These deformations also make registration more complex. For 3D reconstruction histologic images are registered to each other. This can be done using anatomical landmarks like blood vessels [111]. The registration is even more challenging when histologic images from different stains should be registered, as each stain emphasizes different structures [107]. Registration of histologic images to other image modalities is rare. For example, H&E images have been registered to MRI [112, 113] and CT, which will be further discussed in Section 3.2.4. This provides additional challenges, as the surgical extraction of tissue for histologic images can greatly deform the tissue.

Face-Vertex Meshes
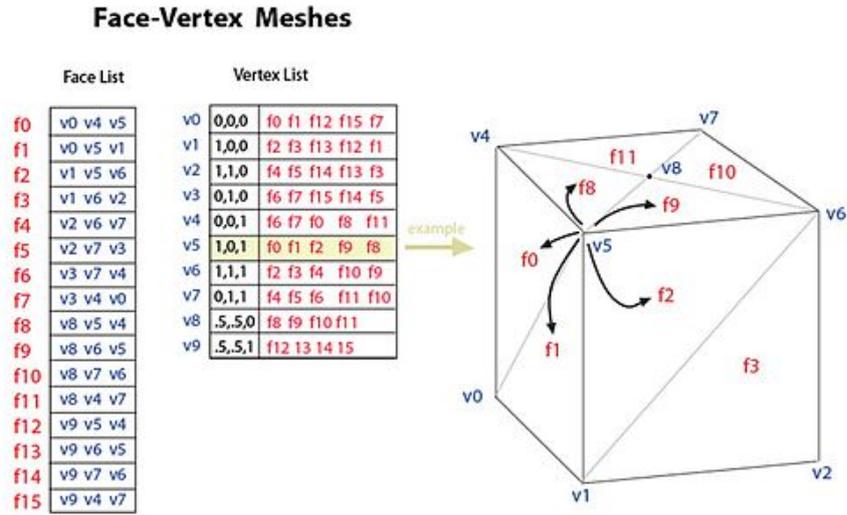
Figure 3.4: Mesh consisting of vertices and faces [114]
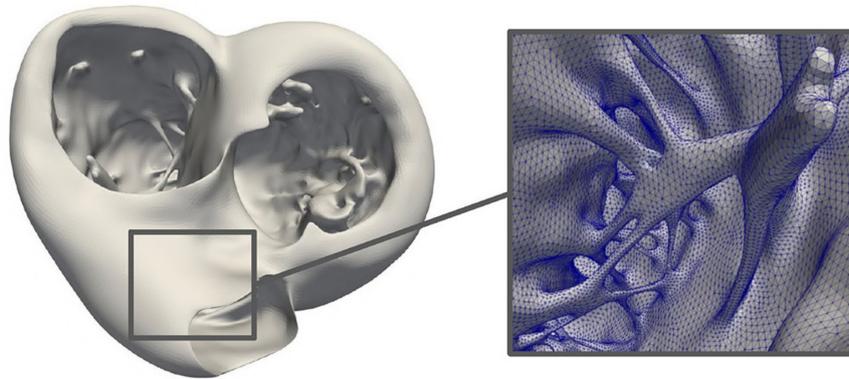
Figure 3.5: Example of a mesh showing the geometry of a heart [118]

3.2.1 3D models from histological images

3D models are generated from various image data. Popular methods are statistical shape models and statistical appearance models [115]. In recent years, deep learning methods like variational autoencoders or autoencoder generative adversarial nets also gained popularity [116, 117]. Due to the large difference between these image data and histologic images, these approaches cannot be easily transferred to histologic image data. Surface meshes consist of vertices, faces and edges. Commonly, the meshes are stored as a list of vertices and faces, as illustrated in Figure 3.4. Figure 3.5 shows a surface mesh of a heart.

Feuerstein et al. [119] researched the reconstruction of 3D histologic images using synthetic data and a rat kidney. Before the embedded tissue was cut, blockface images were taken. These allowed registration of the histologic images with the blockface images as well as a registration between consecutive slices. This registration is helpful to reduce artifacts in histologic images (like holes, folding and tears) which occur during the cutting, staining and placement on microscopic slides.

Cifor et al. [120] described the reconstruction of 3D volumes from histologic images without a reference volume from other imaging modalities. They applied their approach to a Nissel-stained mouse brain. In the first step, they rigidly registered consecutive slices. Then, the gray/white matter boundary is extracted and the extracted surfaces are smoothed using mean curvature flow. From this flow, a displacement field is estimated, and based on this transformations are estimated and applied to the original 2D images.

Braumann et al. [121] reconstructed 3D tissue volumes from histologic images to assess cervical tumor invasion. The serially sliced sections were registered with a rigid registration, color adaption, and non-linear registration. The differences between adjacent images were small and negligible for the registration.

In this thesis, histologic images for the 3D analysis of intracranial aneurysms are used. The histologic images in Chapter 6 are collected post mortem and therefore show the aneurysm and the parent vessel. In contrast to the images of the previously described works, there are large gaps between the images. Chapter 7 also uses histologic images. These images also have gaps between them. Furthermore, several stainings are used.

Research question 1: How can a 3D model of the intracranial aneurysm wall be derived from 2D histologic image data?
Histologic images can show fine details of the aneurysm wall. The available data collected post mortem show the aneurysm as well as the parent vessel. These rare and useful 2D data should be used to generate a 3D model of the aneurysm wall for further analysis and realistic simulations. Due to the unique properties of the intracranial aneurysm data (for example distance between slices, deformation due to loss of blood flow) the previously described approaches are insufficient and a new algorithm has to be developed.

Research question 1 a: How to generate a mesh from a point cloud if the points are unevenly distributed?
This questions arises while answering the previous questions. Due to some unique properties of histologic images unusual point clouds occur where commonly available mesh generation algorithms fail. Therefore, a new mesh generation algorithm has to be developed.
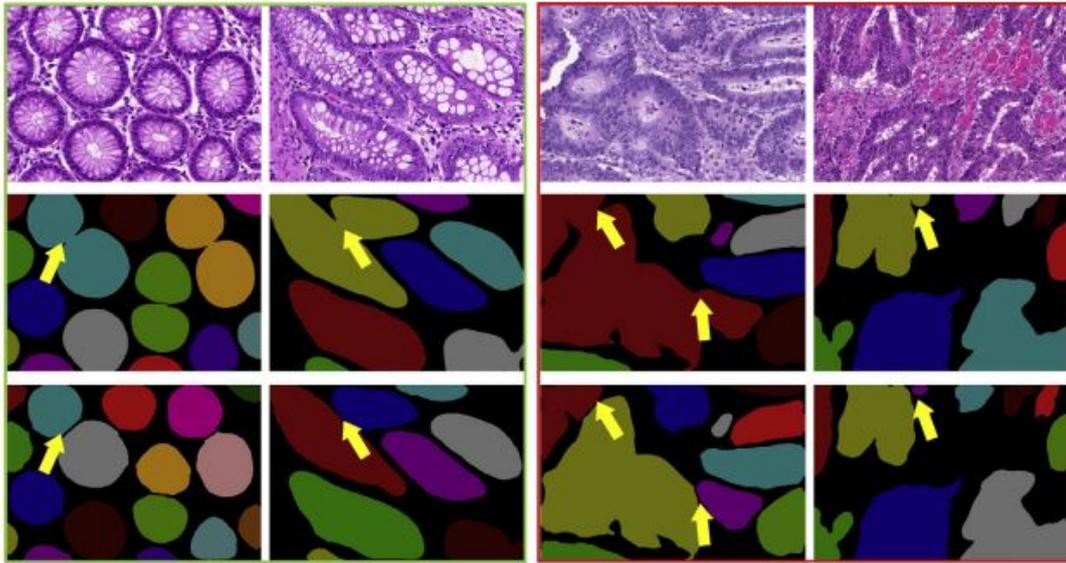
Figure 3.6: First row: original images, second row: segmentation using deep learning without integrating contour information, bottom row: segmentation result of contour-aware network [123]

3.2.2 Segmentation of histological images

Several approaches exist to support the analysis of histologic images. Typical tasks are the segmentation of cells, nuclei, or tissue and the classification of images. These tasks are solved using image processing or machine learning.

Machine learning is often used to classify tissue (for example into different grades, cancer/healthy tissue). Common supervised machine learning techniques in histology are support vector machines, random forest and convolutional neural networks. Unless a deep learning approach is used, it is necessary to define features. Unsupervised learning, like k-means, autoencoder, and principal component analysis, is used for clustering and anomaly detection [122].

Chen et al. [123] introduced deep-contour-aware networks for object instance segmentation in histologic images. They used their net to segment glands and nuclei. The integration of contour awareness improved the segmentation of overlapping structures, as hihglighted with arrows in Figure 3.6.

Histologic images are stained with different solutions. Depending on the tissue preparation the tissue colors can vary. To reduce the inter-slide variability, sometimes color normalization is applied. Zarella et al. [124] described an algorithm to relate color with histological structures.

Janowczyk et al. [125] presented possible tasks of histophatologic image analysis which could be solved with deep learning. The three main tasks were segmentation, detection and classification. They described the workflow of deep learning for histopathologic image analysis. The first step is to decide on a neural net

design. After that the selection of suitable image patches for training and validation has to be done. The success of the training heavily depends on a set of training data which reflect all possible variations. The next step is the training of the neural net and the last step of the workflow is the validation.

Taylor-Weine et al. [126] described the potential of machine learning for liver biopsy evaluation. They used histologic images from 1992 patients. 45081 H&E stained images and 20343 trichrome stained images were used. They first trained a CNN to distinguish between unusable image parts (background, areas of poor focus, debris, tissue folds) and usable tissue. Only the latter was used for further analysis. Based on pixel-wise annotation from experienced pathologists they trained additional CNNs to segment the usable tissue. From this, 198 features (for example fraction of tissue area predicted to be fibrotic) were calculated and used for machine learning prediction of cirrhosis and liver-related clinical events.

There are no techniques specific for histologic images of intracranial aneurysms. Compared to histologic images routinely collected during biopsies, for example for cancer diagnosis, histologic images of aneurysms are rare. In Chapter 6 different segmentation methods for histologic images of intracranial aneurysms are explored.

Research question 1 b: What segmentation approach is suited to support analysis of histologic images of intracranial aneurysms?
Automatic segmentation can be used to guide data exploration or prepare data for further automatic processing and analysis. Histologic images can be analyzed with various algorithms using classical image processing or deep learning. For tissues where a histologic analysis is part of the clinical routine, for example liver biopsy, various studies regarding automatic segmentation and tissue analysis exist. Histologic images of aneurysms are rare and not used in clinical routine. Therefore, automatic segmentation is not yet available. Aneurysms are pathological changes and a wide variance of the tissue in the aneurysm wall is expected.

3.2.3 Virtual inflation for histology

The post mortem ex vivo analysis of aneurysms is challenging, as the shape of the aneurysms can be alternated during the extraction and fixation process. The main difficulty is the collapsing of the vessel and aneurysm due to the loss of blood flow inside. This was addressed by Saalfeld et al. [20]. They described virtual inflation for histologic and OCT images of post mortem ex vivo aneurysms. They manually segmented the inner and outer contours and equally sampled the contours. Then, they calculated the wall thickness and the normals at the points of the inner contour. The inner points are projected on a circle and the rest of the wall is adjusted accordingly. With linear interpolation, several steps between the original images and the inflated images with a perfect circular inner contour can be calculated (see Fig. 3.7).
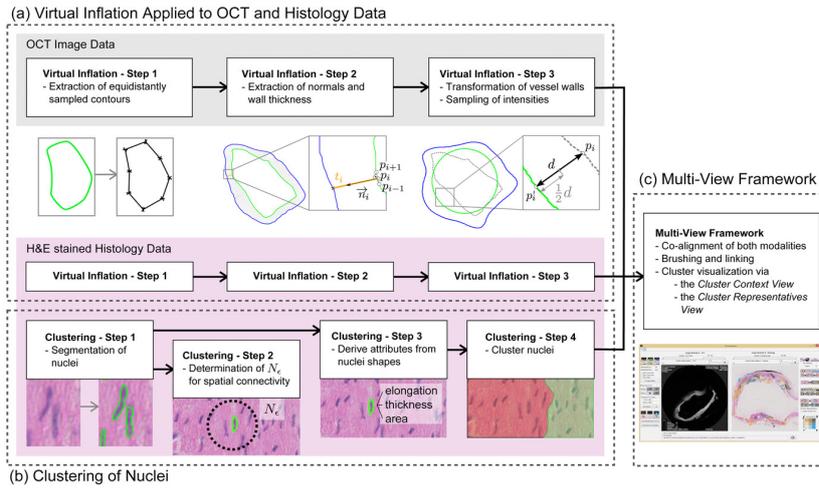
Figure 3.7: Virtual inflation of histologic images [20]
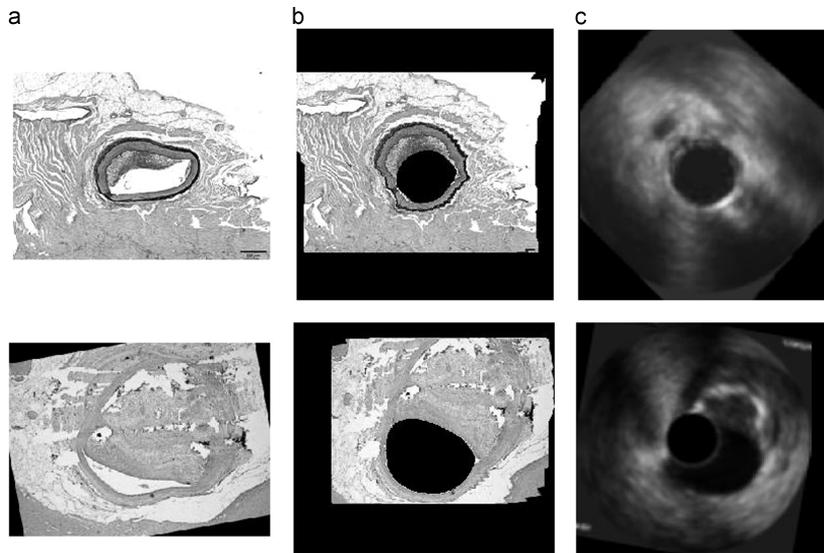
Figure 3.8: Histologic images before (a) and after (b) inflation. c) corresponding IVUS images [127]

Athanasiou et al. [127] proposed virtual inflation for histology and microCT of vessels. Their inflation first requires manual registration of the images to intravascular ultrasound. The inflation is then based on the differences in the vessel contours (see Fig. 3.8).

Research question 2: How can deformation during tissue collection be handled?

Tissue collection for further imaging like histology or microCT leads to deformation of the tissue. Especially due to the loss of blood flow inside the vessel and aneurysm the shape is alternated. This has to be considered in aneurysm wall analysis using histologic images.

3.2.4 Histology and microCT

Several studies used microCT as well as histologic images. microCT images are CT images (recall Section 2.2.1) which allow the analysis of structures in the μm range [128]. Often, histologic images are used to verify findings in other imaging methods or to find a correlation between the presence of specific cell types, for example inflammatory cells, and other aneurysm characteristics.

Senter-Zapata et al. [129] compared microCTs of tissue sections before and after embedding in paraffin. They found that the volume decreases between 19.2% and 61.5%. Furthermore, they compared the widest cross-sectional microCT diameter to the corresponding histologic slide. The histologic measure was 15.7% longer than the microCT.

Jessen et al. [130] used microCT and histology to compare different stents. They artificially created aneurysms in New Zealand white rabbits and explanted the aneurysm at 30, 90, and 180 days after treatment (see Fig. 3.9). They did not register the H&E stained images to the microCT images, but during the analysis of the histologic images, the 3D microCT was used as a reference for the coil positions.

Cebral et al. [131] derived a vascular model from preoperative 3D imaging and performed hemodynamic simulation. During surgery, they collected a tissue sample and used microCT to reconstruct a tissue model. On this sample, they manually marked features identified on the surgical video or ex vivo photos of the tissue sample. They also imaged the tissue sample using multiphoton microscopy. Thin walls were associated with high WSS. Thicker regions were associated with lower WSS and atherosclerotic and hyperplastic-looking wall parts.

In Chapter 7 a combination of preoperative imaging, hemodynamic simulation and microCT and histologic images of intraoperatively collected tissue is presented.

Research question 3: How can various 2D and 3D information be combined for exploration of the aneurysm wall?
Preoperative imaging, hemodynamic simulation, microCT and histologic images provide a wide variation of information. For a new way to explore the aneurysm wall, these should be combined and presented in a way that allows experts to gain further insight into the aneurysm wall.
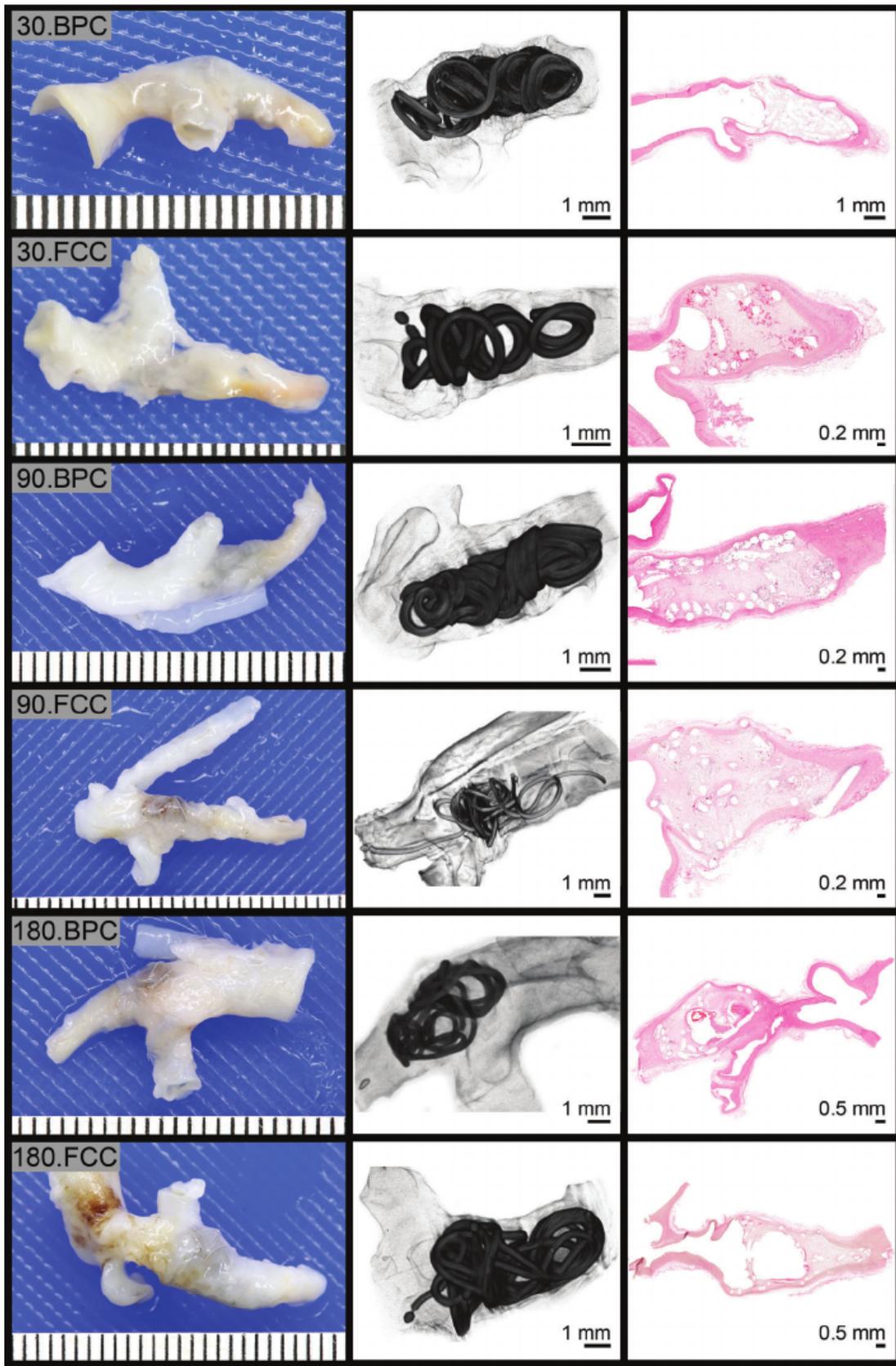
Figure 3.9: Left: explanted aneurysm, middle: microCT, right: histologic images; 30,90 and 180 days after treatment with coil; FCC: foam-coated coil, BPC: bare platinum coils [130]

3.3 Black blood MRI in aneurysm research

Besides CT angiography and MRI angiography, a new imaging technique has recently become interesting for aneurysm diagnosis: BBMRI. In contrast to classical MRI, the blood appears dark and a part of the vessel wall is visible (recall Section 2.2.2). While not yet widely used in clinical routine, this could change in the future. In 2022 Raz et al. [71] recommended the usage of BBMRI for treatment evaluation. In the following, several studies regarding the usage of BBMRI for aneurysm analysis and rupture risk assessment are presented. A major problem is the subjective wall enhancement segmentation. Chapter 8 will present a tool for consistent, user-independent and objective wall enhancement segmentation.

Vessel wall enhancement is often divided into strong/avid, mild, and no wall enhancement. In most studies, this classification is done subjectively by experienced neuroradiologists. Objective approaches use post-contrast quantification of signal intensity and measure focal aneurysmal wall enhancement and circumferential aneurysmal wall enhancement. While being a promising technique, currently standardized protocols for image acquisition are missing. Vessel wall enhancement is not well defined and the histologic correlate of aneurysm enhancement is not consistent.

Liu et al. [132] analyzed 61 aneurysms. In 33 of these, wall enhancement was detected by medical experts. Aneurysms with wall enhancement had a significantly higher ISUIA grade (recall Section 2.1.2) than aneurysm without wall enhancement. Larger aneurysms were more prone to show wall enhancement, but wall enhancement was also found in smaller aneurysms. The authors suspect that wall enhancement could be an indication for wall stability and as such improve the risk evaluation of intracranial aneurysms.

Antiga et al. [133] used a thin-walled carotid bifurcation phantom to analyze the reliability of wall thickness estimation based on black blood MRI. Figure 3.10 shows the difference of measured and predicted wall thickness for an artificial normal carotid bifurcation. The two main sources for differences are partial volume errors and obliqueness artefacts.

In a study by Fu et al. [134] a correlation between symptoms and wall enhancement was found. Two radiologists were asked to determine whether aneurysm wall enhancement was present or not. With a similar approach, Edjlali et al. [135] observed that wall enhancement can be more frequently found in unstable aneurysms than in stable aneurysms.

Roa et al. [136] compared different objective measurements for wall enhancement and concluded that a measurement based on the aneurysm–to–pituitary stalk contrast ratio is the most reliable method and robust regarding different manufactures and magnet strength. They only classified the aneurysms into aneurysms with or without wall enhancement.
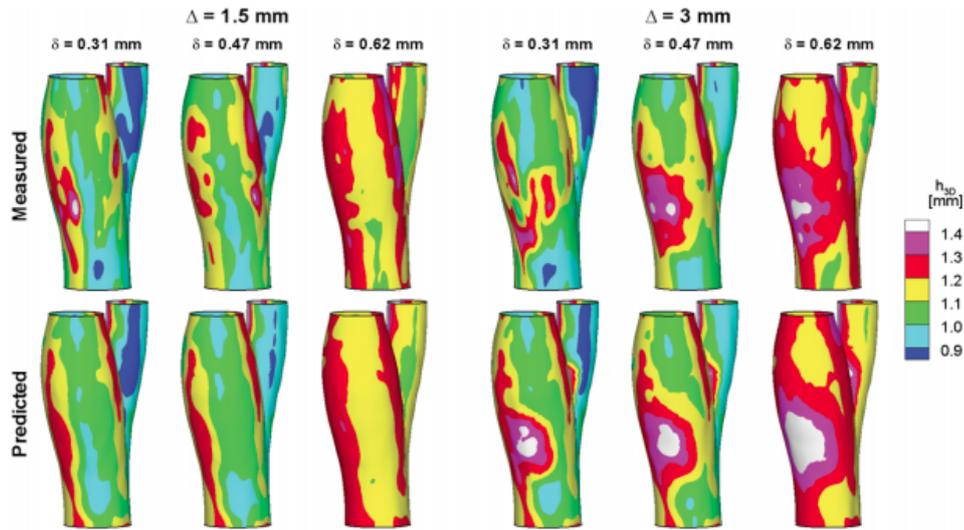
Figure 3.10: Top row: thickness computed from lumen and outer wall surface reconstruction from MRI images; bottom row: prediction from analytical model based on true thickness of the carotid bifurcation model [133]

Hemodynamic parameters are often used in aneurysm research. Several studies analyzed the relation between wall enhancement and hemodynamic parameters. Blood flow simulation and hemdoynamic parameters for intracranial aneurysms are explained in Section 3.1. Aneurysms of 22 patients, of whom 16 showed wall enhancement, were analyzed by Khan et al. [137]. Wall enhancement was correlated with lower wall shear stress, lower sac-averaged velocity, and larger aneurysm size and size ration. Zwarzany et al. [138] analyzed 64 small unruptured intracranial aneurysms and found that aneurysms with wall enhancement were larger, had a higher dome-to-neck ratio, and a more irregular shape than aneurysms without wall enhancement.

Fanning et al. [139] researched aneurysm wall enhancement in the context of follow-up imaging after treatment with coils. In 18.6% of the patients treated with bare platinum coils wall enhancement occurred. The authors suspect that the wall enhancement represents a normal healing response.

In a study by Edjlali et al. [140] two readers with more than four years of experience determined for 108 aneurysms whether circumferential wall enhancement was present (see Fig. 3.11). Wall enhancement was not connected to the aneurysm size, but occurred more often in unstable aneurysms.

Nagahata et al. [141] analyzed 61 ruptured and 83 unruptured aneurysms of 117 patients. Using pre-and post-contrast MRT images they classified the aneurysms into aneurysms with strong, faint, and no wall enhancement. 81.9% of the unruptured aneurysms did not show wall enhancement, 13.3% showed faint wall enhancement and 4.8% strong wall enhancement. Only 1.6% of the ruptured aneurysms did not show wall enhancement, 24.6% showed faint wall enhancement and 73.8% of the ruptured aneurysms had strong wall enhancement.
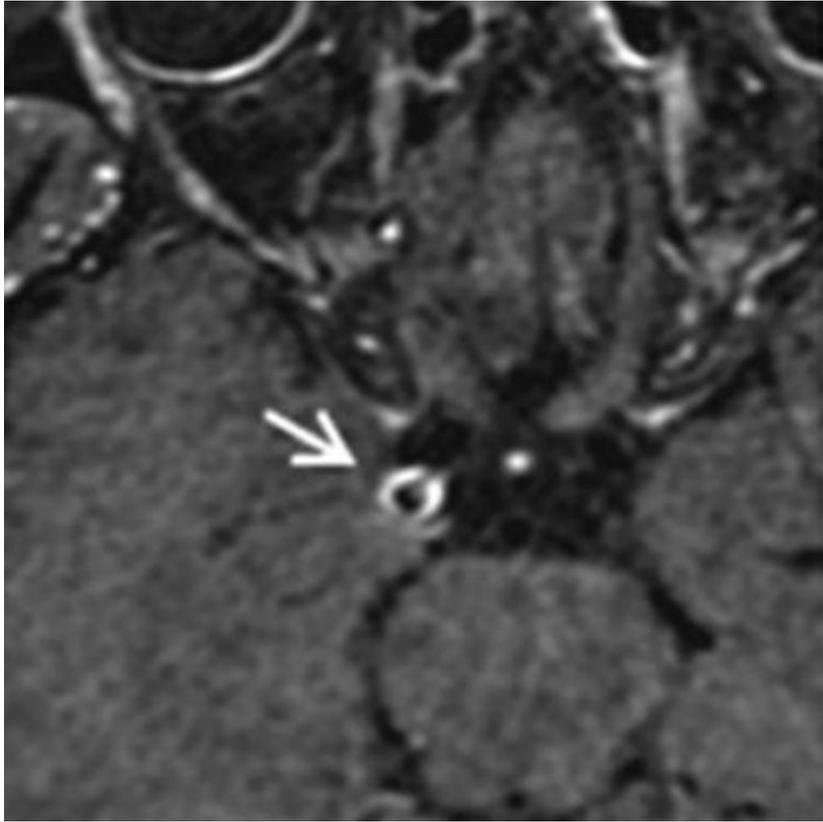
Figure 3.11: Wall enhancement in BBMRI [140]

Hadad et al. [142] et al. analyzed 23 unruptured aneurysms from 20 patients. For each aneurysm, a hemodynamic simulation was carried out. Wall enhancement was manually segmented by two teams of experienced researchers. Overall 72 wall enhancement regions were identified, 40.56% in the aneurysm body, 18.25% at the dome and 14.19% at the neck. Wall enhancement regions had a lower mean wall shear stress.

A study of 38 aneurysms showed that wall enhancement is effective for differentiating stable, unruptured aneurysms and evolving (growing or causing symptoms, e.g. a neurological deficit) aneurysms. For a quantitative wall enhancement analysis pre- and post-contrast images were used. A significant difference was only found in the extent of the enhancement, but not in the strength of the enhancement [143].

In a recent study, Fu et al. [144] analyzed the wall enhancement of 341 unruptured aneurysms of 267 patients. Out of these aneurysms, 93 were symptomatic with sentinel headache or oculomotor nerve palsy. Two experts determined whether no wall enhancement, focal wall enhancement, or circumferential wall enhancement was present. In addition to this qualitative analysis, a quantitative wall enhancement index was calculated based on pre- and post-contrast wall intensities and pre- and post-contrast white matter intensities. Circumferential wall enhancement and a higher wall enhancement index were more frequently observed in symptomatic than in asymptomatic aneurysms.

Omodaka et al. [145] also calculated a wall enhancement index (WEI). With a volume of interest (VOI), they manually traced enhanced regions and searched for the VOI with the largest average signal intensities. Their WEI calculation also took the signal intensity of the stalk and brain parenchyma in post- and pre-contrast images into account. The VOI for the average signal intensity calculation of the wall enhancement was $0.125mm^3$, for the brain parenchyma $8.0mm^3$ and for the stalk $1.0mm^3$. The WEI in ruptured aneurysms was significantly higher than in unruptured aneurysms.

Galloy et al. [146] analyzed 21 aneurysms. Out of these, 14 aneurysms had signals with an intensity of 0.6 or more of the pituitary stalk intensity and were therefore classified as enhanced. Wall tension was higher in aneurysms displaying wall enhancement. Areas of low wall tension were mainly found around aneurysm blebs.

In a small study with only 39 participants with overall 40 aneurysms, vessel wall enhancement after endovascular treatment was common and not useful for aneurysm recurrence prediction. Besides subjective assessment, the aneurysm-to-pituitary stalk contrast enhancement ratio was determined [147].

Pradivtseva et al. [148] analyzed the impact of different image acquisition parameters on the vessel wall enhancement. They also found that slow blood flow increased signal intensities and MSDE reduced flow-related signal enhancement. Regarding the voxel size, the results varied. For one of the three patients, a smaller voxel size ($0.7mm^3$) lead to more efficient blood suppression, while for the other two a larger voxel size ($0.9mm^3$) was better.

Research question 4: How can the aneurysm wall be included in rupture prediction?

BBMRI can show wall enhancement around intracranial aneurysms. This non-invasive imaging technique has the potential to be used in clinical routine. Previous studies suggest that wall enhancement can be used as indicator for aneurysm rupture. Including BBMRI could provide useful information for individual treatment decisions. Automatic segmentation of wall enhancement could simplify the usage of BBMRI.

Research question 4 a: How can wall enhancement be segmented?

A major limitation of the previous presented studies is the subjective wall enhancement identification. An objective, user-independent wall enhancement segmentation is needed.

3.4 Summary

The intracranial aneurysm wall is an important factor in aneurysm rupture. Imaging of the wall is challenging. For clinical routine, black blood MRI could be used. This still requires further research. Previous wall enhancement research heavily relies on manual, subjective wall enhancement segmentation. In Chapter 8, a tool for semi-automatic, objective wall enhancement segmentation is presented.

Histologic images provide a detailed insight into the aneurysm wall. They require several processing steps, for example segmentation of tissue and virtual inflation. Chapter 6 and Chapter 7 describe algorithms for processing histologic images of intracranial aneurysms with large gaps and various stainings.

4 Related Work - Mesh processing and hemodynamic analysis

This section first describes the diagnosis, treatment, and ongoing research on intracranial aneurysms. Then, different image acquisition techniques and their usage in vessel and aneurysm imaging are presented. After that, related works on histologic image processing, BB-MRI, and 3D models of aneurysms are summarized.

4.1 Mesh processing for surface meshes

In this section, several mesh processing algorithms with a focus on mesh processing for surface meshes (see Section 3.2.1) of intracranial aneurysms are described. Meshes of intracranial aneurysms are used for various tasks, for example the calculation of morphological parameters or hemodynamic simulation. Especially mesh processing for aneurysms with geometric deep learning is discussed. Deep learning on images has been successfully used in various tasks, including aneurysm detection [149, 150, 151]. In this work, geometric deep learning on point cloud and meshes is used. These neural nets can be applied independent from the image modality. Major limitations of these neural nets are their high computational and memory cost [152]. Popular benchmarks show everyday objects and humans and are less complicated and smaller than medical meshes. These limitations are addressed in Section 9.1.1.

4.1.1 Mesh segmentation and classification for aneurysms

Mesh segmentation divides the mesh into several parts, as shown in Figure 4.1. Closely related is also the segmentation of point clouds. Very few works on aneurysm segmentation exist. Mesh segmentation can be done with or without machine learning and some deep learning approaches exist. Most common in intracranial aneurysm research is the segmentation into aneurysm and parent vessel (Fig. 4.2). This requires th preprocessing of the mesh to only include a small part of the vessel.
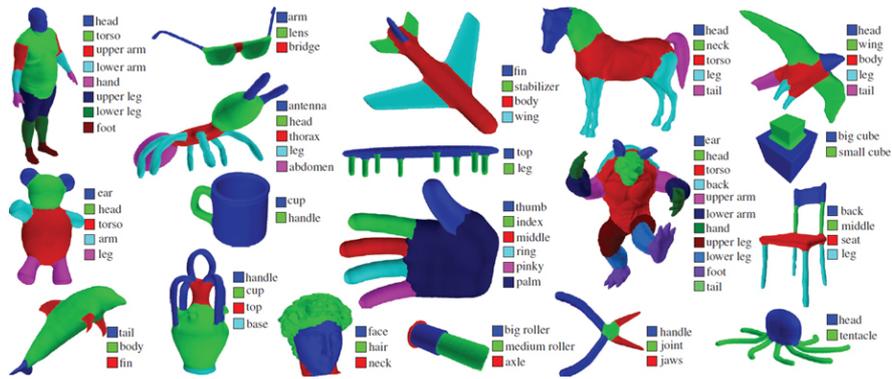
Figure 4.1: Examples of mesh segmentation [153]

Early approaches of mesh segmentation contained region growing, hierarchical clustering, iterative clustering, spectral analysis, and implicit methods. In these, different mesh attributes are used, for example, planarity, higher degree geometric proxies (spheres, cylinders, cones, quadrics), differences of normals or dihedral angles, curvature, geodesic distances on the mesh, symmetry, convexity, medial axis, and shape diameter [154].
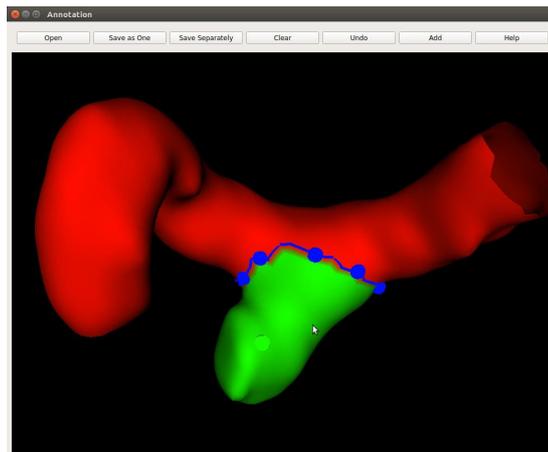
Figure 4.2: Aneurysm (green), neck curve (blue) and parent vessel (red) in annotation tool by Yang et al. [155]

Kaick et al. [156] presented a non-parametric segmentation algorithm for point clouds and meshes. Their algorithm is suitable for point clouds with missing parts. The number of segments is not defined before the segmentation. First, the point cloud is divided into weakly convex parts based on the visibility (see Fig. 4.3). These segments are then merged by analyzing the volumetric signature. In the last step, the borders of the segments are refined with point-level graph cut optimization.
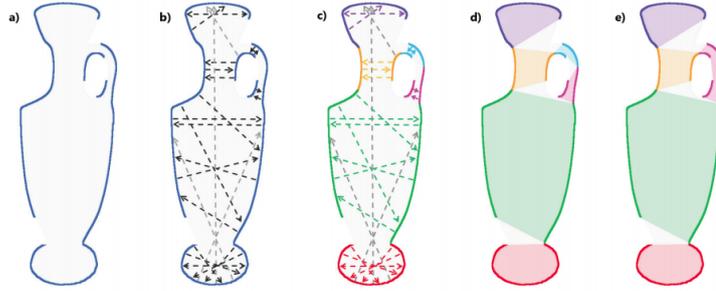
Figure 4.3: Part characterization: (a) A point cloud with missing parts is given. (b) We compute the visibility between points in the shape. (c) The visibility information is used to decompose the shape into weakly-convex parts. Here, lines of sight within components are colored according to their component colors, while lines of sight between different components are grey. (d) The weakly-convex parts are analyzed to find adjacent parts with similar geometric properties. (e) Adjacent similar parts are merged to produce the final segmentation of the shape [156]

MeshCNN [157] provides deep learning for mesh classification and segmentation. Five edge features (dihedral angle, two inner angles, edge-length ratio of each adjacent triangle) are used. The segmentation net follows the U-net design. In the pooling layer, the mesh is reduced to its relevant parts by an edge collapse operation (Fig.4.4).

Zhang et al. [158] segmented intracranial aneurysms into aneurysm and parent vessel. As shown in Figure 4.5, they used several regional and global descriptors. Using gentle AdaBoost they trained a binary classification model. They only used 8 aneurysms, which all had the same topology (one aneurysm, one inlet, two outlets). With the high variance in aneurysm and vessel shapes, this is too limited for broad use.

Yang et al. [155] compared several deep learning algorithms for binary segmentation into aneurysm and parent vessel. Furthermore, they compared several deep learning algorithms for point clouds and meshes with different resolutions. The best results for the vessel segmentation were achieved with PointConv [159] on 2048 points (IoU 94.65% for vessel and 79.53% for aneurysm) and the best aneurysm segmentation with SO-Net [160] on 2048 points (IoU 94.46% for vessel and 81.40% for aneurysm). MeshCNN achieved 90.34% on vessels and 71.60% on aneurysms. In general, segmentation results were worse for aneurysms with a small size ratio. Based on this, a pipeline for aneurysm segmentation was developed. After semi-automatic reconstruction of surface models of brain arteries, intracranial aneurysms are automatically detected. Small fragments of the surface model are sampled and PointNet++ is used to classify these into segments with or without aneurysms. SO-Net is used to segment the aneurysms in the fragments where an aneurysm is present. This avoids the major problem of a large class imbalance when segmenting the aneurysm on the whole surface model [161].
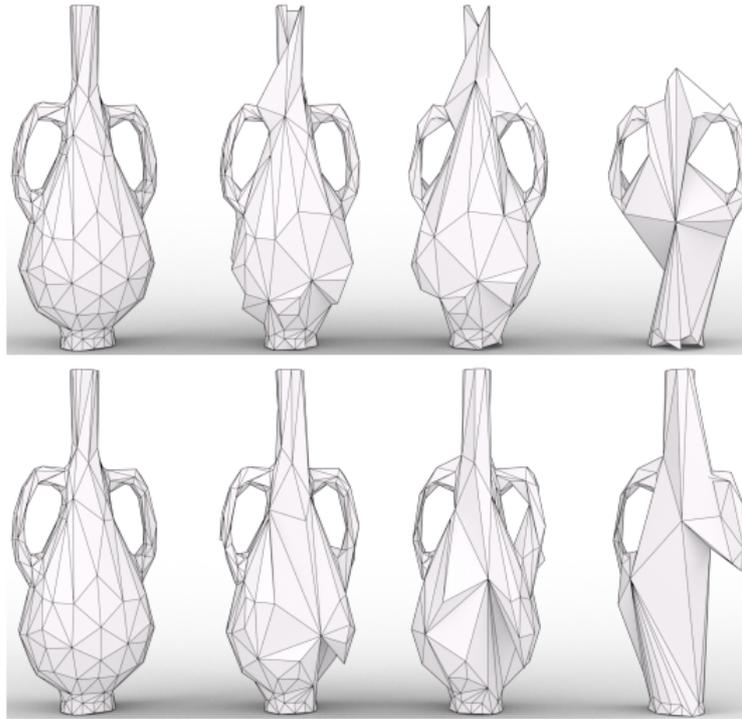
Figure 4.4: Pooling operation in MeshCNN: Depending on the task different edges are collapsed [157]

(a) Curvature ($|\kappa_1 \kappa_2|$)   (b) PCA ($s_1/(s_1 + s_2 + s_3)$)   (c) SDF ($\pi/6$)

(d) VSI ($\pi/6$)   (e) AGD (50th percentile)
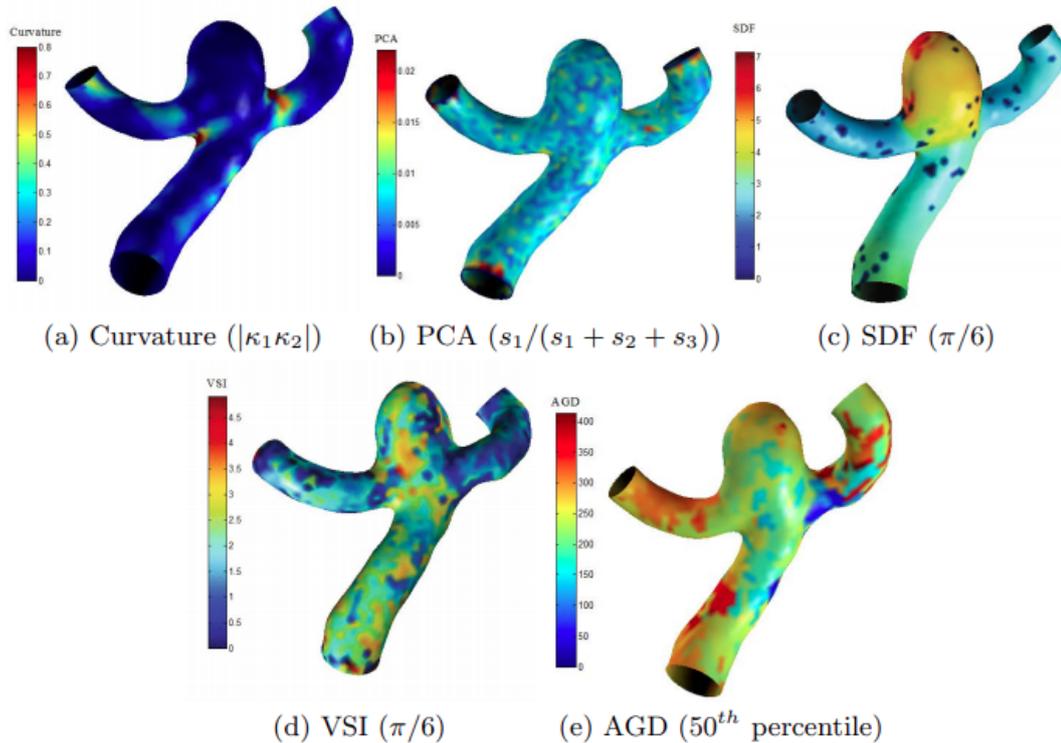
Figure 4.5: Features used for aneurysm and parent vessel segmentation: curvature, shape direction (based on covariance of coordinates), shape diameter function (SDF), volumetric shape image (VSI), average geodesic distance (AGD) [158]

Thomas et al. [162] presented Kernel Point Convolution (KPConv) for deep learning point cloud segmentation and classification. These performed well on ModelNet40 (92.2% accuracy) and segmentation of complex point clouds of outdoor (Semantic3D, 74.6 mIoU) and indoor (S3DIS, 67.1%) scenes.

Another algorithm for mesh classification was presented by Zheng et al. [163]. Surface patches are approximated with polynomials. A patch is characterized by the polynomial parameters, the center point coordinates, and the normal vectors of the surface. Their neural net architecture is based on capsule networks. On the SHREC15 dataset, the MeshCaps neural net achieved an accuracy of 93.8%.

Invantsits et al. [164] presented deep learning rupture prediction using point clouds. They used point-cloud encoding to capture the shape of the aneurysm. For each point, the wall shear stress was included. Furthermore, patient age, sex and aneurysm location are used. The combined feature vector is the input to a fully connected neural network. It achieves an accuracy of 64% and an F2 score of 0.73.

In Chapter 8, a variation of MeshCNN for classification of aneurysms as ruptured or unruptured is presented. Additionally, a user interface to explain the results for users without deep learning knowledge is described. In Chapter 9, variations of MeshCNN and KPConv for wall shear stress prediction are presented.

Research question 4 b: How can the aneurysm shape be used for rupture prediction?
In Section 3.3, the inclusion of wall enhancement into clinical routine was discussed. However, wall enhancement alone might not be enough to predict aneurysm rupture. A major factor is the shape of the aneurysm, which can be described using several morphological parameters (Section 2.1.2). They can be complex and most of them are not used in clinical routine. The deep learning approaches described in this section can be used to classify the shape of an object without manually defined morphological parameters. This could be used for shape-based rupture risk prediction.

4.1.2 Centerline & vessel graph

Aneurysm meshes are used for several further calculations, for example for morphological parameters (recall Section 2.1.2) or hemodynamic simulations (Section 4.2). Some of these need further processing of the aneurysm mesh, for example, centerline calculation (Fig. 4.6) or composing a graph representation of the aneurysm based on the mesh (Fig. 4.7). Structured mesh generation for hemodynamic simulation also requires a centerline.
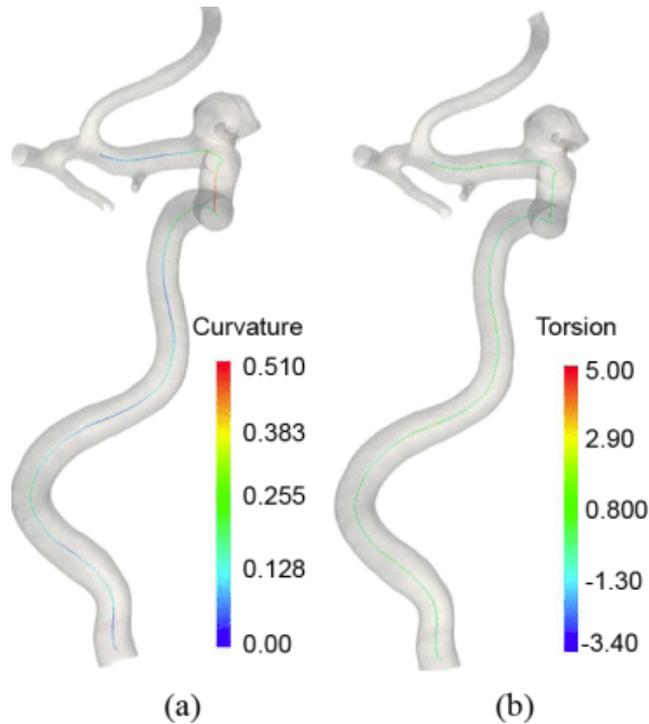
Figure 4.6: Example of centerline inside aneurysm [165]

Centerlines can be detected in 2D and 3D images and meshes. In images, either hand-crafted filters or learned filters are used. Sironi et al. [166] presented a deep learning centerline detection by training regressors to return the distance closest to the centerline. This was successful for aerial images, brightfield microscopy images, and photon images. A great disadvantage of the technique is that for each image type a new neural net has to be trained.

Antiga et al. [167] proposed a centerline calculation for vessels using Voronoi diagrams. Each point of the Voronoi diagram is associated with a maximum inscribed sphere. Centerlines between given points minimize the integral of the radius of maximum inscribed spheres along the path.

Another approach was presented by Wei et al. [168]. They first split the mesh into several cylindrical parts and then calculate the centerline for each cylinder. The centerline extraction is done by optimizing the distance between a centerline
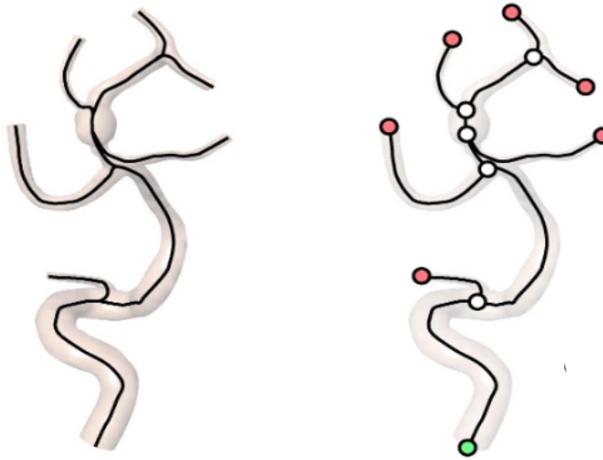
Figure 4.7: Aneurysm and corresponding graph from [176], red: outlet, green: inlet, white: bifurcation

point and surrounding mesh vertices. The algorithm has seven parameters. Especially for the segmentation based on k-means clustering the correct choice of clusters and cluster centers is important.

Bitter et al. [169] presented a centerline algorithm based on binary voxel representations of the objects. They first calculated the distance to the object boundary and generated an gradient vector field. Based on this, they compute an initial centerline. This is then refined. Calculating a sphere around the initial centerline points helps adding branches to the centerline. The sphere calculation has two parameters which have to be set according to the application.

More recent centerline extraction algorithms often utilize deep learning. Gao et al. [170] and Wolterink et al. [171] presented deep learning-based centerline extraction for coronary arteries. Iteratively, a CNN Tracker is used to predict the artery direction and radius. The prediction is done on CT angiography images. Other image-based approaches use the U-Net architectures [172, 173]. A disadvantage of these approaches is the task and image modality-specific training.

Antiga et al. [174] presented an algorithm to decompose models of carotid bifurcation into separate branches. Based on the centerline and the maximum inscribed sphere radius the models were divided into branches. Branches connect at splitting lines. They tested their algorithm on idealized models of branching vessels. Based on their algorithm, Chnafa et al. [175] generated a reduced-order model for estimation of outflow rates with less computational resources compared to 3D simulations. Their model consists of nodes and edges with information like length, equivalent radius, and vectors at the extremities.

Saalfeld et al. [176] used a vessel graph extracted based on the centerline for outflow splitting on multiple aneurysms. The graph included the inlet vessel, outlet vessels and bifurcations. The aneurysm itself was not visible in the graph representation.

In Chapter 9, a new aneurysm graph based on a deep learning mesh segmentation is presented and compared to the graphs introduced here.

Research question 5: How can wall shear stress be included in rupture prediction?
Previous studies showed that hemodynamic parameters like the wall shear stress are related to aneurysm rupture. The simulation requires a time-consuming, often manual, mesh processing. To include wall shear stress into clinical routine, faster and easier hemodynamic parameter determination is necessary.

> **Research question 5 a: How can mesh processing be improved?**
> *By replacing manual mesh processing steps with automatic or semi-automatic approaches the overall effort for simulation can be decreased.*

4.2 Aneurysmal blood flow

The blood flow inside the aneurysm is an important factor for aneurysm rupture. However, blood flow inside the aneurysm cannot be measured directly. Extensive research on modeling and simulation of patient-specific blood flow has been done. In the following, studies on the relation between blood flow and aneurysm rupture are presented. Commonly used hemodynamic features are shown in Figure 4.8. In Chapter 9, tools to support the generation of patient-specific meshes for simulation are presented. A major problem is the transfer from research results into clinical routine as the blood flow simulations are very time-consuming and require expert knowledge. Therefore, Chapter 9 presents deep learning for fast prediction of hemodynamic parameters.

Berg et al. [178] summarized the steps and challenges of hemodynamic modeling of intracranial aneurysms. The basis for simulation are the image, image segmentation, and 3D-model generation from the images. Together with simulation parameters, for example, boundary conditions or blood approximation (Newtonian/non-Newtonian), this heavily influences the simulation results.

The result of a simulation depends on a large number of parameters (for example mesh resolution, distribution of cells in the domain, solver settings). Different teams vary in their decision for simulations. Common assumptions are blood as a Newtonian fluid with a density of 1.05 and 1.06 g/cm^3 and a viscosity of 3.5 or 4.0 cP [179]. Zimmermann et al. [180] analyzed synthetic and patient-specific aorta data. Important factors for correct WSS prediction based on 4D flow MRI data are sufficient spatial resolution and accurate vessel wall segmentation.
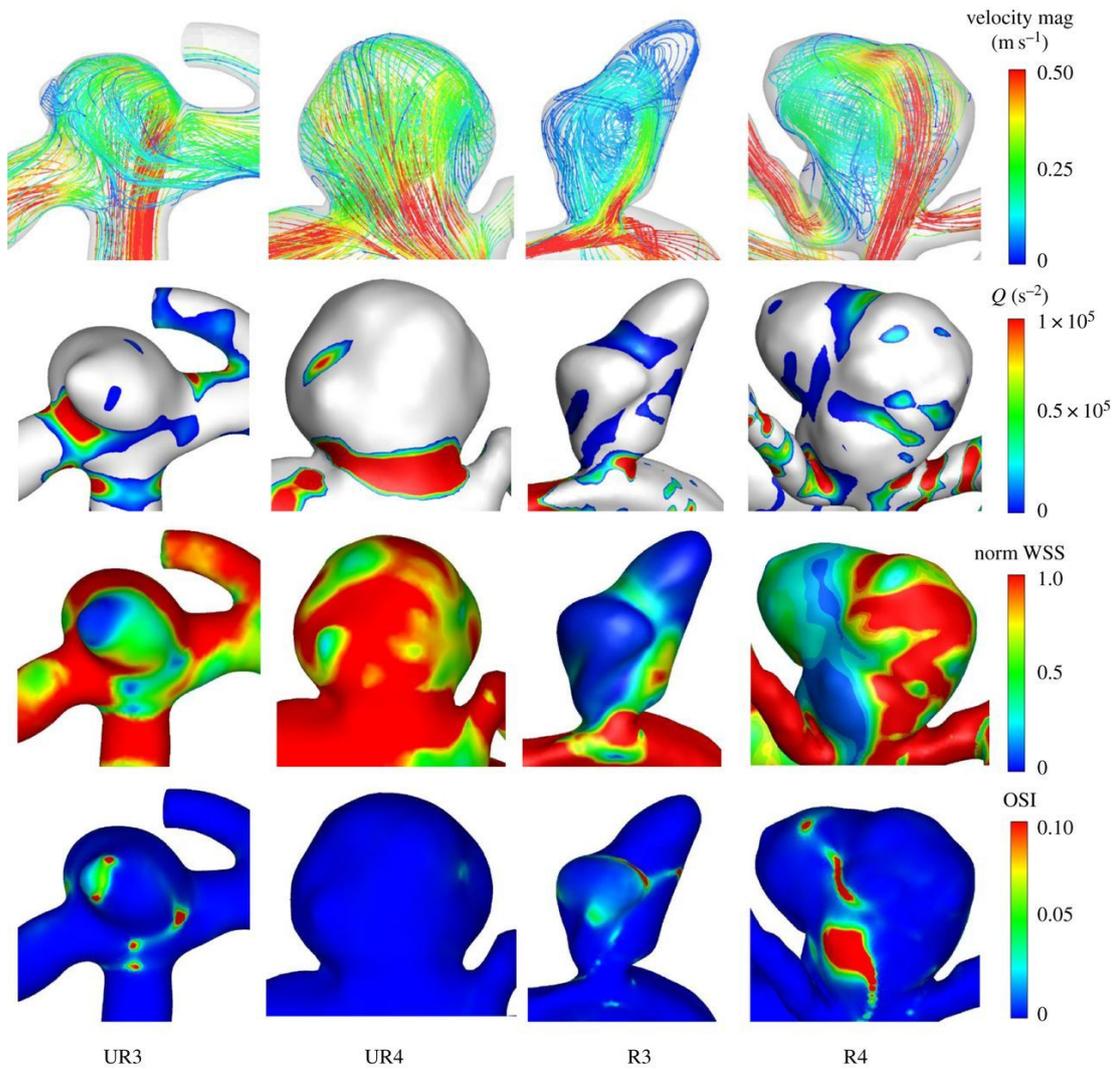
Figure 4.8: Examples of common hemodynamic parameters (velocity, Q-criterion, wall shear stress (WSS), oscillatory shear index OSI) on four aneurysms [177]

Several studies used intraoperative images to examine the aneurysm wall. Regarding wall thickness and WSS conflicting results were reported. Some studies found a connection between high WSS and thin wall, while others showed a connection between low WSS and thin walls [181].

While not being the sole factor for aneurysm formation and rupture, high flow is an initiator for intracranial aneurysm formation. Flow can trigger inflammatory reactions and determines whether an aneurysm is stable or ruptures [182].

Saqr et al. [183] reviewed 1773 articles about computational fluid dynamics for intracranial aneurysms published between 1998 and 2018. 90% of the hemodynamic simulations modeled the blood flow inside the aneurysms as Newtonian. This assumption has a major impact on the calculation of rupture prediction parameters. Newton fluids tend to overpredict the wall shear stress at the aneurysm neck and dome.

Valen-Senstad et al. [184] performed high-resolution CFD on 12 aneurysms (five ruptured, seven unruptured) at or near the middle cerebral artery. The images were collected using CTA and segmented with the Vascular Modeling ToolKit (vmtk) [185]. Eight aneurysms were bifurcation aneurysms. The other four did not arise at the apex of the bifurcation and were classified as sidewall aneurysms. They classified the aneurysms as stable and unstable based on the turbulent kinetic energy. All sidewall aneurysms were classified as stable as they exhibit energies under $10^{-4}\mathrm{m}^2/\mathrm{s}^2$. Five of the bifurcation aneurysms were unstable.

4.2.1 Deep learning for hemodynamic simulations

As discussed in the previous section, hemodynamic parameters could help to accesses the patient-specific rupture risk of an aneurysm. They are not used in clinical routine, as they are too labor- and time-intensive. In the context of hemodynamic simulations, deep learning is used for various task, which can be summarized in two categories. The first category is the usage of deep learning to improve the mesh quality for simulations. The second category is the deep learning prediction of simulation results with the goal to replace time-consuming simulations with fast neural nets.

Huang et al. [186] present deep learning mesh refinement to produce optimal meshes for computational fluid dynamics. Their deep learning approach was restricted to 2D. With a U-net they predicted the number of cells in an area. Vertice and edge positions were not captured by this representation.

Si et al. [187] used deep learning to evaluate the quality of grid surface meshes. The surfaces consisted of up to 121×121 points, equally distributed in two directions and presented in 2D images. With VGG16 [188] a test precision of 0.9863 was reached. An effective evaluation of the mesh quality is important, as it has a large impact on the simulation. The presented deep learning by Si et al. is

restricted to very specific grid surface meshes and cannot be easily extended to work with complex data like patient-specific aneurysm meshes.

Li et al. [189] proposed a neural net architecture based on a point net to predict hemodynamic parameters of coronary arteries. Their network (see Fig. 4.9 and Fig. 4.10) had two different point clouds as input: the model point cloud, which only had the outer points of the model, and the query point cloud, which had the remaining inner points. They used data from 110 patients and added geometric modifications to increase the number of training samples. With sufficient point density (over 2 million points), an accuracy of around 90% was reached. After training, predictions could be obtained within 1 second with deep learning compared to 10 mins with CFD.
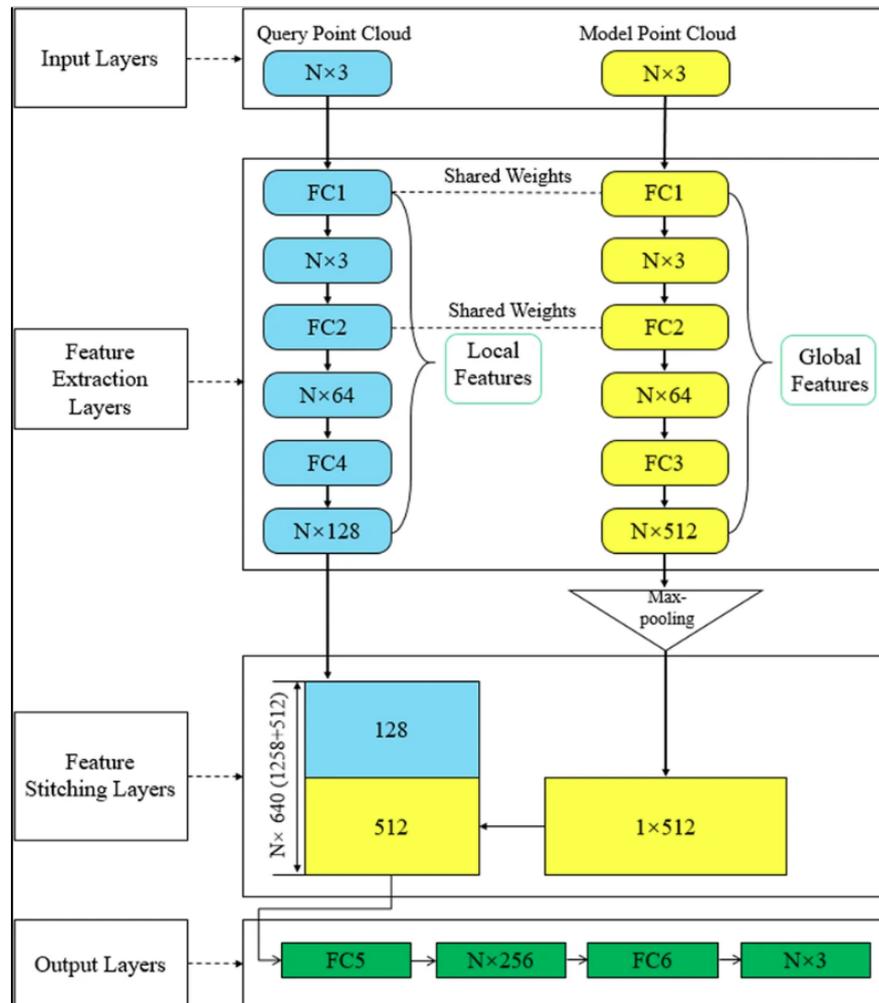
Figure 4.9: Deep learning architecture for hemodynamic parameter predictions based on point clouds [189]
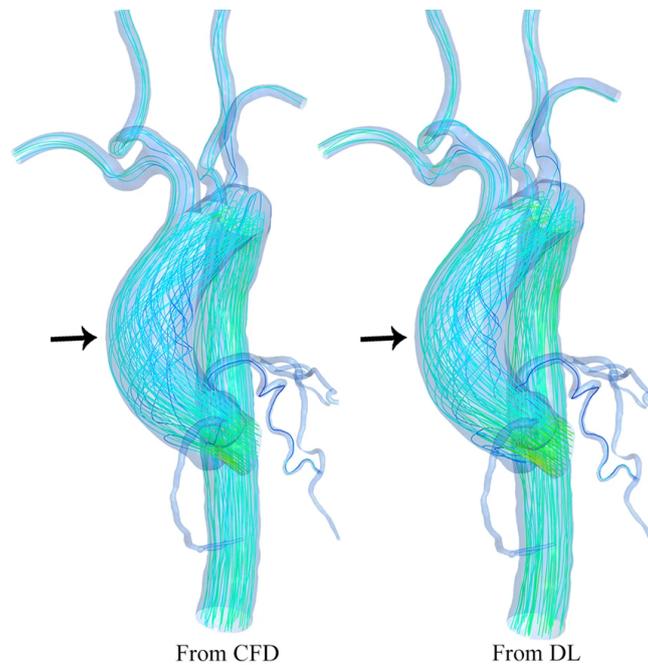
Figure 4.10: Ground truth streamlines and deep learning prediction, black arrow: region of ascending aorta [189]

Gharleghi et al. [190] used deep learning to predict time-averaged wall shear stress in the left main coronary arteries. The prediction took 2 seconds compared to 5 hours CFD simulation. The error was around 10%. They used 127 patient geometries. From the 3D geometries 2D feature maps were derived on which a CNN was trained.

Thamsen et al. [191] evaluated synthetic aorta models for machine learning. Using 154 patients and statistical shape modeling, they created 2652 synthetic cases with hemodynamic properties. They compared static pressure, wall shear stress, secondary flow degree, and kinetic energy over all real and all synthetic data sets, respectively. Real and synthetic data sets showed similar characteristics. They concluded that synthetic data is suitable to be used in machine learning for cardiovascular diseases.

Liang et al. [192] built a statistical shape model using 25 patients and generated 729 thoracic aorta shapes. The surface meshes had 5000 vertices. They first trained an autoencoder on the 3D coordinates from the vertices to capture the shape. Next, the decoder part of the network was replaced to predict either the pressure field, the velocity magnitude field, or the velocity field. The results were consistent with hemodynamic simulation, but took only 1 second instead of 15 min. or more.

Another approach is the usage of graph deep learning. Suk et al. [193] modelled meshes of artificial coronary arteries as graphs. The defined translation invariant features for each vertex based on the normals of the vertices inside a ball. As an indication for the flow direction, for each vertex the geodesic distance to the inlet is given. The neural net architecture is similar to the U-net structure. They created 2000 artificial models of arteries. With an accuracy of 90.5% the WSS vectors could be predicted.

First deep learning approaches for hemodynamic simulations exists. These are mainly developed for aorta models. In Chapter 9, deep learning for wall shear stress prediction of artificial and patient-specific intracranial aneurysms is presented.

Research question 5 b: How can wall shear stress be used in clinical routine?
Hemodynamic simulations require expert knowledge and take a lot of time. Both factors make them unpractical in clinics. As an alternative, WSS prediction with deep learning might be used.

4.2.2 Explainable artificial intelligence

Deep learning has been successful in various tasks. However, often the black box character of deep learning is problematic. To explain what the network is learning and to gain trust, several visualisation tools exist. This is crucial, as deep learning can focus on correlated but not on causal information. For example, visualization of the relevant areas of an image revealed that a deep learning algorithm predicted horses based on the presence of a source tag in the image [194] (Fig. 4.12). An other neural net, trained to classify skin lesions, used the presence of rulers in the images as indication for malignant skin lesions [195]. Explainable artificial intelligence has recently gained popularity [196].
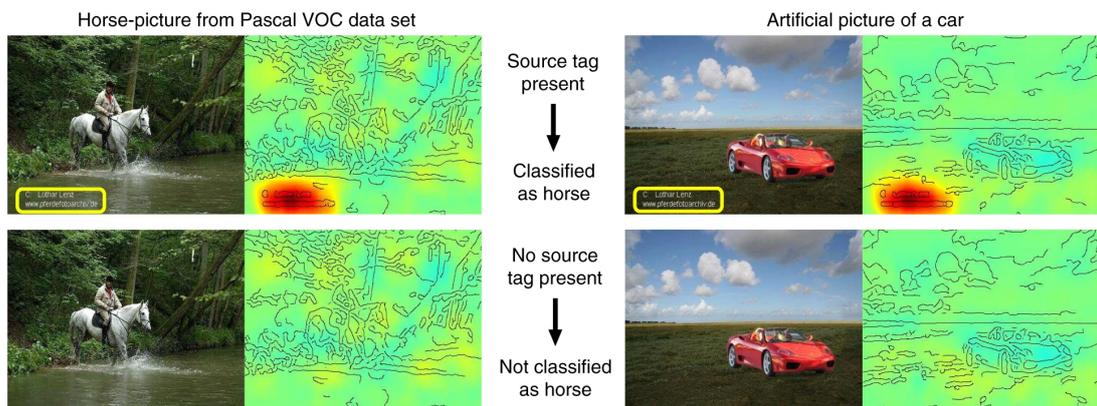

Figure 4.11: Explainable artificial intelligence reveals problematic reasoning, for example detecting a horse based on the source tag [194]

While the term "explainable artificial intelligence" is only used since 2002, earlier diagnosis systems for bacteria-related infections in 1980 were already designed to explain their reasoning [197].

Gillmann et al. [198] presented a visualisation tool for U-nets trained for brain lesion segmentation. There, visualization consists of a selection view (filter and select images), a network view, which shows the network output and the ground truth and AUC, and a context view, where the user can select specific areas of the brain based on the brain atlas to highlight the area in the image. The system was used by experts to answer questions asked by medical collaborators.

Yu and Shi [199] describe four target groups for deep learning visualization (beginners, practitioners, developers and experts) and four visualization goals (teaching concepts, architecture assessment, debugging and improving models and visual explanation). For common deep learning architectures several visualisations for the different tasks exist. In the visual explanation category they further define feature visualization, describing the features various layers pay attention to, and attribution, describing which area of an image is important for the neural net. The classification by Yu and Shi [199] and their examples of deep learning visualization did not include meshes or point clouds.

Lötsch et al. [200] summarized goals of explainable artificial intelligence in biomedicine. The main goal is to achieve trustworthiness of the machine learning system. This is supported by transparency, especially with explanations also understandable for physicians and patients (in contrast to explanations only understandable for mathematicians and computer scientists). Furthermore, the reasoning of the machine learning should follow a logical deduction and be comprehensive for humans. Explanations should be informative and simplify complex machine learning such as deep learning. Similar, Yang et al. [196] present four characteristics of trustable artificial intelligence: valid, responsible, privacy-preserving and explainable.

Rios et al. [201] presented a visualization for the encoding part in point cloud autoencoders. The visualization is based on a 1D convolution operator. The size of the point cloud is preserved throughout the layers and there is a direct correspondence between the activation matrices and the input points. The activation is displayed with color on a scatter plot of the input point cloud. The visualization revealed that the encoder did not learn geometric characteristics but occupancy in the input space. Zhang et al. [202] categorized explainable artificial intelligence methods into intrinsic and post hoc methods (see Fig. 4.12). In the area of medical applications, post hoc methods are more common. While the number of studies including explanation for artificial intelligence rises, only very few provide evaluation. Especially evaluation of the effectiveness by medical experts is rare.
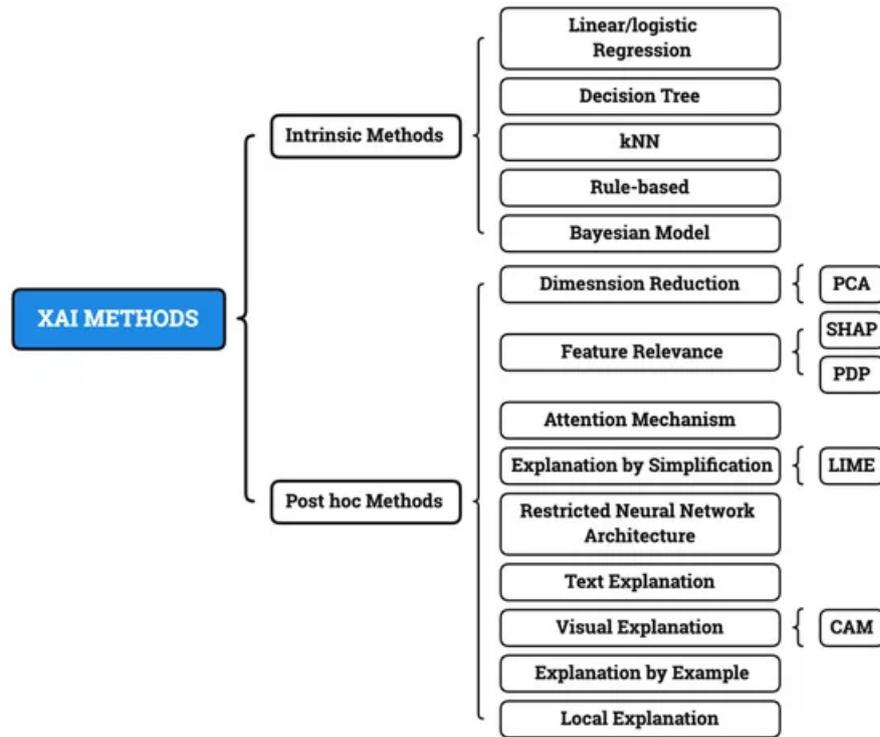
Figure 4.12: Classification of explainable artificial intelligence by Zhang et al.
[202]

In this thesis, several deep learning tools are presented. Especially for the rupture prediction with deep learning a high accuracy is not sufficient to gain the trust of medical experts and patients. Therefore, a user interface to explain what influences the decision of the neural net is needed (Section 8.3). This aligns with the goals by Lötsch et al. [200], as described above.

4.3 Summary

Hemodynamic simulations provide useful insights into the aneurysm. Hemodynamic parameters can be used to estimate the rupture risk of an aneurysm. The simulations are time-consuming and preprocessing of the meshes for simulation requires manual effort. To address the problem of time-consuming simulations, deep learning might be used. Chapter 9 presents tools to reduce the manual effort for mesh processing. Furthermore, instead of time-consuming simulations a geometric deep learning approach for fast prediction of wall shear stress of intracranial aneurysms is presented.

5 Research questions

Currently, the processes leading to aneurysm formation and rupture are not fully understood. Understanding these and predicting aneurysm rupture are crucial elements for optimal treatment of intracranial aneurysms. While the overall questions are too comprehensive to be fully answered in this thesis, several aspects of these are discussed and tools to support further research with histologic images and BBMRI are developed. Here, the research questions raised in the previous chapters are summarized. The questions are answered throughout the next chapters. A summary of the results is given in Chapter 10. An overview of the research topics is shown in Figure 5.1.
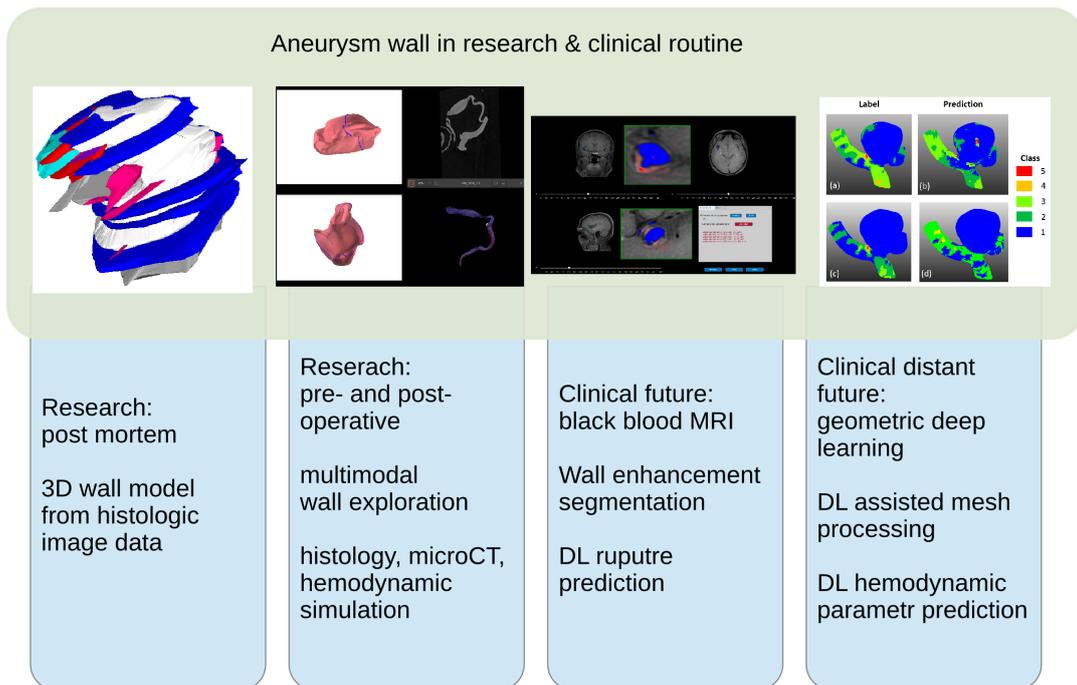
**Figure 5.1:** Overview of topics in this thesis. Research-oriented wall analysis using post mortem data and pre- and post-operatively collected data (research questions 1-3) and clinical-oriented wall analysis based on BBMRI (research question 4). Geometric deep learning might be used to include hemodynamic parameters into clinical routines in the future (research question 5).

1) How can a 3D model of the intracranial aneurysm wall be derived from 2D histologic image data?
Currently, histologic images are the main imaging technique to show details of the aneurysm wall. However, they are only available in 2D (see Section 3.2.1).

a) How to generate a mesh from a point cloud if the points are unevenly distributed?
This questions arises while answering the previous questions. Due to some unique properties of histologic images unusual point clouds occur where commonly available mesh generation algorithms fail (see Section 3.2.1).

b) Which segmentation approach is suited to support the analysis of histologic images of intracranial aneurysms?
Automatic segmentation can be used to guide data exploration or prepare data for further automatic processing and analysis. As they are not used in clinical routines, histologic images are rare and automatic segmentation of the wall tissue is unavailable (see Section 3.2.2).

2) How can deformation during tissue collection be handled?
Tissue collection for further imaging like histology or microCT leads to deformation of the tissue. This has to be taken into account when the aneurysm wall is analyzed using histologic images (see Section 3.2.3).

3) How can various 2D and 3D information be combined for exploration of the aneurysm wall?
Preoperative imaging, hemodynamic simulation, microCT and histologic images provide a wide variation of information. These should be combined for thorough insight into the aneurysm wall (see Section 3.2.4).

4) How can the aneurysm wall be included in rupture prediction?
With black blood MRI some wall parts can be visible. These have to be objectively evaluated to study the correlation between wall enhancement and aneurysm rupture. Another aspect of rupture prediction is the aneurysm shape (see Section 3.3).

a) How can wall enhancement be segmented? A major limitation of the previous wall enhancement studies is the subjective wall enhancement identification. An easy to use tool for objective wall enhancement segmentation should be developed (see Section 3.3).

b) How can the aneurysm shape be used for rupture prediction? Aneurysm rupture prediction for clinical routine should have a minimum user effort, be fast and trusted by doctors and patients. Most complex morphological parameters developed in aneurysm research are never used in clinical routines. Geometric deep learning might be useful for fast predictions based on the aneurysm shape (see Section 4.1.1).

5) How can wall shear stress be included in rupture prediction? Two parts are included here: the improvement of preprocessing data for simulation (see Section 4.1) and the inclusion of WSS in clinical routine (see Section 4.2).

a) How can mesh processing be improved? A variety of often manual and time-consuming processing steps is necessary to produce meshes suitable for hemodynamic simulation and WSS calculation (see Section 4.1.2). Replacing manual processing steps with automatic mesh processing could reduce the effort and time needed.

b) How can wall shear stress be used in clinical routine? Hemodynamic simulations require expert knowledge and take a lot of time. Both factors make them unpractical in clinics. As an alternative, WSS prediction with deep learning might be used (see Section 4.2.1).

6 Understanding aneurysm wall composition - Histology

3D exploration of the intracranial aneurysm wall could enhance the understanding of the processes in the wall. Here, the construction of a 3D wall model based on histologic images is described. Besides a unique 3D view of the wall and the tissues inside the wall, the model can be used for simulations an research of wall interactions. The model does not only include the aneurysm, but also the aneurysm neck and part of the parent vessel. The analysis of the wall and 3D modelling consists of several steps. First, the tissue is segmented (Section 6.2) and a virtual inflation is applied (Section 6.3). Due to the unusual characteristics of the images a new mesh generation algorithm was developed (Section 6.4). Then, a 3D model of the wall and the tissues inside was built (Section 6.5).

6.1 Dataset

From three human cadavers, the Circle of Willis was explanted post-mortem and embedded in paraffin. For a study by Glaßer et al. [20] the aneurysms were marked with red and black ink which was still visible on the histologic images. Cross-sections of the aneurysms were cut using a microtome. The slices are 2 μm thick and 50 μm apart. After H&E staining the slides were digitized using a Hamamatsu Nanozoomer (Hamamatsu Photonics, Hamamatsu, Japan) and have a resolution of .23 μm per pixel. An example is shown in Figure 6.1.

The original images contained two histologic slices per image. These were post-processed, such that one image shows one slice [203]. The pipeline of the model generation is shown in Figure 6.2. The steps are described in detail in the next sections.

6.2 Segmentation

The first step is the segmentation of the aneurysm wall. Three different approaches are compared. For the later steps of the model generation the manual segmentation, which was also used for training the neural net in the deep learning approach, was used to minimize errors. The H&E stained histologic images were segmented to show the changes inside the aneurysm wall. Different tissue types differ by the colour (recall Section 2.2.3), nuclei shape and nuclei
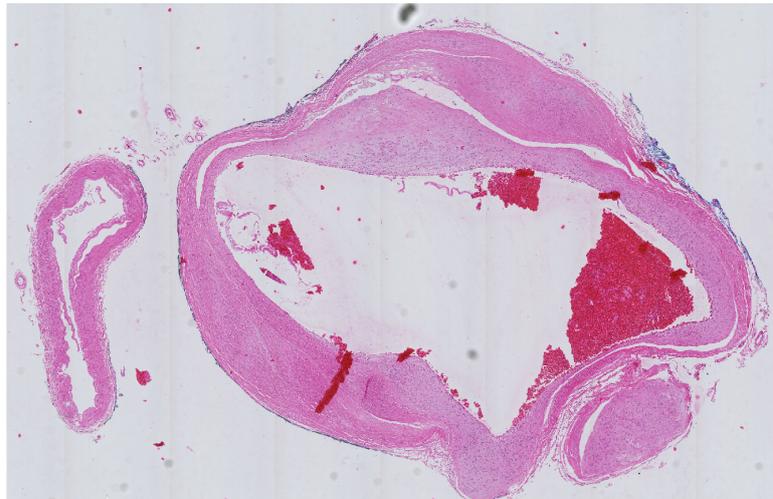
Figure 6.1: Example of histologic slice
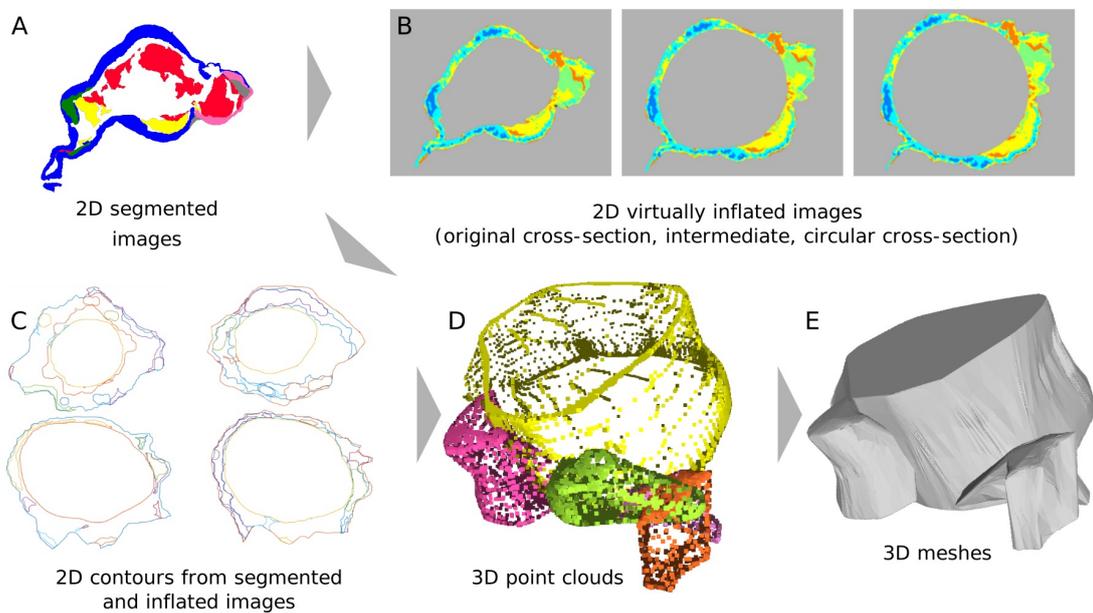
Figure 6.2: Based on segmented histolgic 2D images (A) a model is generated. First, the images are virtually inflated (B) and contours of different tissue types are extracted (C). Then, 3D point clouds (D) and meshes (E) describing the patient-specific wall thickness and wall composition are generated [204].

density. Different tissue types behave differently and have different mechanical attributes, which is relevant for simulations. For a deep learning segmentation of the images tissue classes defined by an expert were used (Section 6.2.3). The advantages and disadvantages of the segmentations are discussed in Section 6.2.4.

6.2.1 Texture analysis and cluster

The first possibility discussed here is semi-supervised clustering. The tissue is segmented into several small parts with similar appearance. The image is partitioned into overlapping 50*50 pixels large patches. For each patch 249 features (83 features for 3 different patch sizes (50*50, 100*100, 150*150)) are calculated. This allows assessment of the patch and its surrounding area. The features calculated are features that were previously used by Kather et al. [205] to successfully segment histologic images. Additionally, features describing the nuclei in the patch are used. The necessary nuclei detection and parametric description were described by Saalfeld et al. [20]. The following features are used:

- histogram:

    - mean

    - variance

    - skewness

    - kurtosis

    - 5th central moment

    - 2th-11th central moment

- local binary patterns

- gray-level co-occurrence matrix

- perception-like filters

    - coarseness

    - contrast

    - directionality

    - line-likeness

    - roughness

- nuclei

- number of nuclei

- average elongation

- average thickness

- average area

- distance from patch center to closest nuclei

Using the Calinski-Harabasz criterion [206] the optimal number of clusters (from possible values between 1 and 40) was determined to be 37. The Calinski-Harabasz criterion evaluates the between-cluster variance (which should be large) and the within-cluster variance (which should be small). Every patch was associated with a cluster and the most likely cluster for each pixel was determined. After that, the results were visually inspected and several clusters were combined. One of the clusters contained the wall parts which had no or very few nuclei. These clusters were further fractionated calculating two automatic thresholds using Otsu's method [207]. The results were smoothed using a median filter.

## 6.2.2 Filter- and threshold-based segmentation
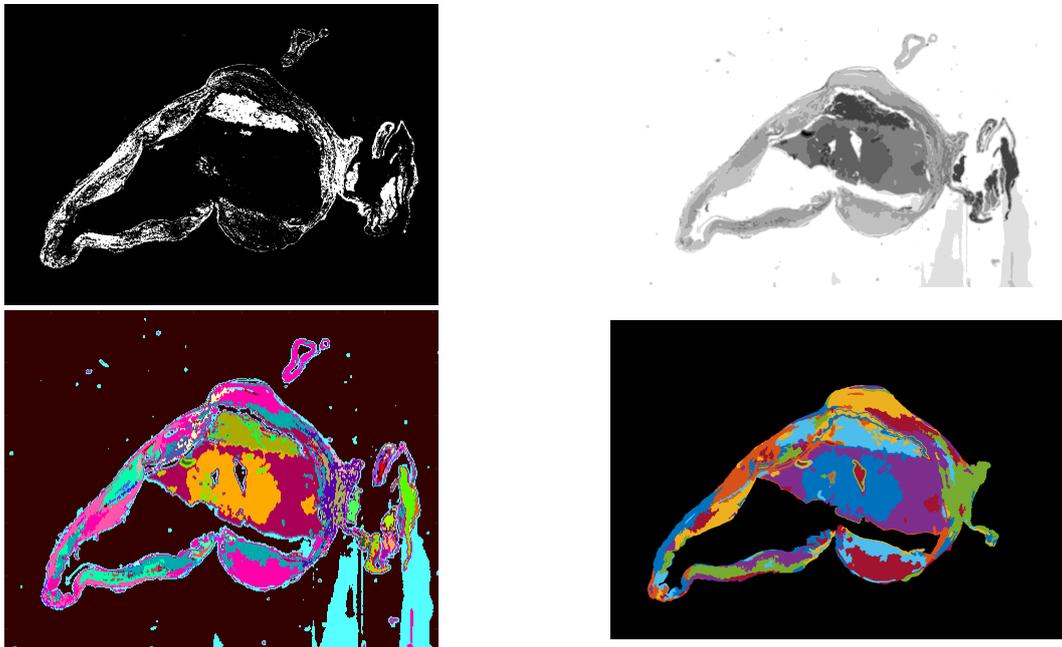
Figure 6.3: Intermediate results of filter- and threshold-based classification: top left: Prewitt Filter and morphological operations, top right: threshold-based segmentation, bottom left: combination of both; bottom right: final segmentation result [208]

The second segmentation approach uses filter- and threshold-based segmentation. Two aspects of the image are analyzed: edges and intensities. Several steps of this method are shown in Figure 6.3. In the first part of the segmentation, the edges are enhanced using the Prewitt filter [209]. To depict areas with high edge density, morphological operations are used to merge edges into larger areas. Edges inside the aneurysm tissue are often the outline of nuclei. Therefore, with the first step, nuclei-rich areas are detected. Tissue without nuclei or only a few nuclei is segmented with an intensity analysis. The image is segmented with eight thresholds, which were determined with Otsu's method [207]. Both analyses (edge-based and threshold-based image analysis) are carried out independently. Afterwards, the segmentations are combined. This yields an over-segmentation with many small areas. The next step is the combination of these small areas to larger areas. Areas are combined with their neighboring areas until one of two stopping criteria are fulfilled. The first stopping criterium is the minimum area size. The second criterium is the number of different areas segmented. The selection of values for these parameters depends on the tissue, the expected number of different tissues and changes of tissues, and the desired resolution of the segmentation. A low minimum area size and a high maximum number of areas is suitable for tissue with frequent changes. With a manual segmentation of the outer and inner aneurysm contour, the background was set to zero [203]. In contrast to the deep learning segmentation (Section 6.2.3) no tissue classes are defined. The image is segmented into areas with similar appearance. The number of tissue areas is often larger than the number of classes because several small, not connected areas can belong to the same class.

6.2.3 Deep learning segmentation

For the third approach a deep learning-based segmentation was developed. Unlike the previously described approaches, this requires the definition of different tissues and manual segmentation to train the neural net. Together with two medical experts, nine different tissue classes were defined (see Fig.6.4) [204]:

- *Mixed textures (1)* include all areas that cannot be classified into one of the other classes. This includes unusual findings and areas where a reliable identification is not possible. In the patch in Figure 6.4, infiltrating red blood cells between connective tissue bundles are shown.

- *Inflammatory cells (2)* show regions with an increased amount of inflammatory cells.

- *Myointimal hyperplasia (3)* (MH).

- *Degenerated wall (4)* shows wall tissues of the aneurysm wall with signs of wall degeneration, defined as loss of mural cells.

- *Decellularized Organizing thrombus (OT) (5)* shows decellularized tissue. In histologic images the origin of this tissue is difficult to determine.

  Three textures are used to describe the thrombus:

– *Red thrombus (6)* (RT), i.e., a fresh thrombus with a lot of red blood cells.

– *Organizing thrombus (7)* (OT).

– *White thrombus (8)* , i.e., a thrombus made of fibrin with very few red blood cells.

- *Intact wall (9)* shows intact wall tissue with linearly organized mural cells, of most likely smooth muscle cells based on the morphology and location.
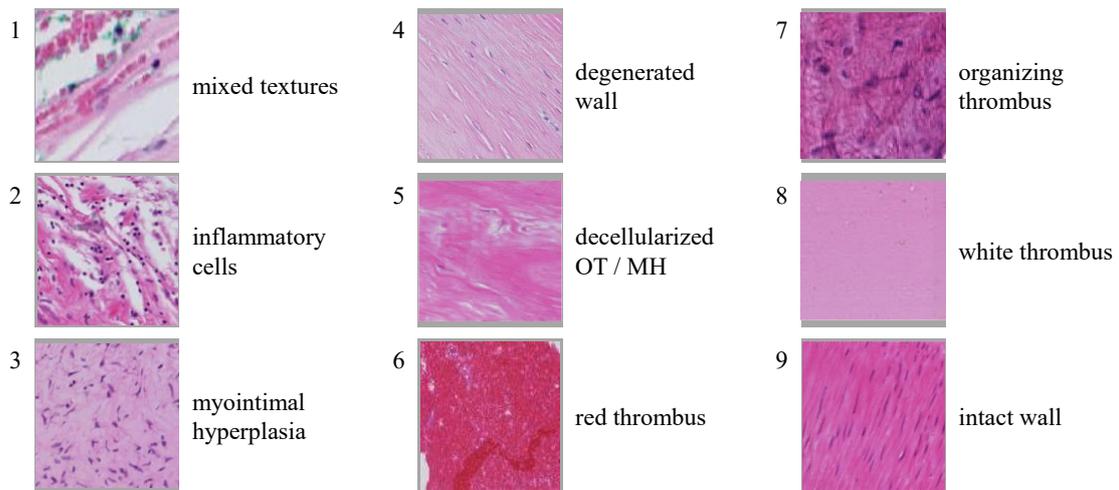
Figure 6.4: Example patches for tissue classification for histologic images of intracranial aneurysms [204]

Due to the image size, it was not possible to use the whole image for deep learning. Resizing the images was not possible, as small details, for example the nuclei, were important characteristics of the classes. Therefore, a patch-based deep learning approach was used. Images were split in 256×256 patches. This results in a very unbalanced dataset with a high number of patches for the background. To reduce the imbalance, not all background patches were selected for the training. The dataset was still imbalanced, as several tissue classes were rarely present in the images. The data was split 60:20:20 for training, test and validation. A U-net [149] with eighteen layers was trained to segment the patches into ten different classes (nine tissue classes and one background class). The net used the adam optimizer and categorical cross-entropy and was trained for 50 epochs.
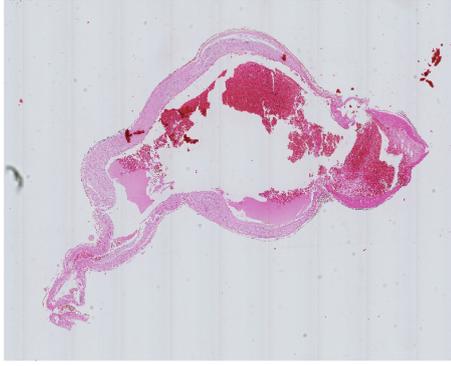
Figure 6.5: Original image
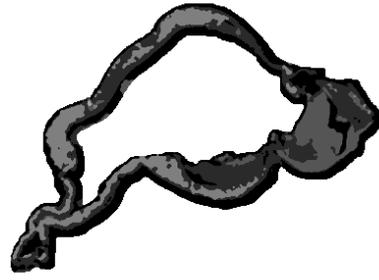
Figure 6.6: Result of image segmentation based on cluster
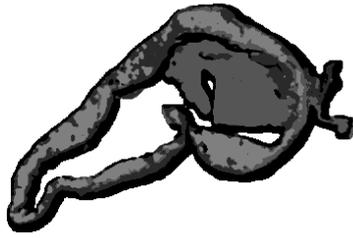
Result of image segmentation based on cluster
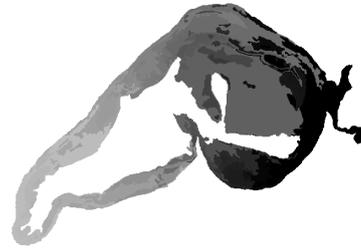
Result of filter- and threshold-based segmentation

Figure 6.7: Comparison of cluster and filter- and threshold-based segmentation

6.2.4 Comparison of different segmentation approaches

Figure 6.7 shows the segmentation of the cluster-based segmentation and the filter- and threshold-based segmentation. The grey values in the image processing segmentation do not have a meaning and different grey values are only used to show the separated areas. In the cluster-based segmentation, the different grey values show the different clusters.

Deep learning achieved an overall accuracy of 60.68% (see Table 6.1). The results differ between the classes; visual inspection revealed that the best results were achieved for red thrombus and myointimal hyperplasia. For white thrombus, intact wall, and infiltrating blood moderate results were achieved. The most problematic classes were rare classes like organizing thrombus (OT) and decellularized OT, which was mostly segmented as white thrombus. Some examples are shown in Fig. 6.8.
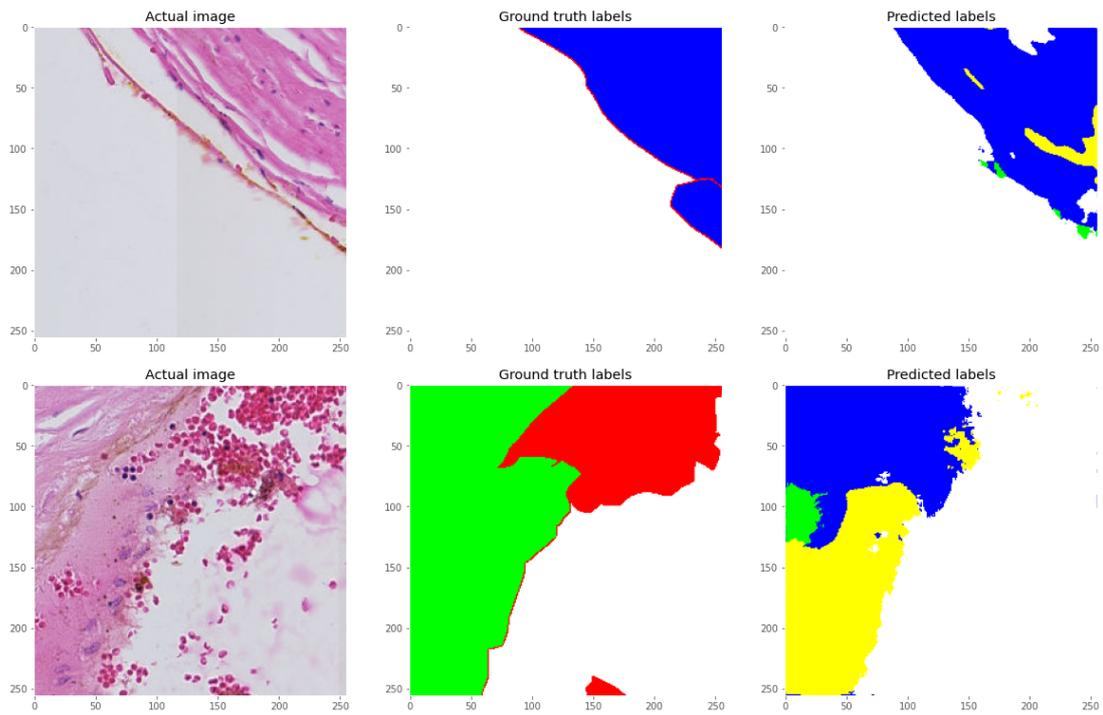
Figure 6.8: Examples of deep learning segmentation; blue: myointimal hyperplasia, red: red thrombus, green: degenerated wall, blue: myoinitmal hyperplasia, yellow: white thrombus.

Table 6.1: Results of semantic segmentation with deep learning

Metric	accuracy	Tversky loss	Dice coeffecent
Training	75.66%	9.2378	0.8718
Validation	57.67%	9.3738	0.7534
Test	60.68%	9.2932	0.8461

The results of the other approaches depend on various parameters. For image processing the expected number of objects and the minimum object size requires careful fine-tuning and the clustering approach strongly depends on the selected features. With the features used here, discriminating different tissues with few or no nuclei was challenging.

The resolution of the manual ground truth segmentation for training the neural network is limited. Small gaps between the tissues or small tissue changes are not segmented. During the segmentation clear borders between different tissue types are drawn. These are not able to reflect slow transitions between different tissue classes. Accuracy calculation for the deep learning segmentation turned out to be unreliable due to different levels of details in the automatic and manual segmentation. The deep learning approach was more detailed, especially small tissue gaps, which were not segmented manually, were successfully detected. Despite being better than the manual segmentation, these areas have a negative impact on the calculated accuracy.

The combination of a high number of classes, a limited number of training examples and highly imbalanced classes was challenging for the deep learning-based approach.

Here, a patch-based approach was used due to the image resolution and current technical limitations. The patches often only show 1-2 classes. Different tissues are not equally distributed over the aneurysm wall. For example, plaques occur on the inside of the vessel, but not on the outside. The patch-based approach omits some information about the tissue position in the wall, which might be helpful for classification.

For the deep learning, a supervised machine learning algorithm, the ground truth, is important. The manual segmentation is a very time-consuming task. The reliability of the manual ground truth segmentation limits the deep learning. The manual segmentation, and therefore the deep learning segmentation, tends to produce larger tissue segments compared to the other algorithms.

In contrast to the other segmentation approaches, deep learning is heavily restricted to the tissue classes present in the training data. Especially in pathological structures like intracranial aneurysms, where a high variance is expected, the more flexible filter- and threshold-based and cluster approach might be advantageous.

6.3 Virtual Inflation

During the acquisition of histologic images, some deformations may occur. One problem are detaching parts at the border of the slice. As the segmentation of these borders was performed manually, this problem could be minimized. The main problem is the deformation due to the missing blood perfusion. After removing the vessel with the aneurysm from the brain and before the fixation in paraffin, the blood is flushed out. The vessel collapses and thus alternates the form significantly (see Fig. 6.9). This would lead to major errors in fluid dynamic

Segmented image before the virtual inflation is applied

Intermediate step 2 of the virtual inflation

Intermediate step 4 of the virtual inflation

Intermediate step 6 of the virtual inflation

Intermediate step 8 of the virtual inflation

Step 10 of the virtual inflation
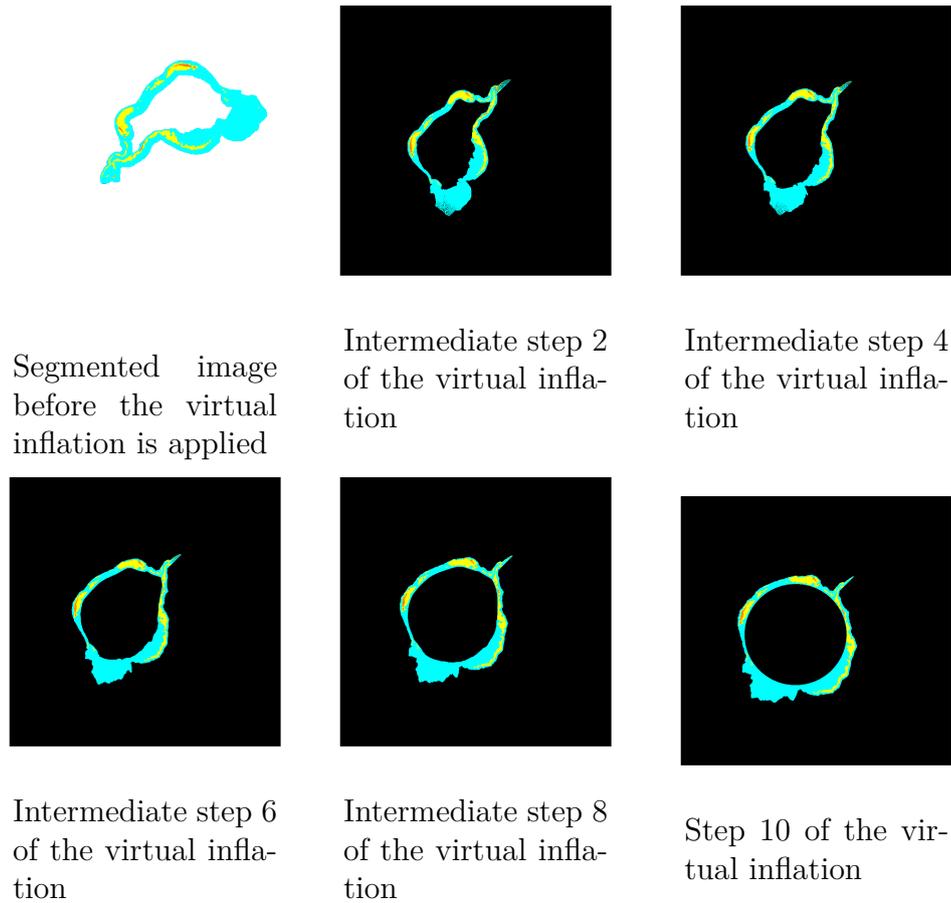
Figure 6.9: Different steps of virtual inflation

simulations. As for these datasets only post mortem, ex vivo images (OCT and histologic images) exist, it was not possible to register the histologic images to images which correctly depict the aneurysm shape, for example in vivo CT or MRT images. Instead, the correction of the aneurysm shape is based on the assumption that the inner vessel and the aneurysm contour, respectively are nearly circular shaped. The inner border shape is influenced by the blood flow filling the vessel and the outer border might be less round due to the influence of surrounding objects. The assumption of a round inner contour of the vessel and aneurysm was supported by observing the behavior when filled with fluid. The segmented images are reduced to 15% of the resolution of the original images. This large reduction is possible because unlike the histologic images, where important information (for example nuclei position and shape) were stored in small details, the segmented images only contain large, uniform areas. The contour points are adjusted to fit the new image resolution. The inner and outer contours were resampled to consist of 4000 points each. For the morphing, 10 intermediate stages were calculated (see Fig. 6.9).

| (a) | (b) | (c) |
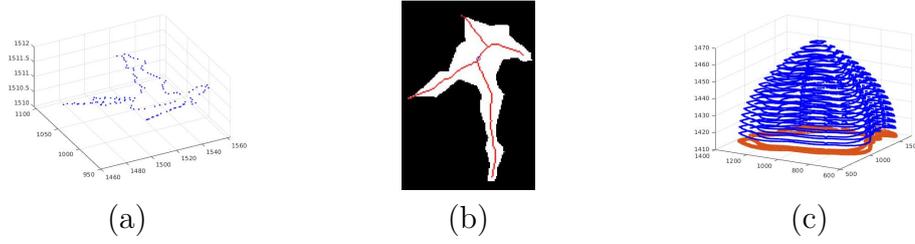
Figure 6.10: a) last contour of a segmented area (as 3D point cloud), b) corresponding binary image, red line: points left after thinning, blue circle: center of the contour, c) example of a dome added to a contour in 3D, red: top contour, blue: added points for the dome [203]

6.4 Mesh generation from histologic images

To generate a 3D mode of the aneurysm, surface meshes of the aneurysm and the various tissue sections have to be constructed. The large gaps between the images are challenging for the mesh generation. Therefore, a new mesh generation algorithm was developed.

After applying virtual inflation to the segmented images, point clouds are derived. During the virtual inflation, the image values are interpolated and the resulting image has more colors than the 10 discrete values used for the segmentation. Before the contours are determined, this is corrected and the image is discretized to 10 colors. For each color a binary image is generated. In this binary image, showing the elements from one label, the contours are extracted using the Moore tracing algorithm modified by Jacob's stopping criteria [210]. Moore-Tracing starts at one point of the object and follows the contour until the start pixel is reached a second time. These contours and the corresponding labels are saved. In the next step, the point clouds are generated. Starting from the first contour, the contours of the following slice are iteratively added. Contours get the slice number times slice-distance as z-coordinate, and contours are grouped as a point cloud if they match. Matching of contours is determined by the label (only contours of the same label can be grouped), the distance between centers of the contour, and the average distance between contour points. After the point clouds are generated this way, they have flat ends (see Figure 6.10). While not visible in the slices, it is expected that the tissue continues between the slices and the elements should be smooth. Therefore, domes are added to the ends. A dome is added by shrinking the contour while keeping the contour centroid constant and adding these points above or below the last and first contour, respectively. Between this new contour and the previous end contour, several contours are interpolated, forming a dome. To determine a centroid inside the contour, even for concave shapes, the following approach was used. The contours were transformed into binary images. In the image, the shape was reduced to a line using a thinning algorithm [210]. The points of this line are inside the shape and are candidates for the centroid. From these candidates, the point with the greatest distance to the closest contour point is selected (see Fig. 6.10).

(a)

(b)

(c)

(d)
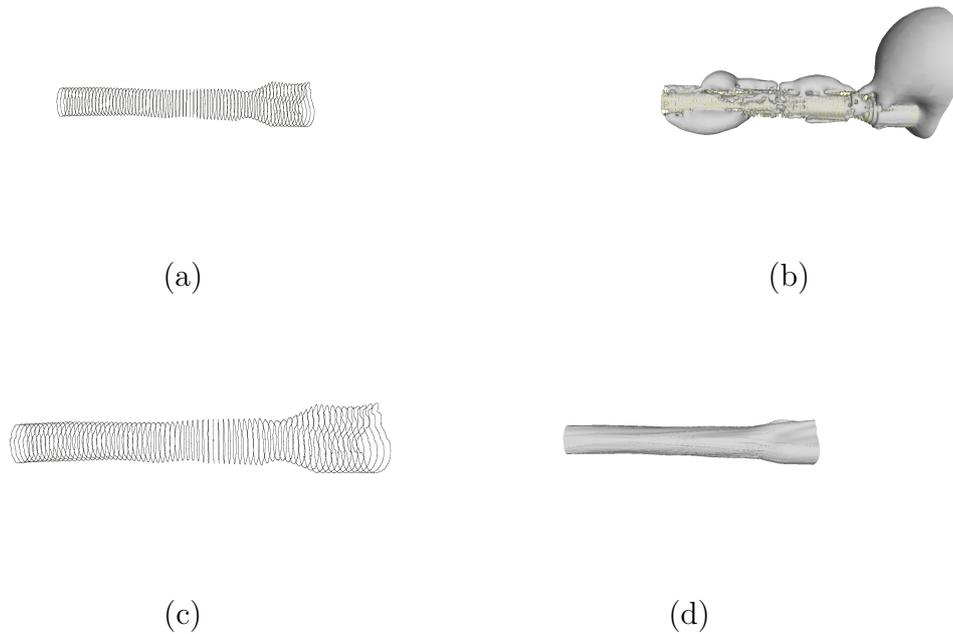
Figure 6.11: (a) Point cloud from vessel contours; (b) The mesh generated by MeshLabs screened Poisson surface reconstruction algorithm; (c) The mesh generated by MeshLabs ball pivoting algorithm; (d) The mesh generated by our shrinking tube mesh algorithm [211, 212].

The point cloud of the contours is used for the mesh generation. It differs from typical point clouds as the points are not evenly distributed. Instead, there are small spaces between points from the same slice and larger spaces between different slices. The second important difference between point clouds for medical applications and other point clouds is the occurrence of edges. In most applications, edges provide important information and point cloud-based mesh generation algorithms try to preserve sharp edges. The contrary occurs for medical images. Here, sharp edges are not expected.

The mesh generation from point clouds often requires a preprocessing or post-processing step to filter noisy points or smooth the mesh.

Figure 6.11 shows how common mesh generation algorithms fail to generate a mesh of the rather untypical point cloud. Therefore, a new mesh generation has been implemented to generate the meshes. In the following, a mesh generation is presented that can produce a smooth mesh without additional preprocessing of the points or mesh smoothing.
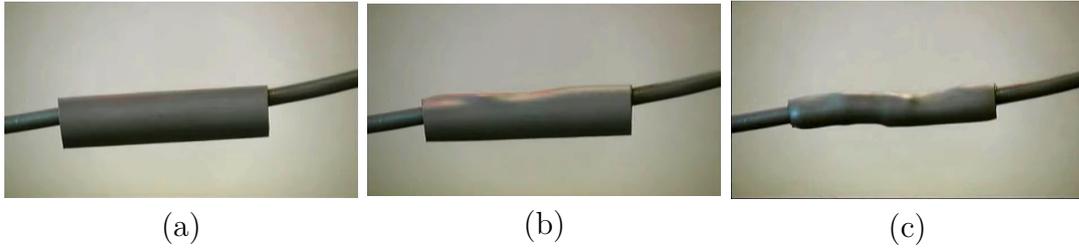
Figure 6.12: (a) Shrinking tube, (b) during heat, (c) fitted shrinking tube [213, 212]

6.4.1 Shrinking tube mesh generation

The presented algorithm models the behavior of a shrinking tube, as illustrated in Fig. 6.12. A shrinking tube is a plastic tube that can be used to isolate wires and is tightly fitted to them by applying heat.

First, a start shape (the shrinking tube) is generated. This mesh is then adjusted to fit the point cloud (Algorithm 1).

Start shape

Three options are tested for the "shrinking tube" shape: a straight cylinder (C_s), the convex hull (CH) of the point cloud, or a cylinder based on the maximum diameter of each slice (C_{max}). To get a cylinder based on the varying diameter for each slice, the diameters are determined. By fitting a spline through these values a function is generated. From the function a cylinder is derived by rotating the function around the x-axis. Optionally, the function can be smoothed before the rotation and therefore creates a smoother cylinder.

Fitting step

The mesh is then adjusted to fit the point cloud. In analogy to a shrinking tube, this step has two parameters: the number of time steps (iterations) and the temperature. Iteratively the mesh is moved closer to the point cloud. It depends on the distance of the point to the mesh how large the influence of a point on the mesh is. The number of mesh points that are adjusted is linear to the distance of a point from the point cloud to the mesh. The distance the mesh vertices are moved towards the point cloud depends on two factors: the temperature parameter of the algorithm and the distance of the point to the mesh. As small distances are likely noisy and very large distances are expected to be the result of artifacts in the segmentation, these should have a smaller impact on the mesh. Therefore, the factor for the distance-based moving is calculated with a quadratic function.

Algorithm 1 ShrinkingtubeMeshGeneration

    [v,f] ← startmesh
    a,b,c ← parabelparameter
    for i=1:1:timesteps **do**
      for j=1:1:size(pointcloud) **do**
        idxMeshNeighbour ← meshpoint closest to pointcloud(j)
        moveDir ← pointcloud(j)-v(idxMeshNeighbour)
        dis ← distance(pointcloud(j),v(idxMeshNeighbour)
        moveFactor=temperature*(a*dis*dis+b*dis+c)
        v(idxMeshNeighbour) ← v(idxMeshNeighbout)+moveFactor*moveDir;
        InfluenceArea ← factorInfluenceArea*dis
        for k=1:1:size(InfluenceArea **do**
          move Neighbours in direction of new Meshpointposition
        end for
      end for
    end for

6.4.2 Results of the shrinking tube mesh generation

The presented shrinking tube mesh generation depends on several parameters. Given that suitable parameters are chosen, it can be applied to a wide variety of point clouds.

The selection of the start shape is crucial. A more tightly fitted start shape like the maximum cylinder with a low smoothing factor is better in preserving the shape while the straight cylinder is optimal to reconstruct cylindrical shape structures (for example vessels) from noisy point clouds.

The presented algorithm produces smooth meshes. Several factors are influencing the result: the time steps and temperature parameters of the fitting step, the start shape, and the parameters of the quadratic function used to calculate the strength of the moving.

Start shape

Two major factors influencing the result are the start shape and the number of vertices. Figure 6.13 shows the different start shapes. C_S and C_{max} will converge to similar results after sufficient time steps. Compared to them, the fitting progress using CH is faster.

Algorithm parameters

Next, the influence of the parameters is analyzed. The fitting of the mesh, defined as the sum of the distances between each vertex of the mesh and the closest
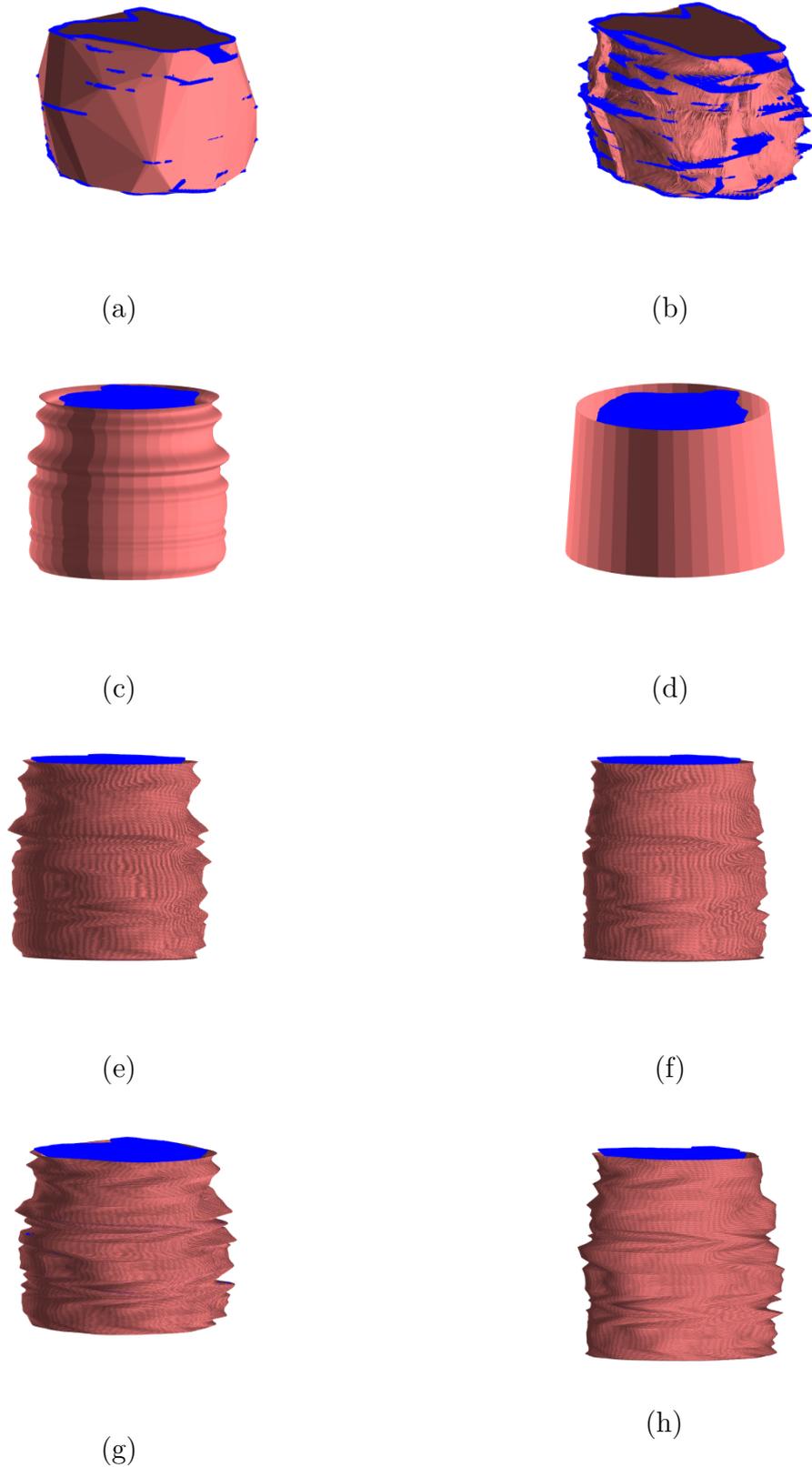
Figure 6.13: Start shapes and behaviour: (a) Start shape: CH, (b) Result of shrinking tube mesh generation from convex hull, (c) Start shape: C_{max}, (d) Start shape: C_S, (e) Intermediate result of mesh generation from c, (f) Intermediate result of mesh generation from d, (g) Result of mesh generation from c, (h) Result of mesh generation from d.
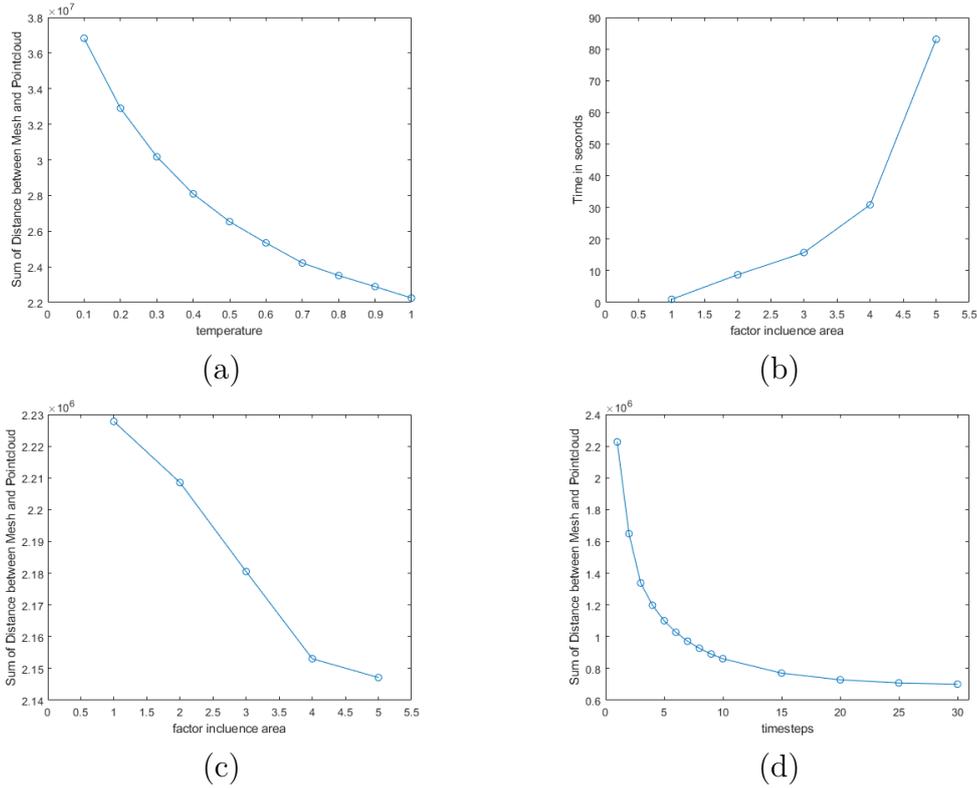
Figure 6.14: Influence of parameter on the fitting of the mesh to the point cloud:
(a) temperature, (c) factor influence area, (d) time steps; Influence
on time: (b) factor influence area.

point of the point cloud, is calculated. Additionally, the calculation time is measured.

Varying only the temperature (between 0 and 1), the difference between the points of the mesh and the nearest points of the point cloud decreases, as shown in Figure 6.14.

A larger influence area leads to a smoother mesh that is fitted closer to the points. The time needed for the shrinking tube mesh generation increases exponentially with the influence area factor (Fig. 6.14). For a mesh with 31,973 vertices and a point cloud with 398,459 points the mesh needed around 90 seconds on standard hardware with an influence factor of 5. This factor results in up to 66 iterations of moving mesh-neighbors. While the time increases linearly with the number of time steps, the mesh does not improve linearly (Fig. 6.14). The optimal values for the parameters depend on the point cloud shape, the target structure, and the number of vertices of the start shape. At the moment, no general recommendation for parameter settings can be given.

Moving factor function

Each vertex is moved depending on the temperature parameter and its distance to the point cloud. The moving factor function regulates the distance of the movement based on the distance between vertex and point cloud. It is selected under
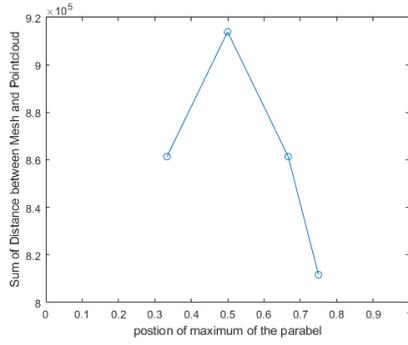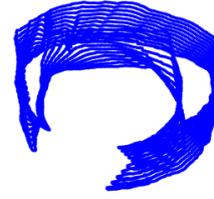
Figure 6.15: (a) Fitting of mesh depending on the position of the maximum of the parable; (b) Challenging point cloud configuration for shrinking tube mesh generation.

the assumption that a small distance (likely noise) and a very large distance (likely artifact) should lead to small vertex movements.

A quadratic equation $y = ax^2 + bx + c$ has three coefficients (a,b,c). In this case, some restrictions are known and help to limit the possible coefficient values. The zero crossings of the function should occur at x=0 and x=maximum distance of a point cloud to the mesh. The function needs to have a maximum with ymax=1. The only variation we looked at was the x-value at which the maximum occurred in relation to the maximum distance of a point cloud to the mesh. Figure 6.15 shows that for the selected mesh a parable with a maximum at half the maximum distance of a point cloud to the mesh is optimal.

Summary of the shrinking tube mesh algorithm

The shrinking tube mesh generation produces smooth meshes without additional postprocessing. It can be applied to imperfect segmentations and might be used for different applications. Compared to image stacks, point clouds from contours only describe the information necessary for the model (for example, no information about the background is stored). The algorithm is robust against the uneven distribution of points. Various parameters influence the behavior and outcome of the algorithm. With enough time steps or a high value for the temperature parameter, the resulting mesh will be tightly fitted to the point cloud.

Due to the medical application and resulting assumption that sharp edges rarely occur, these are not preserved. The algorithm makes some assumptions about the relevance of the points. It is expected that noise and artifacts have a certain characteristic, reflected by the distance between point cloud and mesh. The presented algorithm was used to successfully generate meshes of the aneurysm wall and different tissues inside the wall.

A point cloud derived from nearly closed circles (as shown in Fig. 6.15) is problematic for the algorithm described above. This challenge might be addressed by splitting the point cloud into several smaller point clouds, applying the shrinking tube mesh generation to these, and combining the resulting meshes.

While allowing for adaption to different problems and point clouds, the algorithm has a large number of parameters, and optimizing these can be time-consuming.

6.4.3 3D Model of an intracranial aneurysm

With the previously described algorithm meshes of each tissue segment and the aneurysm outer and inner contours are generated. The meshes are combined to build a model of an intracranial aneurysm. The aneurysm model consists of one mesh describing the inner aneurysm wall, one mesh describing the outer aneurysm wall, and 94 meshes of different wall tissue types (see Fig. 6.16). Most tissue sections can only be traced over a few slices. This results in many small meshes. The mesh generation and the addition of a dome tend to produce meshes slightly larger than the point cloud, therefore small overlappings can occur. For each mesh potential intersecting meshes are determined based on the x-coordinates of the meshes. Then, the candidates are tested for intersections. Using Boolean operations the intersections are removed.
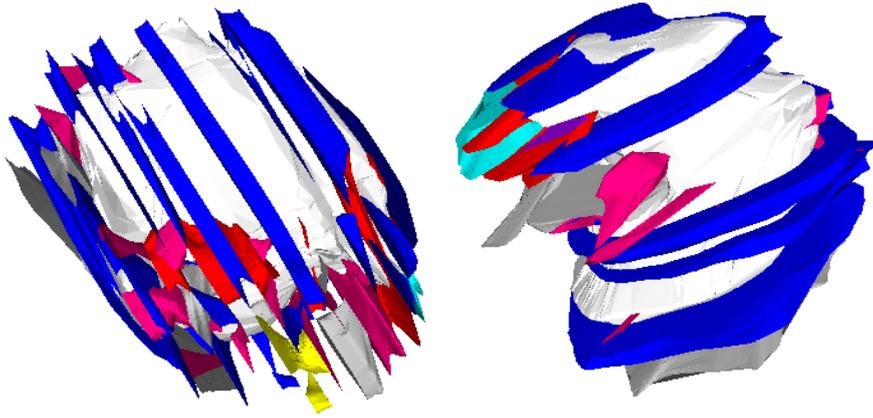
Figure 6.16: Resulting model for one of the aneurysm datasets (without outer mesh) from two different views. White: mesh of inner wall, colored meshes: selected different tissue segments; the model is based on 22 consecutive slices, distance between slices 100 μm, image resolution per slice around 18500 × 6000 the 3D model based on 22 consecutive histologic slices, distance between slices 100 μm, image resolution per slice around 18500 × 6000, white: inner mesh, coloured meshes: various tissue segments, outer mesh is not displayed [203]

Not all parts of the aneurysm wall are included in one of the tissue meshes. Especially in regions with a very heterogeneous wall, the tissue parts can be too small to generate a mesh. Here, only tissues that are visible in at least two slices are included. With the presented adding of a dome, it would be possible to generate 3D meshes from tissue parts even if it is only visible in one slice. However, this would result in even more and smaller meshes, which is - at the current time - not useful for many applications (for example simulations) due to limited computational resources.

6.4.4 Wall tissue analysis in 2D and 3D

In this section, the statistical analysis of the histologic images is described. The area (in the 2D images) and the volume (in the 3D model) of each tissue class are calculated.

2D analysis

The most common classes were myointimal hyperplasia and red thrombus, followed by white thrombus (Fig. 6.17). Myointimal hyperplasia and degenerated wall were mainly found at the outer part and the parent vessel. At the aneurysm dome, decellularized organizing thrombus and organizing thrombus were found. The white thrombus is most present in the first slices, at the aneurysm and one side of the parent vessel (Fig. 6.19). In the next slices, the white thrombus is replaced by the red thrombus. In the following slices,

white and red thrombus are visible inside the aneurysm and the whole parent vessel.
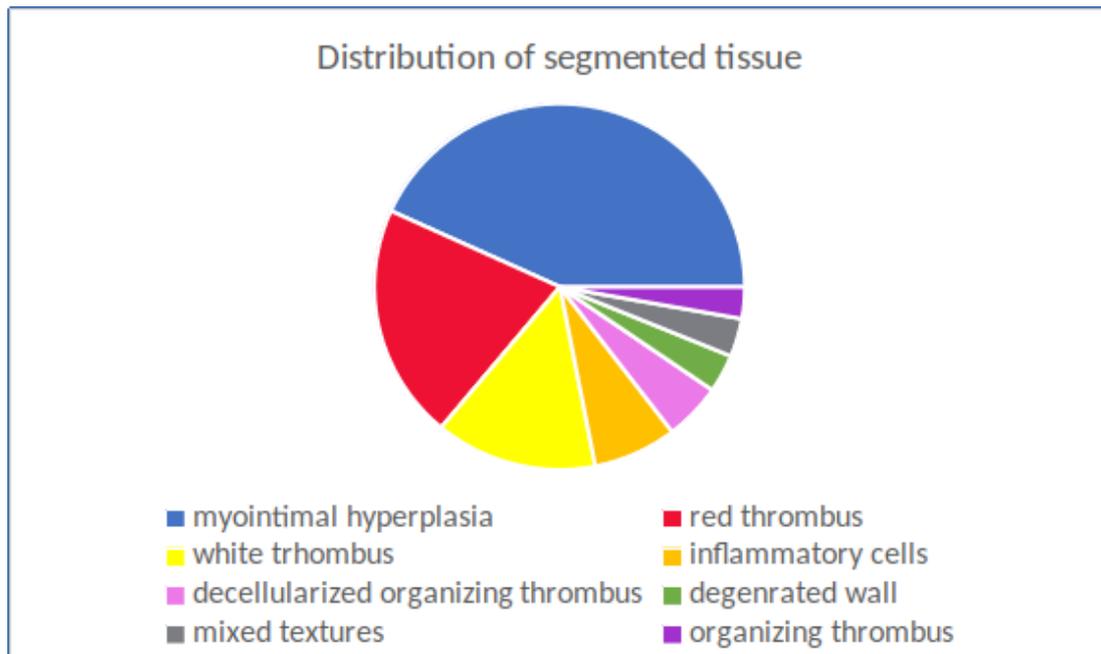
Figure 6.17: Distribution of different tissue types occurring in all histologic images.

3D analysis

Similar to the segmentation in 2D the most present class was myointimal hyperplasia. 20.42% of the aneurysm mesh were not assigned to a class.

In the mesh representation the distribution of the classes changes. This has several reasons. Not all segmented sections are included. A section must be visible in two consecutive slices to be included as a mesh in the 3D representation. Furthermore, the center and the contour have to be similar to connect sections to a mesh. Therefore, small sections, fast-changing sections or very irregular shaped sections are not visible in the mesh representation. These two factors contribute to the vanishing of the classes rarely presented in 2D, liked inflammatory cells and degenerated wall.

While there are many tissue sections of red thrombus in the images, they are underrepresented in the 3D mesh representation. Independent from the tissue segmentation, a segmentation into inner and outer contour was performed. This segmentation was necessary for the virtual inflation, where the inner contour was moved to a more circular shape. As visible in Fig.6.18, there are large sections of disconnected red thrombus in the middle. These are not included in the 3D wall model, as they are inside the vessel. A similar problem occurred for the white thrombus.

This study had several limitations. While the class definition was done by a medical expert, the image segmentation was done by computer scientists.
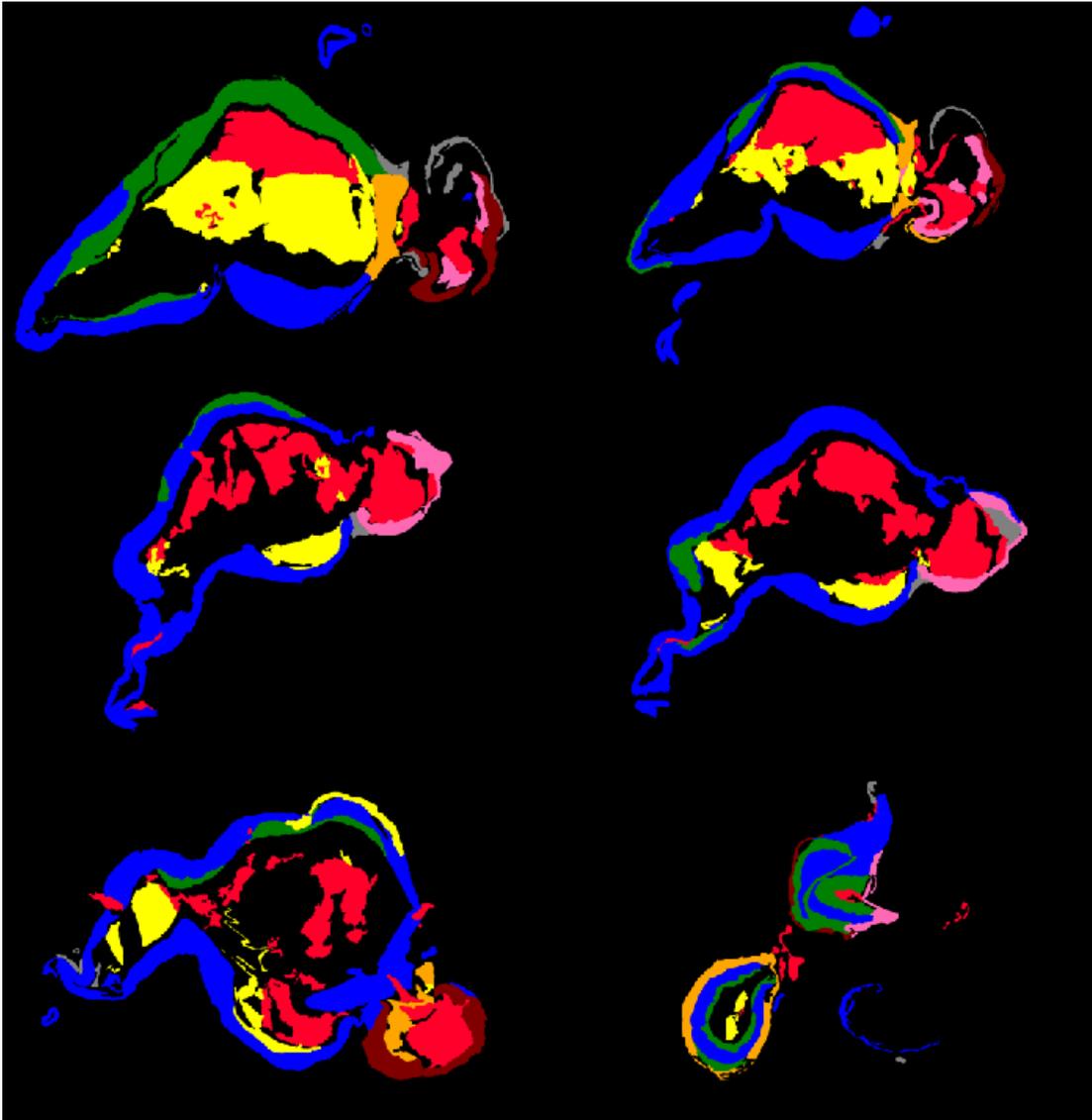
Figure 6.18: Selected segmentations illustrating the behaviour of the thrombus

Table 6.2: Comparison of class distribution in image segmentation and resulting 3D mesh model

class	images	meshes
myointimal hyperplasia	43,20%	66,58%
red thrombus	20,77%	4,83%
white thrombus	14,12%	0,52%
inflammatory cells	7,31%	0,18%
decellularized organizing thrombus	5,03%	1,66%
degenrated wall	3,37%	0,00%
mixed textures	3,37%	4,05%
organizing thrombus	2,82%	1,75%
not segmented	0,00%	20,42%
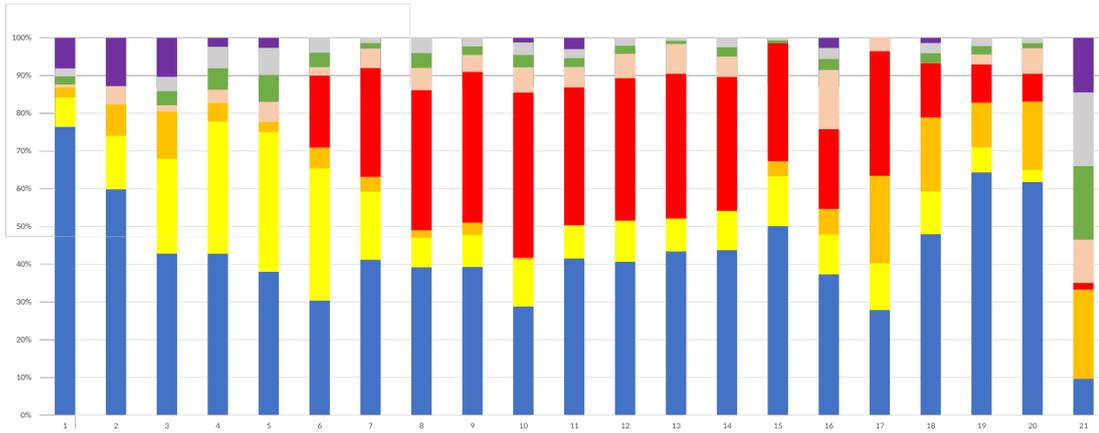
Figure 6.19: Distribution of different tissue types occurring in the histologic images per image; blue: myointimal hyperplasia, yellow: white thrombus, rose: decellularized organizing thrombus, green: degenerated wall, orange: inflammatory cells, grey: mixed textures, red: red thrombus, purple: organizing thrombus

The 3D model has several restrictions. Especially due to the slice distance, small tissue sections are not presented in the 3D model, as they cannot be traced through several slices. The images have a resolution of 0.23 μm per pixel and a slice gap of 50 μm. The mesh representation does not include tissue sections only visible in one slice. Including these has several challenges. The tissue shape between the slices has to be estimated without further information. The inclusion of small tissue segments will largely increase the number of meshes used to describe the aneurysm wall in 3D. This would be unpractical and due to technical limitations not usable in current simulations. In Fig.6.18 each row shows two consecutive slices. In the middle row, each slide contains some degenerated wall (green), but at clearly different positions. Therefore, they cannot be connected and are not included in the mesh representation.

Another aspect is the virtual inflation. For a more realistic 3D shape, virtual inflation is applied during the model generation. This changes the shape of the aneurysm wall and the tissue segments. Together with the large space between slices, this hinders the tracing of tissue sections.

The 2D segmentation includes all visible tissues. For the 3D reconstruction, only the aneurysm wall is used. As visible in Figure 6.18, especially in the top row and the bottom left, the 2D segmentation also contains some small tissue parts, which are not connected to the aneurysm or the vessel.

While the 3D model includes important information and can be used for more realistic simulations of the aneurysm, not all details are captured. For a reliable analysis of the tissue present in the aneurysm wall, the 2D images should be used.

6.4.5 Results of the model generation

The proposed pipeline and the presented algorithms were used to generate a detailed aneurysm wall model from H&E stained images. The aneurysm model has two global meshes describing the inner and outer wall. Smaller meshes in between these two show individual sections of different tissue types. These meshes are often rather small, as most tissues can only be traced over a few slices. Overall, the model consists of 96 meshes, one each for the inner and outer wall, and 94 meshes of tissue segments. Some of these are shown in Figure 6.16. The meshes are generated based on 22 consecutive histologic slices. Smaller tissue segments are not captured by the model, as it requires presence of the tissue in at least two consecutive slices. Therefore, not the whole volume between inner and outer mesh is covered by tissue meshes.

For structural simulations, the whole model with the large number of meshes is challenging. Therefore, two reduced models consisting of three (Model A) and ten (Model B) slices were generated. Figure 6.20 shows the results of the structural simulation done by Samuel Voß based on the reduced models A and B. For each of the models a homogeneous and a heterogeneous configuration is tested. The heterogeneous configuration consists of up to seven different tissue classes. In areas of intact tissue identical wall stress patterns were observed. A more heterogeneous wall stress distribution was caused by the clustering of several tissue classes. The varying mechanical tissue elasticity allows individual components to compensate for the load at different levels. Flexible components have a smaller influence on the stability than stiffer components. Local deformation of the aneurysm wall and mechanical stresses are the result of intraluminal pressure. If the pressure increases, the wall stress also increases until the maximum wall strength is exceeded and aneurysm rupture occurs.

The in-plane resolution of the histologic images was excellent and showed a high level of detail. Due to the large gaps between slices, the resolution in the third direction is limited. The model only includes tissues visible in several slices. Therefore, tissue parts which are too small compared to the large gap between slices are disregarded.

The heterogeneous tissue class presentation inside the wall provides a challenge for the reconstruction. Over time, the aneurysm wall changes due to remodeling and thrombosis of the wall. These frequent changes result in many different, small sections while large regions of the same texture are rare.

The presented model shows clear borders between different tissues. As in reality there is a smooth transition and borders are blurred, the expressiveness of the model is limited. Using surface meshes to represent the different tissues requires clear borders. In the future, transition classes or a representation as volume mesh with cell-specific properties could be used to generate a more realistic model.
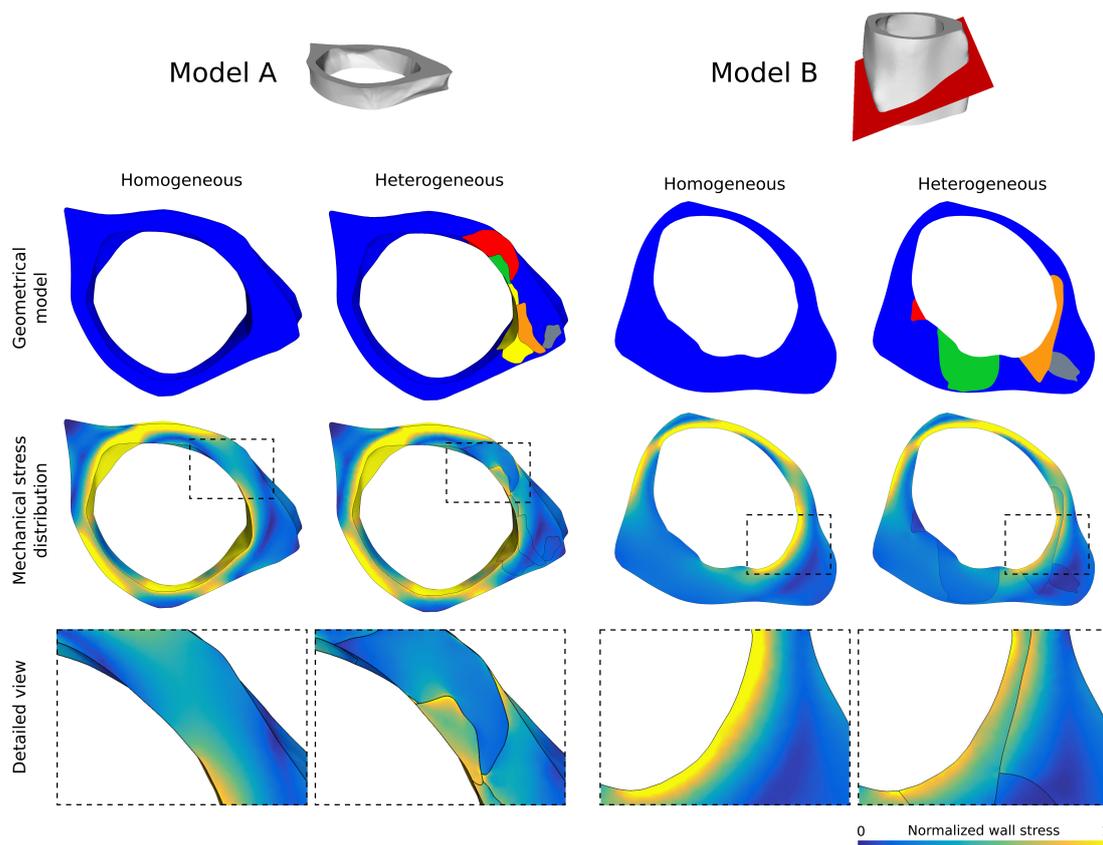
Figure 6.20: Reduced models A and B of the patient-specific vasculature as homogeneous configuration and heterogeneous configuration. Top: model composition from different tissue classes; middle: resulting mechanical wall stress distribution of the structural simulations of the wall under intraluminal blood pressure; bottom: detailed view of the local wall stress distribution [203]

Each tissue mesh contains a single tissue type. Within this tissue type nor further details are available. The model might be further enhanced by including information like fiber direction instead of a uniform tissue model.

As no in-vivo information about the lumen shape was available, the artificial inflation assumed a round shape.

The presented 3D model can be used for simulation. Very small tissue sections are not included in the model. Therefore, for small details the 2D image data is superior to the 3D view. While healthy vessels show three distinctive layers, aneurysm walls are pathological and differ greatly. Therefore, models based on healthy tissue can only be partially transferred to intracranial aneurysms. To asses the individual strength of an aneurysm, a detailed and patient-specific model is necessary. As the simulation results show, inclusion of different tissues affects the simulation outcome. A mix of several different tissue sections results in a more heterogeneous wall stress distribution. Advanced wall models allow more realistic and reliable simulations. The described pipeline represents early steps towards such modeling approaches.

7 Understanding aneurysm wall composition - Histology and microCT

While the previous chapter focused on reconstruction solely from histologic data, here a different approach using multimodal image data is described. Histologic images are combined with microCT of the collected tissue and preoperative imaging of the aneurysm lumen. The wide selection of image modalities allows a comprehensive exploration of the wall (see Fig. 7.1). MicroCT and histologic images using various stainings show the tissue inside the wall. The aneurysm shape is available from preoperative imaging. Hemodynamic simulation adds further information about the wall, for example the wall shear stress.

7.1 Dataset

The multimodal data was acquired from a patient with an intracranial aneurysm at the middle cerebral artery. Pre-operative 3D angiography data was used to extract a 3D surface model of the aneurysm and its parent vessel. During surgical intervention, the aneurysm dome was resected and scanned afterwards via microCT yielding a stack of microCT image data. Hence, during surgery and tissue collection the shape of the tissue is strongly alternated. From this dataset, calcification masks were generated [131]. Next, histologic images based on the fixated, stained and sliced aneurysm dome were photographed. Four histologic stains were used (Fig. 7.2): Hematoxylin and eosin (H&E), alpha smooth muscle actin (aSMA), Oil Red o (Oro) and masson trichrome (MT). The stainings are further explained in Section 2.2.3.

7.2 Image preprocessing

Before the data is visualized, several preprocessing steps for the histologic data and the microCT data were necessary.
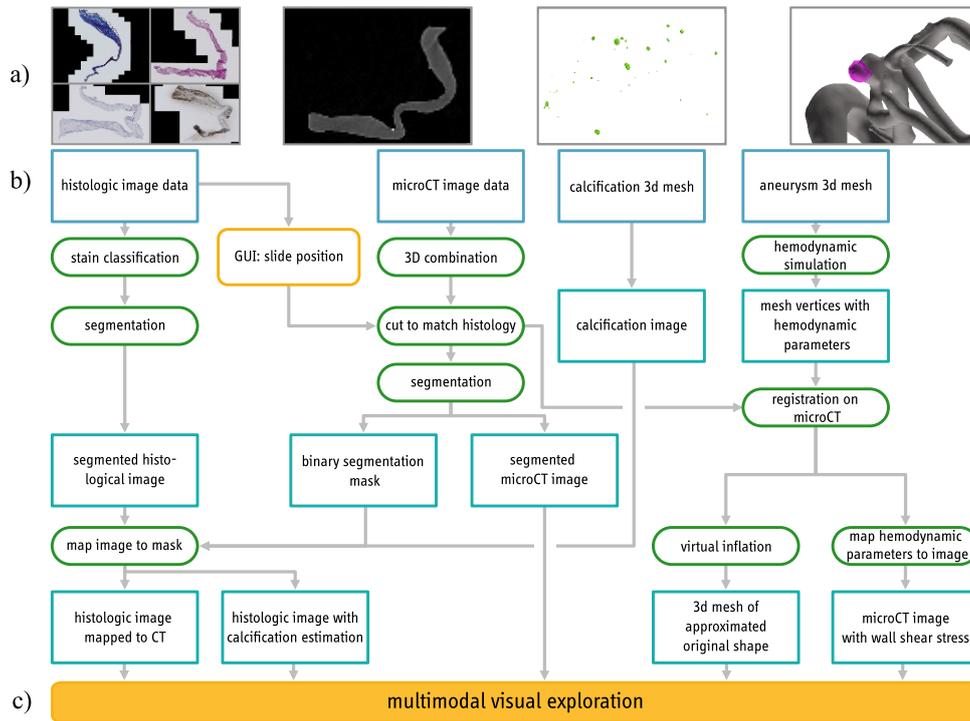
**Figure 7.1:** Pipeline overview with a) histologic and microCT data, calcification segmentation and 3D IA surface model (grey) and 3D resected dome surface model (pink), b) the steps to combine this data and c) the resulting visual exploration.


(a) H&E   **(b)** MT   **(c)** Oro   **(d)** aSMA
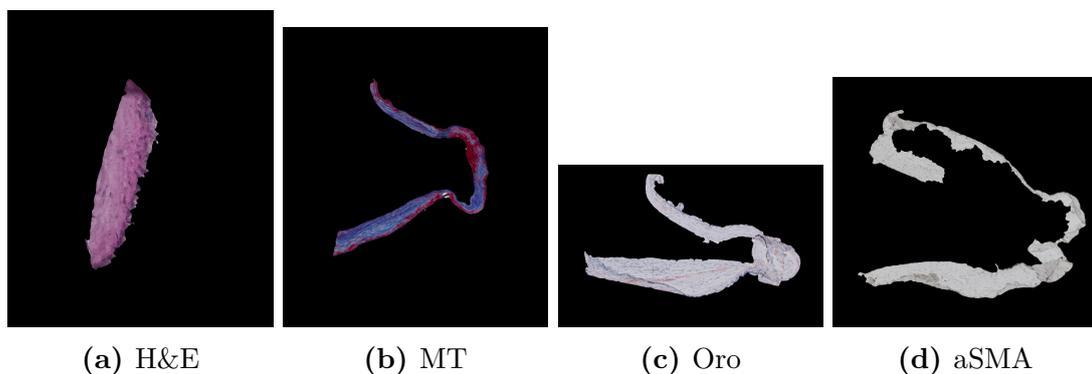
Figure 7.2: Segmentation of different stainings used in the histologic images

7.2.1 Stain classification

As different stainings have different image characteristics, the first step is to identify the staining. To classify the stainings into four classes (H&E, MT, aSMA and Oro) a deep neural net using the GoogLeNet architecture is used. The network is 22 layers deep and trained with downsized RGB images with 500x500.

7.2.2 Tissue segmentation

The images are segmented in tissue and background. The different staining methods result in different colors and saturation. H&E and MT where clearly darker and could be easily distinguished from the light background in contrast to ORO and aSMA stainings.

For aSMA, H&E and ORO-stained images, two thresholds were determined using Otsu's method [207]. One threshold separated the object from the black padding of the scanning process, the other roughly segmented the tissue from the slide background yielding a binary segmentation mask. As the slides can contain some dissected tissues or other impurities, the mask may falsely contain small objects that were removed. The final segmentation was refined with geodesic active contours [214] using the masks as initial state.

For MT stained images, all steps apart from the active contour method were repeated, since the dark staining achieved a better contrast to the background and mask refinement was not necessary.

7.2.3 Processing of microCT images

Including microCT images of the tissue before sectioning allows visualization of the shape of the tissue sample and detecting calcification inside the aneurysm wall.

The microCT images corresponding to the histologic images are generated. Therefore, a 3D image is constructed by stacking the 2D microCT images. To generate the new microCt images, the positions of the histologic images have to be determined. During the image collection, part of the tissue was removed or slices were corrupted and discarded. These missing slides are not documented. More slices than available for the project were collected, but the exact number of slices is unknown. This missing information complicates the reconstruction of the slice positions.

A tool to guide the slice position selection was developed (see Fig.7.3). First, the overall number of slices (available slices and placeholder slices for removed sections) is set and the possible slice thicknesses, which depend on the settings used for cutting, are set. A start point and an end point define the line along which the tissue was cut. On the left side, the sections (colored: available, grey: removed
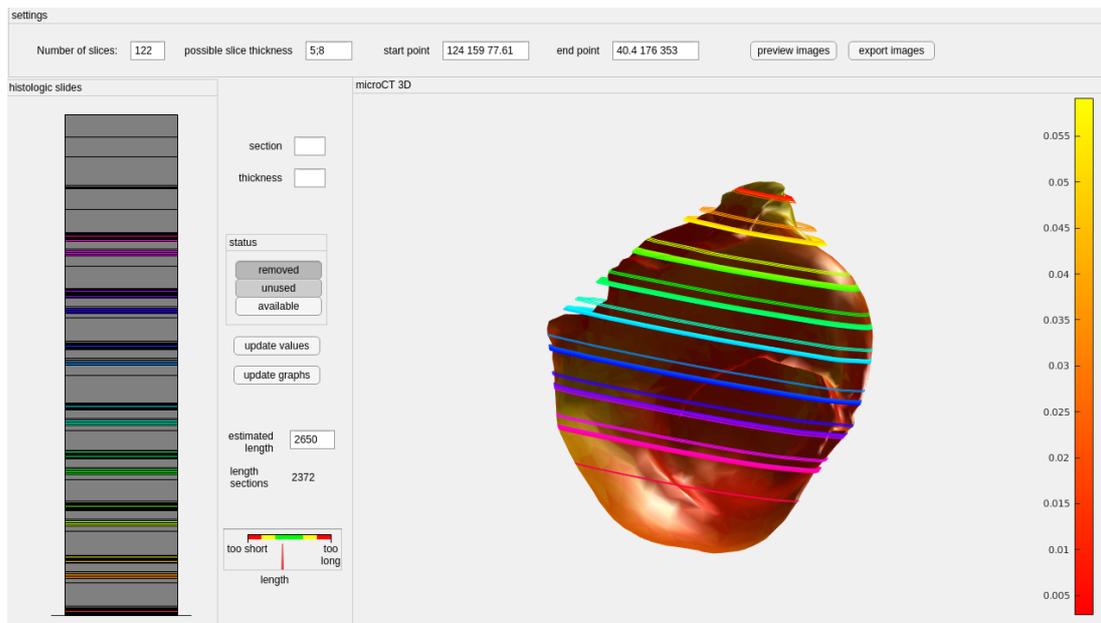
Figure 7.3: User interface for alignment of the histologic slides. On the left, the sections (colored: available, grey: removed tissue or unavailable slides) are shown. On the right, a 3D model extracted from the microCT is shown together with the estimated slide positions.

tissue or unavailable slices) are shown. For each section, the thickness and the status can be set. On the right side, a 3D model of the tissue generated based on the 3D microCT image is shown together with the estimated slice positions. The user can set the estimated length of the tissue sample and compare this to the sum of the histologic slices. A preview of all images allows comparing the current selection with the histologic images (Fig. 7.4). The mesh is color-coded with the mesh thickness to further guide the user. A 3D image of the same size as the 3D image from the microCT data is generated. The vertices of the surface mesh are mapped into the image, resulting in a 3D image showing the outline of the aneurysm and the calcifications. The image is then filled and registered to the 3D microCT image with a rigid transformation based on the normalized gradient field similarity measure [215].

The registered 3D image of the calcification is then sliced with the same planes as the microCT image (Fig. 7.5).

7.2.4 Combining histology and microCT

After the described processing, for each histologic image a corresponding microCT image and a segmentation mask showing calcifications are available. These information are combined. This is achieved by transferring the histologic image information into a mask of the microCT image.

The image and the mask of the microCT image are registered based on the outer contour of the tissue. The contour of the aneurysm dome in the microCT image and the contours of the histologic image are each split into outer and inner
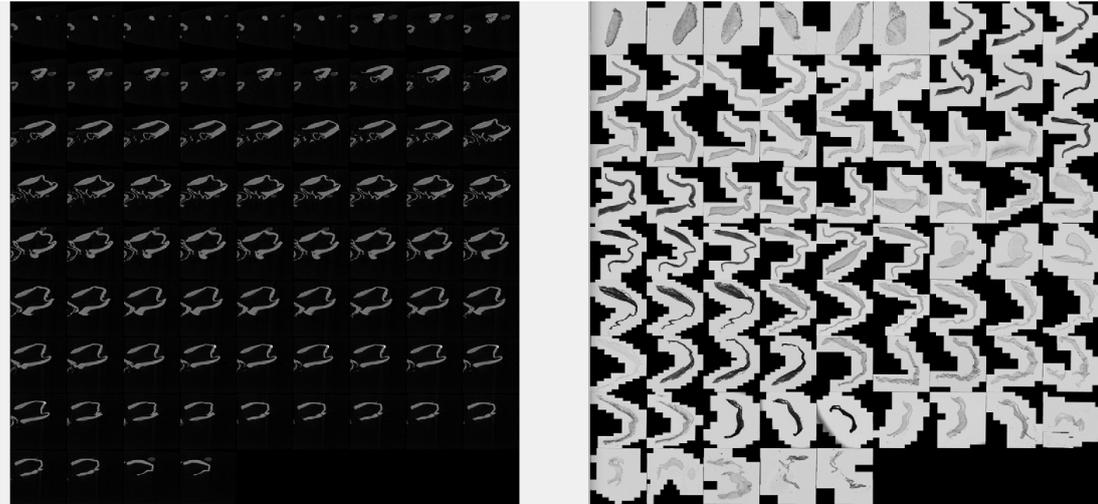
Figure 7.4: Left: image preview from microCT cutting, right: histologic images
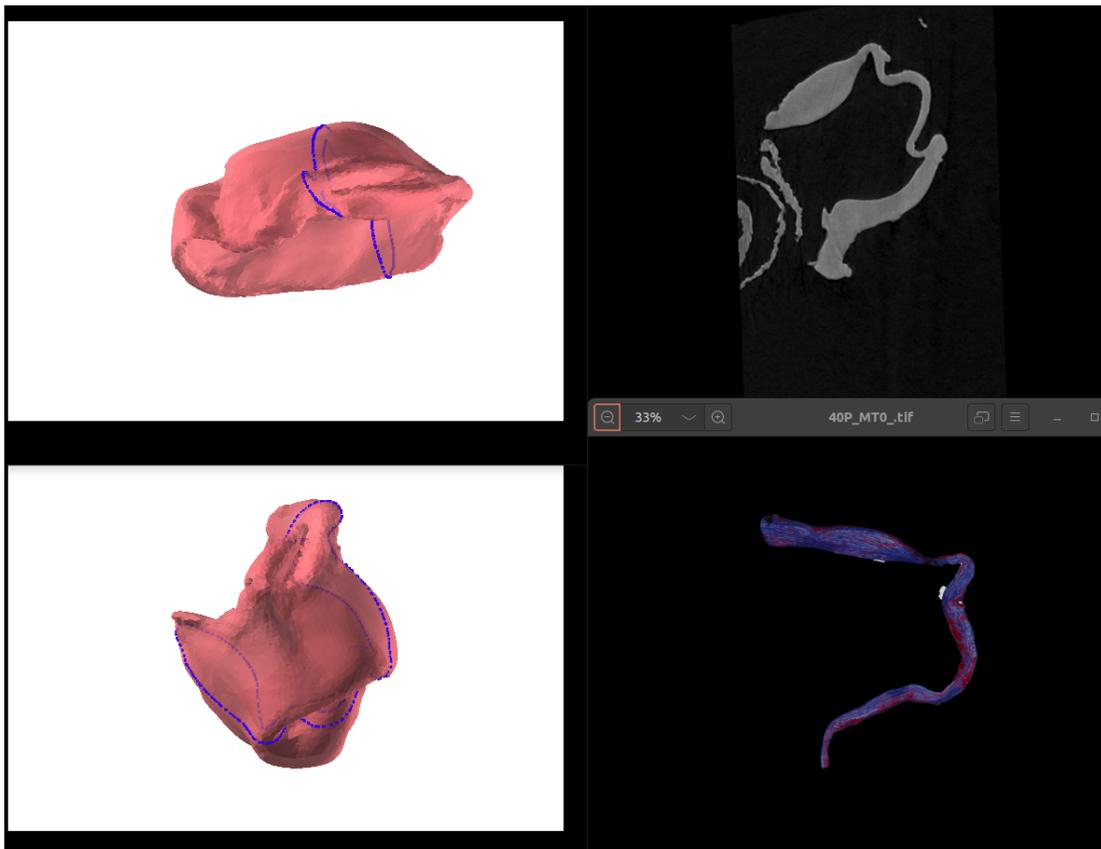
Figure 7.5: Mesh with outline of section, corresponding histologic section and microCT image
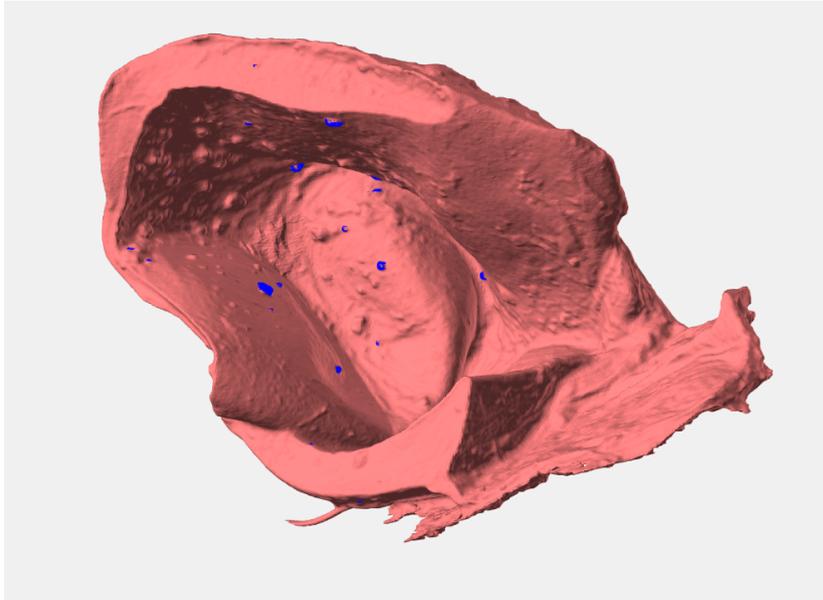
Figure 7.6: Surface mesh with calcification

contours. To do this, the center of the contour is calculated. For each contour point, intersections of the line between the center and the contour point and the polygon described by the contour are determined. If no intersections beside the contour point itself are found, the point belongs to the inner contour, otherwise, the contour point is added to the outer contour (see Fig. 7.7). While the majority of the points is correctly classified, a small number of points is falsely labeled as outer contour. These are identified in a postprocessing step and added to the inner contour.

The information from the histologic images is then transferred to the segmentation mask of the microCT image. A line between an inner contour point and an approximately opposite outer contour point is selected in the histologic image. Based on the previous registration the corresponding line in the microCT mask is determined. The values along the line in the histologic image are transferred to the line in the microCT image. The calcification segmentation is used to check if the values are mapped to an area where calcification was present. In that case, the corresponding histologic image coordinates are stored and used to show the approximate area of calcification in the histologic image. This is repeated for all inner contour points, and for each inner contour point several lines to outer contour points are selected. Due to this, some pixels in the mask will get visited several times and the average value is used. To reduce blurring the number of times a pixel value can be updated is limited.
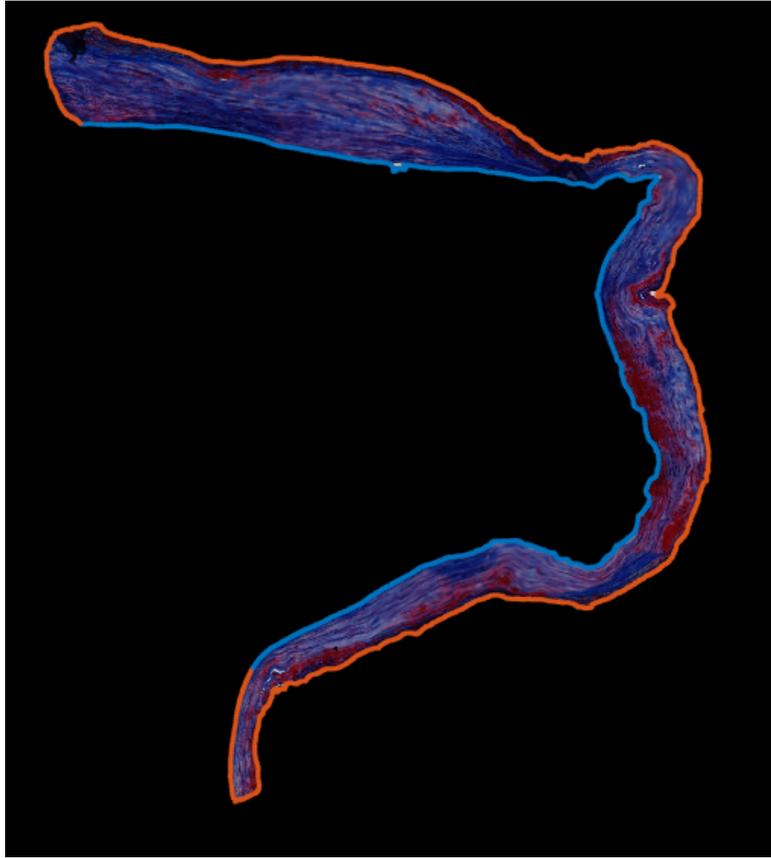
Figure 7.7: MT stained image with inner (blue) and outer (orange) contour.

In order to obtain hemodynamic parameters, like wall shear stress, a hemodynamic simulation was carried out. The preoperative 3D intracranial aneurysm model was used for hemodynamic simulation carried out in STAR-CCM+ 2020.1 (Siemens PLM Software Inc., Plano, TX, USA). Blood was modeled as an incompressible and Newtonian fluid with a density of 1055 $\frac{kg}{m^3}$ and dynamic viscosity of 0.004 $Pa \cdot s$. Boundary conditions of the domain were modeled as follows: Time-dependent flow waveform from a healthy volunteer, rigid vessel walls with no-slip condition, and zero-pressure assumption at the outlets [216]. The simulation was provided by Philipp Berg (Laboratory of Fluid Dynamics and Technical Flows, Otto von Guericke University).

7.3 Shape correction based on preoperative aneurysm model

During the tissue collection, the sample changes its shape. The tissue sample used here has two major alternations: a fold on top of the tissue and sides which are squeezed together. The fold on top cannot be removed with the available information. The preoperative aneurysm model is used to adjust the tissue shape. The inner contour of the tissue should follow the aneurysm shape.

The first step is the separation of the tissue mesh vertices into inner and outer points. The inner points of the bowl-shaped dome sample are the points that build the outline of the aneurysm lumen and should follow the shape of the preoperative aneurysm mesh. First, the mesh center is calculated. All vertices are assigned a label (inside or outside) based on their visibility from the center. The tissue is not a perfect semi-sphere, so some points at the inner tissue side are not visible from the center. In the next step, this is addressed by looking at the neighbors of the vertices and assigning the most frequent label to the vertex. The result is shown in Figure 7.8.
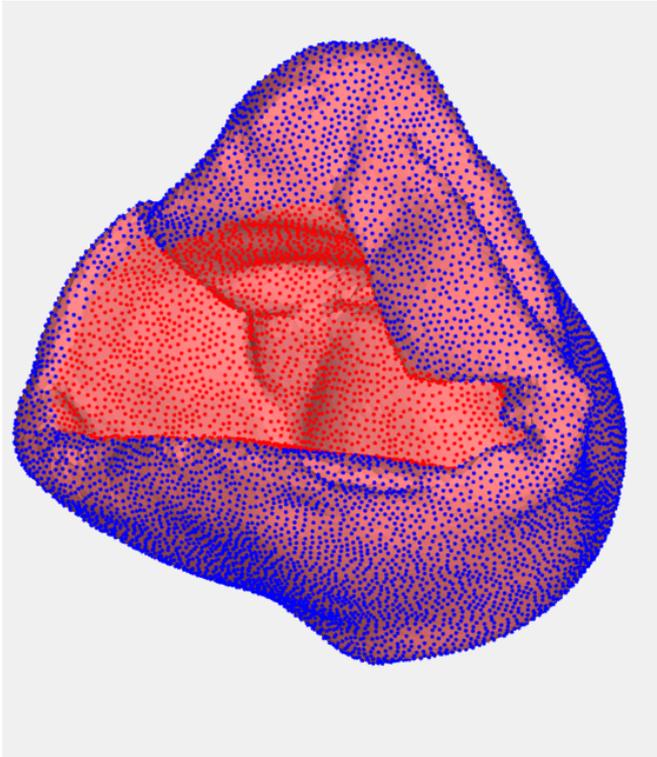
Figure 7.8: Tissue mesh with inner (red) and outer (blue) vertices

After determining the inner points of the tissue mesh, these are moved to fit the shape of the aneurysm mesh. The initial tissue shape is manually registered to the aneurysm. The tissue mesh is then iteratively deformed. In each iteration, the inner points are moved in direction to the center of the nearest aneurysm mesh points. After all inner points are moved, the outer points are moved based on the average movement of the nearest inner points. The results are shown in Figure 7.9.
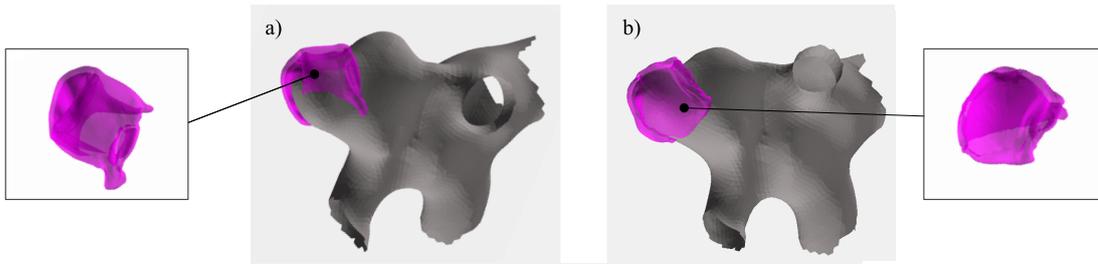
Figure 7.9: In a), the 3D aneurysm mesh (grey) and resected dome mesh (pink) is shown. In b), the virtual inflation was applied to the dome surface mesh.

7.4 Visual exploration

To explore the aneurysm wall, a visualization combining the various information was developed. The microCT and histologic images are combined as described in Chapter 7.2.4.

For a mapping of hemodynamic information (e.g. WSS), the values are assigned to each vertex of the 3D IA surface model. The 3D surface of the resected IA dome (which is already co-aligned to the 3D IA surface model) is co-registered to the 3D surface extracted from the microCT data via the iterative closest point algorithm [217]. The transformation matrix from this co-registration is then applied to the 3D IA surface model as well. Finally, each voxel of the microCT is assigned with the parameter values of the closest aneurysm mesh vertex.

We repeat this procedure for the inflated surface mesh of the IA dome. The inflated mesh is cut at the extracted positions of the histologic slices. This produces binary images corresponding to the histologic slices but showing the inflated 2D shapes of the tissue. Similar to the microCT data, the information of the histologic images is mapped to the inflated 2D shapes as well.

The information are combined in a visual exploration tool (see Fig. 7.10). On a 3D model of the tissue the WSS is depicted with color. A white line on the model indicates the currently selected slide. The segmented histologic image is shown on the right and the segmented microCT image in the middle. For the microCT image, three different views are possible: the segmented microCT image, the microCT image with WSS values, or the microCT image with calcification segmentation. For the histologic image the user can choose between the histologic image or the histologic image mapped to the microCT shape. Furthermore, the correlation can be explored by selecting a point on the microCT image which will show a circle around the corresponding area in the histologic image.

Figure 7.10: Visual exploration of combined microCT and histology; left: 3D model with WSS, white line indicates the current slice; middle: segmented microCT image, right: segmented, corresponding MT-stained histologic image

7.5 Results and discussion

In Figure 7.11, Figure 7.12 and Figure 7.13 the microCT image with calcification, the segmented histologic image with the estimated position of the calcification, and the histologic image mapped to the microCT image for different stainings are shown. Figure 7.14 shows the mapping from a histologic image to microCT, where large differences between the histologic and the microCT image occur.

The algorithm achieved the best results for the middle part of the aneurysms. One problem is the estimation of the image position and generation of corresponding microCT images. In the middle part of the aneurysm, there are less variations and small differences in the position still generate very similar images. At the outer parts, small variations of the estimated image position can lead to larger variations in the microCT images. The second challenge is the split into inner and outercontour. For the middle part, the u-shape allows to clearly distinguish between inner and outercontour. Both contours can be found in the histologic images as well as in the microCT images. For roughly oval shape these cannot be defined. While a split in two contour parts is possible (for example left and right contour or upper and lower contour), these are not necessarily corresponding in both images due to rotation and flipping during the image collection.

The mapping of image values into another shape was further validated by mapping the histologic image to its own segmentation mask. Then, the similarity between histologic image and mask was systematically decreased by applying dilation with different sized disks on the mask. Mapping to the histologic segmentation mask produced an image very similar to the original image (correlation coefficient of gray images 0.989). The correlation coefficient decreased with increasing dilation (0.9496 for disk size 5, 0.9107 for disk size 15, 0.8412 for disk size 50). With the increasing difference between the original shape and the target, the mapping gets more blurred and details are lost (Fig. 7.15).
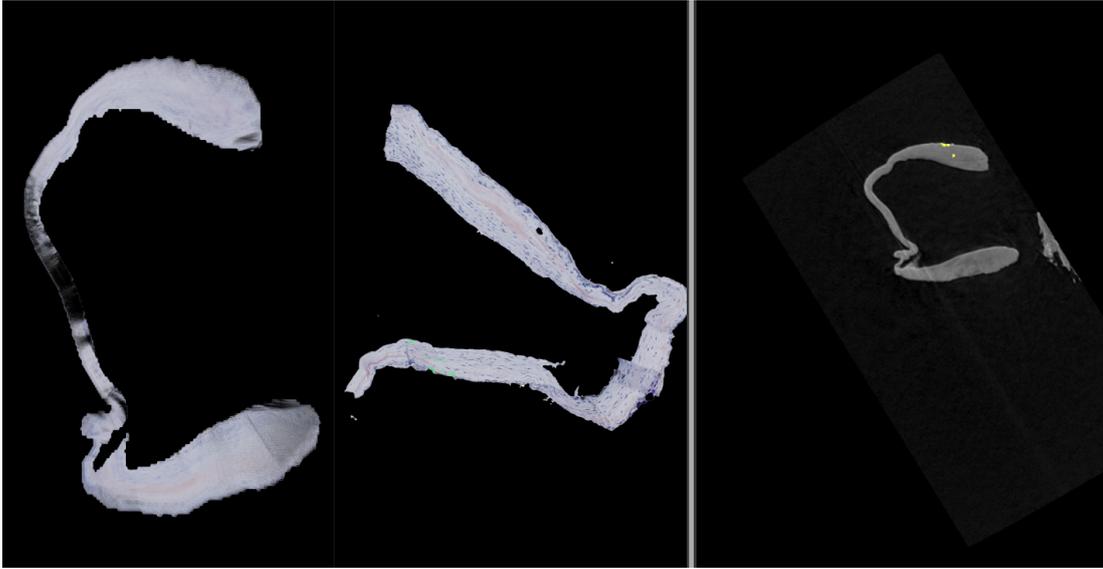
Figure 7.11: Oro, left: mapped to microCT, middle: segmented image with estimation of calcification position (green), right: microCT image with calcification segmentation (yellow)
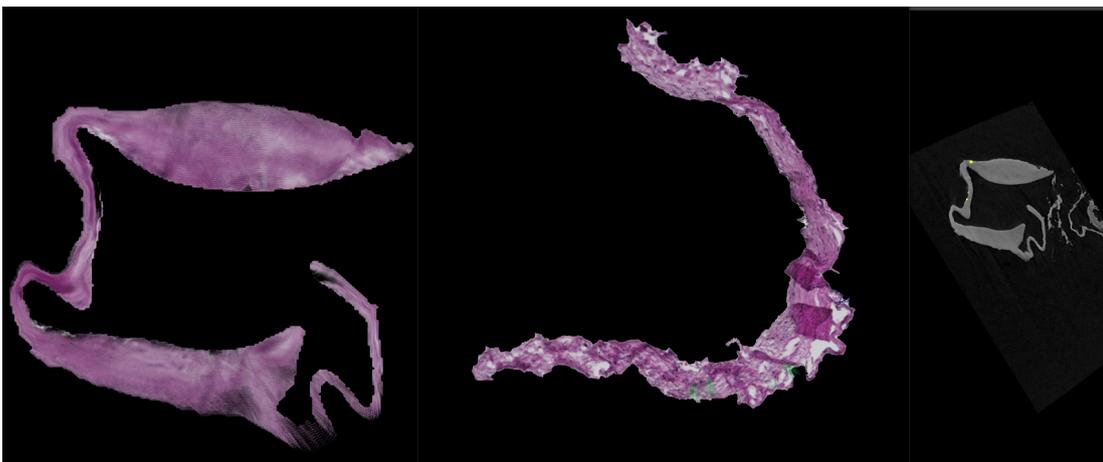
Figure 7.12: H&E, left: mapped to microCT, middle: segmented image with estimation of calcification position (green), right: microCT image with calcification segmentation (yellow)
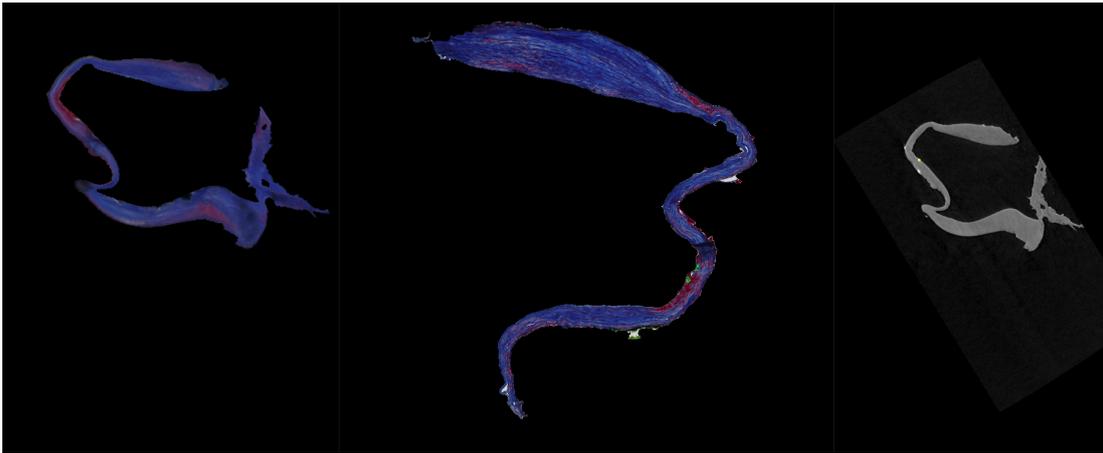
Figure 7.13: MT, left: mapped to microCT, middle: segmented image with estimation of calcification position (green), right: microCT image with calcification segmentation (yellow)
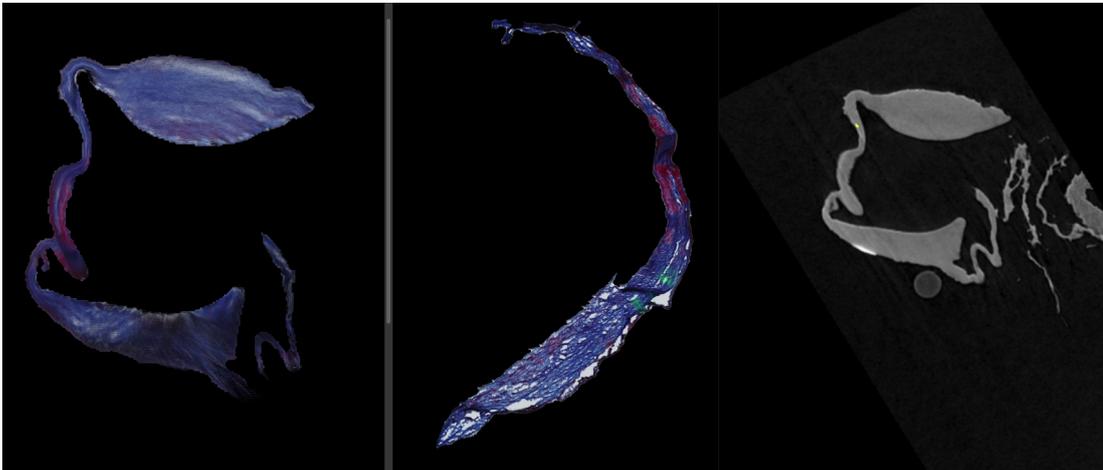

Figure 7.14: MT, left: mapped to microCT, middle: segmented image with estimation of calcification position (green), right: microCT image with calcification segmentation (yellow)
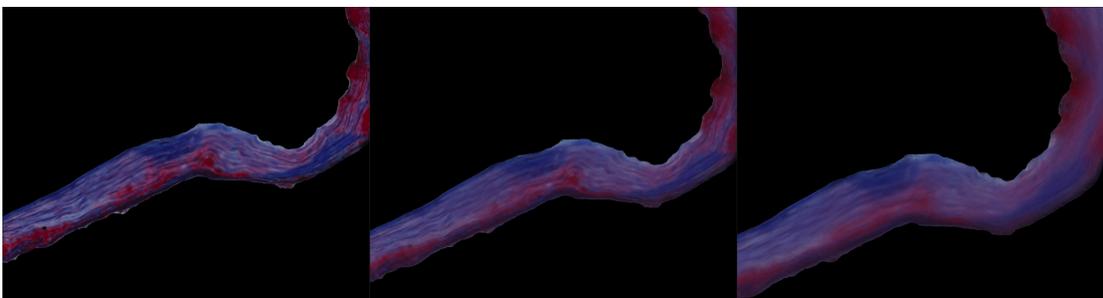

Figure 7.15: Detail view of mapping into own segmentation mask (left), slightly dilated mask (disk size 15, middle) and more dilated mask (disk size 50, right).

The presented datasets are very rarely available and with an increasing number of endovascular intracranial aneurysm treatments, fewer surgical interventions are performed (recall Section 2.1.3). This further limits the collection of resected dome tissue for research purposes, and histologic analysis becomes less available. Although strong deformation during the tissue processing and differences in histologic stainings prevent an automatic co-registration, the histologic information is necessary for understanding aneurysm wall composition. The presented pipeline can combine the multimodal data and provides insight into the complex intracranial aneurysm wall even when an automatic registration is not possible. For the presented approach, the length of the sample was approximated based on the sum of all section thicknesses and was used as a guide in the slide positioning tool. This must be used carefully, as it might be misleading. Senter-Zapta et al. [129] measured the diameter of the largest cross-section in histology and microCT yielding a 15.7% larger diameter in histology. Further studies on measures in microCT and histology are needed to evaluate how the tissue changes at different stages during tissue processing.

During surgery, only a small part of the aneurysm wall can be collected and the tissue is deformed during the process and afterwards. The preoperative 3D model only shows the aneurysm lumen and not the aneurysm wall tissue. This complicates the registration of the aneurysm to the collected tissue. Therefore, the accuracy of the WSS mapped to the microCT image is limited.

Here, no correlation between histology, calcification and WSS was evident. A major limitation is the small variance of the WSS at the collected tissue. Tissues from other areas or intracranial aneurysms with varying hemodynamic forces might be more expressive.

Two medical experts with experience in histologic image analysis analyzed the data based on the program. The resected dome only covered a small part of the IA. Compared to the rest of the aneurysm, the WSS was not conspicuous. Focusing on the WSS at the resected dome, the middle part of the tissue had a lower WSS than the outer parts. The experts stated that the transition from low WSS to high WSS is interesting, especially the possibility to compare this region with the different histological stainings. In the resected dome sample no correlation between calcification and particularities in the histologic images were found.

Calcification was mostly present in one half of the tissue. In this part, the WSS was slightly higher.

The experts also compared the thicker part of the resected tissue with the different histologic images provided by our visual exploration approach. First, they focused on the wall thickness and cellularity evaluation and analyzed the correlated HE and MT stainings. In addition, they defined a lipid accumulation in the ORO-stained images and a slight loss of smooth muscle cells in the aSMA-stained images, see Figure 7.16. These findings are very important for understanding the IA wall composition. The presented pipeline is suitable for comprehensive multimodal visual exploration of the aneurysm and the aneurysm wall. It combines histologic and microCT images and 3D surface meshes of the
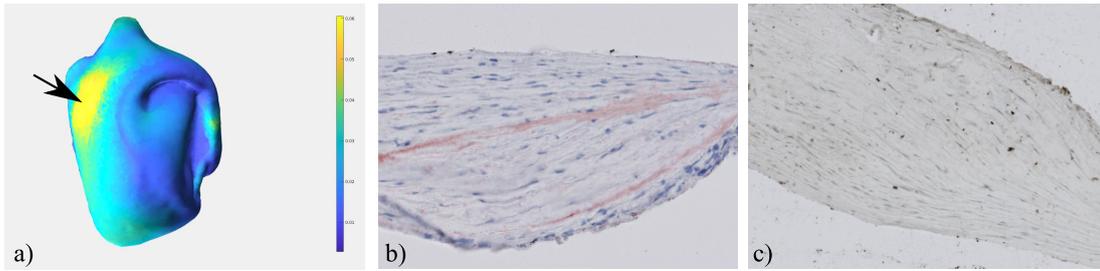
Figure 7.16: Exploration of the resected IA dome by mapping the wall thickness to color (a) and analyzing corresponding histological images. The ORO staining shows a lipid accumulation (red) especially in the region with increased wall thickness (b). The aSMA staining reveals a smooth muscle cell structure that is globally organized for this area. Also a slight loss of smooth muscle cells was visible in the area of lipid, when comparing the adjacent sections.

aneurysm and the resected dome. The tool combines 2D and 3D data. The histologic data uses a variety of stainings, is incomplete and insufficient for 3D reconstruction on its own. The pipeline can be easily extended to include further stainings. The tool enables the user to find a correlation between wall characteristics (histologic structures, wall thickness or calcification) and hemodynamic forces.

8 Understanding aneurysm wall in clinical routine - Vessel wall imaging

This chapter covers two aspects: the objective segmentation of wall enhancement and rupture prediction based on the aneurysm shape. Here, the focus is solely on the segmentation of wall enhancement and provide tools for future objective and reliable wall enhancement research. As this imaging technique is not yet widely used, the number of datasets available here is too limited for a meaningful analysis of the relation of wall enhancement and aneurysm rupture. While a large number of morphological parameters exists in aneurysm research, these are rarely used in clinical routine as they are too complicated to extract. Here, a geometric deep learning approach is described. With deep learning the aneurysm shape can be extracted without complex parameter calculation. To build trust into the deep learning prediction a user interface showing what the neural net learns is also developed. Geometric deep learning is a promising approach to predict aneurysm rupture. In the future, the shape-based deep learning prediction could be combined with the wall enhancement analysis to further enhance aneurysm rupture prediction.

8.1 Dataset

For the analysis of wall enhancement in black blood magnetic resonance imaging (BBMRI) 25 images were available. Two of these showed patients with aneurysms but without wall enhancement. For the other images, segmentations of the wall enhancement by experts were available.

From the segmented aneurysm, 3D surface models can be generated and analyzed. Besides the segmentation and analysis of wall enhancement, these could also be analyzed and used for rupture risk assessment. Therefore, aneurysm surface mesh processing and analysis will also be described in this chapter. However, only very limited BBMRI data was available and the data used for mesh processing and analysis also uses surface meshes from other imaging modalities. This includes meshes from an internal database, as well as meshes from the Aneurysik database [9].

8.2 Wall enhancement in vessel wall imaging

As discussed in Section 3.3., wall enhancement might be used for rupture risk assessment of intracranial aneurysms. To support an objective identification and segmentation of wall enhancement, a semi-automatic segmentation tool was developed. This was then used to compare wall enhancement in different imaging sequences.

8.2.1 Wall enhancement definition

Here, wall enhancement is defined as light grey values near the aneurysm. As the absolute grey values in MRI images cannot be compared directly, the intensities are evaluated in comparison to a reference value from the same image. The threshold for the values which are determined as enhanced is set as percentages of a reference value. As a reference value, the grey value of the pituary stalk is used. Several nuances of wall enhancement are segmented to allow for a refined evaluation of wall enhancement and its connection to aneurysm rupture.

8.2.2 Segmentation tool

First, a BBMRI image is loaded. Then, the pituitary is estimated by searching for bright circles near the center in the image slices. The brightest value is proposed as the reference value. The user has three options to adjust the reference value: set the reference value to the brightest value occurring in the image, manually type in a value or select a new value by selecting a point in the image. In the last case, the brightest value near the selected point is used to account for imprecise point selection. With that option, a faulty automatic pituitary selection can be easily corrected.

The user can select between 1 and 10 nuances for wall enhancement and set the corresponding thresholds as percentages of the reference value. While 1 or 2 wall enhancement classes (strong/weak wall enhancement) align with previous research, a more fine-graded segmentation might be useful for further research on the relation of wall enhancement and rupture. Additional to the semi-automatic reference value selection it is necessary to segment the aneurysm. This is done by setting a seed point in the middle of the aneurysm and performing region growing. After the aneurysm segmentation is performed, the neighboring voxels can be determined and, according to their values, the amount of enhancement can be defined. The segmentations are displayed in the tool. The aneurysm segmentation is overlayed in blue and the wall enhancement segmentation in red, where a darker red depicts a higher wall enhancement and a transparent red a lower wall enhancement. A summary of the wall enhancement segmentation is displayed and shows the amount of voxel and volume of each enhancement nuance.
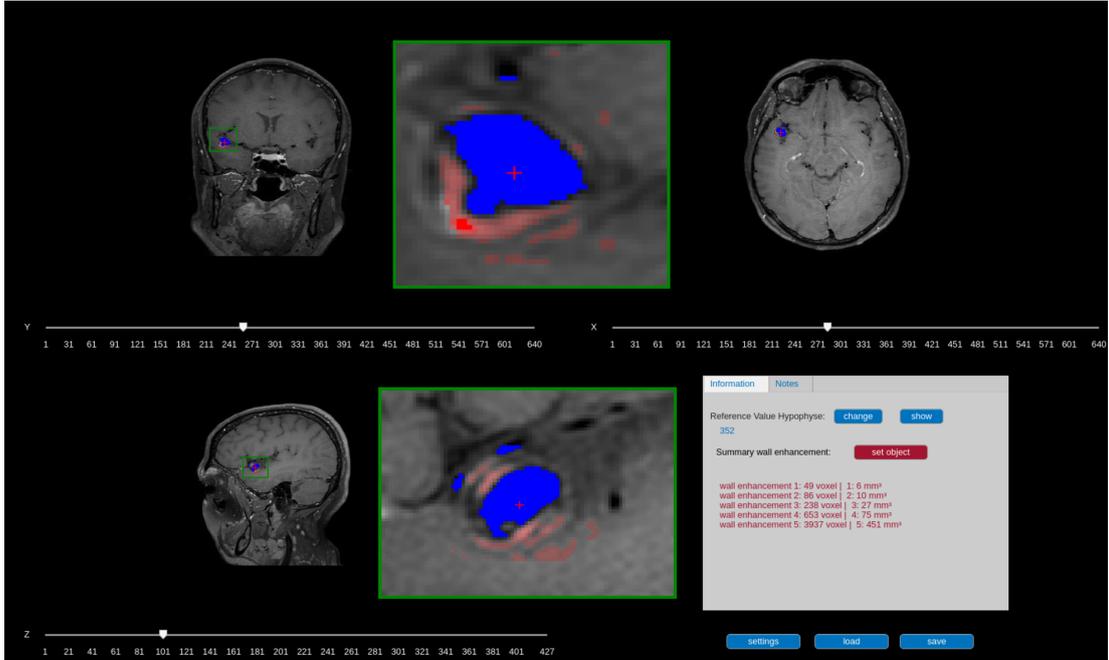
Figure 8.1: Prototype of wall enhancement segmentation tool with zoomed in view of segmentation (green rectangles). Blue: aneurysm/vessel, red cross: cursor position, red overlay: segmented wall enhancement.

Table 8.1: Thresholds used for wall enhancement segmentation

	class 1	class 2	class 3	class 4	class 5
a	85%	75%	70%	65%	60%
b	75%	65%	55%	45%	35%
c	70%	60%	50%	40%	30%
d	60%	50%	40%	30%	20%

8.2.3 Experiments

The wall enhancement segmentation tool was used in two different experiments. In the first experiment, the segmentation tool was used to segment wall enhancement around intracranial aneurysms for ten patients. The wall enhancement segmentation divided the wall enhancement into five groups. The thresholds are given as a percentage of the intensity at the pituitary. Four sets of thresholds (a,b,c,d) are explored (Table 8.1).

The wall enhancement segmentations of the tool were compared with manual, binary segmentations.

In the second experiment the tool was used to compare two BBMRI sequences, VISTA and MSDE (recall Section 2.2.2). The same thresholds as above were used. For eleven patients the segmentation images from both sequences were segmented.

8.2.4 Results and discussion

With the presented segmentation tool the wall enhancement of several patients was segmented. The segmentations were compared to manual segmentations.

Comparison to manual segmentation

The segmentation results of the automatic segmentation differ depending on the selected thresholds. When all classes are combined, the automatic segmentation includes a larger volume than the manual segmentation. Figure 8.5 shows this exemplary for patient 1 and patient 4. For patient 4, the additional segmentation volume increases with lower thresholds. For patient 1, this does not happen, as already all voxels in the search area around the aneurysm are segmented with the highest threshold set (a). In both cases, the volume of the higher wall enhancement classes increases with lower thresholds. The same can be seen in Figure 8.4, where the segmented volume of each wall enhancement class is shown for patient 7 and patient 12.

Sometimes the manual segmentation includes voxels with intensities much smaller than the reference value at the pituitary. For example, in patient 10, the manual segmentation includes many voxels of low intensities. As Figure 8.6 shows, even with the lowest threshold combination (d), where the minimum threshold to include voxels in the wall enhancement segmentations is 20% of the maximal pituitary intensity, some voxels of the manual segmentation are below this threshold. With lower thresholds, more of the manual segmentation is included and sorted in a higher wall enhancement class (Fig. 8.2).

In Figure 8.3, the manual segmentation volume is compared to the volume segmented as wall enhancement class 1. The necessary threshold to achieve a segmentation volume of wall enhancement class 1 comparable to the manual segmentation is between 55% and 65%. For patient 5 a threshold between 45% and 55% would be optimal.

Small inaccuracies might be present in the manual segmentation due to several circumstances. The voxelization of the smooth contours can lead to small differences at the segmentation border. The algorithm evaluates each voxel individually and decides whether wall enhancement is visible and which wall enhancement class the voxel belongs to. Partial volume effects might influence the segmentation. It is unlikely that a manual segmentation would be that detailed. Instead, an expert likely evaluates several voxels together. Therefore, the manual segmentation is more prone to include voxels with darker intensity.

A problem for manual segmentation might be the unreliable perception of grey values [218, 219]. While the computer evaluates the exact intensity value and compares it to the reference value, human perception of grey intensities is influenced by the surrounding values. Depending on the adjacent voxels the same value might appear lighter or darker to a human performing the segmentation.
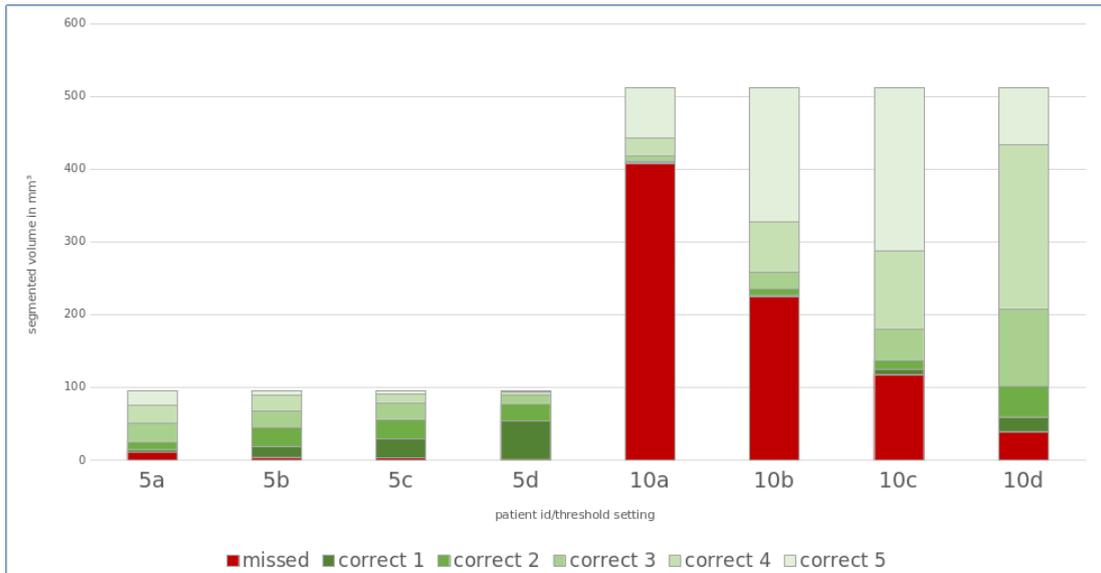
Figure 8.2: Comparison of wall enhancement segmentation of our tool with manual segmentation for patient 5 and 10: missed volume (volume segmented by expert but not by the tool) and correct volume (volume segmented by both; for the tool the corresponding wall enhancement class of the segmentation is shown)
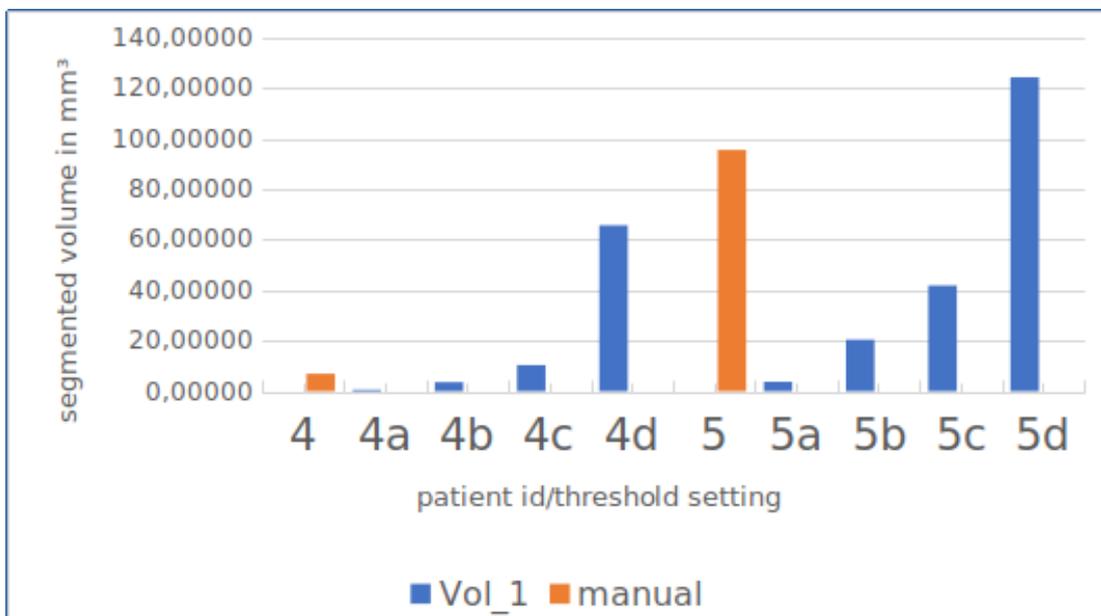
Figure 8.3: Comparison of segmented volume of manual enhancement and automatic segmentation of wall enhancement class 1 for patient 4 and 5
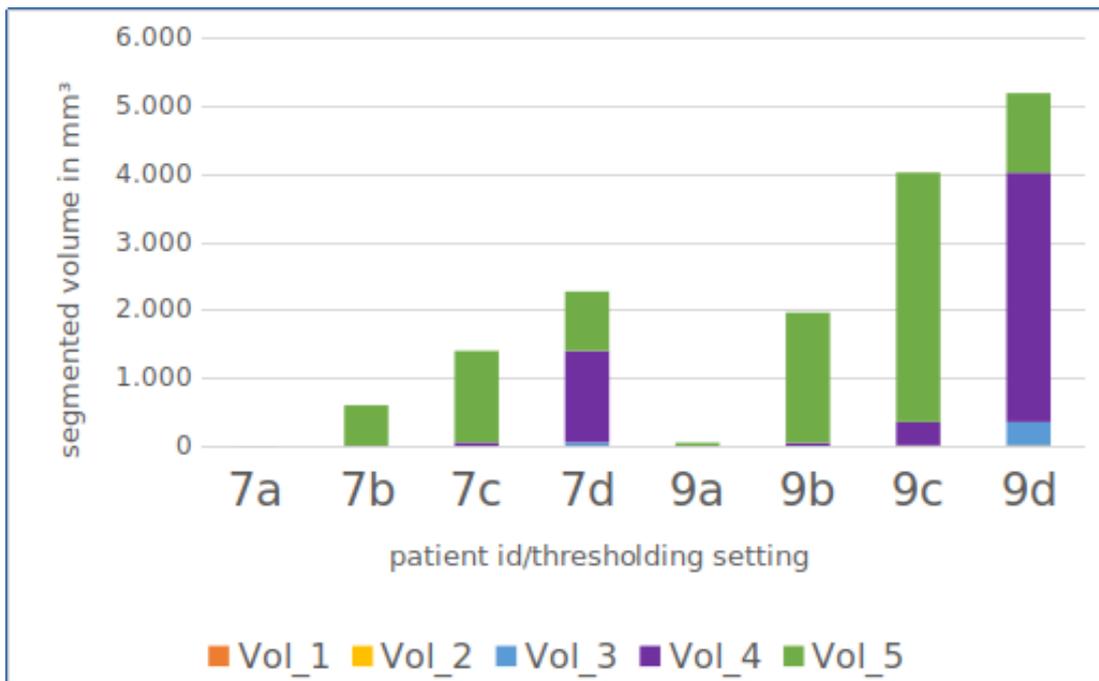
Figure 8.4: Result of automatic segmentation: Volume of each wall enhancement class for patient 7 and patient 9 (wall enhancement class 1 and 2 occur in 9c and 9d in very small amounts (less than 5 mm^3)
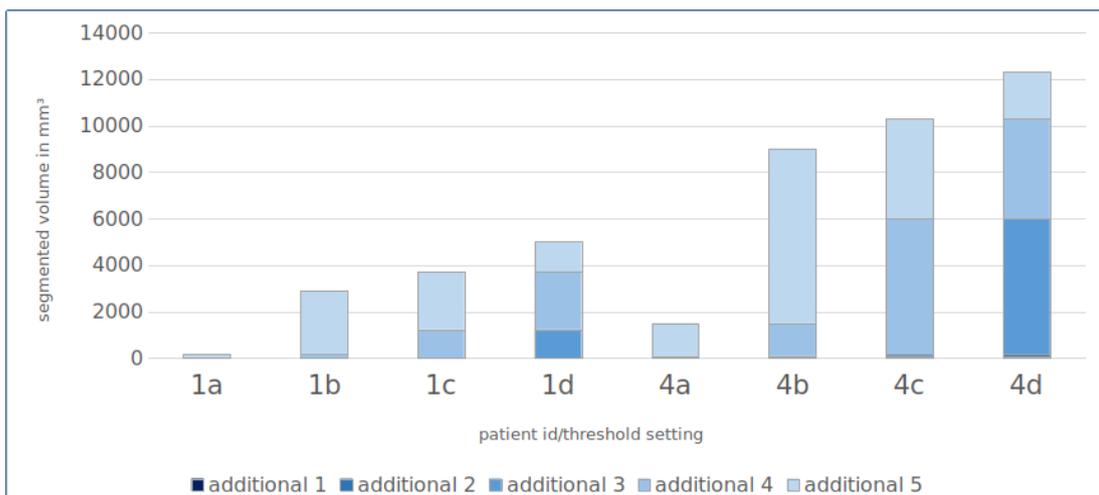
Figure 8.5: Additionally segmented volume of each wall enhancement class in patient 1 and 4
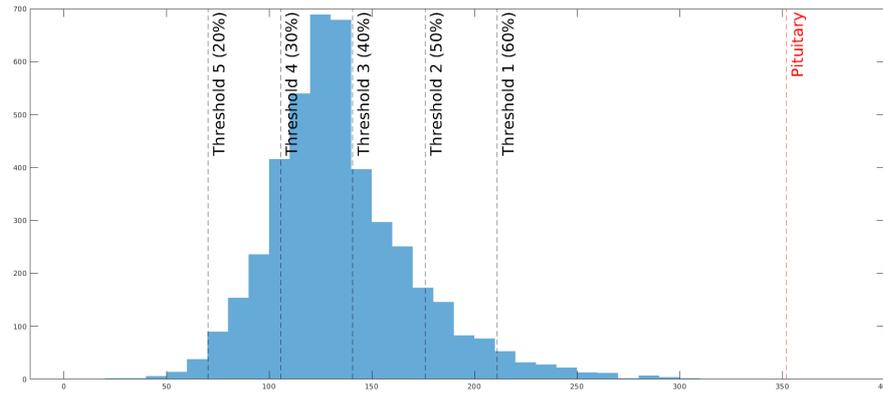
Figure 8.6: Histogram of voxel intensities inside manual segmention of patient 10 and corresponding thresholds d

The automatic segmentation is therefore more constant and reliable in the evaluation of grey intensities.

Here, the automatic segmentation was only compared to one manual segmentation per patient. Different persons might provide slightly different segmentations and it would be interesting to compare the automatic segmentation to other manual segmentations. Additionally, further configurations for the automatic segmentation (number of wall enhancement classes, thresholds) could be considered.

This segmentation works on individual voxels. To better correspond with human segmentations it might be useful to develop an algorithm that decides on wall enhancement not on individual voxels but on small groups. Furthermore, the overall shape (for example avoiding small holes) might be taken into account to fit manual segmentations.

While a consistent and reproducible definition of wall enhancement is used, it is challenging to find thresholds suitable for all datasets. To include all of the manually segmented wall enhancement areas, low thresholds ($<20\%$ or smaller) can be necessary. At the same time, these tend to include larger areas not included in the manual segmentations and increase the volume of the higher wall enhancement classes. The optimal thresholds might be further evaluated by comparing the different segmentation and resulting volumes for the wall enhancement classes to the rupture risk. That might determine which configuration for the automatic segmentation produces the best results for rupture risk prediction.

Comparison of different sequences

The overview (Fig. 8.7) shows that often in MSDE a larger area is segmented than in VISTA. For the higher wall enhancement classes (Fig. 8.7, block 1-3), the difference is small. In the lower wall enhancement classes, the differences between the sequences are larger.

Figure 8.7: Difference between wall enhancement area in MSDE and VISTA; rows: patient id; column: threshold set; block: wall enhancement class; yellow/red: wall enhancement in MSDE larger than in VISTA, blue: wall enhancement in VISTA larger than in MSDE
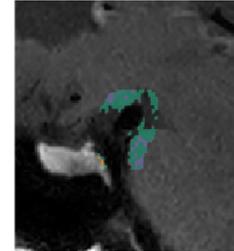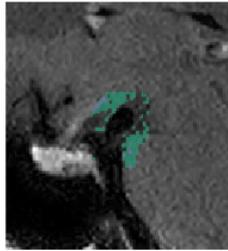
Figure 8.8: Patient 1, wall enhancement in MSDE

Figure 8.9: Patient 1, wall enhancement in VISTA

Figure 8.8 and Figure 8.9 show the wall enhancement with lowest thresholds (60%, 50%, 40%, 30% and 20% of the pituitary are used as thresholds for wall enhancement classes 1 to 5).
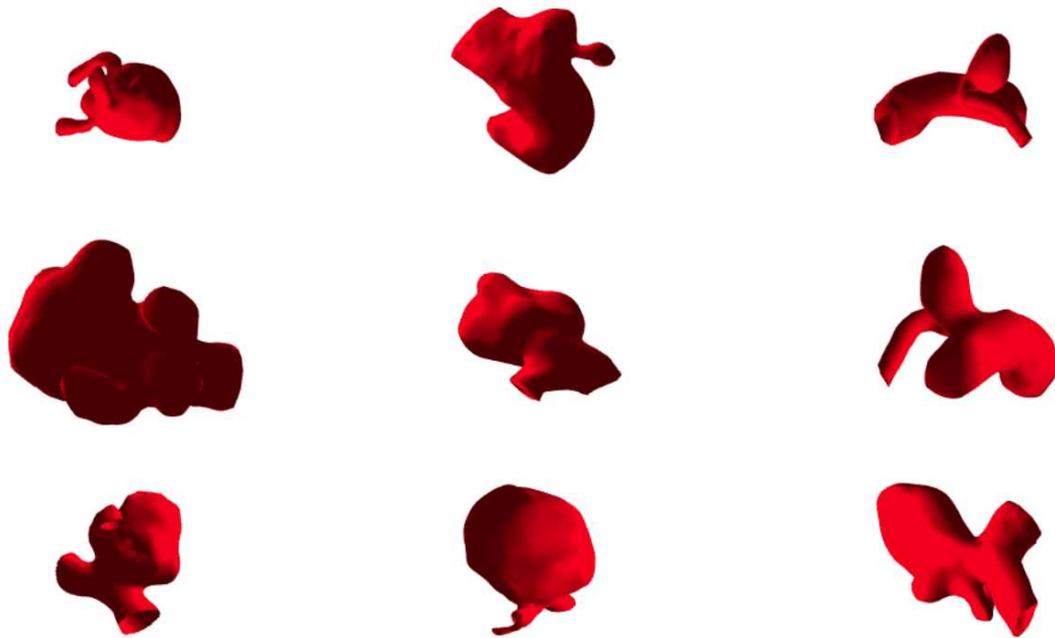
Figure 8.10: Example of meshes used for training (aneurysm with parent vessel)

8.3 Aneurysm rupture prediction with deep learning

This section first describes several experiments on the prediction of aneurysm rupture with deep learning on patient-specific 3D geometries. The second part focuses on the visualization of the results for doctors to build trust in deep learning predictions and understand what is learned by the neural net.

8.3.1 Geometric deep learning aneurysm rupture prediction

In this study, 3D meshes of intracranial aneurysms from the publicly available Aneurisk dataset [9] and meshes derived from aneurysm images collected at the University Hospital Magdeburg between 2010 and 2020 were used.

Each mesh shows at least one aneurysm and various surrounding vessels. The meshes are cut so that each mesh only shows the aneurysm and the parent vessel (see Fig. 8.10). Two different mesh cutting approaches are used: manual mesh cutting using MeshLab and a semi-automatic mesh cutting. For the semi-automatic approach, the meshes were first automatically segmented into parts based on convexity [220] (see also Section 2.5.1). The next step is the manual identification of sections belonging to the aneurysm and the vessel sections directly at the aneurysm (parent vessel). Figure 8.11 shows the result of the automatic part segmentation. From these partsy the user selects the aneurysm and the parent vessel. Figure 8.12 shows an example of the mesh after semi-automatic mesh cutting.

Next, the meshes are remeshed to a similar number of faces.
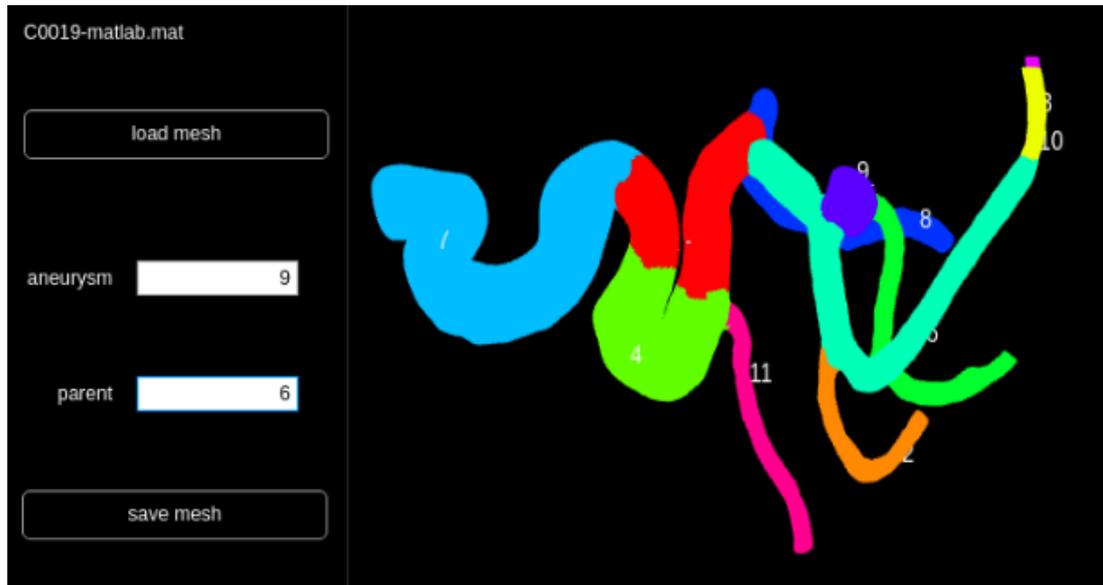
Figure 8.11: Semi-automatic mesh cutting: after automatic part segmentation the aneurysm and parent vessel are selected. Each automatically segmented section is shown in a different color.

Figure 8.12: Result of semi-automatic mesh cutting: right: mesh showing only the aneurym, and left: mesh of aneurysm with parent vessel

Several algorithms were used: MeshNet [221] and MedMeshCNN [222] for classification of meshes, and Pointnet++[223] for point cloud classification. Each algorithm has a different focus. Pointnet++ only uses the vertices of the mesh. MeshNet calculates several features for each face of the mesh, while MedMeshCNN calculates features per edge.

Pointnet++ is the extension of Pointnet [224]. It adds a hierarchical point set feature learning. Pointnet++ can be used for classification and segmentation.

MeshNet uses the face centers as a spatial descriptor. The mesh structure is captured using the face corners and normals. In mesh convolution blocks these features are aggregated with neighboring information.

MedMeshCNN uses five features per edge: dihedral angle, inner angles of the two adjacent faces and edge-length ratio for each face. Then, an edge collapse process is used for mesh pooling (recall Section 4.1.1).

8.3.2 Results of rupture prediction

Table 8.2 shows selected results of deep learning classification for intracranial aneurysms.

The best classification was achieved with MeshNet on meshes showing the aneurysm and parent vessel according to the semi-automatic, convexity-based mesh cutting. The test accuracy on 20 ruptured and 20 unruptured aneurysms was 82.5%. The training data consisted of 150 aneurysms (89 ruptured/61 unruptured).

Both mesh-based classifications (MeshNet and MeshCNN) were superior to the classification on point clouds.

MeshNet was best in classification of meshes showing the aneurysm and parent based on semi-automatic cutting. The performance on meshes showing only the aneurysm, likewise using the semi-automatic mesh cutting, was slightly worse.

In this study, for MedMeshCNN the manually cut meshes were better than the semi-automatic ones. On the contrary, the semi-automatic meshes were better for MeshNet.

While the results suggest that deep learning on 3D data might be useful for aneurysm rupture prediction, there are several limitations. The number of training data is small, especially as there is a high variance in intracranial aneurysm shape.

Each algorithm has a large number of parameters. Additionally, several choices of data preprocessing are possible. The possibility cannot be ruled out that other parameter choices lead to different results.

Some parameter combinations are limited by current hardware capacity. Due to technical limitations, batch size, mesh size and neural net size cannot be changed independently.

Table 8.2: Selected results of deep learning aneurysm classification (RIA: ruptured intracranial aneurysm, UIA: unruptured intracranial aneurysm)

algorithm	dataset	training data	test data	parameters	accuracy
MeshNet	**aneurysm and parent, based on convex split**	**RIA: 89 UIA: 61**	**ruptured: 20 unruptured: 20**	**max number faces: 1025 learn rate: 0.0001 batch size: 2**	**test: 82,5% train: 99,33% at epoch 73**
MeshNet	only aneurysm	RIA: 42 UIA: 42	ruptured: 20 unruptured: 20	max number faces: 5000 learn rate: 0.0001 batch size: 2	test: 80% train: 100% at epoch 95
MeshNet	manual cut, only bifurcation aneurysms	RIA: 34 UIA: 26	ruptured: 10 unruptured: 10	max number faces: 5000 learn rate: 0.0004 batch size: 2	test: 80% train: 85% at epoch 92
MeshNet	aneurysm and parent, based on convex split	RIA: 61 UIA: 61	ruptured: 20 unruptured: 20	max number faces: 5000 learn rate: 0.0004 batch size: 2	test: 72,5% train: 90,98% at epoch 138
MedMeshCNN	aneurysm and parent, manual cut	RIA: 108 UIA: 198	ruptured: 10 unruptured: 10	max input edges: 17000 learn rate: 0.0002 batch size: 8	test: 70% at epoch 21
MedMeshCNN	aneurysm and parent, based on convex split	RIA: 62 UIA: 62	ruptured: 20 unruptured: 20	max input edges: 17000 learn rate: 0.0001 batch size: 2 without curvature	test: 65.0% at epoch 4
PointNet++	aneurysm and parent, manual cut	RIA: 73 UIA: 73	ruptured: 20 unruptured: 20	number of points: 5000 learn rate: 0.002 batch size: 4	test: 67,5% epoch: 197

The semi-automatic cutting based on the automatic, convexity-based part segmentation encourages consistent mesh cutting between users. While the variation between users is minimized compared to the manual cutting, the variation between aneurysms increases. The length of the included parent vessel changes, as the automatic part segmentation can split up the parent vessel into a few large or several smaller parts, depending on the curvature. In contrast, the manual cutting includes similar large portions of the parent vessel. Therefore, this splitting could add some useful attributes, as it indirectly encodes the curvature of the vessel, or hinder the deep learning with unnecessary information and larger variation between data.

Compared to other mesh classification tasks, like classification of furniture, aneurysm classification is not easily solvable for a human. Risk factors like female gender, age and smoking might not be visible in the aneurysm shape. Currently, the available data is too small to evaluate whether shape as sole basis for rupture prediction is feasible or not. Very similar shapes might have a different outcome depending on other patient attributes. Including patient features might improve the results. In the future, rupture prediction based on a combination of shape, patient features and wall enhancement could be used.

8.3.3 Visualization of deep learning rupture prediction

Here, a visualization for the MedMeshCNN deep learning classification is described. The visualization is aimed at persons of the medical field with no or limited deep learning knowledge.

Datasets and neural net training

Due to the time-consuming training of neural nets a very small dataset was used for the prototype. The dataset consists of 46 aneurysm surface meshes for training (23 ruptured and 23 unruptured) and 10 meshes for testing (5 ruptured and 5 unruptured). The meshes were remeshed to around 5000 edges. 25 epochs of training on a NVIDIA GeForce RTX 2070 8GB took around 23 hours. The patient-specific meshes were randomly selected from the Aneurisk database and an own database, which includes aneurysm data collected between 2010 and 2021 together with clinical partners at various hospitals.

Several neural nets based on the MedMeshCNN architecture were trained. The training parameters were constant (maximum number of input edges 9000, convolution filter 32 64 128 256 512, pooling resolution 7000 5000 4000 2000 1000 , batch size 6, learn rate 0.00002). The original features (dihedral angle, symmetric opposite angles, symmetric ratios) as well as curvature are considered. Several neural nets using one or more of these features are trained.

User interface design

The user interface consists of five different sections, shown as tabs at the top. The first section shows a short information page. The remaining sections are mesh, accuracy, confusion matrix and data overview. With exception of data overview, each of these sections consists of control elements in the left third of the tool and displays the desired information on the right side. The control panel also offers an information section for the current view.

Mesh This section focuses on a single patient. A specific patient and a neural net are selected by the user. The prediction of the neural net is shown. The user can switch between the reduced mesh view (generated during the MedMeshCNN training, Fig. 8.14) or a colormap. The colormap shows the distance to the closest point and the most important areas, respectively. A large distance (less important area) is shown in blue, a short distance in yellow. If the reduced mesh is selected, the original mesh is displayed above the reduced mesh. Underneath the mesh of the current patient, two smaller meshes showing similar patients and their attributes as well as rupture status are shown (Fig. 8.13). It is also possible to compare two patients or different neural nets for one patient (Fig. 8.15).
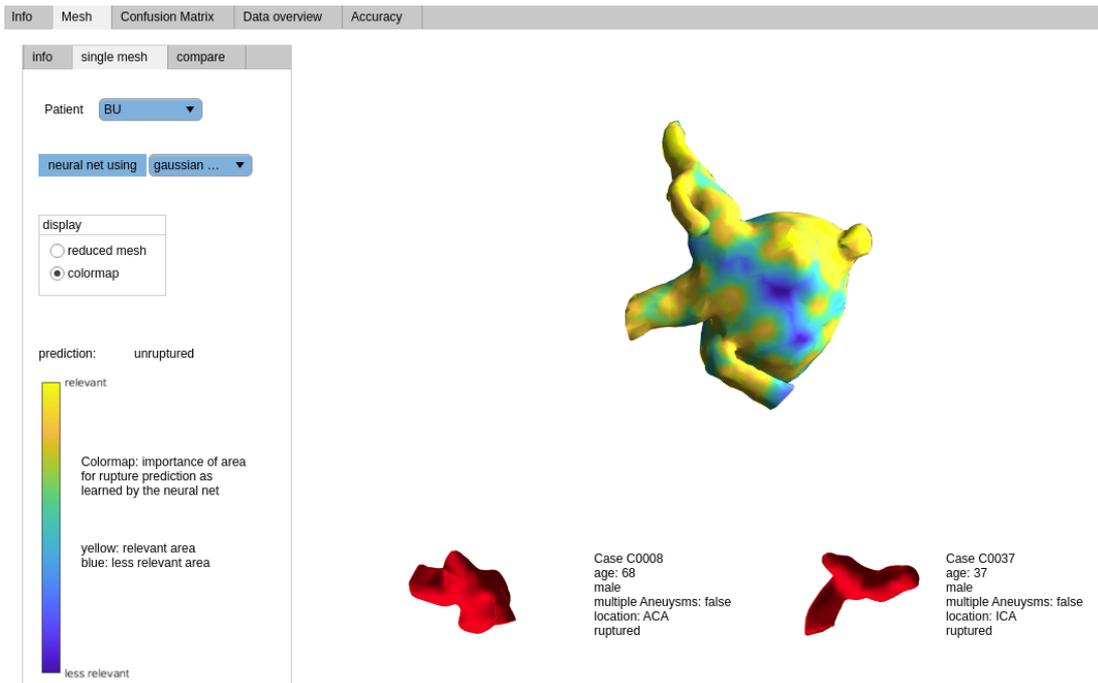
Figure 8.13: Patient-centered mesh view; left: control elements to select patient and mesh, right: large color-coded mesh showing relevant areas for deep learning (blue: less relevant, yellow: highly relevant) of the selected patient; bottom: meshes and information of two similar patients
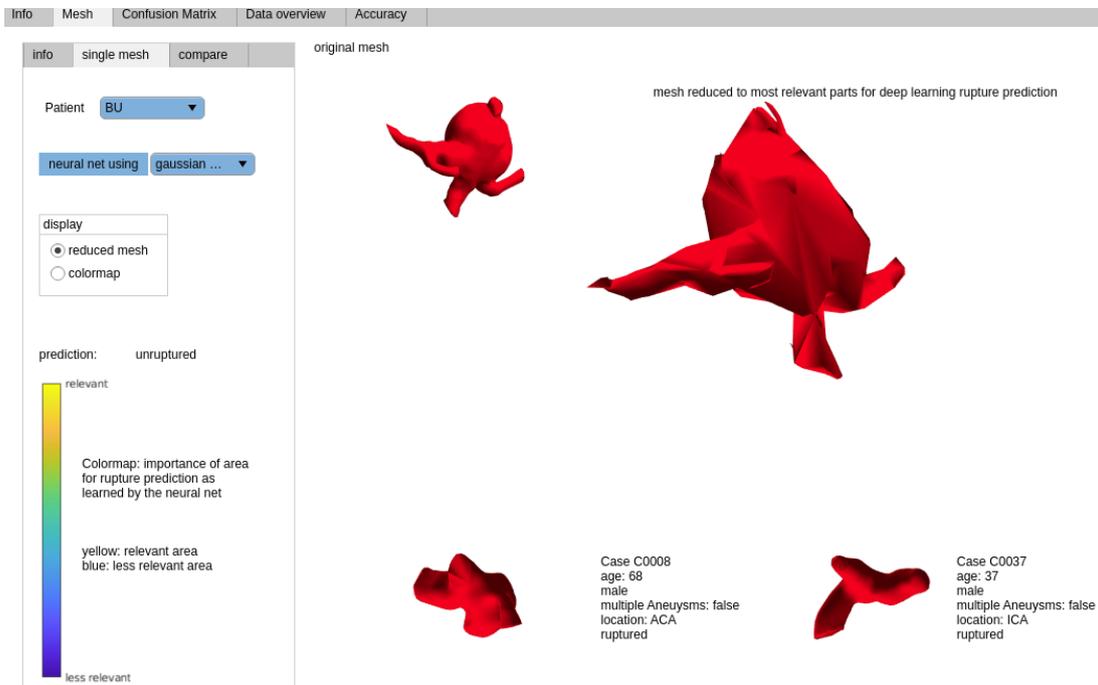
Figure 8.14: Patient-centered mesh view; left: control elements to select patient and mesh, right: reduced mesh view of the selected patient, the original mesh is shown in the top left corner; bottom: meshes and information of two similar patients
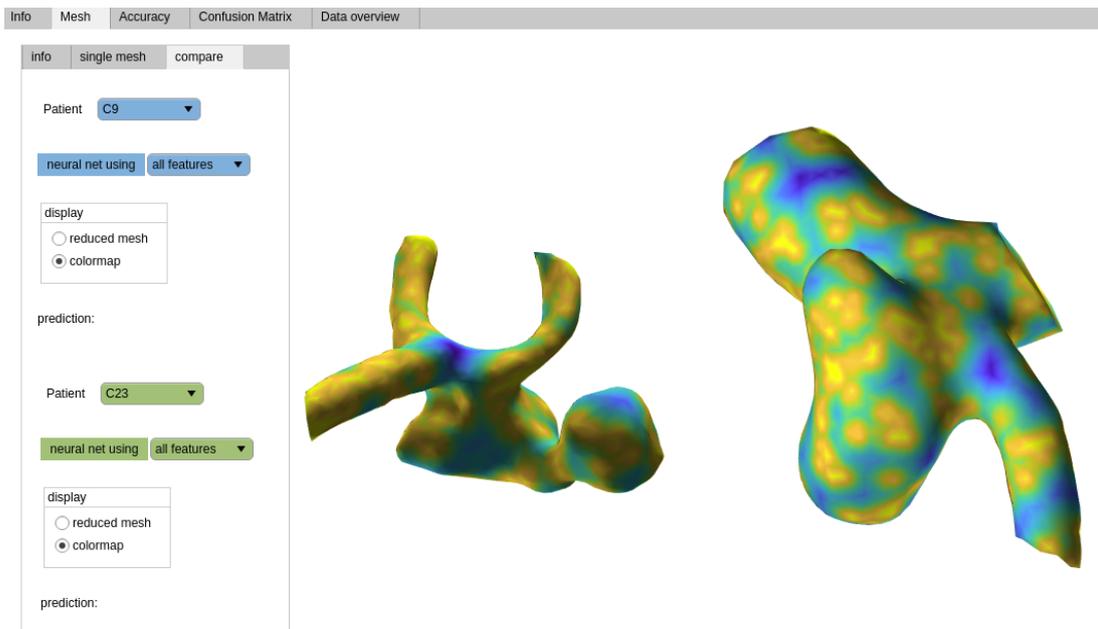
Figure 8.15: Patient-centered mesh view; left: control elements to select patient and mesh, right: large color-coded mesh showing relevant areas for deep learning (blue: less relevant, yellow: highly relevant) of two selected patients

Accuracy Accuracy shows the training and test accuracy for different neural nets. While training, test and validation are commonly used in deep learning evaluation, in this visualization aimed at non-experts only training and test data are shown. In the first, simpler view the user can select two neural nets to compare. For each one a short comment can be displayed. In the second view, all possible neural nets can be selected using check boxes. The user can select as many neural nets as they want and compare them.

Confusion Matrix Again on the left side, the user can select the neural net for which the results are displayed. Additionally, a specific dataset can be selected. If the dataset contains the necessary patient information, the user can further filter the dataset by characteristics often used in aneurysm diagnosis (sex, age, previous SAH, location, size, hypertension, recall Section 2.1.2). The confusion matrix shows the number of patients for each prediction and the true rupture status combination. If one of the confusion matrix fields is selected, examples of aneurysms of this category are shown next to the confusion matrix.

Data overview The data overview shows nine example meshes from the data set. They are sorted into three categories based on the predictions of all neural nets: consistently wrong, consistently right and neural net depending.
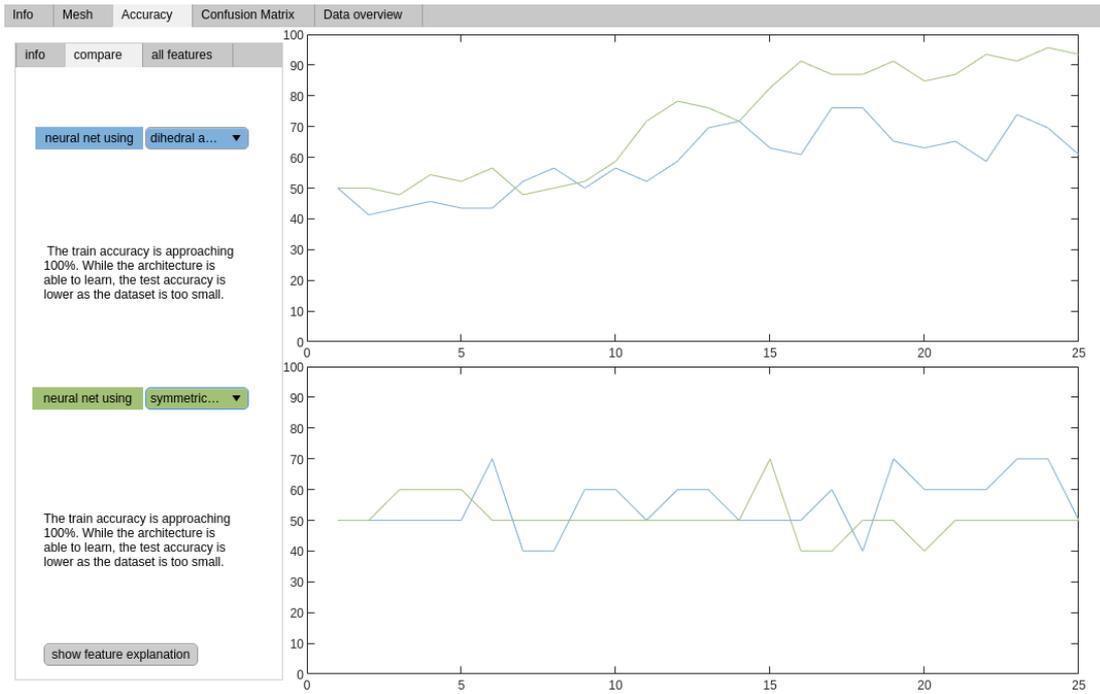
Figure 8.16: Train and test accuracy for two neural nets and explanatory comments

Figure 8.17: Accuracy matrix for various neural nets and filters for patient attributes; right: examples of aneurysms correctly classified as ruptured

8.3.4 Results and discussion

MedMeshCNN uses several features (dihedral angle, curvature, symmetric ratios, symmetric opposite angles) to capture the mesh. In the presented visualization tool, several neural nets using only one of the features are included. This allows the exploration of how different features impact the deep learning. However, this is not a feature visualization as described in the deep learning visualization overview by Yu and Shi [199]. In contrast to image deep learning, mesh deep learning requires to present the mesh in a way that can be used for deep learning. This is done using mesh features. These features are different to the features the neural net learns.

The tool was presented to physicians and medical engineers, who are familiar with intracranial aneurysms. None of the participants had in-depth knowledge of deep learning. There was no time limit and the option to ask questions during the presentation. Afterwards, the participants were asked to fill out a structured questionnaire regarding the tool. Free comments were also welcome. Five participants had a medical background in neurosurgery and five participants were from computer science or fluid simulation.
The visualization tool is able to answer several questions:

- Which area of the aneurysm is relevant for the deep learning prediction?
  This can be seen in the mesh view. The color-coded meshes show which areas are most important to the selected neural net.

- How do different surface features impact the result?
  We trained several neural nets using the features described in the MeshCNN architecture and Gaussian curvature. The mesh view shows how each feature results in neural nets focusing on different areas of the aneurysm. The accuracy view shows the behavior during the training.

- Is this neural net reliable for this patient?
  The mesh view enables the user to see which parts were relevant for the neural net and check if that is sensible, for example a prediction solely based on the parent vessel might be less convincing. Furthermore, the user can compare the result to similar patients and validate whether the prediction is consistent with previous cases. Another option is using the confusion matrix view and filtering for similar patients based on patient characteristics. This can reveal how reliable the neural net is for a certain sub-group.

- How accurate is the prediction and when does it fail?
  This can mainly be seen in the accuracy and confusion matrix view. In the confusion matrix view, examples of meshes which were wrongly classified are shown.
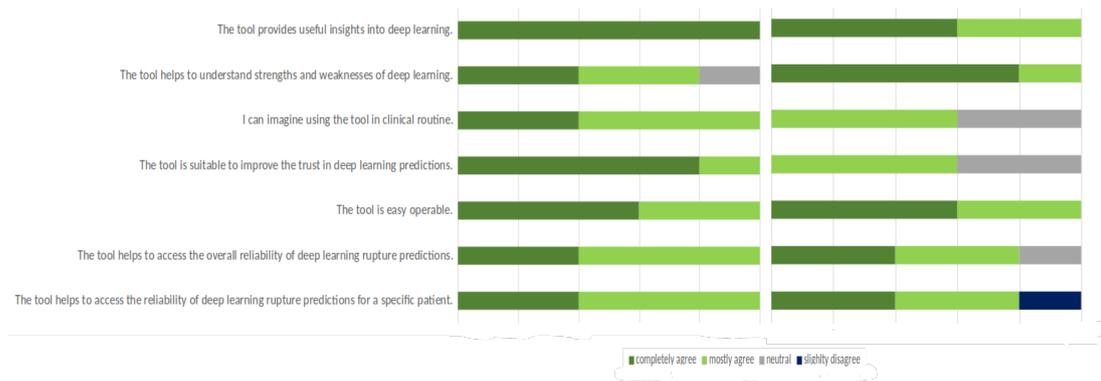
Figure 8.18: Answers to overall impression; left: physicians, right: other participants

User feedback

All participants agreed that the tool provides useful insights into deep learning. The agreement was slightly stronger in the group of the physicians (all five completely agreed) than in the other group (three completely agreed, two mostly agreed, see Fig. 8.18). All physicians could imagine using the tool in clinical routine.

Nine participants found the color-coded mesh very easy to understand, one found the color-coded mesh easy to understand. Several comments on the color scale endorse the usage of blue for less relevant areas, but would prefer red for the most relevant parts. One participant commented that he would prefer a reverse color coding, with blue indicating the most relevant area. The reduced mesh was considerably harder to interpret, especially for the physicians. All physicians all agreed that the mesh view was useful for understanding deep learning and evaluating the patient-specific reliability of the neural net by comparing the prediction to similar patients and validating the plausibility of the areas with larger impact on the result. The confusion matrix was well liked and the participants agreed that it is easy to understand and useful in accessing the reliability of the deep learning predictions. The data overview received mixed responses. On the structured questionnaire, one person indicated that the data overview was hard to understand, one response was neutral and the rest found it understandable. The comments revealed that further information would be interesting for the user. For example, also displaying the patient information along the meshes and showing the color-coded versions from the mesh view. The accuracy view was also perceived as useful and easy to understand.

133

Impact of features

Especially the combination of mesh view and accuracy view are also helpful for analyzing neural nets from a developer point of view. Training with a reduced number of features compared to the original architecture allows analyzing the neural net in an ablation study and analyzing the impact that each feature has.

Figure 8.19 shows how different neural nets process the same aneurysm. The blue areas were less important than the yellow areas. The results of five different neural nets are show. Four of these only use one feature (dihedral angle, opposite angles, symmetric ratios or Gaussian curvature). The last one includes all features. The parent vessel was relevant for most neural nets. The neural net using only the dihedral angle was less interested in the parent vessel, as only a small part near the outlet was important to this neural net. The other single feature neural nets displayed moderate interest in the overall parent vessel with several small more interesting spots at various places. For the neural net trained with all features, the whole parent vessel is important.

For the neural net with all features, the neck between parent vessel and aneurysm is less important. This can also be seen in the neural nets using opposite angles and Gaussian curvature. In contrast, the neural nets using dihedral angle and symmetric ratios stronger emphasize the neck area. For the neck area, the opposite angles seem to have a large impact.

On the aneurysm itself, each neural net displays a different behavior. In the aneurysm area, the neural net with all features is most similar to the neural net with only symmetric ratios. Similarly, on the bleb different areas are important to different neural nets.

Despite only including one of the features from original MeshCNN architecture, all neural nets were able to learn the classification task (see Fig. 8.20). The neural net using only Gaussian curvature as feature was slowly learning compared to the other neural nets. The neural net using opposite angles was very fast in learning the classification and reached a training accuracy of over 90% in less than 25 epochs. While not as fast, the neural net using only the dihedral angle was less prone to overfitting than the others and reached a test accuracy of 70%. The neural net with all features achieved a train accuracy of 93.4%, but only 60% test accuracy.

The overall responses, especially from the physicians, were positive and encouraging. In the future, deep learning-based rupture risk assessment could be a helpful tool in clinical routine. While the non-physician group overall also found the tool useful, their responses were slightly more critical. As these participants were from computer science or hemodynamics, likely a more in-depth, mathematical-technical explanation would have been better suited.

For the prototype, similar meshes were manually selected and comments on the training and test data plots where manually written. This could be replaced by an automatic selection of similar patients and computer-generated comments based on automatic analysis of the plots [225].
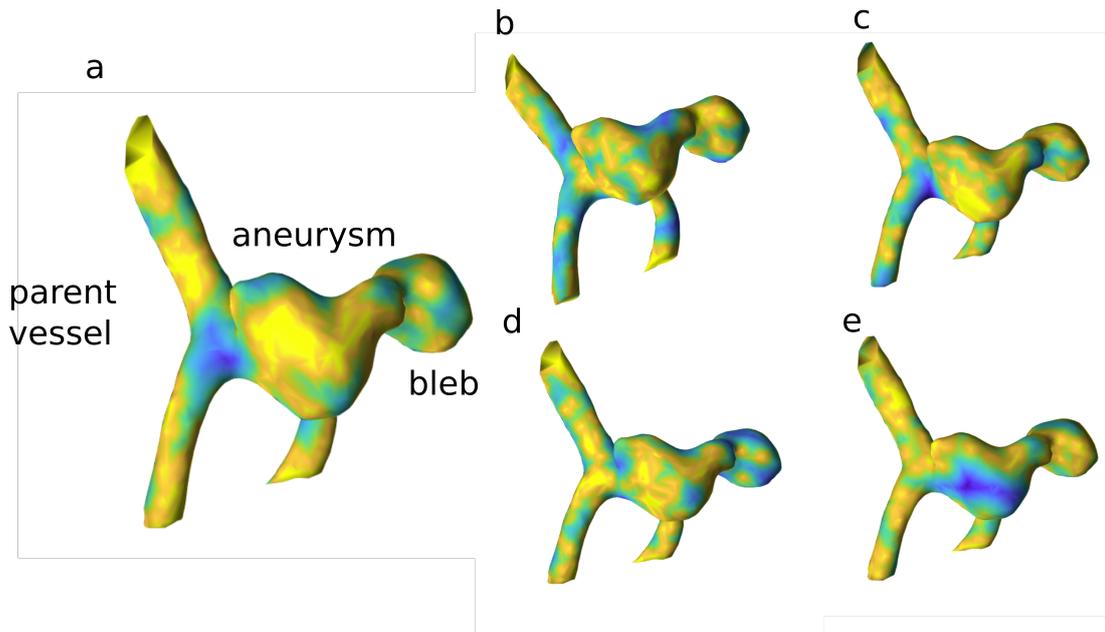
Figure 8.19: Yellow: area relevant for neural net, blue: area less relevant; neural net using a) all features, b) only dihedral angle, c) only opposite angles, d) only symmetric ratios, e) only Gaussian curvature
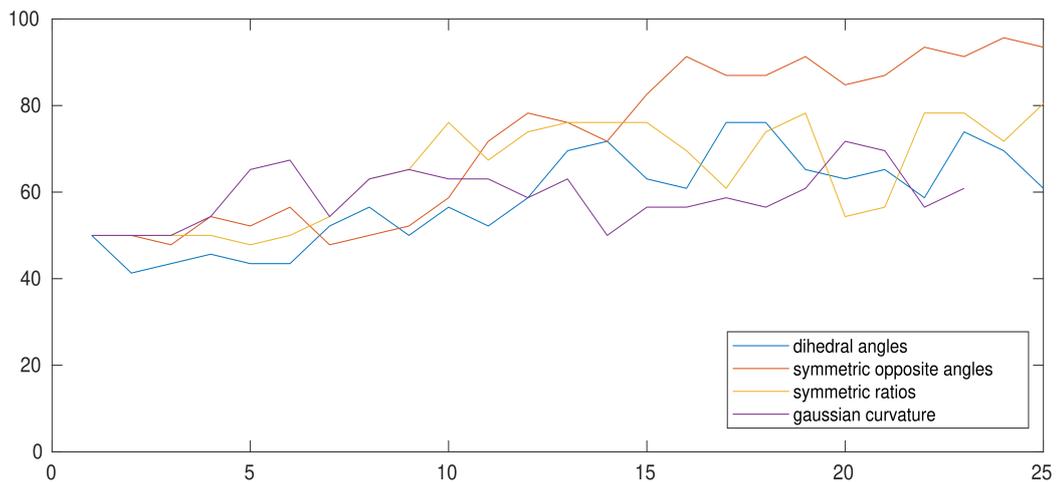
Figure 8.20: Train accuracy for neural net using dihedral angle (blue), symmetric opposite angles (red), symmetric ratios (yellow) or Gaussian curvature (purple)

Focus of this study was the evaluation of the visualization. Therefore, only a very small dataset was used to keep the training time reasonable. However, we expect a larger dataset to display a similar behavior. Not all features are necessary, as the neural nets were able to learn with only one feature. If trained with only one feature, using only the opposite angles could be promising if overfitting can be reduced with a larger number of training data. Otherwise, a neural net only based on the dihedral angle might be the best choice. Despite the low number of training data, a test accuracy of 70% was reached.

The neural net using all features does not focus on the neck area. While a rupture on the aneurysm neck is very rare, the neck is commonly used in morphological features, for example in the aspect ratio (aneurysm height/aneurysm neck width).

9 Understanding aneurysm wall in clinical routine - Wall shear stress

An important aspect of aneurysm research is the analysis of hemodynamic parameters like the wall shear stress. Preparing high-quality meshes for hemodynamic simulations can be a complex and time-consuming task. Several mesh processing steps require user input. Here, several mesh processing options for consistent and easy mesh preparation for hemodynamic simulation and other analyses are presented. The second part of this chapter focuses on the inclusion of WSS in clinical routine. Not only the mesh processing but also the simulation itself is time-consuming. This is impractical for clinical routine. Instead of time-consuming simulations, the WSS could be predicted with geometric deep learning. Section 9.2 describes wall shear stress prediction with geometric deep learning for artificial aneurysms. Section 9.3 presents wall shear stress prediction for patient-specific meshes.

9.1 Aneurysm mesh processing

From CT or MRI a surface mesh of the aneurysm is generated and further processed to calculate the wall shear stress and evaluate the rupture risk. Here, several tools for (semi-)automatic mesh processing and analysis are presented. An overview of the steps is shown in Figure 9.1. After the mesh is segmented into parts and information about the parts are collected in the semantic graph, and centerline and outlets are calculated, these can be used for various applications. The currently most commonly used approaches for rupture risk prediction, morphological parameters, and hemodynamic simulations can benefit from the presented aneurysm processing.
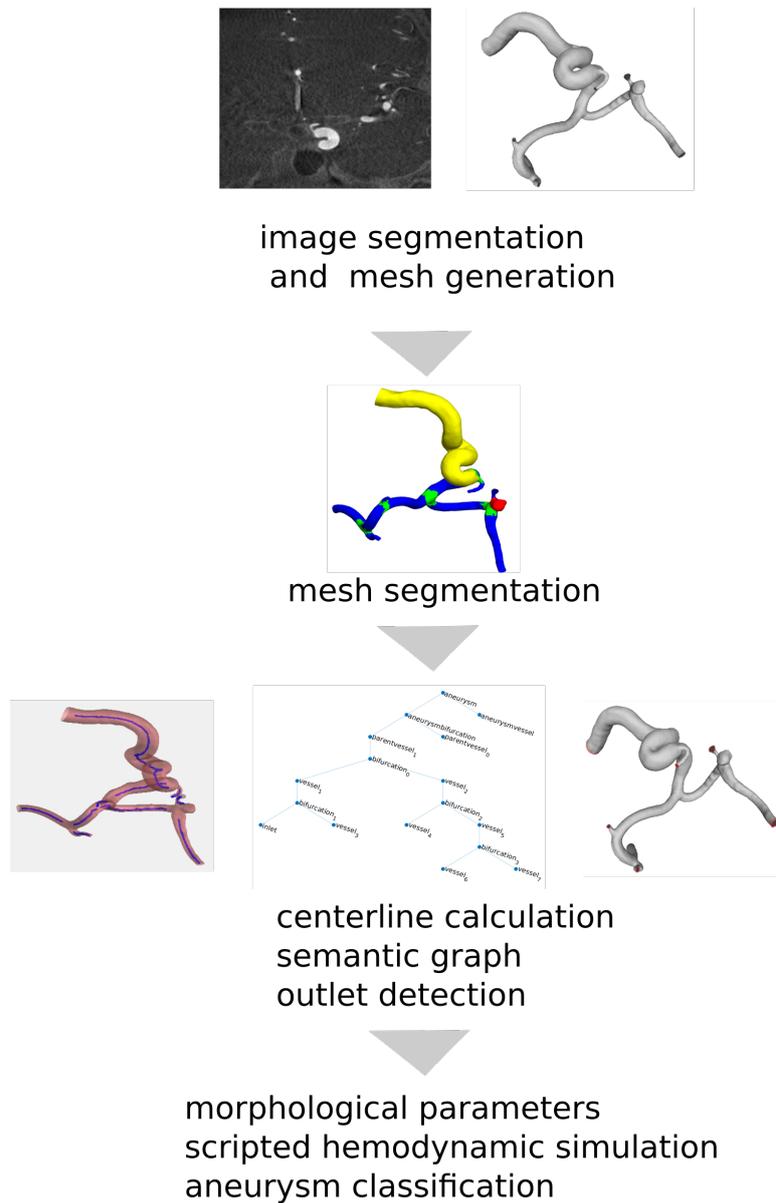
Figure 9.1: Overview of aneurysm processing and analysis

9.1.1 Mesh segmentation

To support further processing of the aneurysm mesh, the mesh is segmented into several parts. These parts are aneurysm, vessel, inlet vessel, and bifurcation. This segmentation is done with a variation of the MeshCNN neural net. The neural net was alternated to use sparse matrices, which decreased the memory consumption and allowed to work with larger meshes. Additionally, the loss function was adjusted to include weights to handle the imbalanced distribution of the segmentation classes. This was done by Lisa Schneider in her master thesis and published as medMeshCNN [222].

MeshCNN and medMeshCNN label the edges of a surface mesh. Overall 94 surface meshes from the Aneursik dataset [9] and aneurysms from previous projects
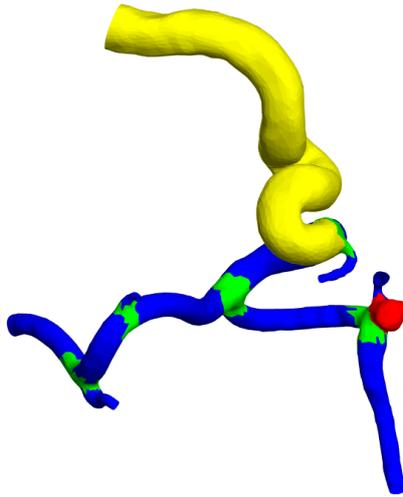
Figure 9.2: Segmentation of an intracranial aneurysm in inlet (yellow), vessels (blue), bifurcations (green) and aneurysm (red); edge segmentation mapped to faces

at the university were manually segmented with blender [226]. With a mean of 51.6% and 28.7%, vessel and inlet were the most common classes and bifurcation (11.6%) and aneurysm (8.2%) were the less common classes. 66 meshes were used for training; test and validation each used 14 meshes. The weights for the weighted cross-entropy loss function were 0.3 for aneurysm and bifurcation and 0.2 for inlet and vessel.

Deep learning can also be used to segment the vascular domain. The vascular domain is the area around the aneurysm (Fig. 9.3). Before a hemodynamic simulation is carried out, a mesh is often reduced to the vascular domain. The vascular domain is not well defined and more arbitrary than the part segmentation discussed above. Two deep learning approaches are compared for mesh segmentations of the vascular domain: MedMeshCNN and graph deep learning. Expert segmentation of 40 meshes for training and 10 meshes for testing were used.

For MedMeshCNN, edges in the region of interest are labeled one, and all other edges that should be removed from the mesh, as zero. The meshes were remeshed to have 19,200 faces. Table 9.1 shows the parameters used for MedMeshCNN. A suitable number of pooling layers and convolutional filter sizes was empirically determined. Based on these, further experiments regarding the variance in mesh size and the weighted loss function were carried out.

As an alternative to the edge-based MedMeshCNN approach, graph deep learning was tested. In this case, the segmentation into two classes is modeled as a node classification problem. Each node represents a vertex of the mesh and is labeled one or zero, like the edge labels for MedMeshCNN. The net consists of two graph layers and a linear layer for classification, as shown in Figure 9.4. The net is trained for 10 epochs with Adam optimizer and batch size 1.
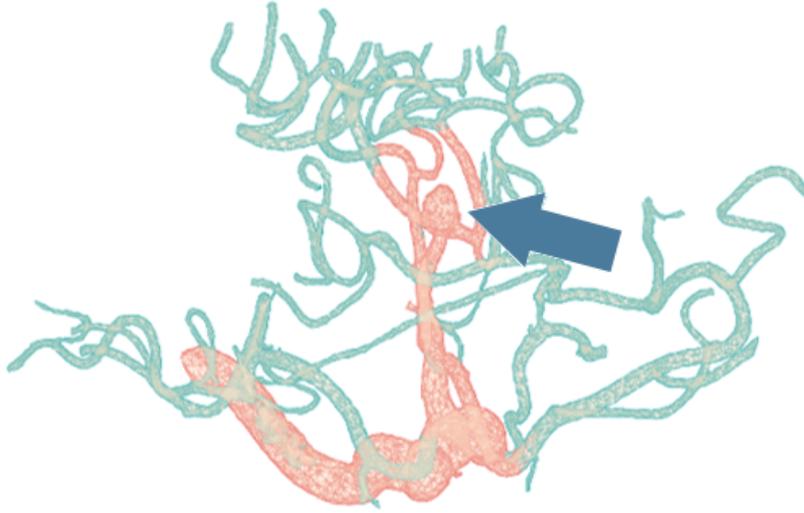
Figure 9.3: Example of initial 3D model containing an aneurysm (arrow) with surrounding vessels. The vascular domain that is of interest is depicted in red.

Table 9.1: Parameters for MedMeshCNN segmentation of the vascular domain

Parameters	
batch size	2
maximum input edges	30,000
convolution filters	16; 32; 64; 128; 256
pooling layers	25,000; 20,000; 10,000; 5,000
residual blocks	1
number of augmented meshes	20
learning rate policy	lambda
learning rate	0.001

For the graph deep learning approach, the meshes are not remeshed. The mesh is transformed to an undirected graph. Each vertex becomes a node and these are connected based on the edges defined by the faces of the mesh. To add spatial information to this graph representation, several node features are assigned to each node: the vertex normal, the edge length and the vertex angle (see Fig. 9.5). These features describe the position of a vertex in relation to the surrounding vertices. We also consider coordinates as features. While the features coordinates and vertex normal have a fixed length, the length of the number of face angles depends on the number of faces which include the vertex. We considered two options for this problem: padding with 0 to match the largest number of features or to average. This leads to 41 and 15 features per node, respectively. Two options for the edge weights of the graph are explored: a constant edge weight of one or the edge length.
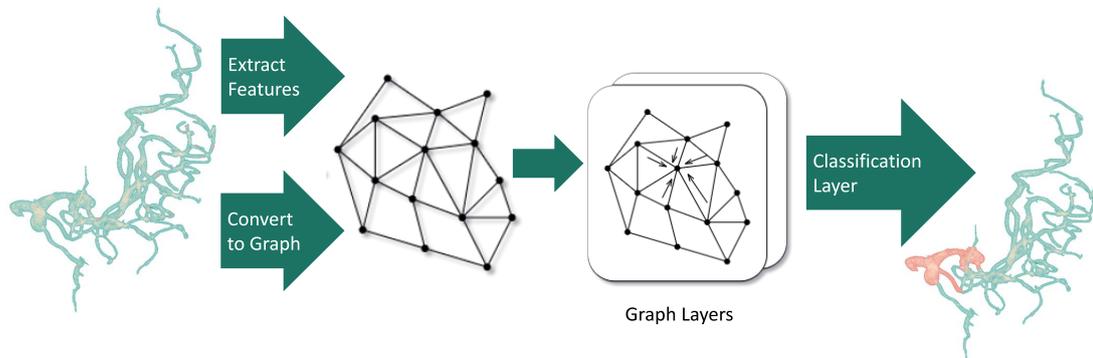
Figure 9.4: Graph deep learning architecture for mesh cutting
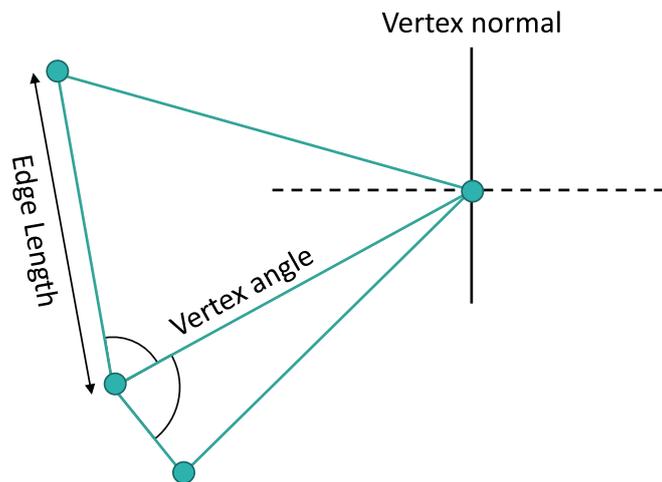
Figure 9.5: Node features used for graph deep learning

9.1.2 Outlet detection

Another step in mesh processing is the detection of outlets. For this, the first step is the extraction of feature edges. A feature edge is defined as an edge, which belongs to only one triangle, or an edge which belongs to more than two triangles, or an edge whose adjacent triangles have an angular deviation greater than theta [227]. Due to the preprocessing of the mesh for the segmentation algorithm, the second case (more than two triangles) should not occur. If the aneurysm mesh has open endings, the first case occurs at these endings. The last case occurs, if the aneurysm mesh is closed. A closed aneurysm mesh typically has an approximate 90 degree at the end, while at most other places the mesh is smoother and less sharp angles occur. Therefore, theta is set as 70 degree. While this identifies feature edges, which often represent the outlets, sometimes feature edges can occur at other places. To filter out the false-positive results, groups of close feature edges are analyzed. To describe an outlet, the feature edges have to describe a roughly circular structure and the included vertices should be approximately in one plane. For groups of edges, where these conditions are fullfilled, the corresponding vertices and faces are determined. The largest outlet of the mesh is defined as the inlet.

9.1.3 Centerline

The centerline is often used for further calculations. The centerline should not be alternated by or calculated inside the aneurysm. Here, the part segmentation helps to split the problem of centerline calculation into smaller problems. As the aneurysm is segmented, this part can be skipped during the centerline calculation. The centerline is only calculated inside the vessels. These have a tubular structure. Each vessel is handled separately. The centerline is calculated using vmtk and the seed points are automatically set based on an automatic outlet detection.

9.1.4 Aneurysm graph from part segmentation

Based on the part segmentation, a semantic graph representation of the aneurysm and the vessels is generated. The segmentation of the parts works on edges and returns a label for each edge. The segmentation does not further distinguish between two different vessels. This distinction is added after the segmentation. Each part is assigned a unique numeric label, where the hundreds digit represents the label given by mesh segmentation and further digits are used to create a unique identifier. For each vertex, the labels of the corresponding edges are analyzed. If different edge labels occur at the same vertex, these indicate a connection between the two parts. A graph reflecting the part connections is built.

The next step is analyzing the graph to gain more information about the relation between the different parts (see Fig. 9.7). Based on the number of bifurcations between a vessel and the aneurysm, each vessel is assigned a level. Vessels directly
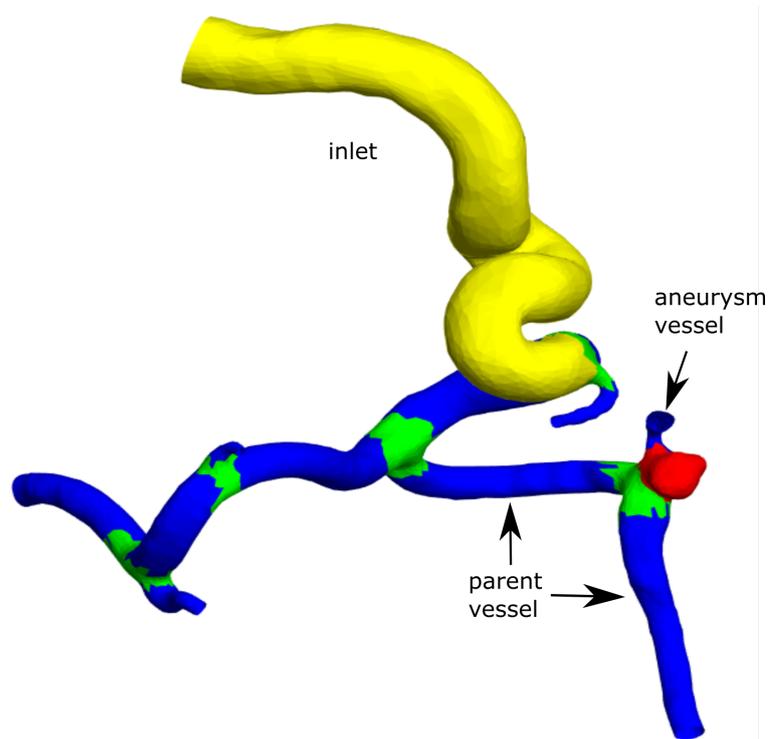
Figure 9.6: Segmented surface mesh; distinction between aneurysm vessel, parent vessel and other vessels is done in the semantic graph representation, as shown in Fig. 9.7

at the aneurysm are labeled aneurysm vessels. The bifurcation underneath the aneurysm is labeled as the aneurysm bifurcation. Parent vessels are vessels directly connected to the aneurysm bifurcation. This process automatically refines the segmentation labels and provides helpful information for further processing.

9.1.5 Aneurysm analysis

The results of mesh segmentation, centerline, outlet detection and semantic graph can be used in various applications. Some of these are discussed in the following.

While several approaches for parent vessel reconstruction exist, this segmentation offers the possibility to solely measure the parent vessel without relying on interpolated and approximated data.
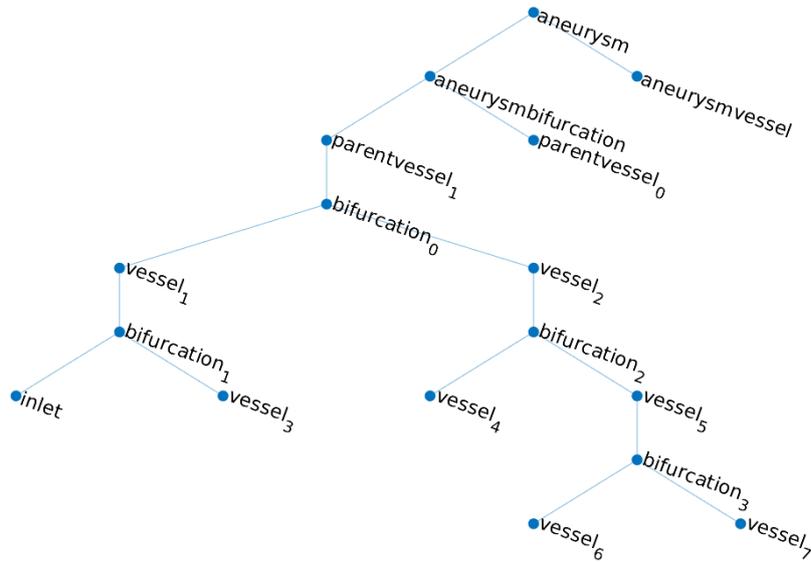
Figure 9.7: Abstract semantic representation as graph, corresponding aneurysm is shown in Fig. 9.6

Preprocessing for simulations

Hemodynamic simulation can provide valuable information for aneurysm rupture risk assessment. At the moment, the surface mesh is often manually processed to prepare for simulation, for example, cutting and inlet and outlet definition. Therefore, results may vary and the process is time-consuming. The presented segmentation and semantic graph can be a step towards scripted, automatic simulations.

Mesh cutting

Previously, deep learning to segment the vascular domain was described. Based on previous, manual, ambiguous segmentations, this area can be automatically segmented and used for simulation. The results depend on the training segmentations. Alternatively, the mesh segmentation into different parts could be used to segment a user-independent area around the aneurysms based on objective criteria.

For hemodynamic simulations, inlets and outlets are defined. The positions of these are crucial for the simulation results. To keep the conditions constant over several aneurysms and receive comparable results, a constant inlet and outlet definition is required. With the aneurysm graph, segmentation information about the vessel level is extracted. These can be used to decide on the included vessels around the aneurysms, for example only the parent vessel or all vessels up to a certain level. As the bifurcation areas are known, it is easily avoidable to cut those areas, as they might produce misleading outlets.

The distinction into near and far vessels by Cebral et al. [228] was based on the distance to the ostium. The presented segmentation indirectly includes the segmentation of the ostium as the edges between the aneurysm and the aneurysm bifurcation. Therefore, the provided segmentation can be used to automatically generate the classification described by Cebral et al. [228]. A major disadvantage of the solely distance-based method is the risk to get hemodynamic measures at bifurcations instead of vessels.

Morphological parameter

The segmentation into aneurysm and other parts is common in aneurysm analysis and preprocessing for morphological parameter calculation. Several semi-automatic and automatic algorithms for this task already exist. This normally only includes the aneurysm and the parent vessel. Here, the surrounding vessels are also included as vessel level-specific morphological parameters.

The presented segmentation allows a precise calculation of the parent vessel diameter. The area beneath the aneurysm is identified as the aneurysm bifurcation. As the aneurysm could change the diameter at that part of the parent vessel, this section is excluded from the parent vessel diameter calculation. The start and end of the parent vessel are defined by the bifurcations. This allows a uniform parent vessel evaluation and reliable comparison between parent vessels of different aneurysms. As parent vessel diameter either the average or the maximum diameter of the parent vessel can be measured.

9.1.6 Results and discussion

In this Section, the results of various mesh processing steps are presented and discussed. This includes various mesh segmentations, centerline detection, comparison of the presented aneurysm graph to other graphs and analysis of morphological parameters based on the graph.

Mesh segmentation

The segmentation was evaluated as the Intersection over Union (IoU). The segmentation varied between the classes, with only 37.0% for the bifurcation, 69.8% for the inlet, 71.4% for the aneurysm and 74.8% for the vessels.

Once the training is completed, the aneurysm segmentation can be performed automatically. Currently, the automatic segmentation for aneurysm meshes is focused on separating aneurysm and parent vessel. This segmentation is more advanced and allows for a complex and meaningful segmentation of the mesh.

Another automatic segmentation method is mesh segmentation based on convexity [156]. For aneurysms without blebs it can automatically segment the

aneurysm and several vessel parts. However, these parts are missing the semantic interpretation offered by the deep learning segmentation. Additionally, the deep learning segmentation is better in capturing the wide variation of aneurysm shapes, for example, aneurysms with blebs.
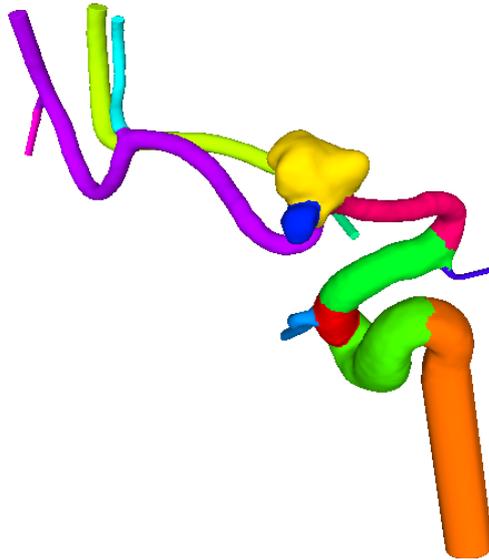
Figure 9.8: Aneurysm and bleb are separated by the automatic part segmentation of Kaick et al. [156]
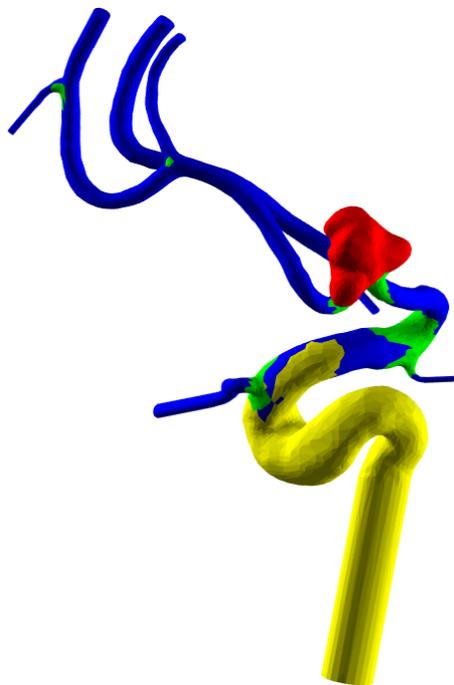
Figure 9.9: Result of deep learning mesh segmentation

The highest accuracy for segmentation of the vascular domain was 88%. Figure 9.10 shows an example of the MedMeshCNN prediction on a mesh from the
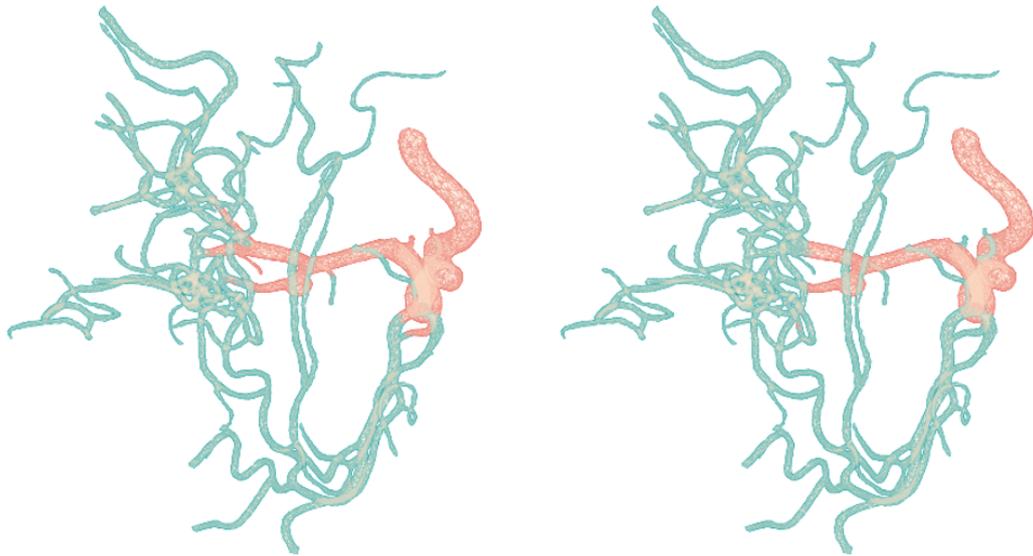
Figure 9.10: Prediction of MedMeshCNN (left) for the region of interest of the vascular domain compared to the labeled test data set (right). The same color-coding as in Fig. 9.11 is applied.

Table 9.2: Results of MedMeshCNN with different weights

weights	[0.4, 0.6]	[0.125, 0.125]
accuracy	86	88
IoU vessel	84	85
IoU vascular domain	59	61
Mean IoU	72	73

test data set. The neural net predicts a connected area around the aneurysm. In some cases, like shown in Figure 9.11, small vessels are not included in the segmentation.

As Table 9.2 shows, the results are only slightly impacted by changing the weights of the loss function. A larger impact could be observed based on the variance in the dataset. With a reduced dataset, where the number of vertices was between 24k and 36k compared to the whole dataset with 19k to 159k vertices before remeshing, an IoU of 0.81 was reached.

The graph neural network achieved an accuracy of 76%. However, there was a major problem with the class imbalance leading to an IoU of 76% for the vessel area and only 0.03% for the vascular domain. Visual inspections also confirmed that while a high accuracy was reached, the segmentation was insufficient (see Fig. 9.12).

The experiments showed that, despite reducing the information available from some vertices, using the average number instead of padding to accommodate nodes with a large number of adjacent faces did not change the accuracy. Adding the coordinates as node features also improved the results (see Table 9.3). As Table 9.4 shows that including the edge length as edge weights in the graph
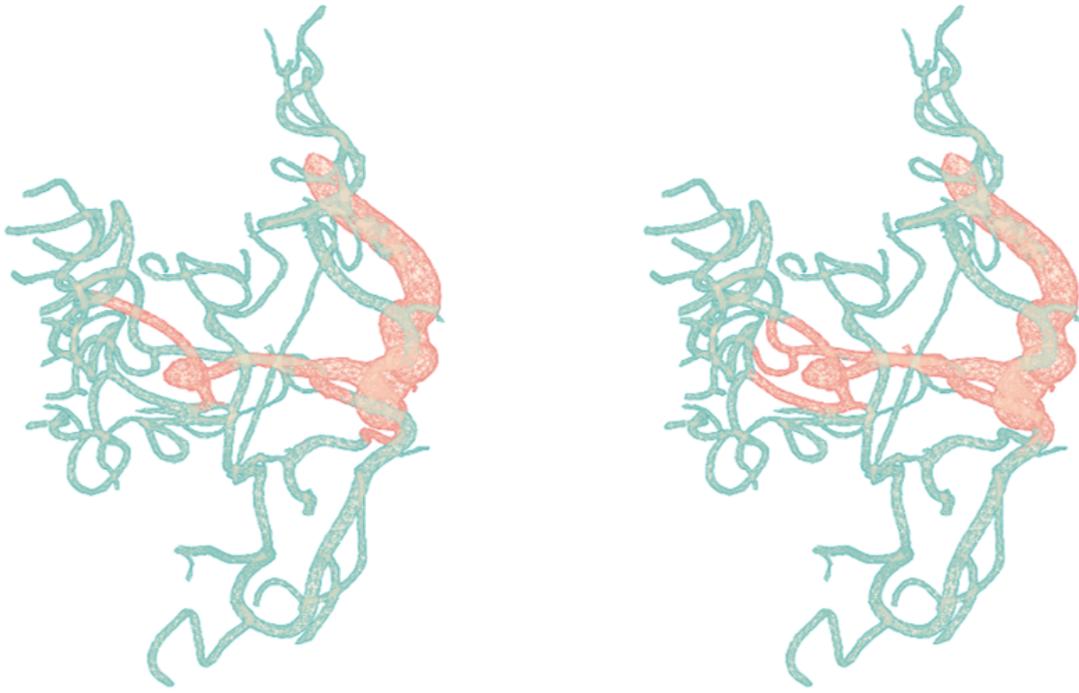
Figure 9.11: Prediction of MedMeshCNN (left) for the region of interest of the vascular domain compared to the labeled test data set (right). Some smaller branches are not segmented. The region of interest is color-coded in red, the whole vascular domain is color-coded in blue.

Table 9.3: Influence of coordinates as feature, padding to average

	without coordinates	with coordinates
accuracy	76	76
IoU vessels	76	76
IoU vascular domain	0.03	5
mean IoU	38	38

representation of the mesh does not improve the performance compared to a constant edge length of one.

Segmentation of the vascular domain is a complex and, as automatic solutions are unavailable, time-consuming task. The main difference between the mesh cutting presented here and previously described aneurysm mesh segmentation [222, 155] is the arbitrary character of the segmentation. While bifurcations and aneurysms are distinctive geometric properties of the mesh, the vascular domain is more complex to define. Vessels included in the vascular domain and vessels outside of the domain mainly differ in their position relative to the aneurysm, but not in shape. The vascular domain normally includes part of the vessel the aneurysm occurs at. The length of the included vessel area is not well defined and there is no change in the mesh itself marking the end of the vascular domain. It can be influenced by the distribution of other vessels along the parent vessel and near the aneurysm and the study goal. Especially for hemodynamic studies, where extrusion of the outlets is desired, cutting the vessel in a way to leave space for

Table 9.4: Influence of edge length as edge weight, padding to average, inclusion of coordinates

|	constant edge weight	edge length
accuracy	76	76
IoU vessels	76	76
IoU vascular domain	5	0.03
mean IoU	38	38
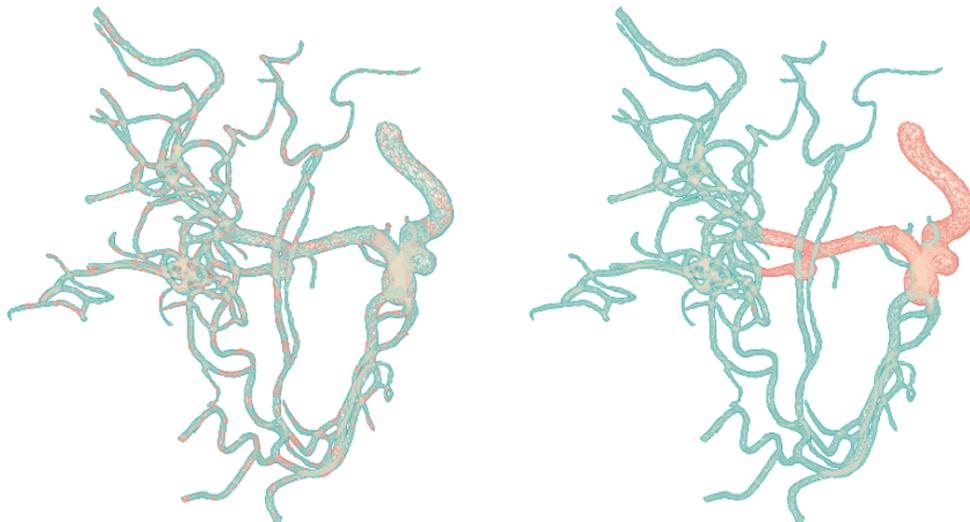
Figure 9.12: Prediction of mesh GNN (left) for the region of interest of the vascular domain compared to the labeled test data set (right). The same color-coding as in Fig. 9.11 is applied.

extrusion of the outlet can be challenging.

Due to the limited amount of data, the mesh cutting process cannot be reliably extended to all aneurysms yet. However, first experiments show promising results and suggest that automation might be possible once sufficient data is collected. Especially with MedMeshCNN the prediction of the vascular domain is possible. While graph deep learning did not yield as good results as MedMeshCNN, there are various design choices which are not tested yet. In the first experiments a lower number of features did not change the accuracy and a constant edge weight decreased the segmentation quality. Adding coordinates as node features did slightly improve the results. In the future, other node features might further improve the segmentation with graph deep learning. In the future, this could be further explored, for example by enhancing the coordinates with constant position and alignment of the mesh by positioning the aneurysm at the origin with the parent vessel along (for sideway aneurysms) or orthogonal (for bifurcation aneurysms) to the x-axis.

Comparison of graph representations

Graph representations of aneurysms have been used for simulations. We compare our semantic graph with other aneurysm graphs.
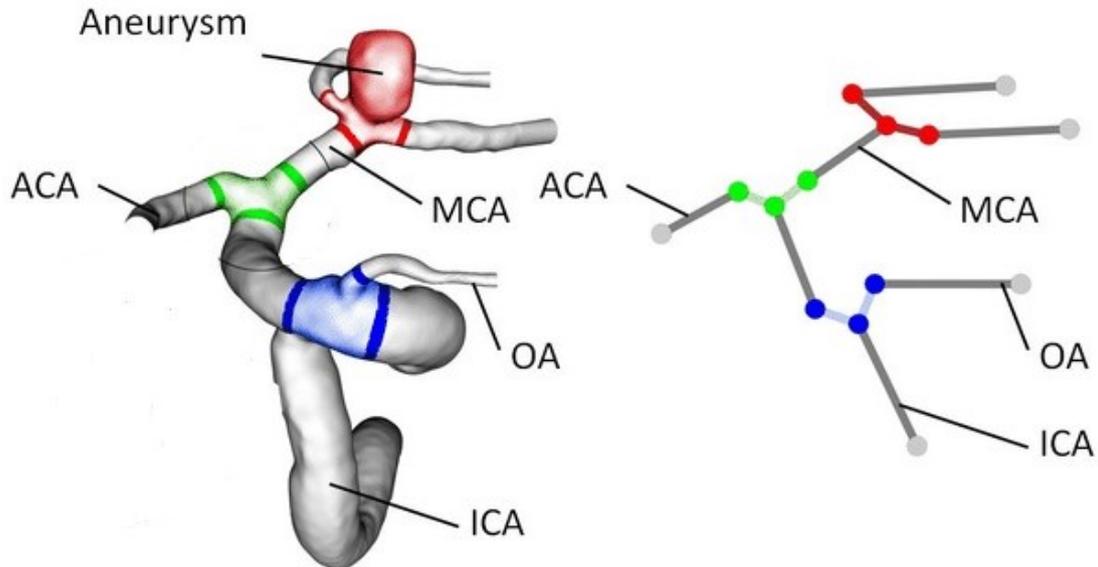
Figure 9.13: Aneurysm and corresponding graph from [175]

Chnafa et al. [175] introduced a graph representation of aneurysms for outflow rate estimation. The presented segmentation provides the necessary information for these abstractions. Unlike the aneurysm graph presented here, their graph splits each bifurcation into several parts. The presented segmentation could be refined to include this information.
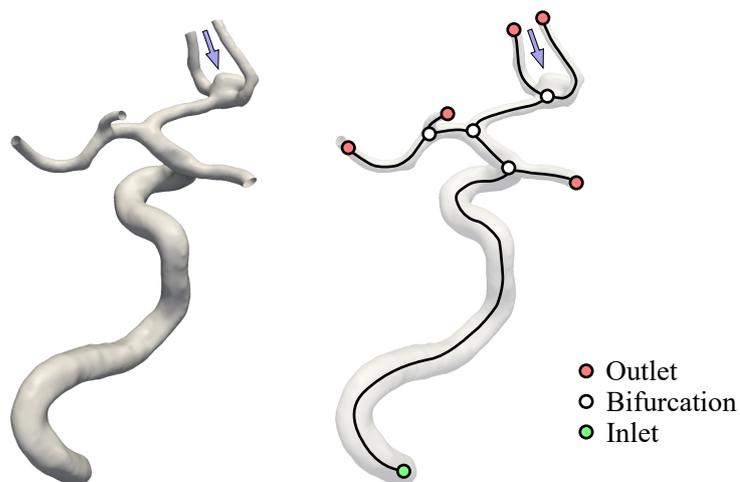
Figure 9.14: Aneurysm and corresponding graph from [176], red: outlet, green: inlet, white: bifurcation

Another graph was presented by Saalfeld et al. [176]. None of the graph representations shows the aneurysm itself. The semantic graph presented here does include the aneurysm.

Morphological parameter

In previous studies, the aneurysm location was an important factor in accessing aneurysm rupture (recall Section 2.1.2). This opens up the question why aneurysms at specific locations are more likely to rupture. The aneurysm location contains information about the local surrounding structures, for example, the diameter and curvature of the vessels leading to the aneurysm. This information can be extracted by using the previously presented part segmentation.

For five levels of vessel segments the number of vessels at this level, the average vessel length at this level and the average, minimum, maximum, and variance of radius, curvature, and torsion are calculated. All parameters are calculated based on the centerline. The radius is calculated as the radius of maximum inscribed spheres.
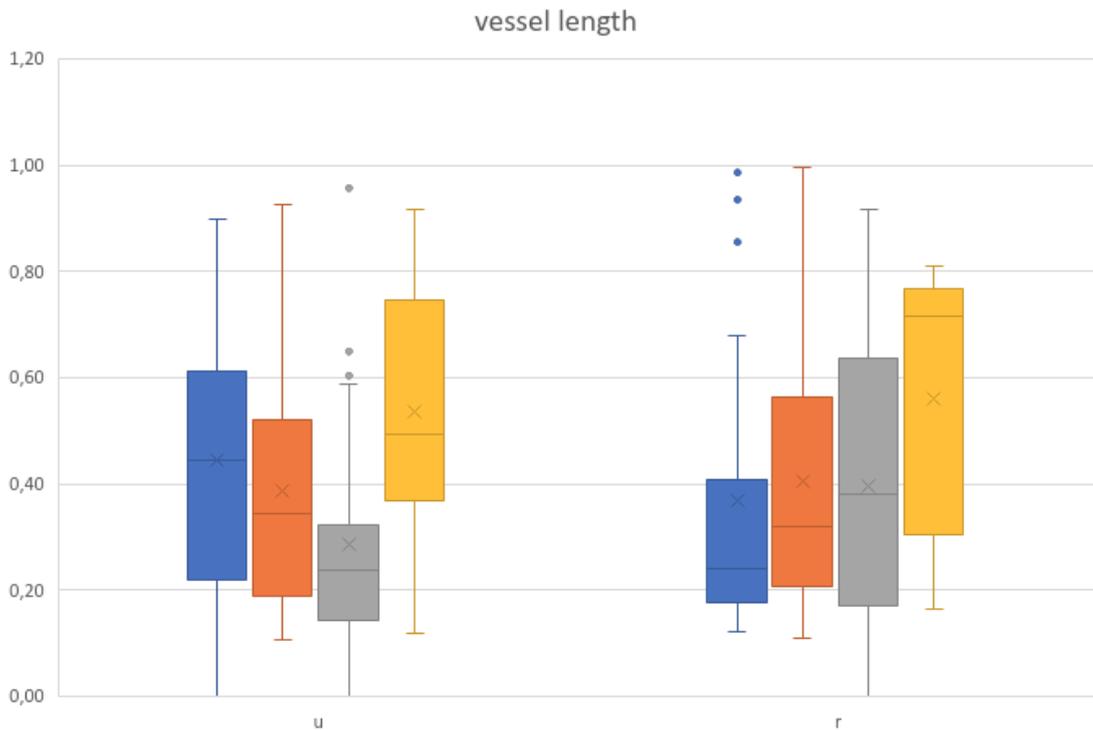
Figure 9.15: Average vessel length per vessel level
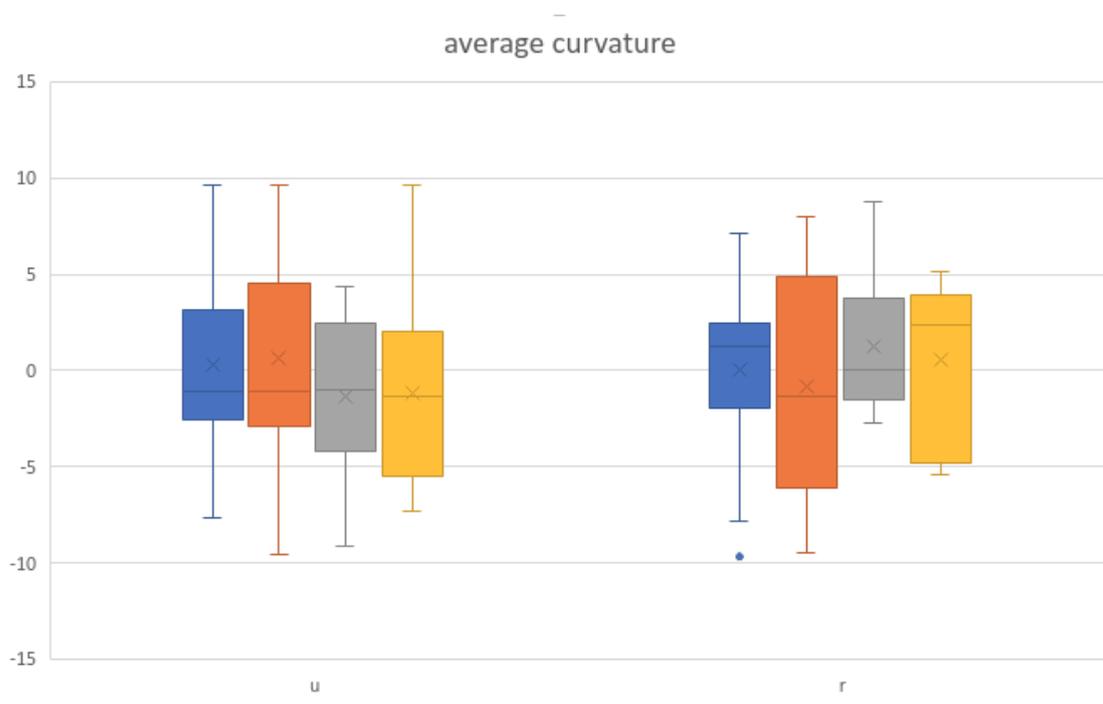
Figure 9.16: Average curvature per vessel level
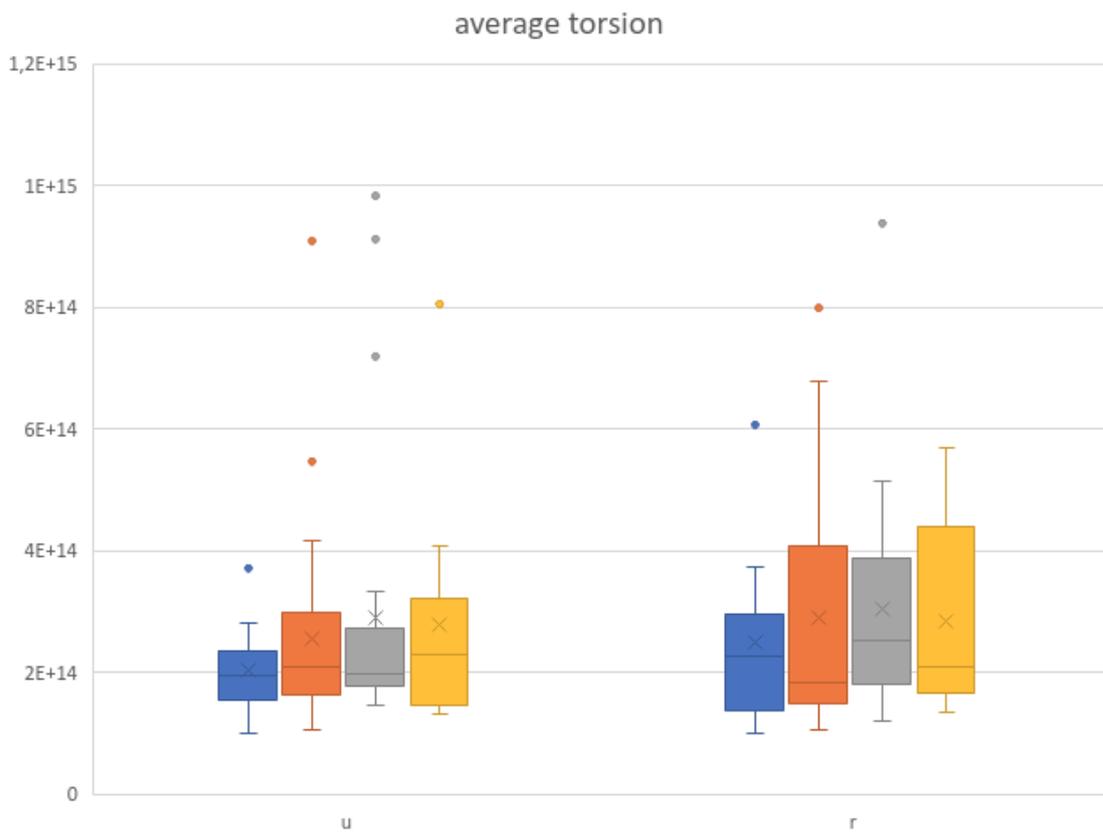
Figure 9.17: Average torsion per vessel level

Figure 9.18 shows the number of vessels occurring at each vessel level for ruptured and unruptured aneurysms. 23 ruptured and 30 unruptured aneurysms were used for this comparison. Up to five vessel levels were included. Not all aneurysm models included vessels up to level five. Ruptured aneurysms tend to have slightly more vessels at level two and three compared to unruptured aneurysms. As most of the meshes used in this study only have vessels up to level four, only the first four levels were included for further analysis.

The average torsion and curvature for all levels was slightly higher in ruptured aneurysms than in unruptured aneurysms (see Fig. 9.17 and Fig. 9.16). The average vessel length of the first two levels was higher in unruptured aneurysms.
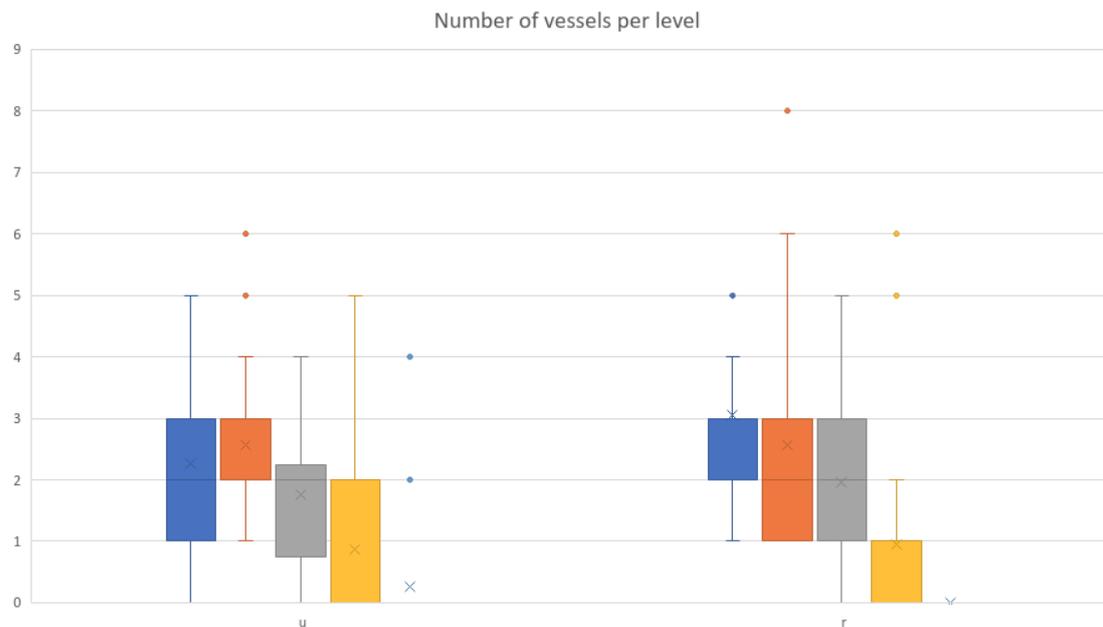
Figure 9.18: Number of vessels per level for ruptured and unruptured aneurysms

9.2 Deep learning wall shear stress prediction for artificial aneurysms

Hemodynamic simulations of the blood flow inside the aneurysm provide helpful information about several parameters, for example, wall shear stress. However, they are time-consuming and require expert knowledge. Therefore, they cannot be done directly in the clinic, but have to be outsourced instead. This process delays treatment decisions, and additional time is needed for second consultations after the results are returned to the doctor.

Table 9.5: Parameters of real world aneurysms that were characterized by a roundly shaped saccular aneurysm at the vessel bifurcation. Provided are min, max and average values (in degree and mm, respectively) for the parameters described in Fig. 9.19

	r_i	r_1	r_2	r_a	d	α	β
average	2.53	1.87	1.75	2.09	3.67	97.31	93.77
min	1.81	0.96	1.04	1.11	1.65	64.00	60.00
max	3.38	2.48	2.58	3.44	6.15	157.00	120.00
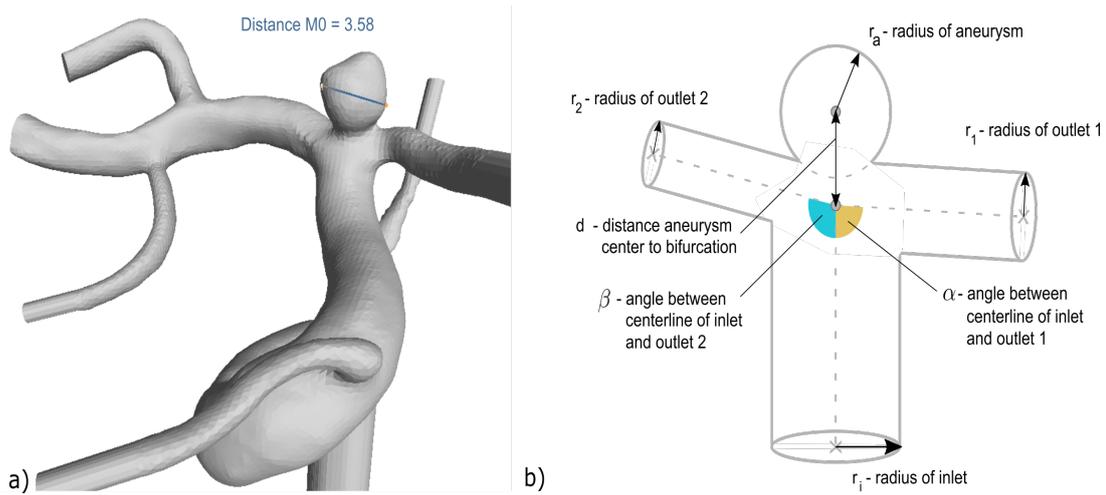
Figure 9.19: Overview of parameters for artificial aneurysm creation; a) example of reference aneurysm with measure of aneurysm diameter; b) concept of artificial aneurysm creation with seven parameters

9.2.1 Artificial aneurysm configuration

The simplified, artificial bifurcation aneurysms were created with CAD software by Philipp Berg. Each geometry consists of three cylinders, representing one inlet vessel and two outlets and a sphere for the saccular bifurcation aneurysm. The aneurysm creation has seven adjustable parameters (see Fig. 9.19): the radius of the inlet (r_i), the radius of the first outlet (r_1), the radius of the second outlet (r_2), the radius of the aneurysm (r_a), the distance between aneurysm center and bifurcation (d), the angle between the first outlet and the inlet (α), and the angle between the second outlet and the inlet (β). In order to extract realistic default values for these parameters, 200 patient-specific 3D aneurysm models from previous studies were analyzed. The cases which have a high agreement with the artificial configuration (i.e. spherical, saccular bifurcation aneurysm) were selected, yielding 13 reference cases. Their average, minimum and maximum values are shown in Table 1. The artificial aneurysms were created with randomly generated parameters in the same range of the values of the reference aneurysms.
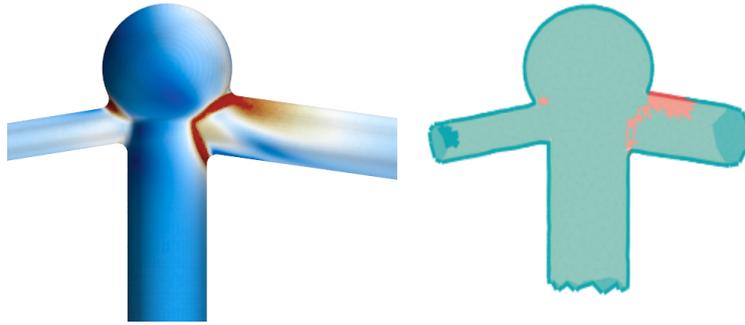
Figure 9.20: Depiction of the resulting WSS (left) and a corresponding ground truth segmentation for training (right).

9.2.2 Hemodynamic simulations

Hemodynamic simulations were performed by Samuel Voß in order to assess the WSS of the artificial aneurysm geometries. For this purpose, each flow domain, containing vessels and aneurysm, was spatially discretized into volumetric cells (1.2 to 2.4 million cells for each configuration depending on the domain size). Blood was modeled as incompressible and laminar fluid with a density of $1055\,\mathrm{kg/m^3}$ and dynamic viscosity of $0.004\,\mathrm{Pa\,s}$. Boundary conditions of the domain were modeled as follows: Constant velocity of $0.3\,\mathrm{m/s}$ as inflow into the parent artery, rigid vessel walls with no-slip condition, and zero-pressure assumption at the outlets. The total simulation time was $5\,\mathrm{s}$ (quasi-steady, time step of $0.01\,\mathrm{s}$) while only the time range of $[3\text{-}5]\,\mathrm{s}$ was used for temporally averaging the WSS field. In total, 145 artificial aneurysms were simulated with STAR-CCM+ 13.06 (Siemens PLM Software Inc., Plano, TX, USA). Finally, aneurysm surface and temporal averaged WSS magnitude values were exported for further analysis.

The aneurysm surfaces are remeshed using the ACVD algorithm [229] to obtain a similar number of edges. The deep learning approach requires one label per edge while the WSS magnitude values from the flow simulation were obtained at vertices. Thus, the edge labels are calculated as the average WSS of the associated vertices. Areas of high WSS are defined based on a reference value. This reference value is the median of the maximum WSS per aneurysm. Areas, where the WSS is larger than 0.4 times the reference value, are defined as areas of high WSS. An example is shown in Figure 9.20.

A deep learning mesh segmentation is trained using the medMeshCNN architecture [222]. For the first experiment, a small dataset consisting of 24 training meshes and 3 test meshes is used. The second experiment included 123 training and 10 test meshes. Due to problems in the feature calculation, the last experiment comprised 118 training and 9 test meshes.

Instead of transforming the mesh information to 2D, the algorithm directly works with 3D surface meshes. Deep learning segmentation is used to predict areas of high WSS. Further experiments included a variation of the edge features used. In experiments 3,4 and 5 Gaussian curvature [230] and in experiment 5 mesh

Table 9.6: Parameters of the experiments, where # denotes the experiment number, *GC* the Gaussian curvature and *MC* the mean Gaussian curvature.

#	training	test	additional features	pooling resolution	batch size	weighted loss
1	15	3	-	2500 2000 1500 1000 750	10	0.2 0.8
2	123	10	-	2500 2000 1500 1000 750	10	0.2 0.8
3	123	10	*GC*	2500 2000 1500 1000 750	10	0.2 0.8
4	123	10	*GC* & *MC*	2500 2000 1500 1000 750 500	5	0.01 0.99
5	118	9	*GC* & thickness	2500 2000 1500 1000 750 500	5	0.01 0.99
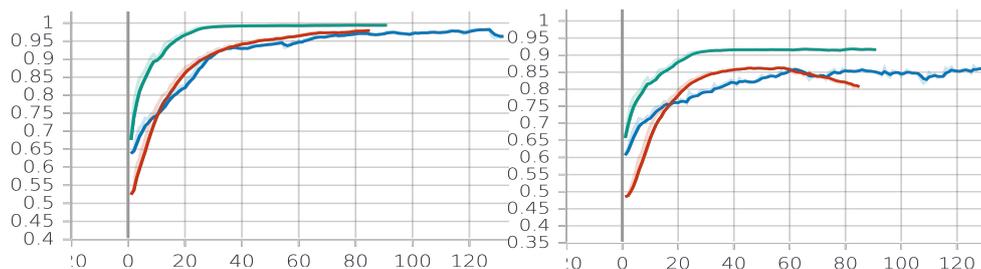
Figure 9.21: Training (left) and test (right) accuracy per epoch of experiment 2 (without additional features; red), experiment 3 (GC; green), experiment 4 (GC&MC; blue).

thickness [231] (defined as the diameter of the maximum inscribed sphere) are added to the feature calculation. Both features were first calculated for each vertex and then mapped to the corresponding edges. The parameters of each experiment are summarized in Table 9.6.

9.2.3 Results and discussion

The training accuracy of the first experiment was constantly increasing and approaching 100 %. However, the test accuracy was far worse (between 61 % and 68 %) and decreasing after 50 epochs.

Increasing the number of training meshes improved the test accuracy, as shown by the second experiment (see Fig. 9.21). Again, overfitting occurred and the test accuracy decreased after epoch 40. In Figure 9.22, the result for one of the test meshes is shown. The corresponding simulation result and ground truth are shown in Figure 9.20. While an accuracy of over 85 % is reached, the visual inspection shows some differences. Only a small part of the large WSS area is predicted by the net. But additional spots on the wall are falsely predicted.

For the third experiment, the Gaussian curvature was included as a feature. As visible in Figure 9.21, this leads to a test accuracy of over 91 %. Unfortunately, this accuracy was reached by labeling most edges as normal WSS, omitting the high WSS class.
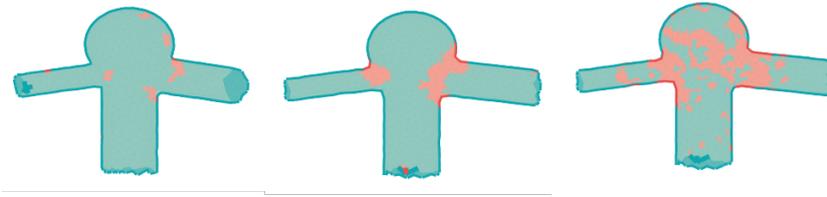
Figure 9.22: Result of experiment 2 (left), 4 (middle) and 5 (right).

To overcome the problem of the vanishing high WSS class, the weights of the loss function were adjusted. Experiment 4 additionally included the mean Gaussian curvature as a feature. Thus, an accuracy of 85% was reached (compare Fig. 9.21). Figure 9.22 shows the prediction of the net. Compared to experiment 2, there are fewer but larger predicted high WSS areas. The net from experiment 4 predicts a larger area as high WSS than the ground truth segmentation for the deep learning shows. Compared with the original simulation result, both areas of high WSS are segmented by the net. The high WSS in the larger vessel is not completely segmented.

In experiment 5, in addition to the curvature features, the mesh thickness was included. This did not improve the results. The test accuracy stayed below 80% and WSS areas were scattered over the whole mesh (see Fig. 9.22).

Prediction of high WSS areas with the trained net needed 43 seconds on average per mesh.

A major limitation is the used dataset. As seen in the first two experiments, increasing the number of training examples improves the test accuracy. Here, artificially created intracranial aneurysms were used. These shared the same basic geometry, a bifurcation aneurysm with a proximal parent and two distal outflow vessels. *medMeshCNN* is able to learn the geometry based on meshes and mesh features. While the geometries of the meshes are similar, the variance in the segmentation is higher. This might hinder the training and complicate generalization. Including the curvature and adjusting the weights of the loss function improves the results.

Another factor that needs further research is the choice of suitable thresholds for the generation of the segmentation ground truth data. In experiment 4, a larger high WSS area around the junction was predicted than shown in the ground truth. A modified threshold value (lower reference value) might result in a better agreement between ground truth segmentation, deep learning WSS prediction, and simulation results.

9.3 Deep learning wall shear stress prediction for patient-specific aneurysms

In further experiments the WSS prediction was applied to patient-specific aneurysm geometries.

Compared to deep learning on meshes, deep learning on point clouds is slightly better established and used more often. It also has been used successfully used in deep learning WSS prediction (see also 4.2.1). For the deep learning WSS prediction on patient-specific geometries the KPConv-Net [162] architecture was used. As with the previous MedMeshCNN, additional features are included. Here, curvature, FFPH [232] and SHOT [233] are used as additional features.

9.3.1 Data collection and preprocessing

In a shared data base of the Computer Science Faculty and the Laboratory of Fluid Dynamics and Technical Flows from the Otto-von-Guericke University Magdeburg and the STIMULATE Research Campus results of several projects for aneurysm research were collected retrospectively from 2010 to 2021. From these databases 118 meshes showing 130 aneurysms were collected for the WSS prediction.

In contrast to the previous study on artificial aneurysms, parameter choices and boundary conditions for the hemodynamic simulations are not constant, as the simulation data was collected retrospectively from several studies. We assume that all considered simulations meet the current standard of hemodynamic aneurysm research and that the patient-specific WSS is representative. 12 outliers were removed based on mesh quality and unusual WSS values. The number of vertices varies between the meshes in a range from 20k to over 140k.

To prepare the simulation data for deep learning, extensive preprocessing is necessary. The first step is loading the simulation result and exporting the surface mesh and the WSS values in a format suitable for further processing. This is done using Paraview [234]. In the next step, Meshlab [211] is used for mesh simplification and removing non-manifold faces. Additional parameters are calculated in Python. The pipeline is shown in Fig. 9.23.

9.3.2 Deep learning segmentation

The neural net was trained with 80 point clouds of aneurysms, 25 were used for validation and 13 for testing. The experiments cover a variation of the neural net parameters (learning rate, gradient descent, sampling values) and of preprocessing variables (number of classes, scaling, class division; see Tab. 9.7).

As additional features Gaussian curvature, FFPH and SHOT were used. FFPH and SHOT were calculated solely on the vertices of the mesh. To limit the size of each dataset, principal component analysis (PCA) [236] is applied to FFPH and SHOT separately to reduce the number of features to 2 and 3, respectively.
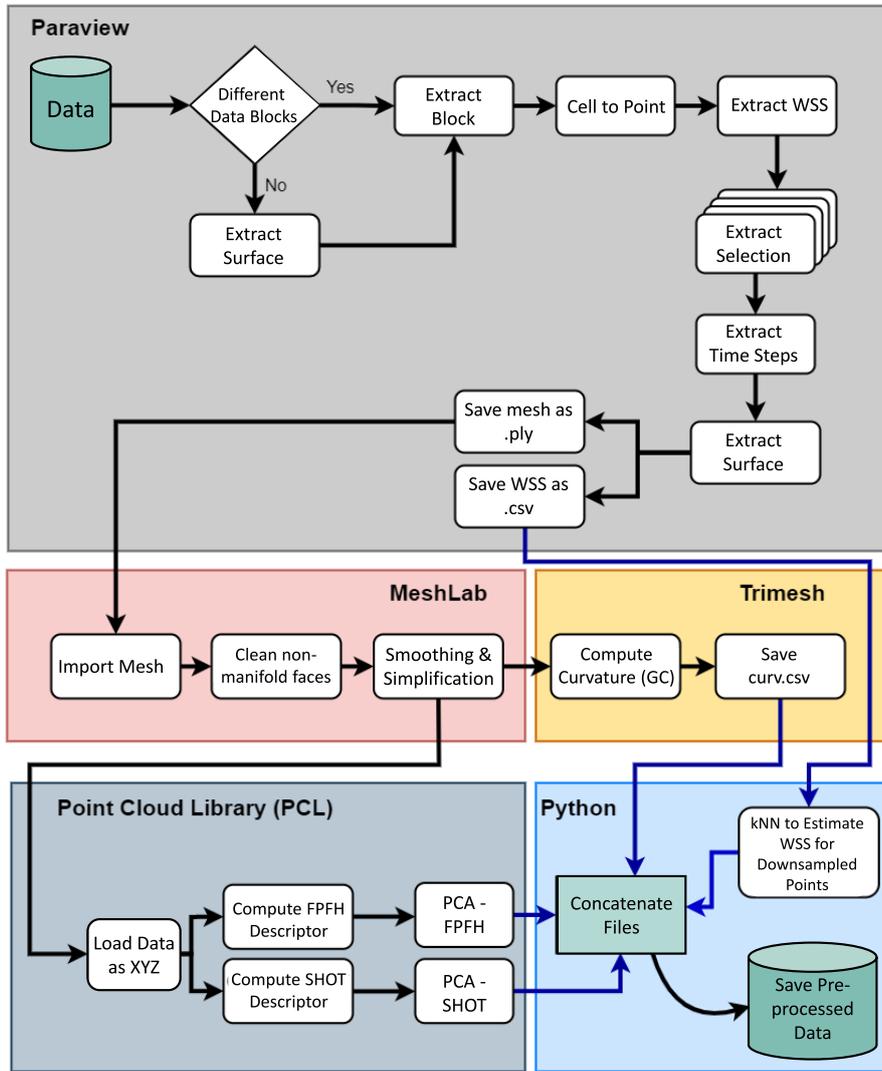
Figure 9.23: Preprocessing pipeline to prepare simulation data for deep learning [235]

9.3.3 Results and discussion

The results are shown in Table 9.8. The WSS prediction on patient-specific geometries reached an accuracy of 90.80% and an mIoU of 39.02.

Several parameters affect the deep learning. The subsampling rate, which describes the number of sampling points that are fed into the network, has an impact on the run time. A subsampling rate of 0.02 was faster and achieved a better overall accuracy compared to a subsampling rate of 0.005 (20-25 seconds/ 130-140 seconds per epoch).

A learning rate of 0.001 was slightly better than a learning rate of 0.01. A learning rate of 0.1 was unsuitable and the loss curve was volatile.

The two classes used for the artificial aneurysms severely limits the information of the WSS distribution. Here, we explored deep learning segmentation into 3, 5 and 7 classes. The number of classes and the thresholds used for

Table 9.7: Experiments for deep learning WSS prediction; *manually set values; M: mean curvature, G: Gaussian curvature, F: FPFH descriptor, S: SHOT descriptor

ID	features	classes	weights	scaling	class division
1	M	5	0.08, 0.08, 0.11, 0.20, 0.51	Local	[0, 0.2, 0.4, 0.6, 0.8, 1]
2	MG	5	0.08, 0.08, 0.11, 0.20, 0.51	Local	[0, 0.2, 0.4, 0.6, 0.8, 1]
3	MGFS	5	0.04, 0.06, 0.12, 0.25, 0.52	Local	[0, 0.2, 0.4, 0.6, 0.8, 1]
4	MGF	3	0.11, 0.18, 0.71	Local	[0, 0.33, 0.66 ,1]
5	MGF	3	0.10, 0.10, 0.80*	Local	[0, 0.33, 0.66 ,1]
6	MGF	3	0.32, 0.21, 0.47	Global	[0, 0.02, 0.12, 1]*
7	MGF	3	0.36, 0.26, 0.38	Global	[0, 0.02, 0.12, 1]*
8	MGF	3	0.10, 0.10, 0.80*	Global	[0, 0.02, 0.12, 1]*
9	MGF	3	0.01, 0.01, 0.98*	Global	[0, 0.02, 0.12, 1]*

Table 9.8: Results of deep learning WSS prediction

ID	train acc	val acc	test mIoU	train mIoU	val mIoU	test mIoU
1	81.00	73.76	65.67	48.10	31.20	24.07
2	80.50	75.21	67.96	44.40	31.50	26.09
3	81.40	71.69	63.35	48.40	27.69	23.41
4	**89.80**	**82.15**	**81.25**	**62.00**	**40.89**	**39.02**
5	**90.80**	**84.49**	**82.33**	**55.10**	**42.65**	**36.26**
6	81.20	66.16	53.58	66.70	46.94	30.20
7	81.20	60.88	55.90	69.00	43.29	36.69
8	69.70	57.76	54.43	52.20	40.80	36.83
9	52.20	40.91	39.53	30.90	24.13	23.30

the WSS class influence the imbalance between classes and the variation within classes. In these experiments, the accuracy decreased with a higher number of classes. For 3 classes an accuracy over 80% was feasible, for 5 classes the accuracy was between 60% and 80% and for 7 classes the accuracy stayed below 60%.

Different scalings were tested for 3 and 5 classes. Global scaling of the WSS over all datasets and local scaling for each dataset to [0,1] was compared. Equal class division (for example ≤0.33, between 0.33 and 0.66,>0.66 for three classes) and customized unequal class division was compared. Global scaling with equal class division was unsuitable, as it resulted in a skewed distribution where over 80% of the points were in the lowest WSS class. While local scaling achieved the best results in terms of accuracy and IoU, visual inspection favors global scaling with unequal class distribution (see Fig. 9.24).

While additional features were necessary for WSS prediction with MedMeshCNN, here only a small improvement was observed. Adding FPFH and SHOT together with mean curvature as feature to the point cloud resulted in an improvement of 5% mean IoU after 100 epochs.

Here, the WSS prediction was reduced to a segmentation of different WSS classes.
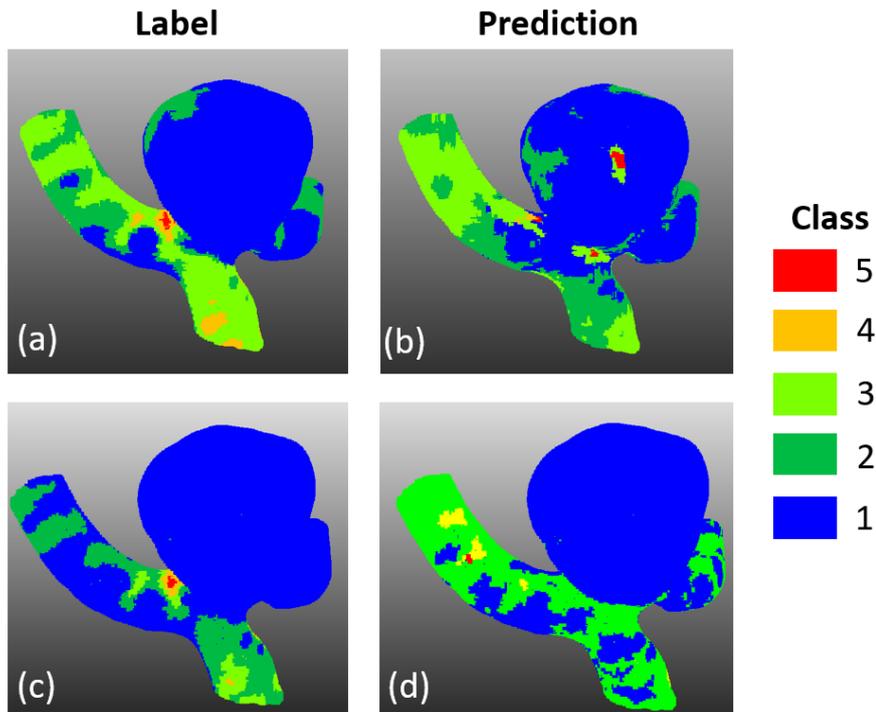
Figure 9.24: Comparison of labeled data (left) and prediction (right) for five classes and global unequal scaling (top row) and five classes with local scaling (bottom row).

This is sufficient to quickly identify regions of high or low WSS, for example in a clinical setting. For other use cases where more detailed and concrete values are needed, this is unsuitable. In this case, prediction of values, for example with deep learning regression, might be better.

While for our experiments a lower number of classes achieved better results, only a limited number of possibilities was tested. It is possible that a higher number of classes and different thresholds could lead to less variance within a class and therefore be easier to learn.

Current technical limitations restrict the size of data suitable for deep learning. Here, downsampling is used to reduce the point cloud and PCA to focus on the most relevant features. Both steps also omit some information.

Section 9.2 and Section 9.3 showed that fast prediction of wall shear stress with geometric deep learning is possible. While refinement of the described approaches and extension to other hemodynamic parameters is still needed, in the future this could be used to include hemodynamic parameters into clinical routines. Further research in the area of geometric deep learning for hemodynamic parameters also requires sufficient ground truth data. For this and other hemodynamic research, further automation of the mesh processing, as described in 9.1, could be an advantage.
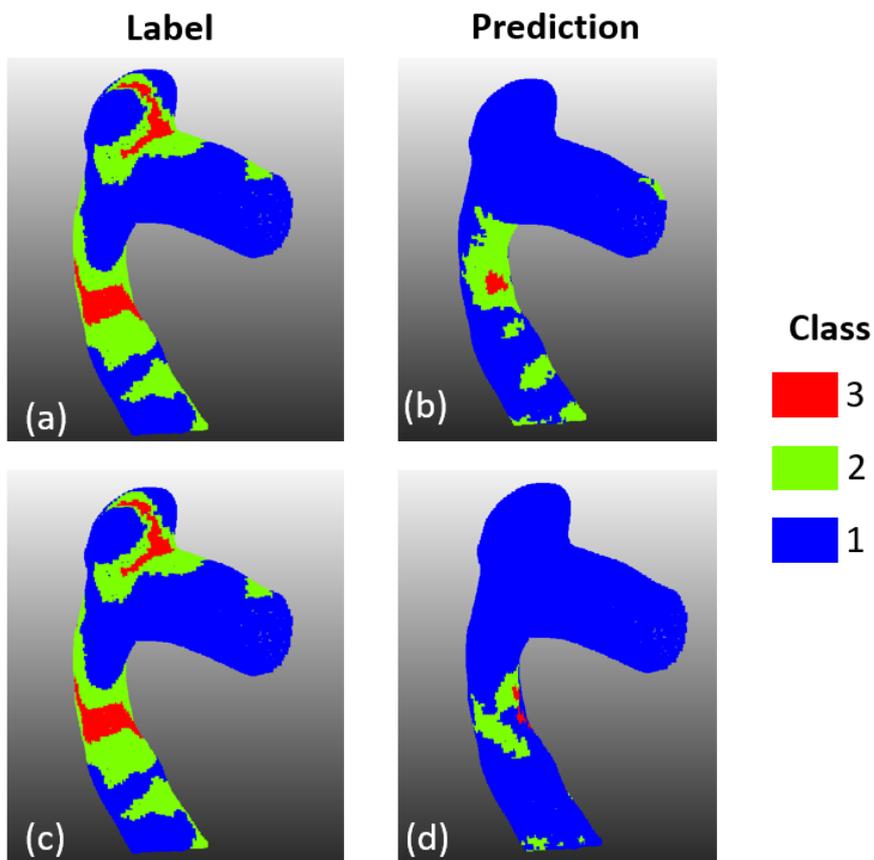
Figure 9.25: Comparison of labeled data (left) and (right) from experiment 4 (top row) and experiment 5 (bottom row).

10 New insights into the intracranial aneurysm wall

In this thesis, several tools for the analysis of the intracranial aneurysm wall were developed. The results were presented in several papers [208, 212, 203, 204, 237, 222, 238].

10.1 Answers to previously derived research questions

Here, short answers to the questions asked in Chapter 5 are given. Questions 1-3 aim at an improved understanding of the aneurysm wall and the processes occurring in the wall during aneurysm formation. Several tools to provide a new view and a new way to explore the wall are presented. Questions 4 and 5 ask for ideas that allow for an inclusion of wall information (like wall enhancement and wall shear stress) into clinical routine in the future.

1) How can a 3D model of the intracranial aneurysm wall be derived from 2D histologic image data?
A 3D model can be generated by segmenting the images, deriving point clouds of different tissue types and generating 3D models from sparse point clouds (Sec. 6, [203, 204]). The large gaps between slides and the deformation during tissue collection and image generation are major challenges for 3D model generation. A virtual inflation (Sec. 6.3 and Sec. 7.3) can be used to reduce this.

> **a) How to generate a mesh from a point cloud if the points are unevenly distributed?**
> Due to the unique properties of histologic images unusual point clouds occur and commonly available mesh generation algorithms fail. This can be addressed by an algorithm which models the behavior of a shrinking tube and is iteratively fitted to the points to generate a smooth mesh (Sec. 6.4.1,[212]).

b) Which segmentation approach is suited to support the analysis of histologic images of intracranial aneurysms?

Several different tissue types are found inside the aneurysm wall. In Section 6.2.3, ten classes (inflammatory cells, myointimal hyperplasia, degenerated wall, decellularized wall, red thrombus, white thrombus, organizing thrombus, mixed textures, intact wall) are defined. These can be segmented with deep learning. The inside of the aneurysm wall is highly heterogeneous [204, 208]. After analyzing three different approaches, deep learning segmentation is most promising for the generation of 3D models with semantic information of the aneurysm wall. However, it is restricted to known tissue types and adequate training data is challenging to collect (Sec. 6.2).

2) How can deformation during tissue collection be handled?

Tissue collection for further imaging like histology or microCT leads to deformation of the tissue. In Section 6.3, a virtual inflation for 2D histologic images is applied. Section 7.3 describes a virtual inflation in 3D based on preoperative imaging [204, 239].

3) How can various 2D and 3D information be combined for exploration of the aneurysm wall?

Preoperative imaging, hemodynamic simulation, microCT and histologic images provide a wide variation of information. In Section 7, a pipeline to combine these is described. This includes stain classification, guided user interaction to match histology and microCT, mapping between histologic images and microCT images and virtual inflation. The information are combined in a visual exploration tool [240].

4) How can the aneurysm wall be included in rupture prediction?

With black blood MRI some wall parts can be visible. These have to be objectively evaluated to study the correlation between wall enhancement and aneurysm rupture. Another aspect of rupture prediction is the aneurysm shape.

a) How can wall enhancement be segmented?

For an objective analysis of wall enhancement in black blood MRI a semi-automatic segmentation tool, which evaluates the enhancement based on the pituitary stalk intensity, was developed (Sec. 8.2, [238]).

b) How can the aneurysm shape be used for rupture prediction?

Aneurysm rupture prediction for clinical routine should have a minimum user effort, be fast and trusted by doctors and patients. Here, deep learning-based approaches with minimum user effort were presented. For analysis of the vessels around the aneurysm, the first step is a mesh deep learning segmentation. For this, MeshCNN was extended to work with complex and large medical data. After segmentation into aneurysm, vessels and bifurcations, an aneurysm graph is generated. Based on the additional information

of the graph, analysis of the surrounding vessels was carried out (Sec. 9.1.5, [239]). Based on this segmentation and graph, parameters describing the vessels around the aneurysm were derived. Vessels near a ruptured aneurysm showed a slightly higher average torsion and curvature than unruptured aneurysms (Sec. 9.1.6, [239]). Instead of using manually defined features, deep learning could be used to capture the aneurysm shape. Geometric deep learning is able to capture the aneurysm shape and predict aneurysm rupture. A user interface was able to explain the deep learning prediction to medical experts (Sec. 8.3.1, [241]).

5) How can wall shear stress be included in rupture prediction?
Two parts are included here: the improvement of preprocessing data for simulation and the inclusion of WSS in clinical routine.

a) How can mesh processing be improved?
The mesh processing can be improved by automating steps and reducing the required user interaction. A variety of often manual and time-consuming processing steps is necessary to produce meshes suitable for hemodynamic simulation and WSS calculation. This includes mesh segmentation, outlet detection and centerline calculation (Sec. 9.1, [242]).

b) How can wall shear stress be used in clinical routine?
Hemodynamic simulations require expert knowledge and take a lot of time. Both factors make them unpractical in clinics. Deep learning on point clouds or meshes could be used to predict WSS in a very short time without expert input. This was shown on artificial aneurysms (Sec. 9.2, [237]) and patient-specific aneurysm models (Sec. 9.3.2, [243]).

10.2 Future work

In the future, the presented work should be extended and the presented algorithm should be applied to more data. Insight into the aneurysm wall is a crucial factor for understanding the processes of aneurysm formation and development. In the future, this could lead to new treatment options, for example if part of the process could be stopped with medication. Histologic images provide the most detailed view of the wall. Here, a 3D model based on these images was constructed. This could be further enhanced if images with a smaller gap between them are collected. As the tissue has to be removed, histologic images from aneurysms can only show the aneurysm wall at that moment. It is not possible to observe the aneurysm wall at several time steps. To understand how the healthy vessel wall is remodeled and an aneurysm occurs, images and 3D models from various patients are needed. In the future, the presented approach could be used to reconstruct more 3D models showing the aneurysm wall from various patients.

As described in Section 2.2.4, more image modalities showing various aspects of vessel walls have been developed. Similar to the pipeline in Chapter 7, a combination of various image modalities could generate new insights into the aneurysm wall. The proposed pipeline might be extended with additional images, for example OCT. Additionally, the deformation occurring during tissue collection has to be tested. Currently, this is hindered by the limitation of preoperative imaging of the wall.

In the future, BBMRI could be commonly used in clinical routine. Based on the presented tool, further evaluation on rupture prediction and wall enhancement should be carried out. Especially the segmentation into five wall enhancement classes with varying intensity opens up new possibilities. In the future, the segmentation could be further enhanced, for example with an automatic deep learning aneurysm segmentation. It could be extended for other applications, for example arteriovenous malformations.

Further research on geometric deep learning for aneurysm meshes is needed. In the future, deep learning could be included in the clinical routine to predict aneurysm rupture. This requires a suitable database and visualization of the results for doctors and patients. Besides the shape of the geometric deep learning prediction presented in this work, other factors like patient attributes (for example age and risk factors like smoking or hypertension) should also be included. Additionally, hemodynamic parameters could be included in clinical routine in the future. For research, further automation of the mesh processing with geometric deep learning could simplify hemodynamic aneurysm research. For use in a clinical setting, more advanced deep learning predictions of hemodynamic parameters are necessary. This includes deep learning prediction for non-scalar parameters, parameters inside the aneurysm and prediction with respect to patient-specific blood flow conditions.

Abbreviations

AGD	**average geodesic distance**
ASL	**arterial spin labeling**
$aSMA$	**alpha-smooth muscle actin**
AUC	**(area under the curve**
$(A)WE$	**(aneurysm) wall enhancement**
$BBMRI$	**black blood MRI**
$BRAT$	**Barrow ruptured aneurysm trial**
CAD	**computer-aided design**
CFD	**computational fluid dynamics**
CH	**convex hull**
CNN	**convolutional neural network**
CSF	**cerebrospinal fluid**
CT	**computed tomography**
CTA	**computed tomography angiography**
$DANTE$	**delay alternating with nutation for tailored excitation**
DL	**deep learning**
DNA	**deoxyribonucleic acid**
DSA	**digital subtraction angiography**
ECG	**electrocardiography**
$FFPH$	**fast point feature histogram**
FSE	**fast spin echo**
GNN	**graph neural network**
GC	**Gaussian curvature**
$H\&E$	**Hematoxylin and Eosin**
IA	**intracranial aneurysm**
$(IA)DSA$	**(intra-aortic) digital subtraction angiography**
$iMSDE$	**improved motion-sensitized driven equilibrium**
IoU	**intersection over union**
IR	**inversion recovery**
$ISUIA$	**international study of unruptured aneurysms**
IVH	**intraventricular hemorrhage**
$IVUS$	**intravascular ultrasound**

KPConv	**kernel point convolution**
MC	**mean Gaussian curvature**
MCA	**middle cerebral artery**
MeshCNN	**mesh convolutional neural network**
MH	**myointimal hyperplasia**
MRI	**magnetic resonance imaging**
MRA	**magnetic resonance angiography**
mRS	**modified Rankin Scale**
MSDE	**motion-sensitized driven equilibrium**
MT	**Masson's Trichrome**
OCT	**optical coherence tomography**
Oro	**Oil red O**
OT	**organizing thrombus**
PC	**phase contrast**
PCA	**principal component analysis**
PHASES	**population, hypertension, age, size of aneurysm, earlier subarachnoid hemorrhage, site of aneurysm**
RIA	**ruptured intracranial aneurysm**
RT	**red thrombus**
SAH	**subarachnoid hemorrhage**
SDF	**shape diameter function**
SHOT	**signature of histogram orientations**
SI	**signal intensity**
SVM	**support vector machine**
SPACE	**sampling perfection with application-optimized contrasts using different flip angle evolution**
SPAMM	**spatial modulation of magnetization method**
SSFP	**steady-state free precession**
SWI	**susceptibility-weighted imaging**
TOF	**time-of-flight**
TSE	**turbo spin-echo**
UIA	**unruptured intracranial aneurysm**
UIATS	**unruptured intracranial aneurysm treatment score**
VISTA	**volume isotropic spin-echo acquisition**
vmtk	**vascular modeling toolkit**
VOI	**volume of interest**
VSI	**volumetric shape image**
VWMRI	**vessel wall MRI**
WEI	**wall enhancement index**
WSS	**wall shear stress**

Bibliography

[1] L. M. Kadasi, W. C. Dent, and A. M. Malek, "Cerebral aneurysm wall thickness analysis using intraoperative microscopy: effect of size and gender on thin translucent regions," *Journal of NeuroInterventional Surgery*, vol. 5, no. 3, pp. 201–206, 2013.

[2] H. U. Chengazi and A. A. Bhatt, "Pathology of the carotid space," *Insights into Imaging*, vol. 10, feb 2019.

[3] M. Neugebauer, V. Diehl, M. Skalej, and B. Preim, "Geometric reconstruction of the ostium of cerebral aneurysms," in *Vision, Modeling and Visualization*, pp. 307–314, The Eurographics Association, 2010.

[4] I. Wanke and A. Dörfler, *Intracranial Vascular Malformations and Aneurysms.* Springer Berlin Heidelberg, 2008.

[5] "aneurisme." https://sml.snl.no/aneurisme. Accessed: 2022-08-15.

[6] A. W. Keedy, "An overview of intracranial aneurysms," *McGill Journal of Medicine*, vol. 9, pp. 141 – 146, 2006.

[7] N. Ajiboye, N. Chalouhi, R. M. Starke, M. Zanaty, and R. Bell, "Unruptured Cerebral Aneurysms: Evaluation and Management," *The Scientific World Journal*, vol. 2015, pp. 945–955, 2015.

[8] G. Yong-Zhong, H. August, and M. v. Alphen, "Pathogenesis and histopathology of saccular aneurysms: review of the literature," *Neurological Research*, vol. 12, no. 4, pp. 249–255, 1990.

[9] Aneurisk-Team, "Aneuriskweb project website." http://ecm2.mathcs. emory.edu/aneuriskweb. Accessed: 2022-05-01.

[10] Z. Zhang, X. Mu, and X. Zhou, "Dexmedetomidine alleviates inflammatory response and oxidative stress injury of vascular smooth muscle cell via α2ar/PI3k/AKT pathway in intracranial aneurysm," 2022. preprint, Accessed: 2022-06-02.

[11] J. Morgan, D. Kudo, H. Sato, J. Ai, M. Lawton, and T. N. Hashimoto, "Abstract 112: Roles of platelets in aneurysm formation and rupture," *Stroke*, vol. 53, p. 112, 2022.

[12] M. Korostynski, R. Morga, M. Piechota, D. Hoinkis, S. Golda, T. Dziedzic, A. Slowik, M. Moskala, and J. Pera, "Inflammatory responses induced by the rupture of intracranial aneurysms are modulated by mirnas," *Molecular Neurobiology*, vol. 57, p. 988–996, 2020.

[13] N. Rajagopal, Y. Yamada, A. Balaji, T. Kawase, and Y. Kato, "Rare cases of multiple unruptured intracranial aneurysms: Illustrative report and review on management options," *Interdisciplinary Neurosurgery*, vol. 18, pp. 100–114, 2019.

[14] T. F. Dinger, M. D. Oppong, C. Park, M. Said, M. Chihi, L. Rauschenbach, O. Gembruch, C. Deuschl, K. H. Wrede, V. Lenz, C. Kleinschnitz, M. Forsting, U. Sure, and R. Jabbarli, "Development of multiple intracranial aneurysms: beyond the common risk factors," *Journal of Neurosurgery*, pp. 1–8, 2022.

[15] "Brain aneurysm symptoms amp; treatment: Pacific stroke amp; neurovascular center." https://www.pacificneuroscienceinstitute.org/stroke-neurovascular/conditions-and-treatments/aneurysm/,images: https://commons.wikimedia.org/wiki/File:Circle_of_Willis_-_MRI, _MIP_-_Superior_view.png https://commons.wikimedia.org/wiki/File:Circle_of_Willis_en.svg. Accessed: 2022-06-01.

[16] F. Salimi Ashkezari, F. Detmer, F. Mut, B. Chung, A. Yu, C. Stapleton, A. See, S. Amin-Hanjani, F. Charbel, B. Rezai Jahromi, M. Niemelä, J. Frösen, J. Zhou, S. Maiti, A. Robertson, and J. Cebral, "Blebs in intracranial aneurysms: prevalence and general characteristics," *Journal of NeuroInterventional Surgery*, vol. 13, pp. 226–230, 2020.

[17] S. F. Salimi Ashkezari, F. Mut, B. J. Chung, A. K. Yu, C. J. Stapleton, A. P. See, S. Amin-Hanjani, F. T. Charbel, B. Rezai Jahromi, M. Niemelä, J. Frösen, S. Maiti, A. M. Robertson, and J. R. Cebral, "Hemodynamics in aneurysm blebs with different wall characteristics," *Journal of NeuroInterventional Surgery*, vol. 13, no. 7, pp. 642–646, 2021.

[18] C. M. Fisher, J. P. Kistler, and J. M. Davis, "Relation of cerebral vasospasm to subarachnoid hemorrhage visualized by computerized tomographic scanning," *Neurosurgery*, vol. 6, no. 1, pp. 1–9, 1980.

[19] J. Rankin, "Cerebral vascular accidents in patients over the age of 60: II. prognosis," *Scottish Medical Journal*, vol. 2, no. 5, pp. 200–215, 1957.

[20] S. Saalfeld, T. Hoffmann, A. Boese, S. Voß, T. Kalinski, M. Skalej, and B. Preim, "Virtual Inflation of the Cerebral Artery Wall for the Integrated Exploration of OCT and Histology Data," *Computer Graphics Forum*, vol. 36, no. 8, pp. 57–68, 2017.

[21] J. Wardlaw and P. White, "The detection and management of unruptured intracranial aneurysms," *Brain*, vol. 123, no. 2, pp. 205–221, 2000.

[22] Y. Kwak, W. Son, Y.-S. Kim, J. Park, and D.-H. Kang, "Discrepancy between mra and dsa in identifying the shape of small intracranial aneurysms," *Journal of Neurosurgery*, pp. 1887–1893, 2020.

[23] K. Shimizu, M. Kushamae, and T. Aoki, "Macrophage Imaging of Intracranial Aneurysms," *Neurologia medico-chirurgica*, vol. 59, no. 7, pp. 257–263, 2019.

[24] D. Wiebers, "Unruptured intracranial aneurysms — risk of rupture and risks of surgical intervention," *New England Journal of Medicine*, vol. 339, no. 24, pp. 1725–1733, 1998.

[25] J. Feghali, A. Gami, R. Xu, C. M. Jackson, R. J. Tamargo, C. G. McDougall, J. Huang, and J. M. Caplan, "Application of unruptured aneurysm scoring systems to a cohort of ruptured aneurysms: are we underestimating rupture risk?," *Neurosurgical Review*, p. 3487–3498, 2021.

[26] C. C. Zuurbier, R. Molenberg, L. A. Mensing, M. J. Wermer, S. Juvela, A. E. Lindgren, J. E. Jääskeläinen, T. Koivisto, T. Yamazaki, M. Uyttenboogaart, J. M. C. van Dijk, M. W. Aalbers, A. Morita, S. Tominari, H. Arai, K. Nozaki, Y. Murayama, T. Ishibashi, H. Takao, R. Gondar, P. Bijlenga, G. J. Rinkel, J. P. Greving, and Y. M. Ruigrok, "Sex difference and rupture rate of intracranial aneurysms: An individual patient data meta-analysis," *Stroke*, vol. 53, no. 2, pp. 362–369, 2022.

[27] T. Suzuki, H. Takao, S. Rapaka, S. Fujimura, C. I. Nita, Y. Uchiyama, H. Ohno, K. Otani, C. Dahmani, V. Mihalef, P. Sharma, A. Mohamed, T. Redel, T. Ishibashi, M. Yamamoto, and Y. Murayama, "Rupture risk of small unruptured intracranial aneurysms in japanese adults," *Stroke*, vol. 51, no. 2, pp. 641–643, 2020.

[28] X. Feng, X. Tong, F. Peng, H. Niu, P. Qi, J. Lu, Y. Zhao, W. Jin, Z. Wu, Y. Zhao, A. Liu, and D. Wang, "Development and validation of a novel nomogram to predict aneurysm rupture in patients with multiple intracranial aneurysms: a multicentre retrospective study," *Stroke and Vascular Neurology*, 2021.

[29] J.-C. Wang, W.-C. Chien, C.-H. Chung, C.-Y. Lin, Y.-H. Chen, M.-T. Liao, W.-I. Liao, C.-C. Hsu, and S.-H. Tsai, "Association between surgical repair of aortic aneurysms and the diagnosis of intracranial aneurysms," *Journal of Vascular Surgery*, vol. 71, no. 2, pp. 481 – 489, 2020.

[30] R. Chen, X. Zan, A. Xiao, R. Guo, L. Xing, L. Ma, C. You, and Y. Liu, "Risk factors for preoperative seizures in pediatric patients with intracranial aneurysms," *Clinical Neurology and Neurosurgery*, vol. 189, pp. 105–116, 2020.

[31] R. Molenberg, M. W. Aalbers, A. Mazuri, G. J. Luijckx, J. D. M. Metzemaekers, R. J. M. Groen, M. Uyttenboogaart, and J. M. C. van Dijk, "The unruptured intracranial aneurysm treatment score as a predictor of aneurysm growth or rupture," *European Journal of Neurology*, vol. 28, no. 3, pp. 837–843, 2021.

[32] B. Neyazi, V. Swiatek, M. Skalej, O. Beuing, K.-P. Stein, J. Hattingen, B. Preim, P. Berg, S. Saalfeld, and Erol, "Rupture risk assessment for multiple intracranial aneurysms: why there is no need for dozens of clinical, morphological and hemodynamic parameters," *Therapeutic Advances in Neurological Disorders*, vol. 13, pp. 1756–1764, 2020.

[33] X. Feng, X. Tong, J. Chen, F. Peng, H. Niu, J. Xia, X. He, P. Qi, J. Lu, Y. Zhao, W. Jin, Z. Wu, Y. Zhao, A. Liu, and D. Wang, "External validation of the phases score in patients with multiple intracranial aneurysms," *Journal of Stroke and Cerebrovascular Diseases*, vol. 30, no. 5, pp. 105–118, 2021.

[34] O. Rousseau, M. Karakachoff, A. Gaignard, L. Bellanger, P. Bijlenga, P. Constant Dit Beaufils, V. L'Allinec, O. Levrier, P. Aguettaz, J.-P. Desilles, C. Michelozzi, G. Marnat, A.-C. Vion, G. Loirand, H. Desal, R. Redon, P.-A. Gourraud, and R. Bourcier, "Location of intracranial aneurysms is the main factor associated with rupture in the ICAN population," *Journal of Neurology, Neurosurgery & Psychiatry*, vol. 92, no. 2, pp. 122–128, 2021.

[35] H. Asgharzadeh, A. Shahmohammadi, N. Varble, E. Levy, H. Meng, and I. Borazjani, "A simple flow classification parameter can discriminate rupture status in intracranial aneurysms," *Neurosurgery*, vol. 87, pp. 557–564, 2020.

[36] N. Varble, V. M. Tutino, J. Yu, A. Sonig, A. H. Siddiqui, J. M. Davies, and H. Meng, "Shared and distinct rupture discriminants of small and large intracranial aneurysms," *Stroke*, vol. 49, no. 4, pp. 856–864, 2018.

[37] Z.-L. Shi, G. Z. Chen, L. Mao, X. L. Li, C. Zhou, S. Xia, Y. Zhang, B. Zhang, B. Hu, G. Lu, and L. J. Zhang, "Machine learning–based prediction of small intracranial aneurysm rupture status using cta-derived hemodynamics: A multicenter study," *American Journal of Neuroradiology*, vol. 42, no. 4, pp. 648–654, 2021.

[38] Y. Yang, Q. Liu, P. Jiang, J. Yang, M. Li, S. Chen, S. Mo, Y. Zhang, X. Ma, Y. Cao, D. Cui, J. Wu, and S. Wang, "Multidimensional predicting model of intracranial aneurysm stability with backpropagation neural network: a preliminary study," *Neurological Sciences*, vol. 42, pp. 7–19, 2021.

[39] N. Amigo, A. Valencia, W. Wu, S. Patnaik, and E. Finol, "Cerebral aneurysm rupture status classification using statistical and machine learning methods," *Journal of Engineering in Medicine*, vol. 235, no. 6, pp. 655–662, 2021.

[40] J. H. Ahn, H. C. Kim, J. K. Rhim, J. J. Park, D. Sigmund, M. C. Park, J. H. Jeong, and J. P. Jeon, "Multi-view convolutional neural networks in rupture risk assessment of small, unruptured intracranial aneurysms," *Journal of Personalized Medicine*, vol. 11, no. 4, p. 239, 2021.

[41] D. P. Roi, J.-D. Mueller, K. Lobotesis, C. McCague, S. Memarian, F. Khan, and K. Mankad, "Intracranial aneurysms: looking beyond size in neuroimaging: the role of anatomical factors and haemodynamics," *Quantitative Imaging in Medicine and Surgery*, vol. 9, no. 4, pp. 537–545, 2019.

[42] "Brain aneurysm treatments: Ut southwestern medical center." https://utswmed.org/conditions-treatments/brain-aneurysm/brain-aneurysm-treatments/. Accessed: 2022-06-01.

[43] Y. Kaku, K. Yamashita, J. Kokuzawa, N. Hatsuda, and T. Andoh, "Treatment of ruptured cerebral aneurysms – clip and coil, not clip versus coil," pp. 9–13, 2009.

[44] J. L. Brisman, "Cerebral Aneurysms," *New England Journal of Medicine*, p. 12, 2006.

[45] P. M. Meyers, A. L. Coon, P. T. Kan, A. K. Wakhloo, and R. A. Hanel, "SCENT trial," *Stroke*, vol. 50, no. 6, pp. 1473–1479, 2019.

[46] L. Pierot, C. Barbe, H. A. Nguyen, D. Herbreteau, J.-Y. Gauvrit, A.-C. Januel, F. Bala, P.-O. Comby, H. Desal, S. Velasco, M. Aggour, E. Chabert, J. Sedat, D. Trystram, G. Marnat, S. Gallas, G. Rodesch, F. Clarençon, S. Soize, M. Gawlitza, L. Spelle, and P. White, "Intraoperative complications of endovascular treatment of intracranial aneurysms with coiling or balloon-assisted coiling in a prospective multicenter cohort of 1088 participants: Analysis of recanalization after endovascular treatment of intracranial aneurysm (areta) study," *Radiology*, vol. 295, no. 2, pp. 381–389, 2020.

[47] K. Ravindran, A. M. Casabella, J. Cebral, W. Brinjikji, D. F. Kallmes, and R. Kadirvel, "Mechanism of Action and Biology of Flow Diverters in the Treatment of Intracranial Aneurysms," *Neurosurgery*, vol. 86, pp. 13–19, 2019.

[48] J. A. Roa, M. Zanaty, D. Ishii, Y. Lu, D. K. Kung, R. M. Starke, J. C. Torner, P. M. Jabbour, E. A. Samaniego, and D. M. Hasan, "Decreased contrast enhancement on high-resolution vessel wall imaging of unruptured intracranial aneurysms in patients taking aspirin," *Journal of Neurosurgery*, pp. 1 – 7, 2020.

[49] M. M. Salem, G. A. Maragkos, S. Gomez-Paz, L. C. Ascanio, L. H. Ngo, C. S. Ogilvy, A. J. Thomas, and J. M. Moore, "Trends of ruptured and unruptured aneurysms treatment in the united states in post-ISAT era: A national inpatient sample analysis," *Journal of the American Heart Association*, vol. 0, no. 0, pp. 169–198, 2021.

[50] J. S. Catapano, C. L. Nguyen, F. A. Frisoli, S. Sagar, J. F. Baranoski, T. S. Cole, M. A. Labib, A. C. Whiting, A. F. Ducruet, F. C. Albuquerque, and M. T. Lawton, "Small intracranial aneurysms in the barrow ruptured aneurysm trial (BRAT)," *Acta Neurochirurgica*, vol. 163, no. 1, pp. 123–129, 2020.

[51] L. Goertz, C. Kabbasch, M. Pflaeging, L. Pennig, K. R. Laukamp, M. Timmer, H. Styczen, G. Brinker, R. Goldbrunner, and B. Krischek, "Impact of the weekend effect on outcome after microsurgical clipping of ruptured intracranial aneurysms," *Acta Neurochirurgica*, vol. 163, no. 3, pp. 783–791, 2021.

[52] C. G. McDougall, R. F. Spetzler, J. M. Zabramski, S. Partovi, N. K. Hills, P. Nakaji, and F. C. Albuquerque, "The barrow ruptured aneurysm trial," *Journal of Neurosurgery*, vol. 116, no. 1, pp. 135–144, 2012.

[53] R. F. Spetzler, C. G. McDougall, F. C. Albuquerque, J. M. Zabramski, N. K. Hills, S. Partovi, P. Nakaji, and R. C. Wallace, "The barrow ruptured aneurysm trial: 3-year results," *Journal of Neurosurgery*, vol. 119, no. 1, pp. 146–157, 2013.

[54] R. F. Spetzler, C. G. McDougall, J. M. Zabramski, F. C. Albuquerque, N. K. Hills, J. J. Russin, S. Partovi, P. Nakaji, and R. C. Wallace, "The barrow ruptured aneurysm trial: 6-year results," *Journal of Neurosurgery*, vol. 123, no. 3, pp. 609–617, 2015.

[55] W. Roentgen, "The x-rays," *Annual Report of the Board of Regents of the Smithsonian Institution*, pp. 137–143, 1898.

[56] J. Radon, "On the determination of functions from their integral values along certain manifolds," *IEEE Transactions on Medical Imaging*, vol. 5, no. 4, pp. 170–176, 1986.

[57] W. H. Oldendorf, "The quest for an image of brain: A brief historical and technical review of brain imaging techniques," *Neurology*, vol. 28, no. 6, pp. 517–517, 1978.

[58] W. H. Oldendorf, "Isolated flying spot detection of radiodensity discontinuities-displaying the internal structural pattern of a complex object," *IRE Transactions on Bio-Medical Electronics*, vol. 8, no. 1, pp. 68–72, 1961.

[59] K. Toennies, *Guide to medical image analysis: methods and algorithms*. Springer, 2018.

[60] A. Elster, "MRA methods," *Questions and Answers in MRI - http://mriquestions.com/mra-methods.html*, p. accessed 27.04.2021.

[61] D. Mandell, M. Mossa-Basha, Y. Qiao, C. Hess, F. Hui, C. Matouk, M. Johnson, M. Daemen, A. Vossough, M. Edjlali, D. Saloner, S. Ansari, B. Wasserman, and D. Mikulis, "Intracranial vessel wall MRI: Principles and expert consensus recommendations of the american society of neuroradiology," *American Journal of Neuroradiology*, vol. 38, pp. 218–229, 2016.

[62] C. Santarosa, B. Cord, A. Koo, P. Bhogal, A. Malhotra, S. Payabvash, F. Minja, and C. Matouk, "Vessel wall magnetic resonance imaging in intracranial aneurysms: Principles and emerging clinical applications," *Interventional Neuroradiology*, vol. 26, pp. 135–146, 2019.

[63] T. J. Mosher and M. B. Smith, "A dante tagging sequence for the evaluation of translational sample motion," *Magnetic Resonance in Medicine*, vol. 15, no. 2, pp. 334–339, 1990.

[64] L. Li, K. L. Miller, and P. Jezzard, "Dante-prepared pulse trains: A novel approach to motion-sensitized and motion-suppressed quantitative magnetic resonance imaging," *Magnetic Resonance in Medicine*, vol. 68, no. 5, pp. 1423–1438, 2012.

[65] A. van der Kolk, J. Zwanenburg, M. Brundel, G. Biessels, F. Visser, P. Luijten, and J. Hendrikse, "Intracranial vessel wall imaging at 7.0-T MRI," *Stroke; a journal of cerebral circulation*, vol. 42, pp. 2478–2484, 2011.

[66] Y. Xie, q. Yang, G. Xie, J. Pang, Z. Fan, and D. Li, "Improved black-blood imaging using DANTE-SPACE for combined carotid and intracranial vessel wall evaluation," *Magnetic resonance in medicine*, vol. 75, no. 6, pp. 2286–2294, 2015.

[67] B. M. W. Cornelissen, E. L. Leemans, B. F. Coolen, E. S. Peper, R. van den Berg, H. A. Marquering, C. H. Slump, and C. B. L. M. Majoie, "Insufficient slow-flow suppression mimicking aneurysm wall enhancement in magnetic resonance vessel wall imaging: a phantom study," *Neurosurgical Focus*, vol. 47, no. 1, pp. 19–23, 2019.

[68] J. Wang, V. Yarnykh, and C. Yuan, "Enhanced image quality in black-blood MRI using the improved motion-sensitized driven-equilibrium (imsde) sequence," *Journal of magnetic resonance imaging*, vol. 31, pp. 1256–63, 2010.

[69] S. J. Cho, S. C. Jung, C. H. Suh, J. B. Lee, and D. Kim, "High-resolution magnetic resonance imaging of intracranial vessel walls: Comparison of 3D T1-weighted turbo spin echo with or without DANTE or iMSDE," *PLOS ONE*, vol. 14, no. 8, pp. 1–10, 2019.

[70] B. Cornelissen, E. Leemans, C. Slump, H. Marquering, C. Majoie, and R. Berg, "Vessel wall enhancement of intracranial aneurysms: Fact or artifact?," *Neurosurgical focus*, vol. 47, pp. 18–28, 2019.

[71] E. Raz, A. Goldman-Yassen, A. Derman, A. Derakhshani, J. Grinstead, and S. Dehkharghani, "Vessel wall imaging with advanced flow suppression in the characterization of intracranial aneurysms following flow diversion with pipeline embolization device," *Journal of NeuroInterventional Surgery*, 2022.

[72] "Histological features of cells." http://histology.med.yale.edu/histological_features_of_cells/home.php. Accessed: 2022-05-30.

[73] H. Alturkistani, F. Tashkandi, and Z. Mohammedsaleh, "Histological stains: A literature review and case study," *Global Journal of Health Science*, vol. 8, p. 72–79, 2015.

[74] R. B. Dettmeyer, *Staining Techniques and Microscopy*, pp. 17–45. Springer International Publishing, 2018.

[75] G. R. Cindy Sampias, "H&E staining overview: A guide to best practices - $https://www.leicabiosystems.com/knowledge-pathway/he-staining-overview-a-guide-to-best-practices/$," Accessed: 2021-04-26.

[76] "Special stains." https://histologyresearchcorefacility.web.unc.edu/special-stains/. Accessed: 2022-05-30.

[77] E. Klatt, "$https://webpath.med.utah.edu/histhtml/manuals/massons.pdf$," Accessed: 2021-04-26.

[78] S. Sohal, "CXA121 tutorial: Staining - $https://www.utas.edu.au//\_\_data/assets/pdf\_file/0004/955813/cxa121tutorial3staininganswers.pdf$," Accessed: 2021-04-26.

[79] S. W. Chea and K.-B. Lee, "TGF-β mediated epithelial-mesenchymal transition in autosomal dominant polycystic kidney disease," *Yonsei Medical Journal*, vol. 50, no. 1, p. 105, 2009.

[80] G. Johnson, "Actin, alpha smooth muscle type," *Pathology Outlines - https : //www.pathologyoutlines.com/topic/stainsalphasmoothmuscleactin.html*. Accessed: 2021-04-26.

[81] O. Skalli, P. Ropraz, A. Trzeciak, G. Benzonana, D. Gillessen, and G. Gabbiani, "A monoclonal antibody against alpha-smooth muscle actin: a new probe for smooth muscle differentiation.," *The Journal of Cell Biology*, vol. 103, no. 6, pp. 2787–2796, 1986.

[82] N. Biltz and G. Meyer, "A novel method for the quantification of fatty infiltration in skeletal muscle," *Skeletal Muscle*, vol. 7, pp. 244–254, 2017.

[83] F. Mokobi, "Masson's trichrome staining." https://microbenotes.com/massons-trichrome-staining/. Accessed: 2022-05-30.

[84] J. G. Fujimoto, C. Pitris, S. A. Boppart, and M. E. Brezinski, "Optical coherence tomography: An emerging technology for biomedical imaging and optical biopsy," *Neoplasia*, vol. 2, no. 1, pp. 9 – 25, 2000.

[85] Y. Liu, Y. Zheng, Q. An, Y. Song, and B. Leng, "Optical coherence tomography for intracranial aneurysms: A new method for assessing the aneurysm structure," *World Neurosurgery*, vol. 123, pp. 194–201, 2019.

[86] S. Saalfeld, T. Hoffmann, A. Boese, S. Voß, T. Kalinski, M. Skalej, and B. Preim, "Histology-based evaluation of optical coherence tomographic characteristics of the cerebral arterywall via virtual inflating," *Proc. of Eurographics Workshop on Visual Computing for Biology and Medicine (VCBM)*, 2015.

[87] S. Saalfeld, T. Hoffmann, A. Boese, S. Voß, T. Kalinski, M. Skalej, and B. Preim, "Virtual inflation of the cerebral artery wall for the integrated exploration of oct and histology data," *Computer Graphics Forum*, vol. 35, pp. 57–68, 2016.

[88] S. Saalfeld, T. Hoffmann, S. Voß, F. Klink, and B. Preim, "Extraction of patient-specific 3D cerebral artery and wall thickness models from "2D" oct and structured-light 3D scanner data," in *Proc of Computer- und Roboterassistierte Chirurgie (CURAC)*, pp. 197–202, 2016.

[89] W. Denk and H. Horstmann, "Serial block-face scanning electron microscopy to reconstruct three-dimensional tissue nanostructure," *PLOS Biology*, vol. 2, no. 11, 2004.

[90] A. Wanner, M. Kirschmann, and C. Genoud, "Challenges of microtome-based serial block-face scanning electron microscopy in neuroscience," *Journal of microscopy*, vol. 259, no. 2, pp. 137–142, 2015.

[91] M. O'Connell, S. Murthy, S. Phan, C. Xu, J. Buchanan, R. Spilker, R. Dalman, C. Zarins, W. Denk, and C. Taylor, "The three-dimensional micro- and nanostructure of the aortic medial lamellar unit measured using 3D confocal & electron microscopy imaging," *Matrix biology : journal of the International Society for Matrix Biology*, vol. 27, pp. 171–81, 2008.

[92] S. Mikula, J. Binding, and W. Denk, "Staining and embedding the whole mouse brain for electron microscopy," *Nature methods*, vol. 9, p. 1198–1201, 2012.

[93] W. Denk, J. H. Strickler, and W. W. Webb, "Two-photon laser scanning fluorescence microscopy," *Science*, vol. 248, no. 4951, pp. 73–76, 1990.

[94] C. A. Combs, A. V. Smirnov, J. D. Rileay, A. H. Gandjbakhche, J. R. Knutson, and R. S. Balaban, "Optimization of multiphoton excitation microscopy by total emission detection using a parabolic light reflector," *Journal of Microscopy*, vol. 228, no. 3, pp. 330–337, 2007.

[95] L. V. Wang and S. Hu, "Photoacoustic tomography: In vivo imaging from organelles to organs," *Science*, vol. 335, no. 6075, pp. 1458–1462, 2012.

[96] A. J. Schriefl, H. Wolinski, P. Regitnig, S. D. Kohlwein, and G. A. Holzapfel, "An automated approach for three-dimensional quantification of fibrillar structures in optically cleared soft biological tissues," *Journal of The Royal Society Interface*, vol. 10, no. 80, pp. 2012–2022, 2013.

[97] C. Peng, H. Wu, S. Kim, X. Dai, and X. Jiang, "Recent advances in transducers for intravascular ultrasound (IVUS) imaging," *Sensors*, vol. 21, no. 10, p. 3540, 2021.

[98] G. Illuminati, P. Nardi, D. Fresilli, S. Sorrenti, A. Lauro, G. Pizzardi, M. Ruggeri, S. Ulisse, V. Cantisani, and V. D'Andrea, "Fully ultrasound-assisted endovascular aneurysm repair: Preliminary report," *Annals of Vascular Surgery*, 2022.

[99] J. Zhang, X. Li, B. Zhao, J. Zhang, B. Sun, L. Wang, J. Tian, M. Mossa-Basha, L. J. Kim, J. Yan, J. Wan, J. Xu, Y. Zhou, H. Zhao, and C. Zhu, "Irregular pulsation of aneurysmal wall is associated with symptomatic and ruptured intracranial aneurysms," *Journal of NeuroInterventional Surgery*, 2022.

[100] L. B. Stam, R. Aquarius, G. A. de Jong, C. H. Slump, F. J. A. Meijer, and H. D. Boogaarts, "A review on imaging techniques and quantitative measurements for dynamic imaging of cerebral aneurysm pulsations," *Scientific Reports*, vol. 11, no. 1, p. 2175, 2021.

[101] R. Kleinloog, J. Zwanenburg, B. Schermers, E. Krikken, Y. Ruigrok, P. Luijten, F. Visser, L. Regli, G. Rinkel, and B. Verweij, "Quantification of intracranial aneurysm volume pulsation with 7t mri," *American Journal of Neuroradiology*, vol. 39, no. 4, pp. 713–719, 2018.

[102] R. Jabbarli, L. Rauschenbach, T. F. Dinger, M. Darkwah Oppong, J. Rode-merk, D. Pierscianek, P. Dammann, A. Junker, U. Sure, and K. H. Wrede, "In the wall lies the truth: a systematic review of diagnostic markers in intracranial aneurysms," *Brain Pathology*, vol. 30, no. 3, pp. 437–445, 2020.

[103] J. R. Cebral, X. Duan, B. J. Chung, C. Putman, K. Aziz, and A. M. Robert-son, "Wall mechanical properties and hemodynamics of unruptured in-tracranial aneurysms," *American Journal of Neuroradiology*, vol. 36, no. 9, pp. 1695–1703, 2015.

[104] P. Jiang, Q. Liu, J. Wu, X. Chen, M. Li, Z. Li, S. Yang, R. Guo, B. Gao, Y. Cao, R. Wang, and S. Wang, "Hemodynamic characteristics associated with thinner regions of intracranial aneurysm wall," *Journal of Clinical Neuroscience*, vol. 67, pp. 185–190, 2019.

[105] K. A. Hackenberg, H. Rajabzadeh-Oghaz, R. Dreier, B. A. Buchholz, A. Navid, D. M. Rocke, A. Abdulazim, D. Hänggi, A. Siddiqui, R. L. Macdonald, H. Meng, and N. Etminan, "Collagen turnover in relation to risk factors and hemodynamics in human intracranial aneurysms," *Stroke*, vol. 51, no. 5, pp. 1624–1628, 2020.

[106] J. R. Cebral, F. Detmer, B. Chung, J. Choque-Velasquez, B. Rezai Jahromi, H. Lehto, R. Tulamo, J. Hernesniemi, M. Niemela, A. Yu, R. Williamson, K. Aziz, S. Sakur, S. Amin-Hanjani, F. Charbel, Y. Tobe, A. Robertson, and J. Frösen, "Local hemodynamic conditions associated with focal changes in the intracranial aneurysm wall," *American journal of neuroradiology*, vol. 40, pp. 510–516, 2019.

[107] M. McCann, J. Ozolek, C. Castro, B. Parvin, and J. Kovacevic, "Automated histology analysis: Opportunities for signal processing," *Signal Processing Magazine*, vol. 32, pp. 78–87, 2015.

[108] M. McCann, J. Majumdar, C. Peng, C. Castro, and J. Kovačević, "Algo-rithm and benchmark dataset for stain separation in histology images," in *International Conference on Image Processing*, pp. 3953–3957, Institute of Electrical and Electronics Engineers Inc., 2014.

[109] "H&E basics part 4: Troubleshooting h&E." https://www.leicabiosystems.com/en-de/knowledge-pathway/he-basics-part-4-troubleshooting-he/. Ac-cessed: 2021-09-30.

[110] S. Kothari, J. Phan, and M. Wang, "Eliminating tissue-fold artifacts in histopathological whole-slide images for improved image-based prediction of cancer grade," *Journal of pathology informatics*, vol. 4, p. 22, 2013.

[111] M. Schwier, T. Boehler, H. Hahn, U. Dahmen, and O. Dirsch, "Registration of histological whole slide images guided by vessel structures," *Journal of pathology informatics*, vol. 4, p. S10, 2013.

[112] G. Xiao, B. N. Bloch, J. Chappelow, E. M. Genega, N. M. Rofsky, R. E. Lenkinski, J. Tomaszewski, M. D. Feldman, M. Rosen, and A. Madabhushi, "Determining histology-MRI slice correspondences for defining MRI-based

disease signatures of prostate cancer," *Computerized Medical Imaging and Graphics*, vol. 35, no. 7, pp. 568 – 578, 2011.

[113] H. Park, M. R. Piert, A. Khan, R. Shah, H. Hussain, J. Siddiqui, T. L. Chenevert, and C. R. Meyer, "Registration methodology for histological sections and in vivo imaging of human prostate," *Academic radiology*, vol. 15, no. 8, p. 1027—1039, 2008.

[114] "Polygon mesh." https://en.wikipedia.org/wiki/Polygon_mesh. Accessed: 2022-05-15.

[115] M. Viceconti, L. Bellingeri, L. Cristofolini, and A. Toni, "A comparative study on different methods of automatic mesh generation of human femurs," *Medical Engineering & Physics*, vol. 20, no. 1, pp. 1 – 10, 1998.

[116] H. Uzunova, M. Wilms, N. D. Forkert, H. Handels, and J. Ehrhardt, "A systematic comparison of generative models for medical images," *International Journal of Computer Assisted Radiology and Surgery*, pp. 10.1007/s11548–022–02567–6, 2022.

[117] R. Hanocka, G. Metzer, R. Giryes, and D. Cohen-Or, "Point2mesh: A self-prior for deformable meshes," *ACM Transactions on Graphics*, vol. 39, no. 4, 2020.

[118] M. Fedele and A. Quarteroni, "Polygonal surface processing and mesh generation tools for the numerical simulation of the cardiac function," *International Journal for Numerical Methods in Biomedical Engineering*, vol. 37, no. 4, pp. 34–35, 2021.

[119] M. Feuerstein, T. Heibel, J. Gardiazabal, N. Navab, and M. Groher, "Reconstruction of 3-D histology images by simultaneous deformable registration," *Medical Image Computing and Computer-Assisted Intervention*, vol. 14, pp. 582–589, 2011.

[120] A. Cifor, T. Pridmore, and A. Pitiot, "Smooth 3-d reconstruction for 2-d histological images," in *Information Processing in Medical Imaging*, (Berlin, Heidelberg), pp. 350–361, Springer Berlin Heidelberg, 2009.

[121] U.-D. Braumann, J.-P. Kuska, J. Einenkel, L.-C. Horn, M. Löffler, and M. Höckel, "Three-dimensional reconstruction and quantification of cervical carcinoma invasion fronts from histological serial sections," *IEEE transactions on medical imaging*, vol. 24, pp. 1286–307, 2005.

[122] D. Komura and S. Ishikawa, "Machine learning methods for histopathological image analysis," *Computational and Structural Biotechnology Journal*, vol. 16, p. 34–42, 2018.

[123] H. Chen, X. Qi, L. Yu, Q. Dou, J. Qin, and P.-A. Heng, "DCAN: Deep contour-aware networks for object instance segmentation from histology images," *Medical Image Analysis*, vol. 36, pp. 135–146, 2017.

[124] M. D. Zarella, C. Yeoh, D. E. Breen, and F. U. Garcia, "An alternative reference space for H&E color normalization," *PLoS ONE*, vol. 12, pp. 1–14, 2017.

[125] A. Janowczyk and A. Madabhushi, "Deep learning for digital pathology image analysis: A comprehensive tutorial with selected use cases," *Journal of Pathology Informatics*, vol. 7, no. 1, p. 29, 2016.

[126] A. Taylor-Weiner, H. Pokkalla, L. Han, C. Jia, R. Huss, C. Chung, H. Elliott, B. Glass, K. Pethia, O. Carrasco-Zevallos, C. Shukla, U. Khettry, R. Najarian, R. Taliano, G. M. Subramanian, R. P. Myers, I. Wapinski, A. Khosla, M. Resnick, M. C. Montalto, Q. M. Anstee, V. W.-S. Wong, M. Trauner, E. J. Lawitz, S. A. Harrison, T. Okanoue, M. Romero-Gomez, Z. Goodman, R. Loomba, A. H. Beck, and Z. M. Younossi, "A machine learning approach enables quantitative measurement of liver histology and disease monitoring in nash," *Hepatology*, vol. 74, no. 1, pp. 133–147, 2021.

[127] L. Athanasiou, G. Rigas, A. Sakellarios, T. Exarchos, P. Siogkas, K. NAKA, D. Panetta, G. Pelosi, f. vozzi, L. Michalis, O. Parodi, and D. Fotiadis, "Computerized methodology for micro-ct and histological data inflation using an ivus based translation map," *Computers in Biology and Medicine*, vol. 65, pp. 168–176, 2015.

[128] S. Judex, Y. Luu, E. Ozcivici, B. Adler, S. Lublinsky, and C. Rubin, "Quantification of adiposity in small rodents using micro-ct," *Methods*, vol. 50, no. 1, pp. 14–19, 2010.

[129] M. Senter-Zapata, K. Patel, P. Bautista, M. Griffin, J. Michaelson, and Y. Yagi, "The role of micro-ct in 3D histology imaging," *Pathobiology : journal of immunopathology, molecular and cellular biology*, vol. 83, pp. 140–147, 2016.

[130] S. L. Jessen, M. C. Friedemann, A. E. Mullen, A.-M. Ginn-Hedman, S. M. Herting, D. J. Maitland, and F. J. Clubb Jr, "Micro-ct and histopathology methods to assess host response of aneurysms treated with shape memory polymer foam-coated coils versus bare metal coil occlusion devices," *Journal of Biomedical Materials Research Part B: Applied Biomaterials*, vol. 108, no. 5, pp. 2238–2249, 2020.

[131] J. R. Cebral, F. Mut, P. Gade, F. Cheng, Y. Tobe, J. Frosen, and A. M. Robertson, "Combining data from multiple sources to study mechanisms of aneurysm disease: Tools and techniques," *International Journal for Numerical Methods in Biomedical Engineering*, vol. 34, no. 11, p. 3133, 2018.

[132] P. Liu, H. Qi, A. Liu, X. Lv, Y. Jiang, X. Zhao, R. Li, B. Lu, M. Lv, H. Chen, and Y. Li, "Relationship between aneurysm wall enhancement and conventional risk factors in patients with unruptured intracranial aneurysms: A black-blood MRI study," *Interventional Neuroradiology*, vol. 22, no. 5, pp. 501–505, 2016.

[133] L. Antiga, B. A. Wasserman, and D. A. Steinman, "On the overestimation of early wall thickening at the carotid bulb by black blood MRI, with implications for coronary and vulnerable plaque imaging," *Magnetic resonance in medicine : official journal of the Society of Magnetic Resonance in Medicine / Society of Magnetic Resonance in Medicine*, vol. 60, pp. 1020–1028, 2008.

[134] S. G. Qichang Fu, C. Liu, K. Wang, and J. Cheng, "Clinical significance of circumferential aneurysmal wall enhancement in symptomatic patients with unruptured intracranial aneurysms: a high-resolution MRI study," *Clinical Neuroradiology*, p. 509–514, 2017.

[135] M. Edjlali, J.-C. Gentric, C. Régent-Rodriguez, D. Trystram, W. B. Hassen, S. Lion, F. Nataf, J. Raymond, O. Wieben, P. Turski, J.-F. Meder, C. Oppenheim, and O. Naggara, "Does aneurysmal wall enhancement on vessel wall MRI help to distinguish stable from unstable intracranial aneurysms?," *Stroke*, vol. 45, no. 12, pp. 3704–3706, 2014.

[136] J. A. Roa, M. Zanaty, C. Osorno-Cruz, D. Ishii, G. Bathla, S. Ortega-Gutierrez, D. M. Hasan, and E. A. Samaniego, "Objective quantification of contrast enhancement of unruptured intracranial aneurysms: a high-resolution vessel wall imaging validation study," *Journal of Neurosurgery*, pp. 1 – 8, 2020.

[137] M. O. Khan, V. T. Arana, C. Rubbert, J. F. Cornelius, I. Fischer, R. Bostelmann, H.-J. Mijderwijk, B. Turowski, H.-J. Steiger, R. May, and A. K. Petridis, "Association between aneurysm hemodynamics and wall enhancement on 3D vessel wall MRI," *Journal of Neurosurgery*, vol. 134, no. 2, pp. 565 – 575, 2020.

[138] Zwarzany, E. Tyburski, and W. Poncyljusz, "High-resolution vessel wall magnetic resonance imaging of small unruptured intracranial aneurysms," *Journal of Clinical Medicine*, vol. 10, p. 225, 2021.

[139] N. F. Fanning, R. A. Willinsky, and K. G. terBrugge, "Wall enhancement, edema, and hydrocephalus after endovascular coil occlusion of intradural cerebral aneurysms," *Journal of Neurosurgery*, vol. 108, no. 6, pp. 1074 – 1086, 2008.

[140] M. Edjlali, J.-C. Gentric, C. Régent-Rodriguez, D. Trystram, W. B. Hassen, S. Lion, F. Nataf, J. Raymond, O. Wieben, P. Turski, J.-F. Meder, C. Oppenheim, and O. Naggara, "Does aneurysmal wall enhancement on vessel wall MRI help to distinguish stable from unstable intracranial aneurysms?," *Stroke*, vol. 45, no. 12, pp. 3704–3706, 2014.

[141] S. Nagahata, M. Nagahata, M. Obara, K. Rei, N. Minagawa, S. Sato, W. Mouri, S. Saito, and T. Kayama, "Wall enhancement of the intracranial aneurysms revealed by magnetic resonance vessel wall imaging using three-dimensional turbo spin-echo sequence with motion-sensitized driven-equilibrium: A sign of ruptured aneurysm?," *Clinical Neuroradiology*, vol. 26, p. 277–283, 2014.

[142] S. Hadad, F. Mut, B. Chung, J. Roa, A. Robertson, D. Hassan, E. Samaniego, and J. Cebral, "Regional aneurysm wall enhancement is affected by local hemodynamics: A 7t MRI study," *American Journal of Neuroradiology*, pp. 195–202, 2020.

[143] H. Endo, N. Mori, S. Mugikura, K. Niizuma, S. Omodaka, K. Takase, and T. Tominaga, "Quantitative assessment of microstructural evolution

of intracranial aneurysm wall by vessel wall imaging," *Neuroradiology*, pp. https://doi.org/10.1007/s00234–021–02877–7, 2022.

[144] Q. Fu, Y. Wang, Y. Zhang, Y. Zhang, X. Guo, H. Xu, Z. Yao, M. Wang, M. R. Levitt, M. Mossa-Basha, J. Zhu, J. Cheng, S. Guan, and C. Zhu, "Qualitative and quantitative wall enhancement on magnetic resonance imaging is associated with symptoms of unruptured intracranial aneurysms," *Stroke*, vol. 52, no. 1, pp. 213–222, 2021.

[145] S. Omodaka, H. Endo, K. Niizuma, M. Fujimura, T. Inoue, K. Sato, S. Sugiyama, and T. Tominaga, "Quantitative assessment of circumferential enhancement along the wall of cerebral aneurysms using MR imaging," *American journal of neuroradiology*, vol. 37, pp. 1262–1266, 2016.

[146] A. E. Galloy, A. Raghuram, M. A. Nino, A. Varon Miller, R. Sabotin, C. Osorno-Cruz, E. A. Samaniego, S. M. L. Raghavan, and D. Hasan, "Analysis of cerebral aneurysm wall tension and enhancement using finite element analysis and high-resolution vessel wall imaging," *Frontiers in neurology*, vol. 12, pp. 764–765, 2021.

[147] Zwarzany, M. Owsiak, E. Tyburski, and W. Poncyljusz, "High-resolution vessel wall mri of endovascularly treated intracranial aneurysms," *Tomography*, vol. 8, no. 1, pp. 303–315, 2022.

[148] M. S. Pravdivtseva, F. Gaidzik, P. Berg, C. Hoffman, L. A. Rivera-Rivera, R. Medero, L. Bodart, A. Roldan-Alzate, M. A. Speidel, K. M. Johnson, O. Wieben, O. Jansen, J.-B. Hövener, and N. Larsen, "Pseudo-enhancement in intracranial aneurysms on black-blood MRI: Effects of flow rate, spatial resolution, and additional flow suppression," *Journal of Magnetic Resonance Imaging*, vol. 54, no. 3, pp. 888–901, 2021.

[149] O. Ronneberger, P. Fischer, and T. Brox, "U-net: Convolutional networks for biomedical image segmentation," in *Medical Image Computing and Computer-Assisted Intervention*, pp. 234–241, Springer International Publishing, 2015.

[150] M. Ivantsits, J.-M. Kuhnigk, M. Huellebrand, T. Kuehne, and A. Hennemuth, "Deep learning-based 3d u-net cerebral aneurysm detection," in *Cerebral Aneurysm Detection and Analysis*, pp. 31–38, Springer International Publishing, 2021.

[151] S. Nousias, G. Arvanitis, A. Lalos, and K. Moustakas, "Fast mesh denoising with data driven normal filtering using deep variational autoencoders," *IEEE Transactions on Industrial Informatics*, vol. 17, no. 2, pp. 980–990, 2020.

[152] H. Wang and J. Zhang, "A survey of deep learning-based mesh processing," *Communications in Mathematics and Statistics*, pp. 10.1007/s40304–021–00246–7, 2022.

[153] E. Kalogerakis, A. Hertzmann, and K. Singh, "Learning 3D Mesh Segmentation and Labeling," *ACM Transactions on Graphics*, vol. 29, no. 3, 2010.

[154] A. Shamir, "A survey on mesh segmentation techniques.," *Comput. Graph. Forum*, vol. 27, no. 6, pp. 1539–1556, 2008.

[155] X. Yang, D. Xia, T. Kin, and T. Igarashi, "Intra: 3D intracranial aneurysm dataset for deep learning," 2020.

[156] O. Kaick, N. Fish, Y. Kleiman, S. Asafi, and D. Cohen-Or, "Shape segmentation by approximate convexity analysis," *ACM Transactions on Graphics*, vol. 34, pp. 1–11, 2014.

[157] R. Hanocka, A. Hertz, N. Fish, R. Giryes, S. Fleishman, and D. Cohen-Or, "Meshcnn: A network with an edge," *Transactions on Graphics*, vol. 38, no. 4, pp. 12–24, 2019.

[158] H. Zhang, Y. Jiao, Y. Zhang, and K. Shimada, "Automated segmentation of cerebral aneurysms based on conditional random field and gentle adaboost," in *Mesh Processing in Medical Image Analysis 2012*, (Berlin, Heidelberg), pp. 59–69, Springer Berlin Heidelberg, 2012.

[159] W. Wu, Z. Qi, and L. Fuxin, "PointConv: Deep convolutional networks on 3D point clouds," in *Conference on Computer Vision and Pattern Recognition)*, pp. 9613–9622, IEEE, 2019.

[160] V. John, M. Nithilan, S. Mita, H. Tehrani, and P. L. P. Sudheesh, Raveendrannair S. and, *SO-Net: Joint Semantic Segmentation and Obstacle Detection Using Deep Fusion of Monocular Camera and Radar*, pp. 138–148. 2020.

[161] X. Yang, D. Xia, T. Kin, and T. Igarashi, "A two-step surface-based 3d deep learning pipeline for segmentation of intracranial aneurysms," 2021.

[162] H. Thomas, C. R. Qi, J.-E. Deschaud, B. Marcotegui, F. Goulette, and L. J. Guibas, "Kpconv: Flexible and deformable convolution for point clouds," *Proceedings of the IEEE International Conference on Computer Vision*, 2019.

[163] Y. Zheng, J. Zhao, Y. Chen, C. Tang, and S. Yu, "3D mesh model classification with a capsule network," *Algorithms*, vol. 14, no. 3, p. 239, 2021.

[164] M. Ivantsits, L. Goubergrits, J. Brüning, A. Spuler, and A. Hennemuth, "Intracranial aneurysm rupture prediction with computational fluid dynamics point clouds," in *Cerebral Aneurysm Detection and Analysis*, pp. 104–112, Springer International Publishing, 2021.

[165] M. Piccinelli, A. Veneziani, D. A. Steinman, A. Remuzzi, and L. Antiga, "A framework for geometric analysis of vascular structures: Application to cerebral aneurysms," *IEEE Transactions on Medical Imaging*, vol. 28, no. 8, pp. 1141–1155, 2009.

[166] A. Sironi, V. Lepetit, and P. Fua, "Multiscale centerline detection by learning a scale-space distance transform," *Proceedings of the IEEE Computer Society Conference on Computer Vision and Pattern Recognition*, pp. 2697–2704, 2014.

[167] L. Antiga, B. Ene-Iordache, and A. Remuzzi, "Centerline computation and geometric analysis of branching tubular surfaces with application to blood vessel modeling," in *WSCG*, 2003.

[168] M. Wei, Q. Wang, Y. Li, W.-M. Pang, L. Liang, J. Wang, K. K. L. Wong, D. Abbott, J. Qin, and J. Wu, "Centerline extraction of vasculature mesh," *IEEE Access*, vol. 6, pp. 10257–10268, 2018.

[169] I. Bitter, A. Kaufman, and M. Sato, "Penalized-distance volumetric skeleton algorithm," *IEEE Transactions on Visualization and Computer Graphics*, vol. 7, no. 3, pp. 195–206, 2001.

[170] R. Gao, Z. Hou, J. Li, H. Han, B. Lu, and S. K. Zhou, "Joint coronary centerline extraction and lumen segmentation from ccta using cnntracker and vascular graph convolutional network," in *2021 IEEE 18th International Symposium on Biomedical Imaging*, pp. 1897–1901, 2021.

[171] J. M. Wolterink, R. W. van Hamersvelt, M. A. Viergever, T. Leiner, and I. Išgum, "Coronary artery centerline extraction in cardiac ct angiography using a cnn-based orientation classifier," *Medical Image Analysis*, vol. 51, pp. 46–60, 2019.

[172] A. Mostafa, A. M. Ghanem, M. El-Shatoury, and T. Basha, "Improved centerline extraction in fully automated coronary ostium localization and centerline extraction framework using deep learning," in *2021 43rd Annual International Conference of the IEEE Engineering in Medicine Biology Society*, pp. 3846–3849, 2021.

[173] A. Dorobanțiu, V. Ogrean, and R. Brad, "Coronary centerline extraction from CCTA using 3D-UNet," *Future Internet*, vol. 13, no. 4, pp. 101–112, 2021.

[174] L. Antiga and D. Steinman, "Robust and objective decomposition and mapping of bifurcating vessels," *IEEE transactions on medical imaging*, vol. 23, pp. 704–713, 2004.

[175] C. Chnafa, K. Valen-Sendstad, O. Brina, V. M. Pereira, and D. A. Steinman, "Improved reduced-order modelling of cerebrovascular flow distribution by accounting for arterial bifurcation pressure drops," *Journal of Biomechanics*, vol. 51, pp. 83 – 88, 2017.

[176] S. Saalfeld, S. Voß, O. Beuing, B. Preim, and P. Berg, "Flow-splitting-based computation of outlet boundary conditions for improved cerebrovascular simulation in multiple intracranial aneurysms," *International Journal of Computer Assisted Radiology and Surgery*, vol. 14, p. 1805–1813, 2019.

[177] N. Varble, G. Trylesinski, J. Xiang, K. Snyder, and H. Meng, "Identification of vortex structures in a cohort of 204 intracranial aneurysms," *Journal of The Royal Society Interface*, vol. 14, no. 130, pp. 117–125, 2017.

[178] P. Berg, S. Saalfeld, S. Voß, O. Beuing, and G. Janiga, "A review on the reliability of hemodynamic modeling in intracranial aneurysms: why computational fluid dynamics alone cannot solve the equation," *Neurosurgical Focus*, vol. 47, no. 1, p. 15, 2019.

[179] K. Valen-Sendstad, A. Bergersen, Y. Shimogonya, L. Goubergrits, J. Brüning, J. Pallares, S. Cito, Pişkin, K. Pekkan, A. Geers, I. Larrabide, S. Rapaka, V. Mihalef, W. Fu, A. Qiao, K. Jain, S. Roller, K.-A. Mardal, R. Kamakoti, and D. Steinman, "Real-world variability in the prediction of intracranial aneurysm wall shear stress: The 2015 international aneurysm cfd challenge," *Cardiovascular Engineering and Technology*, vol. 9, p. 544–564, 2018.

[180] J. Zimmermann, D. Demedts, H. Mirzaee, P. Ewert, H. Stern, C. Meierhofer, B. Menze, and A. Hennemuth, "Wall shear stress estimation in the aorta: Impact of wall motion, spatiotemporal resolution, and phase noise," *Journal of Magnetic Resonance Imaging*, vol. 48, no. 3, pp. 718–728, 2018.

[181] H. Rajabzadeh-Oghaz, A. H. Siddiqui, A. Asadollahi, J. Kolega, and V. M. Tutino, "The association between hemodynamics and wall characteristics in human intracranial aneurysms: a review," *Neurosurgical Review*, pp. 49–61, 2021.

[182] J. Frösen, J. Cebral, A. M. Robertson, and T. Aoki, "Flow-induced, inflammation-mediated arterial wall remodeling in the formation and progression of intracranial aneurysms," *Neurosurgical Focus*, vol. 47, no. 1, pp. 21 – 35, 2019.

[183] K. M. Saqr, S. Rashad, S. Tupin, K. Niizuma, T. Hassan, T. Tominaga, and M. Ohta, "What does computational fluid dynamics tell us about intracranial aneurysms? A meta-analysis and critical review," *Journal of Cerebral Blood Flow & Metabolism*, vol. 40, no. 5, pp. 1021–1039, 2020.

[184] K. Valen-Sendstad, K.-A. Mardal, and D. A. Steinman, "High-resolution CFD detects high-frequency velocity fluctuations in bifurcation, but not sidewall, aneurysms," *Journal of Biomechanics*, vol. 46, no. 2, pp. 402 – 407, 2013. Special Issue: Biofluid Mechanics.

[185] "The vascular modelling toolkit." http://www.vmtk.org/index.html. Accessed: 2022-06-01.

[186] K. Huang, M. Krügener, A. Brown, F. Menhorn, H.-J. Bungartz, and D. Hartmann, "Machine learning-based optimal mesh generation in computational fluid dynamics," 2021. preprint, Accessed: 2022-03-30.

[187] S. Si, Y. Pang, S. Xiao, Y. Liu, L. Qi, and Y. He, "A method of detecting surface mesh quality based on deep learning," in *Lecture Notes in Electrical Engineering*, pp. 742–754, Springer Singapore, 2021.

[188] K. Simonyan and A. Zisserman, "Very deep convolutional networks for large-scale image recognition," 2015.

[189] G. Li, H. Wang, M. Zhang, S. Tupin, A. Qiao, Y. Liu, M. Ohta, and H. Anzai, "Prediction of 3D cardiovascular hemodynamics before and after coronary artery bypass surgery via deep learning," *Communications Biology*, vol. 4, no. 1, pp. 99–107, 2021.

[190] R. Gharleghi, G. Samarasinghe, A. Sowmya, and S. Beier, "Deep learning for time averaged wall shear stress prediction in left main coronary bifurcations," in *International Symposium on Biomedical Imaging*, pp. 1–4, IEEE, 2020.

[191] B. Thamsen, P. Yevtushenko, L. Gundelwein, A. Setio, H. Lamecker, M. Kelm, M. Schafstedde, T. Heimann, T. Kuehne, and L. Goubergrits, "Synthetic database of aortic morphometry and hemodynamics: Overcoming medical imaging data availability," *IEEE Transactions on Medical Imaging*, vol. 40, no. 5, pp. 1438–1449, 2021.

[192] L. Liang, W. Mao, and W. Sun, "A feasibility study of deep learning for predicting hemodynamics of human thoracic aorta," *Journal of Biomechanics*, vol. 99, pp. 109–106, 2019.

[193] J. Suk, P. de Haan, P. Lippe, C. Brune, and J. M. Wolterink, "Mesh convolutional neural networks for wall shear stress estimation in 3d artery models," in *Lecture Notes in Computer Science*, pp. 93–102, Springer International Publishing, 2022.

[194] S. Lapuschkin, S. Wäldchen, A. Binder, G. Montavon, W. Samek, and K.-R. Müller, "Unmasking clever hans predictors and assessing what machines really learn," *Nature Communications*, vol. 10, no. 1, p. 1096, 2019.

[195] A. Narla, B. Kuprel, K. Sarin, R. Novoa, and J. Ko, "Automated classification of skin lesions: From pixels to practice," *Journal of Investigative Dermatology*, vol. 138, no. 10, pp. 2108–2110, 2018.

[196] G. Yang, Q. Ye, and J. Xia, "Unbox the black-box for the medical explainable ai via multi-modal and multi-centre data fusion: A mini-review, two showcases and beyond," *Information Fusion*, vol. 77, pp. 29–52, 2022.

[197] C. Meske, E. Bunde, J. Schneider, and M. Gersch, "Explainable artificial intelligence: Objectives, stakeholders, and future research opportunities," *Information Systems Management*, vol. 39, no. 1, pp. 53–63, 2022.

[198] C. Gillmann, L. Peter, C. Schmidt, D. Saur, and G. Scheuermann, "Visualizing multimodal deep learning for lesion prediction," *IEEE Computer Graphics and Applications*, vol. 41, no. 5, pp. 90–98, 2021.

[199] R. Yu and L. Shi, "A user-based taxonomy for deep learning visualization," *Visual Informatics*, vol. 2, no. 3, pp. 147–154, 2018.

[200] J. Lötsch, D. Kringel, and A. Ultsch, "Explainable artificial intelligence (xai) in biomedicine: Making ai decisions trustworthy for physicians and patients," *BioMedInformatics*, vol. 2, no. 1, pp. 1–17, 2022.

[201] T. Rios, B. van Stein, S. Menzel, T. Back, B. Sendhoff, and P. Wollstadt, "Feature visualization for 3d point cloud autoencoders," in *2020 International Joint Conference on Neural Networks*, pp. 1–9, 2020.

[202] Y. Zhang, Y. Weng, and J. Lund, "Applications of explainable artificial intelligence in diagnosis and surgery," *Diagnostics*, vol. 12, no. 2, p. 237, 2022.

[203] A. Niemann, S. Weigand, T. Hoffmann, M. Skalej, R. Tulamo, B. Preim, and S. Saalfeld, "Interactive exploration of a 3D intracranial aneurysm wall model extracted from histologic slices," *International Journal of Computer Assisted Radiology and Surgery*, vol. 15, pp. 99–107, 2019.

[204] A. Niemann, S. Voß, R. Tulamo, S. Weigand, B. Preim, P. Berg, and S. Saalfeld, "Complex wall modeling for hemodynamic simulations of intracranial aneurysms based on histologic images," *International Journal of Computer Assisted Radiology and Surgery*, p. 597–607, 2021.

[205] J. Kather, C.-A. Weis, F. Bianconi, S. Melchers, L. Schad, T. Gaiser, A. Marx, and F. Zöllner, "Multi-class texture analysis in colorectal cancer histology," *Scientific Reports*, vol. 6, pp. 279–288, 2016.

[206] T. Caliński and H. JA, "A dendrite method for cluster analysis," *Communications in Statistics - Theory and Methods*, vol. 3, pp. 1–27, 1974.

[207] N. Otsu, "A threshold selection method from gray-level histograms," *IEEE Transactions on Systems, Man, and Cybernetics*, vol. 9, no. 1, pp. 62–66, 1979.

[208] A. Niemann, A. Talagini, P. Kandapagari, B. Preim, and S. Saalfeld, "Tissue segmentation in histologic images of intracranial aneurysm wall," *Interdisciplinary Neurosurgery*, vol. 26, pp. 101–107, 2021.

[209] J. M. Prewitt, "Object enhancement and extraction," *Picture Processing and Psychopictoric*, pp. 75–149, 1970.

[210] R. C. Gonzalez, R. E. Woods, and S. L. Eddins, *Digital Image processing using MATLAB*. Upper Saddle River, NJ: Pearson/Prentice Hall, 2004.

[211] P. Cignoni, M. Callieri, M. Corsini, M. Dellepiane, F. Ganovelli, and G. Ranzuglia, "Meshlab: an open-source mesh processing tool.," *Eurographics Italian Chapter Conference*, vol. 1, pp. 129–136, 2008.

[212] A. Niemann, B. Preim, and S. Saalfeld, "Shrinking tube mesh: combined mesh generation and smoothing for pathologic vessels," *Current Directions in Biomedical Engineering*, vol. 6, no. 1, pp. 202–206, 01 May. 2020.

[213] Unknown, "Video of heat shrink tube before and after," *https://commons.wikimedia.org/w/index.php?title=File%3AVideo_of_Heat_shrink_tube_before_and_after.ogv*, p. accessed 30.03.2020.

[214] V. Caselles, R. Kimmel, and G. Sapiro, "Geodesic active contours," *International Journal of Computer Vision*, vol. 22, no. 1, pp. 61–79, 1997.

[215] E. Haber and J. Modersitzki, "Intensity gradient based registration and fusion of multi-modal images," in *Medical Image Computing and Computer-Assisted Intervention – MICCAI 2006*, (Berlin, Heidelberg), pp. 726–733, Springer Berlin Heidelberg, 2006.

[216] P. Berg, D. Stucht, G. Janiga, O. Beuing, O. Speck, and D. Thévenin, "Cerebral blood flow in a healthy circle of willis and two intracranial aneurysms: computational fluid dynamics versus four-dimensional phase-contrast magnetic resonance imaging," *Journal of biomechanical engineering*, vol. 136, no. 4, pp. 1–9, 2014.

[217] P. J. Besl and N. D. McKay, "Method for registration of 3-d shapes," in *Sensor fusion IV: control paradigms and data structures*, vol. 1611, pp. 586–606, International Society for Optics and Photonics, 1992.

[218] R. Haak, M. J. Wicht, M. Hellmich, G. Nowak, and M. J. Noack, "Influence of room lighting on grey-scale perception with a CRT-and a TFT monitor display," *Dentomaxillofacial Radiology*, vol. 31, no. 3, pp. 193–197, 2002.

[219] W. Jacquet, R. G. Cleymaet, and P. Bottenberg, "Grey value contrast sensitivity of dental practitioners in function of luminance and age," *Dentomaxillofacial Radiology*, vol. 48, no. 6, pp. 2018–2028, 2019.

[220] O. van Kaick, N. Fish, Y. Kleiman, S. Asafi, and D. Cohen-Or, "Shape segmentation by approximate convexity analysis," *ACM Trans. on Graphics*, 2014.

[221] Y. Feng, Y. Feng, H. You, X. Zhao, and Y. Gao, "Meshnet: Mesh neural network for 3D shape representation," vol. 33, pp. 8279–8286, 2019.

[222] L. Schneider, A. Niemann, O. Beuing, B. Preim, and S. Saalfeld, "Medmeshcnn – enabling meshcnn for medical surface models," *Computer Methods and Programs in Biomedicine*, vol. 210, pp. 106–112, 2021.

[223] C. R. Qi, L. Yi, H. Su, and L. J. Guibas, "Pointnet++: Deep hierarchical feature learning on point sets in a metric space," in *Advances in Neural Information Processing Systems* (I. Guyon, U. V. Luxburg, S. Bengio, H. Wallach, R. Fergus, S. Vishwanathan, and R. Garnett, eds.), vol. 30, Curran Associates, Inc., 2017.

[224] C. R. Qi, H. Su, K. Mo, and L. J. Guibas, "Pointnet: Deep learning on point sets for 3d classification and segmentation," *arXiv preprint arXiv:1612.00593*, 2016.

[225] L. Spitz, U. Niemann, O. Beuing, B. Neyazi, I. E. Sandalcioglu, B. Preim, and S. Saalfeld, "Combining visual analytics and case-based reasoning for rupture risk assessment of intracranial aneurysms," *International Journal of Computer Assisted Radiology and Surgery*, vol. 15, no. 9, pp. 1525–1535, 2020.

[226] B. O. Community, *Blender - a 3D modelling and rendering package*. Blender Foundation, Stichting Blender Foundation, Amsterdam, 2018.

[227] Matlab, "Feature edges." https://de.mathworks.com/help/matlab/ ref/triangulation.featureedges.html, 2013.

[228] J. Cebral, F. Mut, J. Weir, and C. M. Putman, "Quantitative characterization of the hemodynamic environment in ruptured and unruptured brain aneurysms," *American journal of neuroradiology*, vol. 32, pp. 145–151, 2011.

[229] S. Valette, J.-M. Chassery, and R. Prost, "Generic remeshing of 3D triangular meshes with metric-dependent discrete voronoi diagrams," *Transactions on Visualization and Computer Graphics*, vol. 14, pp. 369–381, 2008.

[230] D. Cohen-Steiner and J.-M. Morvan, "Restricted delaunay triangulations and normal cycle," *Proceedings of the Annual Symposium on Computational Geometry*, pp. 312–321, 2003.

[231] M. Inui, N. Umezu, and R. Shimane, "Shrinking sphere: A parallel algorithm for computing the thickness of 3D objects," *Computer-Aided Design and Applications*, vol. 13, no. 2, pp. 199–207, 2016.

[232] R. B. Rusu, N. Blodow, and M. Beetz, "Fast point feature histograms (fpfh) for 3d registration," *2009 IEEE International Conference on Robotics and Automation*, pp. 3212–3217, 2009.

[233] S. Salti, F. Tombari, and L. Di Stefano, "Shot: Unique signatures of histograms for surface and texture description," *Computer Vision and Image Understanding*, vol. 125, pp. 251–264, 2014.

[234] J. P. Ahrens, B. Geveci, and C. C. Law, "Paraview: An end-user tool for large-data visualization," in *The Visualization Handbook*, 2005.

[235] A. Mandal, "Master thesis," 2021.

[236] I. T. Jolliffe and J. Cadima, "Principal component analysis: a review and recent developments," *Philosophical Transactions of the Royal Society A: Mathematical, Physical and Engineering Sciences*, vol. 374, no. 2065, pp. 2065–2072, 2016.

[237] A. Niemann, L. Schneider, B. Preim, S. Voß, P. Berg, and S. Saalfeld, "Towards deep learning-based wall shear stress prediction for intracranial aneurysms," in *Bildverarbeitung für die Medizin 2021*, pp. 105–110, 2021.

[238] A. Niemann, N. Larsen, B. Preim, and S. Saalfeld, "Wall enhancement segmentation for intracranial aneurysm," vol. 6, pp. 202–206, 2020.

[239] A. Niemann, D. Behme, N. Larsen, B. Preim, and S. Saalfeld, "Deep learning based semantic vessel graph extraction for intracranial aneurysm rupture risk management," *unpublished*.

[240] A. Niemann, A. Mandal, L. Kuttya, V. Sudhia, P. Berg, B. Preim, and S. Saalfeld, "Multimodal exploration of the intracranial aneurysm wall," *unpublished*.

[241] A. Niemann, B. Preim, and S. Saalfeld, "Explainable AI: geometric deep learning rupture prediction on patient-specific meshes of intracranial aneurysms," *unpublished*.

[242] A. Niemann, B. Preim, and S. Saalfeld, "Centerline and blockstructure for fast structured mesh generation," *unpublished*.

[243] A. Niemann, B. Preim, and S. Saalfeld, "Enhancing intracranial aneurysm rupture risk assessment with deep learning on patient-specific 3D geometries," *unpublished*.